Measuring and manipulating chiral light-matter interaction on the attosecond timescale

Debobrata Rajak

université de BORDEAUX

École doctorale des Sciences Physiques et de l'Ingénieur

Mesure et contrôle de l'interaction lumière-matière chirale à l'échelle attoseconde.

THÈSE

présentée et soutenue publiquement le

16/01/2023

pour l'obtention du

Doctorat de l'université de Bordeaux

Spécialité lasers, matière et nanosciences

par

Debobrata RAJAK

Directeur : Yann MAIRESSE

Composition du Jury :

M. Yann MAIRESSE	Directeur de recherche, CNRS (Talence)	**Directeur de thèse**
M. Eric CORMIER	Professeur des universités, Université de Bordeaux (Talence)	Président du jury
Mme Lou BARREAU	Maître de conférences, Université Paris Saclay (Orsay)	Examinatrice
M. Thierry RUCHON	Directeur de recherche, CEA, LIDYL (Gif-sur-Yvette)	Rapporteur
Mme Caterina VOZZI	Directrice de recherche, CNR- Politecnico di Milano (Milan, ITALIE)	Rapporteure

Centre Lasers Intenses et Applications, UMR 5107
Université de Bordeaux, CNRS, CEA
43 rue Pierre Noailles, 33400, Talence, France

Acknowledgements

First and foremost, I would like to warmly acknowledge the members of my jury, Thierry Ruchon, Caterina Vozzi, Eric Cormier and Lou Barreau for reviewing my PhD thesis and attending my defence. I would also like to thank them for examining my thesis, which is a tedious task, which they all have enthusiastically accepted this task and I am sincerely grateful for it.

I would also like to thank my PhD supervisor, Yann Mairesse for all the help and support. I will be forever grateful for your support especially during the COVID lockdowns, acclimatization in France and all throughout the preparation of the manuscript. Thank you for the support and help with the french translations and paperwork. Thank you for your honest feedbacks and help as this has helped me to nurture myself to become a better scientist and a person in the process. I have truly enjoyed working with you.

I would also like thank Valérie Blanchet, my unofficial second supervisor. Thank you for the support and help throughout my thesis especially with my acclimatization process. I truly enjoyed working with you although the COLTRIMS had other plans in its mind. Thank you for the beers and deep conversations. Thank you for your honest feedbacks, it has definitely helped me. Thank you for your patience and zen attitude.

I would also like to thank Nirit Dudovich, my unofficial third supervisor. Thank you for the discussions and help throughout my thesis. It was great working with you. Thank you Omer, Chen, Noa and Shaked it was a pleasure to work with you.

Thank you Antoine, Etienne, and Sandra for being such wonderful people to work with. Thank you Fabrice, for the wonderful discussions on PECD, non-dipole interactions and Octopus. It was a pleasure discussing from quantum mechanics to wars all the way up to economics. Thank you Bernard for the wonderful discussions over a glass of wine. Thank you Samuel, it was a pleasure working with you. I might be stealing some of your jokes, they are hilarious. Thank you Dominique for the lunch table discussions and the discussions on lasers over a smoke. I will take this opportunity to thank Baptiste for his wonderful lectures on SFA and discussions. I would also like to thank Stéphane for his endless laser support. I would also like to thank Jérôme and Patrick. I warmly thank Romain, Anatoly and Nikita for their help in the arduino projects, labview and numerous other technical help. I also warmly thank the administrative staff, Céline, Sonia and Sophie, for helping me getting through the paperwork with ease. Laurent and Franck, I warmly thank you for the help in the mechanics workshop. I thank Richard and Gaëtan for all the help especially with setting up the remote monitoring service. Gaëtan I will miss our discussions. I can not cite every single person of the lab for all the good moments spent together, but let me assure you all that I have really enjoyed being in the nice and helpful atmosphere

that you have extended to me.

I would like to thank my family for their continuous support. I would also like to thank my friends for making my life a bit more interesting.

Special thanks to all the photons and to all the chiral molecules, especially α-Pinene, that I have ionized.

Contents

Résumé

Les molécules chirales existent sous deux formes miroir, appelées énantiomères, qui ne sont pas superposables. Elles ont les mêmes propriétés physiques et chimiques. La chiralité moléculaire est une propriété fondamentale du monde microscopique qui régit toute la biosphère. Tous les organismes vivants sont constitués de blocs élémentaires chiraux (par exemple, des sucres ou des acides aminés). Comme les processus biologiques sont sensibles à la chiralité, révéler les aspects dynamiques de la chiralité est d'une importance primordiale pour la chimie, la biologie et la pharmacologie. Comme les énantiomères d'une molécule chirale ont les mêmes propriétés chimiques et physiques, il est extrêmement difficile de les distinguer les uns des autres. Ils ne peuvent être distingués que par leur interaction avec une sonde chirale, par ex. par des processus chimiques impliquant d'autres molécules chirales. Ces processus chimiques sont induits par des interactions électroniques, qui se produisent sur des échelles de temps atto-femto-pico seconde, et sont sensibles à la structure moléculaire.

Dans cette thèse, nous utilisons la lumière ultracourte polarisée circulairement et elliptiquement, qui agit comme une sonde chirale, pour étudier les interactions lumière chirale-matière à des échelles de temps atto-femto seconde. Lorsqu'une distribution de molécules chirales orientées de manière aléatoire est ionisée à l'aide d'une lumière polarisée circulairement, les électrons éjectés sont émis de manière asymétrique dans la direction de propagation du laser. Cette émission asymétrique des électrons dépend du sens de rotation de la lumière polarisée circulairement et de l'énantiomère considéré. En utilisant ce phénomène, nous étudions la chiralité moléculaire en modifiant l'ellipticité et la longueur d'onde du rayonnement ionisant ainsi que son intensité, et à l'aide de techniques de détection synchrones. En changeant l'ellipticité et la longueur d'onde du rayonnement ionisant, nous sommes en mesure d'effectuer une analyse multidimensionnelle de l'interaction lumière chirale-matière en régime de champ multiphotonique.

En augmentant encore l'intensité du rayonnement électromagnétique, il devient possible d'atteindre des valeurs de champ électrique similaires au potentiel de liaison atomique/moléculaire. Lorsqu'un atome/molécule est exposé à des champs électromagnétiques aussi intenses, la barrière de potentiel de l'atome/molécule est considérablement modifiée par le champ électromagnétique. Cette modification est un processus dynamique, se produisant au cours de l'oscillation du champ électromagnétique, c'est-à-dire sur l'échelle de temps de l'attoseconde (il suffit de 500 as pour qu'un champ électrique visible passe de son pic à zéro). Au maximum du champ laser, la barrière de potentiel moléculaire est considérablement abaissée et les électrons peuvent sortir par effet tunnel dans le continuum. Ces électrons sont alors accélérés par le champ laser oscillant et peuvent suivre différentes trajectoires. Certains d'entre eux peuvent

être ramenés vers le cœur ionique, conduisant à une variété de processus : re-diffusion, ou recombinaison vers l'ion émettant un photon XUV, ou encore diffraction sur le potentiel moléculaire lui-même. Ces phénomènes sont appelés « auto-imagerie ». Nous montrons comment il est possible d'étudier les interactions lumière chirale-matière grâce à l'auto-imagerie, ce qui permet de mesurer des informations structurelles et dynamiques avec des résolutions sans précédent - Angströms et attosecondes.

Abstract

Chiral molecules exist as two mirror forms, so-called enantiomers, that are not superimposable to their mirror image. They have the same physical and chemical properties. Molecular chirality is a fundamental property of the microscopic world which rules the whole biosphere. All living organisms are made of chiral building blocks (e.g. sugars or amino acids). As biological processes are chiral-sensitive, unraveling the dynamical aspects of chirality is of prime importance for chemistry, biology and pharmacology. As the enantiomers of a chiral molecule have the same chemical and physical properties it is extremely difficult to distinguish them from another. They can only be distinguished via their interaction with a chiral probe, eg. through chemical processes involving other chiral molecules. These chemical processes are mediated by electronic interactions, which happen from atto-femto-pico second timescales, and are sensitive to the molecular structure.

In this thesis we use ultrashort circularly and elliptically polarized light, which act as a chiral probe, to study chiral light matter interactions in atto-femto second timescales. When a distribution of randomly oriented chiral molecule is ionized using a circularly polarized light, the ejected electrons are asymmetrically emitted in the laser propagation direction. This asymmetric emission of the electrons depends on the handedness of the circularly polarized light and the chiral molecule. Using this phenomenon, we investigate molecular chirality by changing the ellipticity and wavelength of the ionizing radiation along with its intensity using lock in detection techniques. By changing the ellipticity and wavelength of the ionizing radiation we are able to perform a multidimensional analysis of the chiral light matter interactions in multiphoton field regime.

Upon further increasing the intensity of the electromagnetic radiation it becomes possible to reach electric field values similar to the atomic/molecular binding potential. When an atom/molecule is exposed to such intense electromagnetic fields the potential barrier of the atom/molecule is considerably modified by the electromagnetic field. This modification is a dynamical process, occurring as the electromagnetic field oscillates, i.e. on the attosecond timescale (it takes only ~ 500 as for a visible electric field to go from its peak to zero). At the maximum of the laser field, the molecular potential barrier is lowered significantly and the electrons can tunnel out of this reduced barrier into the continuum. These tunnelled electrons are then driven by the oscillating laser field and can follow different trajectories. Some of them can be driven back to the ionic core, leading to a variety of processes: re-scattering, or recombination back to the ion emitting an XUV photon, or even diffraction from the molecular potential itself. These phenomena are referred to as "self-imaging". We show how it is possible to investigate chiral

light matter interactions through self-imaging, which enables measuring structural and dynamics information with unprecedented resolutions – Angströms and attoseconds.

Chapter 1

Introduction

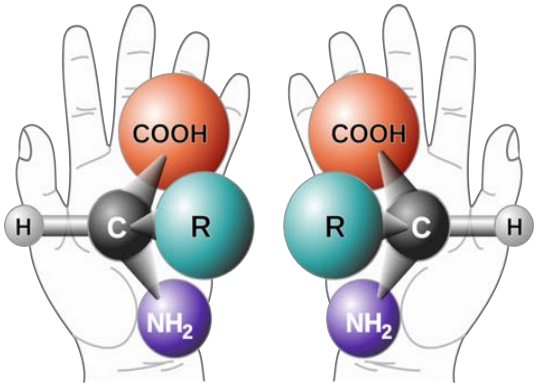

The work conducted in this thesis aimed at investigating chiral light-matter interactions in ultrafast timescales. In particular chiral molecules were studied in gas phase using ultrashort laser pulses in conjunction with kinematically and angularly resolved photoelectron/photoion spectroscopy. This chapter presents a general introduction to the field as well as the structure of the manuscript.

I Chirality

The geometric property due to which mirror images of an object cannot be superposed on to each other is called chirality. For example the palms of our two hands are mirror images of each other but are different. This geometrical property exists in the molecular level too. The two images of a chiral molecule are called enantiomers, and are classified as left or levo (-) and right handed or dextro (+). In general, enantiomers have the same physical and chemical properties (melting point, density, ionization potential, etc.). But they interact differently in chemical reactions involving several chiral compounds. The outcome of such chemical reactions, called enantiospecific, will vary depending on the handedness of the molecules participating. All living organisms are constituted of fundamental chiral building blocks, e.g. sugars and amino-acids, which exist in nature in a predominant enantiomeric form. Due to this enantiospecificity, biological systems do not generally interact the same way with the two enantiomers of a molecule. For example, (+)-Methamphetamine is a strong psychotropic synthetic drug while (-)-Methamphetamine is

an over-the-counter nasal decongestant. Thus, studying chiral molecules is of great importance, especially in pharmacology as many biological process are sensitive to the chiral nature of the molecules.

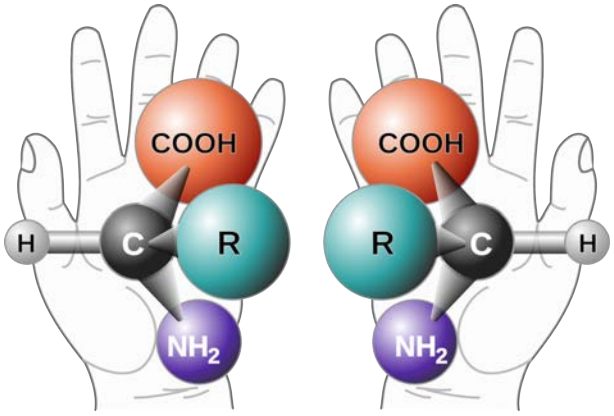

Figure 1.1 – *Concept of chirality, illustrated at the macroscopic scale and molecular scale. Extracted from [PD-USGov-NASA].*

Due to their same chemical and physical properties, it is a challenging task to distinguish and characterize two enantiomers of a molecule. Historically, molecular chirality was studied using light-matter interactions. It was observed by Arago [Arago 11] that the orientation of linearly polarized light gets rotated while passing through a quartz crystal. Similar rotations in the orientation of a linearly polarized light was reported in liquids by Biot [Biot 15] [Biot 19]. The schematics of the experimental setup to measure optical rotation is shown in Fig. 1.2. It was also observed that opposite enantiomers of a chiral molecule rotate the orientation of the linearly polarized in opposite directions, where the magnitude of the rotation is compound-specific. This chiroptical process is called optical rotation or optical activity.

Distinguishing two enantiomers of a chiral molecule requires a chiral element. In optical rotation, this chiral element is given by the observer, who is able to distinguish in which direction the linearly polarized field has rotated. Most chiroptical techniques rely on a different configuration, where it is the light that is chiral. Indeed, right circularly polarized light interacts differently with a chiral molecule of a given handedness compared to a left circularly polarized light. This occurs for instance in absorption circular dichroism (CD), which is defined as the difference in the absorption of light by the enantiomers depending on the helicity of the incident light, as shown in Fig. 1.3. This process occurs over a broad range of wavelengths, from the infrared to the X-ray range, and is a widely used spectroscopic tool. However, the circular dichroism effects are generally rather weak, producing relative signals in the 10^{-4} range. This is due to the fact that they originate from magnetic dipolar transitions, electric quadrupolar, or higher perturbative orders. This makes CD measurements very challenging in diluted samples, which has been a long standing obstacle to observing ultrafast dynamics of chiral molecules in the gas phase.

This challenge was overcome by the advent of new light-matter interaction schemes producing enantiosensitive signals of several percents in the electric-dipole approximation [Ritchie 76] [Powis 00] [Böwering 01]. It was observed that when a distribution of randomly oriented chi-

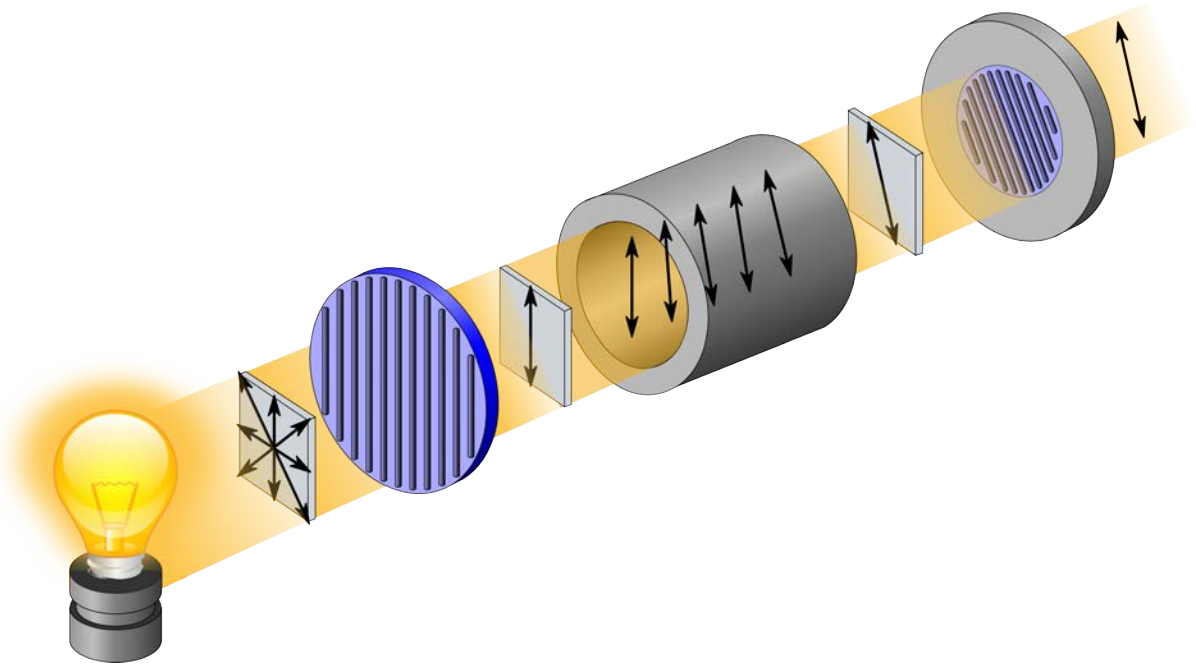

Figure 1.2 – *Principle of operation of a polarimeter to measure optical rotation. We see that when a linearly polarized light is incident on a chiral medium the orientation of the linearly polarized light gets rotated. Extracted from [Kaidor].*

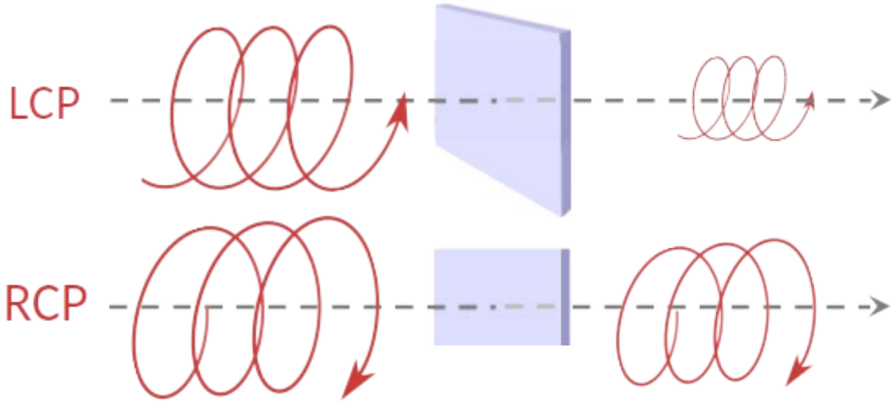

Figure 1.3 – *Principle of absorption circular dichroism, where the absorption coefficient of the chiral media depends on the helicity of circularly polarized light.*

ral molecule of a given handedness is ionized using circularly polarized light, then there is an asymmetric emission of photoelectrons along the propagation direction of the electromagnetic field. This asymmetric emission of photoelectrons is called Photoelectron Circular Dichroism (PECD). It depends on the handedness of the molecule and the helicity of the ionizing radiation, as shown in Fig. 1.4. Typically, these photoelectron asymmetries are in the range of several of percents.

The phenomenon can be understood through a hand-waving analogy of nut and bolts. When a the nut on a bolt is rotated in a clockwise direction this leads to a translational motion of the nut in the forward direction, as shown in Fig. 1.4. By contrast, when the nut is rotated

in an anticlockwise direction, it translates in a backward direction. Similarly, when a chiral molecule of a given handedness is ionized using a left circularly polarized light, more electrons are emitted in the backward direction. Changing the handedness of the ionizing radiation leads to a change in the direction of emission of photoelectrons, as shown in Fig. 1.4.

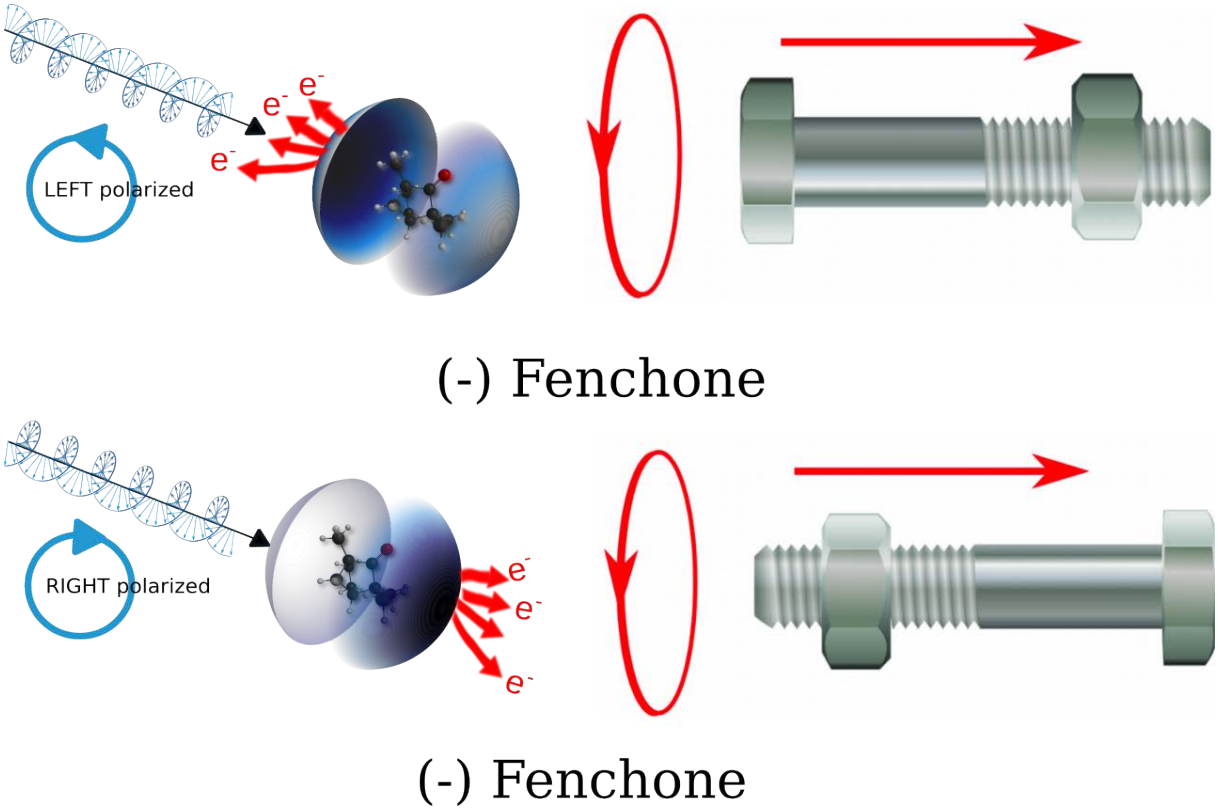

Figure 1.4 – *Principle of photoelectron circular dichroism (PECD) in the ionization of molecules. On the top row we see that when (-) Fenchone is ionized with a left circularly polarized light there is an asymmetric emission of photoelectrons along the light propagation direction. We see that more electrons are ejected in the backward direction. Whereas on changing the helicity of the light photoelectrons are ejected in the opposite direction. This can is analogus to the nut and bolt mechanism where the rotational motion of the nut is converted to a translational motion of the nut along the bolt.*

The PECD phenomenon has been evidenced for more that two decades [Ritchie 76] [Powis 00] [Böwering 01] [Nahon 04] [Lux 12] [Beaulieu 16] [Beauvarlet 22] and has given rise to many investigations. Most of them were conducted in the single-photon ionization regime, using synchrotron radiation [Böwering 01] [Nahon 04], and proved a very high spectroscopic sensitivity of this observable. PECD was then extended to the multiphoton and strong field regimes, giving rise to new questions. What is the role of resonances in the dichroic signal in multiphoton transitions? Is it possible to isolate the effect of bound-continuum and continuum-continuum transitions? How does the chirosensitive asymmetry vary with the ellipticity of the ionizing radiation in the non-linear regime? Also, how is the asymmetry affected when we increase the intensity of the ionizing radiation and move from single photon ionization to multiphoton ionization and all the way up to a regime where the strength of the electromagnetic field is show high that it deforms the chiral molecular potential? Are strong fields appropriate to probe chi-

rality? Is it possible to measure chiral laser-induced electron diffraction? Are there important chiroptical processes occurring in photoionization beyond the electric dipole approximation?

In this manuscript we try to answer some of these questions by investigating chiral-light matter interaction at femtosecond (10^{-15} s) and attosecond (10^{-18} s) time scales. This requires state-of-the-art technique to generate circularly polarized attosecond pulses along with strong field and molecular spectroscopy techniques for distinguishing and analyzing the results obtained.

Chapter 2 : describes our state of the art ultrashort high power high repetition rate photon sources and the methods required to characterize them. The two main detectors used throughout the thesis, namely velocity map imaging spectrometer (VMI) and COLTRIMS, are also presented.

In **Chapter 3 :** we use the aforementioned ultrashort light pulses to study chiral light-matter interactions at femtosecond timescales. We show that the use of elliptically polarized light, rather than circular polarized, is extremely beneficial to probe chiral molecules in the multiphoton ionization regime, leading to PhotoElectron Elliptical Dichroism. The PEELD provides a wealth of information with a higher sensitivity than PECD, revealing states which do not participate in PECD. We also discuss a lock-in detection measurement scheme to obtain photoelectron angular distributions and eventually 3D photoelectron elliptical dichroism distributions with high signal to noise ratio. We show that manipulating both the ellipticity and the wavelength of the ionizing laser provides a multi-dimensional approach to decouple the bound-bound and bound-continuum transitions. Last, we present our experimental results on fragment-resolved PECD.

In **Chapter 4 :**, we increase the laser intensity to reach the strong-field regime. This could at first sight look like a bad idea because in this regime the laser field often dominates the electronic dynamics, so that the molecular potential only has a very weak impact on the motion of the outgoing electron. However in elliptical polarization, electrons can be driven back to recollide with their parent ion. We find that the angular distribution of these high energy photo-electrons shows a strong forward-backward asymmetry, resulting from their re-scattering on the chiral ionic potential. The re-scattering electrons can penetrate deep inside the molecular potential, thus encoding structural chirosensitive information in laser induced electron diffraction. Furthermore, the interference between direct and indirect electrons opens the way to chiral photo-electron holography. In a second experiment, we use linearly polarized strong fields to ionize chiral molecules. This could at first sight look like an even worse idea. It is indeed generally assumed that circularly polarized light is needed to reveal chirality. However, we observe a rotation of the photoelectron angular distribution, about the laser propagation axis, depending on the handedness of the molecule. This new effect, conceptually similar to optical rotation, produces surprisingly strong signatures of the interaction between the laser magnetic field and the chiral potential.

Finally, we briefly summarize our results in **Chapter 5 :** and discuss some ongoing projects along with the short and long term perspectives they have opened.

This thesis took place within a collaborative project between Weizmann Institute and CNRS CELIA, Attochiral. Only the results obtained at CELIA are presented in this manuscript. Many experiments were conducted collaboratively, but due to COVID restrictions and lockdowns the

collaboration was held remotely. In addition to the work presented here, I participated in the analysis of several experiments conducted at Weizmann and was in charge of organizing regular meetings between the two teams.

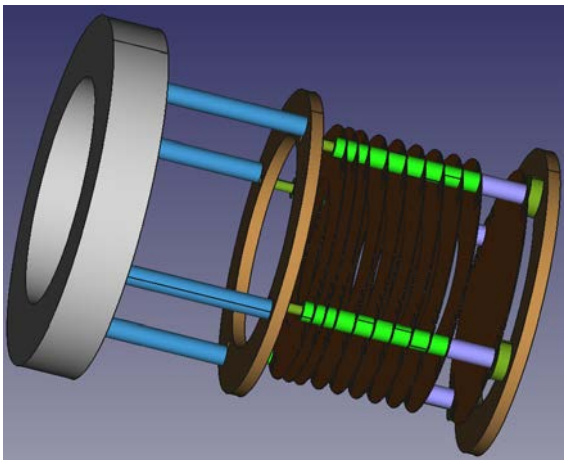

Chapter 2

Experimental Development

I Blast Beat Beamline

In a molecular reaction resulting from absorption of light, such as photo-ionization or photo-dissociation, the dynamical evolution from a given initial to a final state - often passing through short lived intermediate state/s - happens in the natural time and length scales of femtoseconds-attoseconds ($10^{-15} - 10^{-18}$ s) and Angströms (10^{-10} m). To unravel the dynamics at these short timescales, dedicated time-dependent methods are required to isolate and study the characteristic features of the intermediate states. The most commonly used experimental technique to track the time evolution of these photo-induced process is pump-probe spectroscopy. To realize this, one generally use light pulses whose duration is short enough to resolve the time-scale of the process, typically in the order of femtoseconds.

With the advent on laser technology, femtosecond pulses with high peak power could be generated. For many years Ti:sapphire (Ti:Sa) have been the workhorse and unanimous materiel of choice for oscillators and amplifiers to generate ultrashort pulses due to their large gain bandwidth ($700 - 1000$ nm) facilitating the generation of very short pulses [Moulton 86]. Typically with Ti:Sa lasers one can generate pulses as short as 20 fs, centered at 800 nm, with average power of a few tens of W and typical repetition rates between 1 Hz and 10 kHz. These ultrashort and intense pulses are generated using a combination of technical elements like chirped pulse amplification [Strickland 85] and Kerr lens mode locking [Szipöcs 94]. These pulses can be further shortened by spectral broadening, e.g. in gas-filled hollow core fibers [Nisoli 96] etc. The Ti:Sa gain medium is limited due to the short upper state lifetime ($\sim 3.5\mu$s) and quantum defects. This inherently puts limitations on the average power and repetition rate due to the thermal load on the Ti:Sa crystals.

In recent years the pressing issue of handling thermal load has been mediated by using ytterbium-doped optical fibers instead of solid-state crystals [Schmidt 17] [Stark 21]. In this configuration the thermal load of the pump laser is distributed over the whole length of the fiber (high surface to volume ratio) leading to efficient thermal load dissipation, the limitation being the damage threshold of the optical fiber itself. Furthermore, the use of optical fibers,

which have wave-guide properties, helps in the production of stable and compact sources with excellent spatial profiles. The long upper state lifetime of $\sim 900\mu$s facilitates in obtaining very high repetition rates of 2 MHz. The primary drawback of these gain medium is the long pulse duration inherent to their narrower amplification band compared to Ti:Sa .

Throughout my thesis the main primary source of photons was the Blast-Beat system at CELIA provided by Amplitude Systemes (dual Tangerine Short Pulse). It is a Yb doped fiber laser system, made of a single fiber oscillator seeding two amplifiers in parallel. Each amplifier provides an average power of up to 50 W. The pulses are centered at 1030 nm (FWHM = 18.5 nm), with pulse duration of 130 fs. The laser beam at the output of each amplifier has a diameter of 2.7 mm ($I_{max}1/e^2$ diameter) and a very good spatial quality, characterized by a measured M^2 of 1.2 & 1.1 respectively for the two amplifiers . The short pulse duration is achieved thanks to a phase mask placed at the output of the oscillator which pre-compensates the spectral phase distortions in the beam. The repetition rate of the laser can be tuned from 166 kHz to 2 MHz. Changing the repetition rate modifies the pulse energy, intensity and consequently the non-linear phase accumulated in the amplifier. Three predefined phase masks are used to optimize the output pulse duration for different ranges of repetition rates. These masks have been optimized for a 50 W beam. Hence, the laser is always used at maximum power.

The two amplifiers are operated independently but must run at the same repetition rate, defined by the oscillator. The pulses they deliver are in principle passively synchronized, such that one amplifier could be used to generate pump pulses and the other one probe pulses. The whole laser system being a plug-and-play industrial type, is very convenient to operate on a day to day basis. The high repetition rates allows the acquisition of more statistically significant data resulting in better signal-to-noise ratio, especially for coincidence detection and inefficient processes (like High Harmonic Generation). The high average power of the laser imposes using special dielectric and highly reflective ($R > 99.9\%$) mirrors to avoid absorption and heating. Such mirrors, in combination with low thermal drift mounts, are used to ensure the stability of the laser beams.

I. 1 Power modulation and Stability

Power modulation

To minimize the influence of non-linear phase distortions in the amplifiers, which change the pulse duration as well as the spatial the quality of the beam, the laser is operated at full power. Multi-photon ionization and strong field interactions are highly non-linear processes. They are thus extremely sensitive to the intensity of the incident electromagnetic wave. This makes the stability and precision control of the laser output power of utmost importance. To modulate the 50 W at the output of the laser a half waveplate is mounted in front of a fixed polarizer. The angle of incidence of the laser on the polarizer is optimized such that the polarization after it is purely linear. This criterion for selection of the alignment of the polarizer with respect to the half waveplate helps in the reduction of any polarization artifacts in the laser beam, as there is always some amplified spontaneous emission from the laser which can have different orientations of linear polarization. The schematics of the beamline is shown in Fig. 2.1

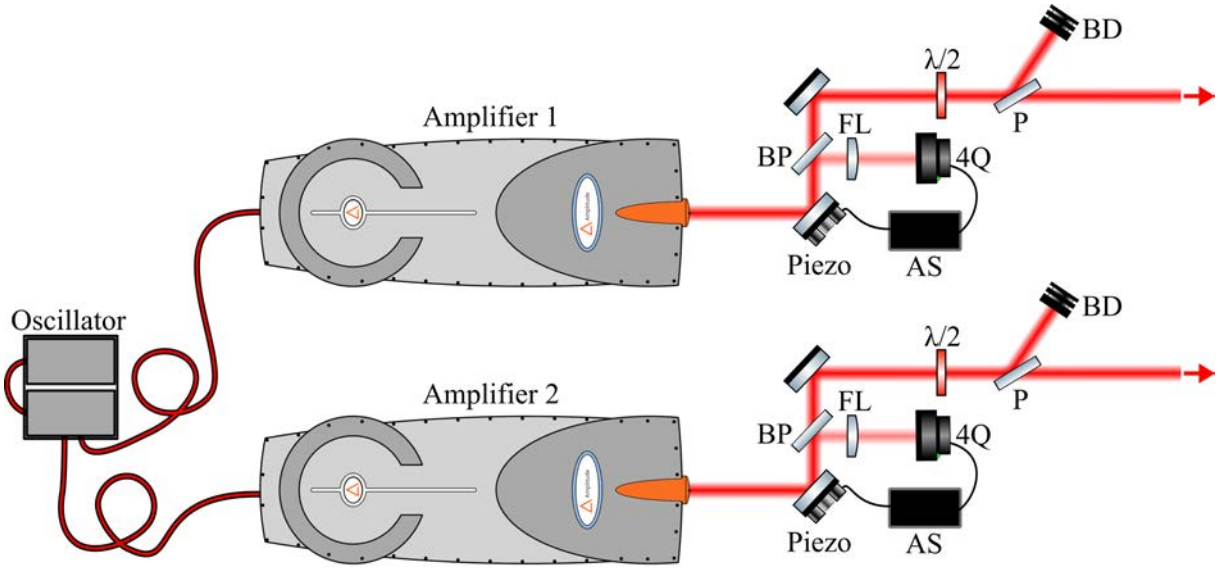

Figure 2.1 – *Fiber laser source, with the active pointing stabilization and the power modulation setup, see text for details. Note BP, 4Q, AS, P and BD stands for Brewster plate, quadrant photo-diode, active stabilization feedback, polarizer and beam dump respectively [Bloch 20].*

Stability

The commercially available Tangerine has 1.2% RMS shot-to-shot energy stability. The long term stability of the laser is essential for experiments involving long term acquisition. Fiber lasers are intrinsically stable due to the fact that the fiber acts as a wave-guide. Furthermore the breadboard on which the amplifier is mounted is actively maintained at a constant temperature to reduce any slow drifts. However there could be fluctuations or drifts in the laser power output and the positioning of the beam over long distances and also after traveling through a lot of optical components, especially through transmittive optics, due to thermal effects and air currents.

To negate these thermal drifts over time, an active beam stabilizer from MRC Systems GmbH is used. The output of the laser directly falls on a piezo actuator mirror, whose reflected beam falls on a Brewster plate. A pick-off is taken from it and is focused by a lens of focal length 150 mm onto a 4-quadrant-diode. The 4-quadrant-diode is equipped with electronic readout for x and y position along with the intensity level on the detector. The piezo actuator mirrors are controlled steplessly via an analog control loop, hence the angular resolution depends on the resolution of the 4-quadrant-diode itself. For the beam size of Tangerine of 2.7 mm the associated angular accuracy that can be achieved by the active beam stabilization system is about ~ 1 μrad. Along with the use of this active beam stabilization system, a cover is generally put on all sides of the laser beam path to reduce the effects from air currents.

With these modifications in place the stability of the laser was measured using an Ophir power meter at a distance of 440 cm, after the power modulation unit, 7 mirrors and 1 polarizer. The power meter was placed at a distance of 75 mm away from a lens of focal length -75 mm. This was done to amplify any fluctuations in the beam pointing. The Ophir power meter can measure the power as well as the x and y position of the beam with a resolution of 10 μm. The temperature under the hood of the optical table was recorded simultaneously.

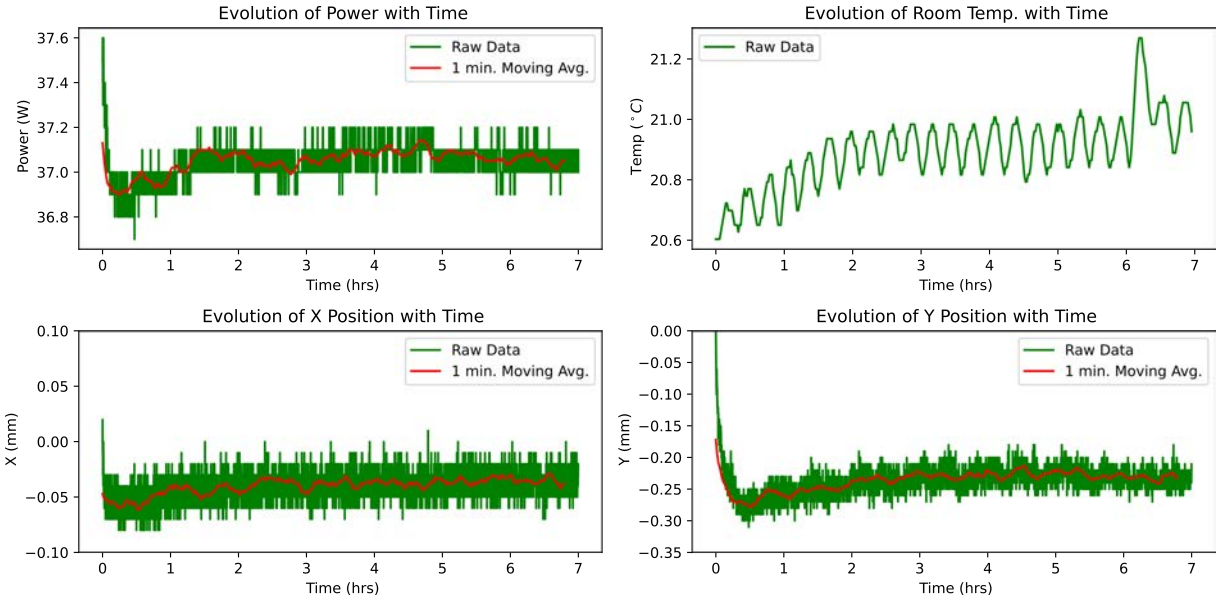

Figure 2.2 – *Stability tests performed on the fundamental harmonics (*1030*nm) at a distance of* $\sim 4.4m$ *away from the exit of the amplifier. (a) Shows the evolution of power (b) temperature under the hood of the optical table in* 7*hrs. The resolution of the power meter being* $0.1\,W$ *and temperature* $0.1°\,C$*. (c) and (d) shows the evolution of the horizontal and vertical position of the laser with time. Note that the resolution of the position is* $10\mu m$*. The red curve is 1min moving point average.*

Figure 2.2 shows the results of a long term stability test for 7 hours from the start-up time. We see that in the initial 30 minutes to 1 hour there is a transient behavior in both the power and the positioning of the laser beam. This corresponds to the warm-up time of the laser. There is a periodic fluctuation of the room temperature with a period of ~ 20 minutes and a peak-to-peak variation of about $0.1 - 0.2$ °C. Along with this periodic oscillation, there is slow increase in the room temperature by ~ 0.3 °C in the first couple of hours, before it becomes stable. After the warm-up period, the laser finally gets relatively stable with fluctuations of 0.2 W RMS for power 50 μm RMS for X and Y positions. This corresponds to an angular fluctuation of the beam of 11 μrad.

I. 2 Frequency Conversion

Tunability of the laser wavelength is an important degree of freedom in non-linear ultra-fast atomic/molecular dynamics, because it enables to selectively choose resonant photo-excitation and controlling the light-matter interaction regime. The central wavelength of the Yb:fiber laser is kept fixed around 1030 nm. To tune the wavelength, specific solutions have been implemented as presented below.

Second Harmonic Generation

Second harmonic of the fundamental laser wavelength, at 515 nm, is generated by impinging the laser on a 1 mm thick type-I β-Barium Borate (BBO) crystal ($\theta = 23.4°$ $\phi = 90°$). The BBO crystal is used in combination with a pair of dichroic mirrors, R515 nm &T1030 nm, to separate the second harmonic from the fundamental laser wavelength. After optimization the orientation of the BBO crystal, the average power of $2\omega_L$ was obtained 19 W, corresponding to a $\sim 38\%$

conversion efficiency and a pulse energy of 115 μJ. The generated $2\omega_L$ is polarized orthogonally to the fundamental laser wavelength. It has been observed that with time the divergence of the $2\omega_L$ generated varies with the incident power of ω_L, due to absorption of moisture by the crystal due to its hygroscopic nature. This results in the change in the focusing conditions with the change in intensity. To negate such effects in the experiments, the BBO is kept inside a oven and heated to a temperature of $\sim$ 100 °C and intensity of the $2\omega_L$ in the experiment is controlled by a half waveplate installed in front of a fixed polarizer in the $2\omega_L$ beam.

Third Harmonic Generation

Third harmonic generation of the fundamental laser wavelength, at 343 nm, is generated using an in-line frequency conversion setup. The fundamental laser wavelength is impinged on the 1 mm thick type-I-BBO crystal, which converts the fundamental laser wavelength into its second harmonic partially. A 1 mm thick calcite crystal is inserted into the beam path of the co-propagating ω_L and $2\omega_L$, to compensate the relative delay between the two wavelength. A second 0.75 mm thick BBO crystal is placed in the beam path to generate the third harmonic ($3\omega_L$). A combination of two dichroic mirrors are used to separate the $3\omega_L$ from the rest. The generated $3\omega_L$ has a 24 % conversion efficiency with an average power of 12 W corresponding to a pulse energy of 72 μJ. It has been observed that there are thermal drifts above 9 W, particularly in the second BBO. Also the similar effects of variation in divergence of $3\omega_L$ with the change in incident power of ω_L on the BBO can be observed.

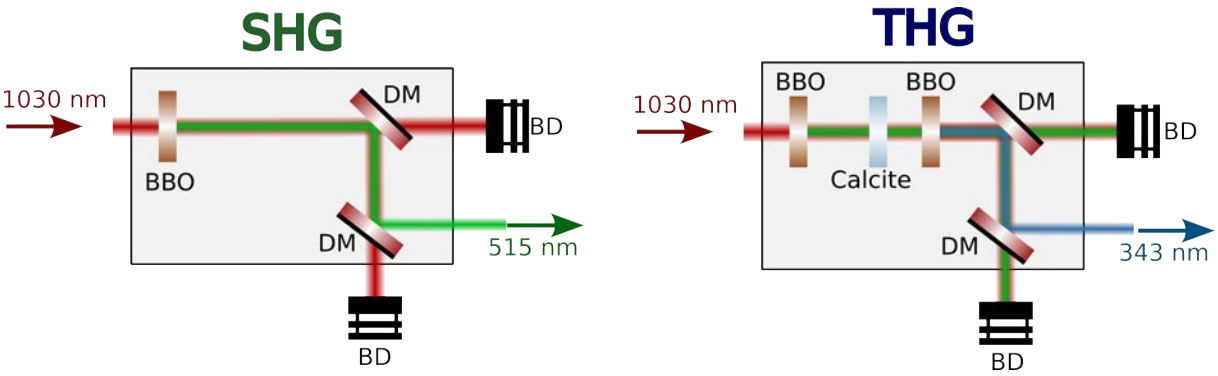

Figure 2.3 – *Schematics of second harmonic generation (SHG) and third harmonic generation (THG). Where BBO stands for β-Barium Borate, DM for Dichroic mirror and BD for beam dump.*

I. 3 Precision Polarization Control

Chiroptical processes constitute the core of this thesis. In the quest to distinguish and probe the dynamics of molecular chirality in femtosecond and attoseconds timescales, circularly/elliptically polarized light is the probe of choice. Some of our experiment will rely on strong field ionization by the fundamental laser beam (Chapter 4). Despite this apparent simplicity, the accurate manipulation of the polarization state of such beams can be challenging. The misalignment of the polarizer in the power modulator or a non-perfect alignment of mirrors in a periscope can alter the polarization state of the light. Furthermore, the wave-plates employed to manipulate the polarization do not necessarily introduce the exact desired phase shift between the polarization components. The situation becomes even more critical for experiments relying on multiphoton

ionization by visible laser pulses (Chapter 3). In principle the frequency conversion process of linearly polarized pulses produces linearly polarized harmonics. However the birefringent nonlinear crystals can alter the polarization state if they are not perfectly aligned. Last, some of our experiments will be using extreme ultraviolet (XUV) radiation produced by high-order harmonic generation. In that case the manipulation and characterization of the polarization state is even more difficult.

The polarization state of an electromagnetic wave is defined by the temporal evolution of the electric field oscillations in space. The period of these oscillations is about 3.43×10^{-15} s at a wavelength of $\lambda = 1030$ nm , which is too fast to be resolved by direct measurements. Conventional photo-detectors are sensitive to the intensity ($I \propto E^2$) of the incident electromagnetic field with a minimum response time of about 100's of picoseconds which is much longer than the optical period. Thus to characterize the polarization state of electromagnetic wave a set of parameters are used, called Stokes parameters.

Stokes Polarization Parameters

A generalized transverse monochromatic electromagnetic field, propagating along the $(+)z$ direction, can be defined by two orthogonal electric field components in a Cartesian co-ordinate system as:

$$\vec{E}(z,t) = E_{0x}\cos(\omega t + \delta_x(t))\hat{e_x} + E_{0y}\cos(\omega t + \delta_y(t))\hat{e_y} \tag{2.1}$$

where E_{0x} and E_{0y} are the electric field amplitudes along direction of the unit vectors $\hat{e_x}$ and $\hat{e_y}$ respectively, ω is the angular frequency and δ_x and δ_y are the phases of the electric field along $\hat{e_x}$ and $\hat{e_y}$ respectively. The above equation can be rearranged by multiplying $\sin(\delta)$ where $\delta = \delta_x - \delta_y$, squaring and summing as :

$$\frac{E_x^2(t)}{E_{0x}^2} + \frac{E_y^2(t)}{E_{0y}^2} - \frac{2E_x(t)E_y(t)}{E_{0x}E_{0y}}\cos\delta = \sin^2\delta \tag{2.2}$$

The equation 2.2 defines the motion of the electric field and traces an ellipse in the $\hat{e_x}$ and $\hat{e_y}$ plane (see Fig. 2.4 (a)). The time average electric field is given as:

$$\langle E_i E_j \rangle = \lim_{T\to\infty} \frac{1}{T}\int_0^T E_i(t)E_j(t)dt(i,j = x,y) \tag{2.3}$$

Thus the time average of equation 2.2 can be expressed as:

$$S_0^2 = S_1^2 + S_2^2 + S_3^2 \tag{2.4}$$

where

$$S_0 = E_{0x}^2 + E_{0y}^2 \tag{2.5a}$$
$$S_1 = E_{0x}^2 - E_{0y}^2 \tag{2.5b}$$
$$S_2 = 2E_{0x}E_{0y}cos\delta \tag{2.5c}$$
$$S_3 = 2E_{0x}E_{0y}sin\delta \tag{2.5d}$$

The parameters S_0, S_1, S_2, S_3 are called the Stokes parameters and are related to the intensity and polarization ellipse of the electromagnetic field through equation 2.5.

The Stokes parameter S_0 defines the intensity of the electromagnetic field. The parameter S_1 defines the linearly vertical or horizontal polarization state and S_2 defines the linearly polarized

electromagnetic field at $\pm 45°$ to the basis vectors $\hat{e_x}$ and $\hat{e_y}$. The parameter S_3 determines the amount of left and right circularly polarization contained in the electromagnetic field, where $S_3 = +1$, $S_3 = -1$ and $S_3 = 0$ respectively correspond to right circularly polarized left circularly polarized and linearly polarized electromagnetic.

The polarization ellipse can be further characterized by the orientation angle ψ and the ellipticity angle χ and can be expressed in term of the Stokes parameters as:

$$\psi = \frac{1}{2}\tan^{-1}\left(\frac{S_2}{S_1}\right), \psi \in [0, \pi] \tag{2.6}$$

$$\chi = \frac{1}{2}\sin^{-1}\left(\frac{S_3}{S_0}\right), \chi \in \left[-\frac{\pi}{4}, \frac{\pi}{4}\right] \tag{2.7}$$

Characterization of Quarter waveplates

Waveplates are the tool of choice to manipulate the polarization properties of light, from the ultraviolet to the infrared range. A quarter-waveplate (QWP) is made of a birefringent material such that the electromagnetic wave associated with the larger index of refraction, ordinary wave (o-wave), is retarded by 90° in phase with respect to that associated with the smaller index of refraction, extra-ordinary wave (e-wave). The optic axis is parallel to the surface of the plate. When a linearly polarized light is incident on the waveplate it is divided into two components o-wave and e-wave. When the incident linearly polarized light makes an angle $\theta = 45°$ with respect to the optic axis it introduces a $\phi = 90°$ or $\lambda/4$ phase shift between the two components with equal amplitude. A quarter waveplate in this configuration thus enables producing a circularly polarized electromagnetic wave.

The quality of the circularly polarized electromagnetic wave produced by the waveplate is determined by the retardation phase ϕ introduced by the waveplate. An ideal quarter-waveplate should have a retardation of $\phi = 90°$ for both $\theta = \pm 45°$. In principle, the ϕ retardation can be defined modulo 360°. In that case the two components of the electric field are phase shifted by more than one optical period. This can be an issue when dealing with ultrashort pulses, since the two components would not perfectly temporally overlap. In the femtosecond regime it is thus necessary to use zero order waveplates, which introduce exactly $\phi = 90°$ between the two components. This sets a drastic constraint on the thickness of the material to be employed. For instance a quartz waveplate introducing $\phi = 90°$ at 1030 nm between ordinary and extraordinary axis should have a thickness of 257.5 nm, which is mechanically challenging. To circumvent this issue, zero order waveplates are manufactured by stacking several plates with opposite orientations, and the phase shift is tuned by adjusting the thickness difference between the plates. Another difficulty that arises when dealing with ultrashort pulses is their broad bandwidth. The waveplates must be able to introduce a given phase shift over a large range of wavelengths. Achromatic or even super-achromatic waveplates are designed to reach that goal, stacking multiple materials with different dispersions. However there is always a tolerance on the actual retardation introduced by a waveplate, and it is neccessary to measure it for applications requiring a precise retardation.

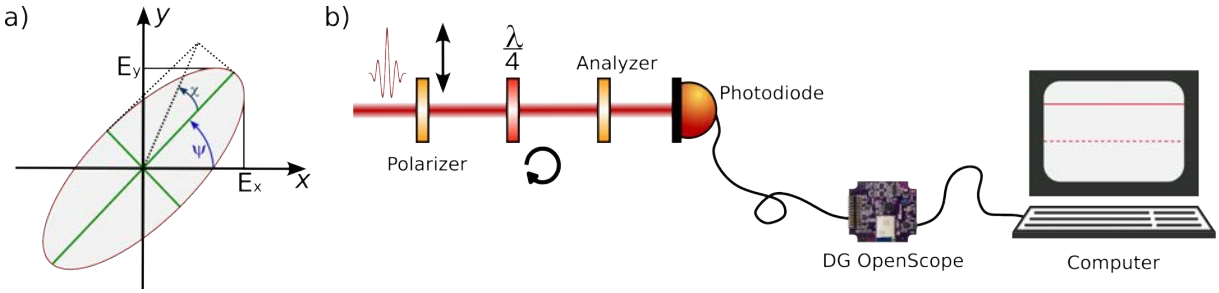

Figure 2.4 – *(a) Polarization ellipse traced out by the electric field, where E_{0x} and E_{0y} are the electric field amplitudes along the direction of unit vectors $\hat{e_x}$ and $\hat{e_y}$ respectively and ψ and χ are the orientation and ellipticity angles. (b) Schematic of the experimental setup to measure the retardation of a $\lambda/4$ waveplate.*

Working Principle: To determine the true retardance of the quarter waveplate we use the crossed polarizer method [Goldstein 03] [Schaefer 07] [Arnoldt 11]. In this method the quarter waveplate is inserted in between two crossed polarizers (polarizer and analyzer). The schematics of the experimental setup is shown in Fig. 2.4. When the fast axis of the quarter waveplate is oriented at 45° with respect to the unit vector along x ($\hat{e_x}$), the intensity after the analyzer can be expressed as as a function of the retardation (ϕ) and the angle (α) made by the transmission axis of the analyzer with the unit vector along x ($\hat{e_x}$) as:

$$I(\alpha, \phi) = \frac{I_0}{4}(1 + \cos(2\alpha)\cos(\phi)) \tag{2.8}$$

Thus measuring the intensity of the laser beam on the photodetector, placed after the analyzer, for $\alpha = 0°$ and $\alpha = 90°$ the retardance of the quarter waveplate can be calculated as:

$$\phi = \cos^{-1}\left(\frac{I(90°, \phi) - I(0°, \phi)}{I(90°, \phi) + I(0°, \phi)}\right) \tag{2.9}$$

The main benefits of the method is that the measurement is independent on the laser source intensity.

To determine the retardation phase ϕ of a quarter waveplate, the laser beam from the Blast Beat laser system is cleaned of any polarization artifacts inherent to the laser by using a thin film polarizer along with a grid polarizer (see Fig. 2.4 (b)). A second grid polarizer called the analyzer is mounted on a rotatable optical mount. The laser power before the polarizer is kept at ~ 1.5 W to make the measurements less sensitive to the amplified stimulated emission from the laser. The analyzer is then rotated to minimize the signal, $\alpha = 0°$, on the photo-diode (DET 100A) with a responsivity of (0.55 A/W) at $\lambda = 1030$ nm. The zero-order quarter waveplates at $\lambda = 1030$ nm are then introduced in between the polarizer and the analyzer and is rotated to minimize the signal on the photo-diode. To eliminate background noise the photodiode is optically shielded. The signal from photo-diode is measured using Digilent OpenScope MZ card and is displayed onto a computer. The photo-diode signal is recorded multiple for $\alpha = 0°$ & $90°$, averaged over $\Delta T = 1$ sec. The measurement is repeated multiple times and the retardation phase is calculated from the expression Eqn. 2.9

The retardation of B.Halle zero-order QWP at $\lambda = 1030$ nm is experimentally found to be 90.09°, which is excellent. On the other hand, the zero-order QWP from Thorlabs at $\lambda = 1030$ nm were measured to be 94.36°. For an achromatic QWP from Thorlabs at $\lambda = 1030$ nm the retardation was measured to be 90.41°.

Polarimetry by the rotating quarter waveplate method

The accurate control of the polarization properties of light is important in any chiroptical interaction. In the strong-field regime, this becomes even more critical. In a conventional circular dichroism experiment, a non-perfectly circular polarization state will result in an achiral background of the measurement. In strong fields, where the highly non-linear interaction is very sensitive to the peak value of the electric field, it is of extreme importance to have the same shape of the laser electric field for opposite ellipticities. We have seen that the shape of the electric field can be characterized by the Stokes parameters, defined by the equation 2.5. The third Stokes parameter S_3 defines the ellipticity of the laser field, and its measurement is of utmost importance for us.

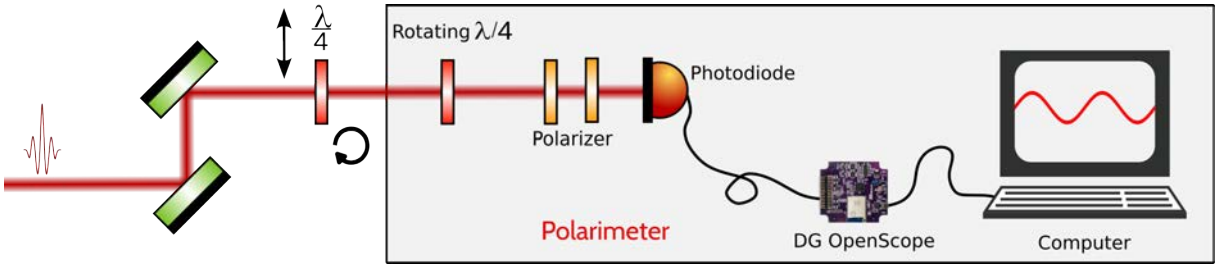

Figure 2.5 – *Schematics of the setup for polarimetry.*

Working Principle:

The Stokes parameters of a light source can be measured by using the rotating quarter waveplate method [Schaefer 07] [Arnoldt 11]. In this method a quarter waveplate is continuously rotated (R-QWP) in front of linear polarizer whose transmission axis is fixed. The intensity of the laser beam is measured, as a function of the angle of the R-QWP, after the linear polarizer using a photodiode. The schematics of the experimental setup is shown in Fig. 2.5. The intensity (I) of the transmitted light measured by the photodiode is given as:

$$I(\theta) = [A - B\sin(2\theta) + C\cos(4\theta) + D\sin(4\theta)] \tag{2.10}$$

where θ is the angle made by the fast-axis of the R-QWP with the unit vector along x ($\hat{e_x}$),

$$A = S_0 + \frac{S_1}{2}; \quad B = S_3; \quad C = \frac{S_1}{2}; \quad D = \frac{S_2}{2} \tag{2.11}$$

From Equn. 2.11 the Stokes' parameters can be retrieved as

$$S_0 = A - C; \quad S_1 = 2C; \quad S_2 = 2D, \quad S_3 = B \tag{2.12}$$

Eqn. 2.10 is a truncated Fourier series with a dc component, second harmonic and two fourth harmonic terms and the amplitudes of these terms gives the Stokes' parameters necessary to

quantify the polarization state of the laser. The question arises, what is the minimum number of data points required to determine the amplitudes A, B, C & D? The answer lies in the Nyquist's sampling theorem, which states that "a continuous time signal can be reconstructed from its samples if it is sampled at a rate at least twice its highest frequency component" [Lee 12]. The maximum frequency component corresponds to 4θ and hence to determine the amplitudes at least 8 data points are required. In practice we vary the R-QWP at a constant speed of $\theta = \Omega t$ while $I(\theta)$ is measured using a photodiode connected to an oscilloscope (see Fig. 2.5). Then using Fourier transform the continuous and the frequency components oscillating at 2Ω and 4Ω is extracted.

The laser beam is initially cleaned of any polarization artifacts inherent to the laser by using a thin film polarizer. The linearly polarized laser beam is incident on to a B.Halle quarter waveplate. The polarized beam, after the B.Halle QWP, is the incident on the R-QWP polarimeter. The quarter waveplate (R-QWP) is mounted on a continuously rotating motorized mount DDR25/M controlled by KDC101 module, rotating at a speed of 1800°/sec. The laser beam then propagates through two fixed and parallelly aligned polarizers and is incident on a photodiode (DET100A). The signal from the photodiode is measured using Digilent OpenScope MZ card and is displayed onto a computer. The photodiode signal is recorded for 20 sec. The schematics of the polarimeter is shown in Fig. 2.5.

As the R-QWP rotates continuously the incident polarization changes from linear to circular and so on. With the transmission axis of the linear polarizers fixed after the R-QWP, it selects only a given polarization component, and thus the measured signal is a sinusoidal function (see Fig 2.6 (b)) which is fast-Fourier transformed (FFT). Depending on the polarization state of the incident electromagnetic field, on the R-QWP, the signal oscillates at $2\Omega_0$ for circular and $4\Omega_0$ for linear polarization. Polarimetry is done for all four linear and circular polarizations. The FFT for linear polarization along the fast axis shows a clear peak at $4\Omega_0$. To determine the quality of the linear polarization state (see Fig 2.6 (c & f)) the ratio of the FFT amplitude at $2\Omega_0$ to that of $4\Omega_0$ is calculated to be 0.0 for both the fast and slow axis. To determine the quality of the linear polarization state (see Fig 2.6 (d & e)) the ratio of the FFT amplitude at $4\Omega_0$ to that of $2\Omega_0$ is calculated to be 3.5×10^{-3} and 3.1×10^{-3} for left and right circular polarization states. The ratio of FFT amplitudes for both the right circular polarizations are the same (see Fig 2.6 (d & g)). The Stokes parameter is extracted using Py-pol library and 0.00 for the linear polarizations and 0.99 for both the circular polarizations. The polarization state are also measured, for both the linear and circular polarization states, with a spiral phase plate (SPP) after the B.Halle QWP (see Fig 2.6 (h & i)). The measured ratio of the FFT amplitudes are 2.1×10^{-3} and 7.8×10^{-3} for linear and circular polarization states respectively. The Stokes parameter is extracted using Py-pol library and 0.00 for the linear polarizations and 0.98 for both the circular polarizations. This measurement shows that the spiral phase plate does not significantly distort the polarization state of the radiation.

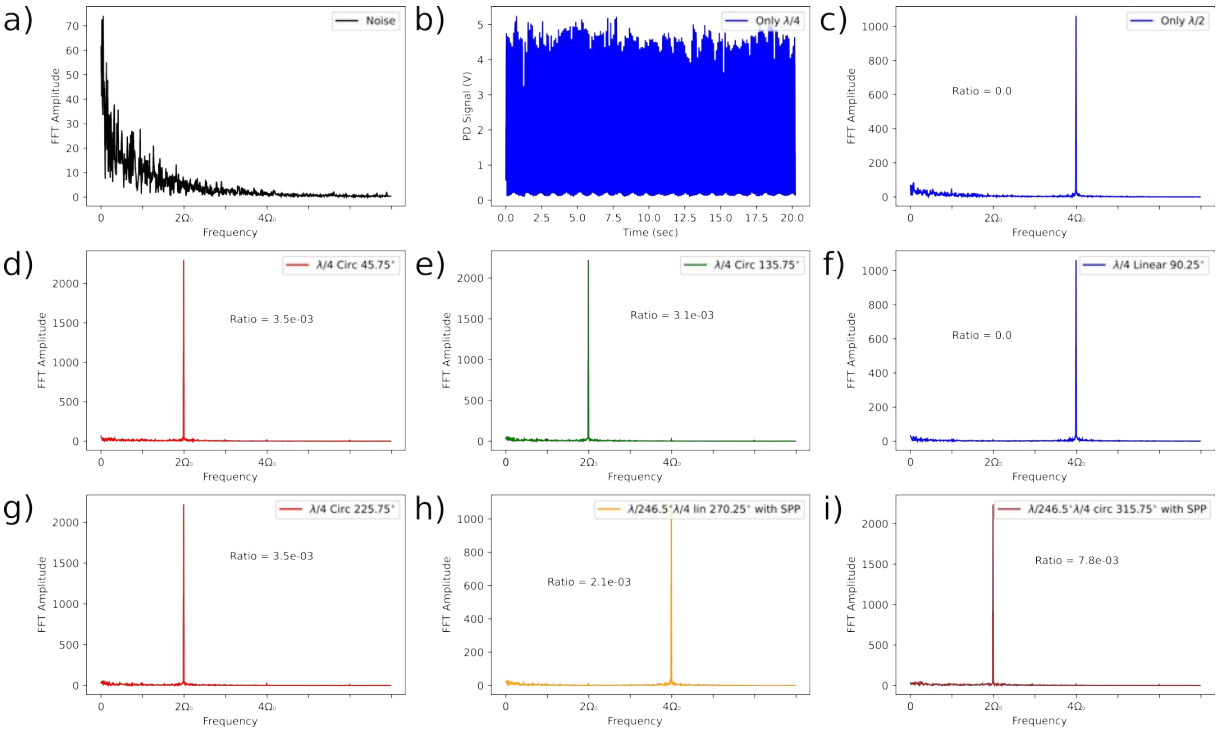

Figure 2.6 – *Polarimetry measurements. (a) FFT of the noise. (b) Signal recorded using the polarimeter using a $\lambda/4$ waveplate. (c) FFT of the signal for a $\lambda/2$ waveplate. A clear peak is observed at $2\Omega_0$ implying that the laser beam after the $\lambda/2$ waveplate is linearly polarized. (d) & (e) FFT of the signal for a $\lambda/4$ waveplate. A clear peak is observed at Ω_0 implying that the laser beam after the $\lambda/4$ waveplate is circularly polarized for a waveplate position $\pm 45°$ about the optic axis. (f) FFT of the signal for a $\lambda/4$ waveplate. A clear peak is observed at $2\Omega_0$ implying that the laser beam after the $\lambda/4$ waveplate is linearly polarized when the optic axis of the waveplate is parallel to the incident linearly polarized pulse. (f) Quality of the circular polarization obtained for the other right circularly polarized beam after the $\lambda/4$ waveplate. (h) & (i) Quality of the linear and circular polarization state obtained after a linearly polarized light is incident on a $\lambda/4$ waveplate and a spiral phase-plate (SPP).*

I. 4 Generation of Circular and Elliptical XUV

I. 4. a High-order harmonic generation

To probe the dynamics of chiral molecules in attosecond timescales requires dedicated time-dependent methods to isolate and study the characteristic response of the molecules. The most commonly used experimental technique is pump-probe spectroscopy. To realize this experiment one generally requires the pump and probe pulses to be in the order of the time-scale of the process, typically in the order of attoseconds. Due to the limited bandwidth of the laser amplifier medium it is impossible to generate laser pulses shorter than a few femtoseconds.

The technology that enabled breaking the femtosecond barrier is high-order harmonic generation (HHG). This process occurs when a gas target, generally a noble gas or small molecules, is impinged with a laser pulse at intensities of $\sim 10^{14}$ W/cm^2 [Ferray 88]. The strong-field response of the medium leads to the generation of broadband coherent radiations at very short wavelength, with attosecond duration. The generating mechanism of these attosecond pulses exploits strong-field ionization and is explained in Chapter 4. The central wavelength of the gen-

erated high order harmonics ranges from extreme ultra-violet (XUV) up to soft x-rays [Chen 10] [Barreau 20] typically ranging from $10 - 500$ eV. The generated high order harmonics are also extremely short pulses and can be in the order of few tens of attoseconds [Zhao 20], making them suitable for pump-probe investigations of electronic dynamics of atoms [Goulielmakis 10], molecules [Calegari 16] and solids [Tao 16]. To give an example of the timescale, in the Bhor-model of a Hydrogen atom it takes about ~ 24 as for an electron, in the ground state, to make one full revolution around the hydrogen nucleus. Thus pump-probe investigations with attosecond pulses allows us to measure, characterize and study of the real-time evolution of the electronic dynamics in atoms [Gaumnitz 17], molecules [Krausz 09] [Nisoli 17] [Marangos 16] and solids through photoionization and transient absorption/reflection spectroscopy.

On one hand, we have seen the versatility of the use of XUV attosecond pulses to measure and characterize electronic dynamics in real-time. While on the other hand circularly polarized XUV radiation from synchrotron have been used to investigate chiral molecules [Nahon 15] and magnetic materials [van der Laan 14]. Thus can we not use circularly polarized XUV attosecond pulses to study the electronic dynamics in chiral molecules in attosecond timescales?

However generating circularly polarized high-order harmonics is not a straight forward process because high-order harmonic generation efficiency exponentially diminishes with the increase in the driving field ellipticity (see section 4) [Budil 93]. A solution consists of producing two two co-linear orthogonally polarized phase-locked high harmonic sources [Azoury 19]. The polarization of the resulting XUV can be tuned by adjusting the relative between the two sources; this is analogous to changing the thickness of a birefringent crystal in the optical domain. The XUV source thus generated although being elegant and versatile in terms of polarization tunability but requires high interferometric stability. In the next three subsections we discuss three HHG configurations in which a single source is manipulated to produce circularly polarized high-harmonics.

I. 4. b Resonant HHG

One solution to produce highly elliptical XUV radiation directly from the HHG process is to perform resonant-HHG. It was shown that high-harmonics generated in SF_6 molecules by a laser field with moderate ellipticities of about 20% could be highly elliptical and have ellipticities of about 80% [Ferré 15a]. The process, although simple, requires that the harmonics emitted are in an energy range where a resonance is at play in the generating process. Furthermore, it was, up to now, only demonstrated using 800 and 400 nm fundamental laser pulses, which enables a strong enhancement of the HHG process due to resonant coupling in between the lowest cationic states of the molecule. We tried this approach and found out that the HHG signal from SF_6 molecules driven by 1030 nm or 515 nm pulses was too low to make a good source [Comby 20b]. We believe that the reason for that is that 1030 nm and 515 nm fields are too far from this ionic resonance to enable strong ionization, preventing the efficient generation of high-order harmonics.

As an alternative, we investigated the resonant high-order harmonic generation in argon atoms, in the vicinity of the ionization threshold. We controlled the ellipticity of the laser by

rotating a half waveplate in front of a fixed quarter waveplate. This allows to keep the main axis of the fundamental polarization ellipse unchanged.

In order to measure the polarization state of the HHG generated, a Rabinovitch-type XUV analyzer was used [Rabinovitch 65]. It is composed of 4 unprotected gold mirrors under 20° grazing incidence. This polarizer has a measured extinction ratio between s and p polarizations above 20 in the $15 - 30$ eV range. It was rotated under vacuum to provide Malus' law curves, from which the polarization direction and ellipticity of the XUV radiation can be extracted. Using Fourier analysis of the recorded XUV signal the ellipticity of the XUV radiation can be extracted. The upper bound of the ellipticity (ϵ_{max}) is extracted using the equation

$$\epsilon_{max} = \sqrt{(I_0 - 2I_1)/(I_0 + 2I_1)} \tag{2.13}$$

where I_0 is the amplitude of the continuous frequency component and I_1 is the amplitude of the oscillating component, extracted from the Fast-Fourier Transform (FFT). Although one can also extract the ellipticities by using the conventional method of fitting the a cosine function to the Malus' law curves but both of the methods have similar accuracy.

Fig. 2.7 shows the polarimetry measurements of harmonics 7 and 9 of the $2\omega_L$ (515 nm). The laser ellipticity was scanned from -55% to $+55\%$, and the polarizer was rotated in the range $\pm 200°$. We see that when the laser ellipticity increases from 0 to 40%, the harmonic signal decreases by one order of magnitude. The signal decays exponentially with laser ellipticity ϵ_l [Budil 93], following $I_q(\epsilon_L) \propto e^{-\beta_q \epsilon_L^2}$, where β_q is the decay rate for harmonic q. Gaussian fits of the data presented in Fig. 2.7 give $\beta_7 = 13.3$ and $\beta_9 = 11.6$. The harmonic maximum ellipticity increases quasi linearly with ϵ_l, but remains low, reaching only 15% at $\epsilon_l = 30\%$ for H7, and is almost zero for H9. This is characteristic of non-resonant HHG as H7 and H9 correspond to photon energies of 16.8 and 21.6 eV, at which the absorption/emission spectrum of argon atoms does not have any particular resonant features. Hence, in these conditions, the high-harmonic ellipticity is known to be lower than that of the driving laser pulse [Antoine 97].

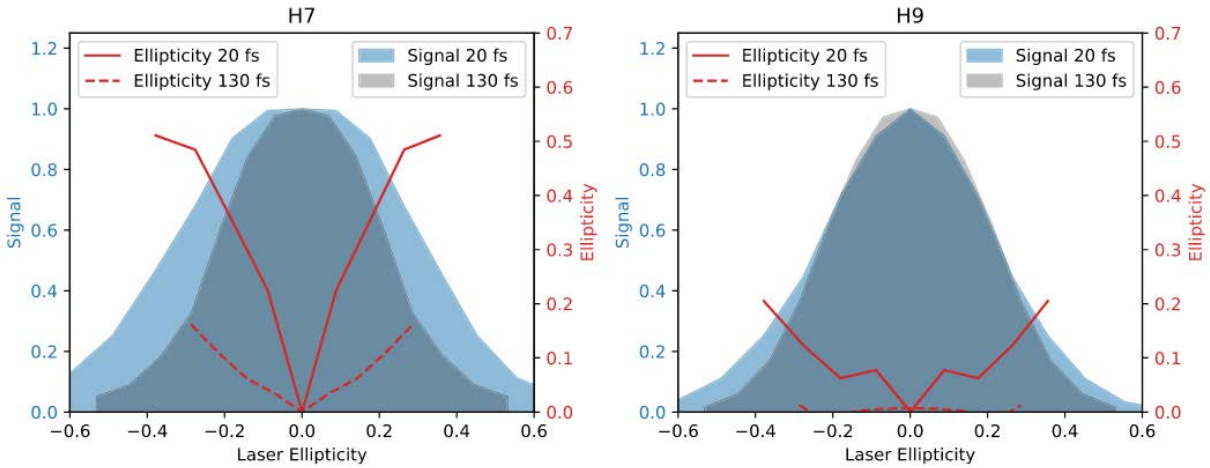

Figure 2.7 – *Elliptical high-harmonic generation driven by 515 nm pulses in argon. Intensity (shaded area) and maximum ellipticity extracted from Malus' law (red line) of harmonic 7 (left) and 9 (right), using 130 fs pulses or postcompressed 20 fs pulses. Extracted from [Comby 20b]*

The same experiment was performed using 20fs 515 nm pulses, postcompressed in a hollow core fiber [Descamps 21]. This postcompression broadens the laser spectral bandwidth from 18 meV FWHM to 260 meV FWHM. The polarimetry measurements of H7 and H9 from the 20 fs–515 nm pulses are presented in Fig. 2.7. While the signal decay rate is similar to the longer duration pulse case for H9 ($\beta_9 = 10.6$), H7 shows a much lower decay rate $\beta_7 = 6.4$. Furthermore, the maximum ellipticity of the harmonic reaches 50% at $\epsilon_L = 30\%$.

The question arises that why the harmonic decay with ellipticity be sensitive to pulse duration? Also, how can highly elliptical harmonics be generated in the absence of a resonance? We believe that this is due to the AC-Stark shift of the Rydberg states by the strong driving laser field. At an intensity of 1×10^{14} W cm^{-2}, the ponderomotive potential is $U_p = 2.5$ eV. This shift is a good approximation of the AC-Stark shift of the ionization potential of the atom and high lying Rydberg states. Harmonic 7, at 16.8 eV, can thus be in the vicinity of Stark-shifted Rydberg states. The broad bandwidth of the pulses, achieved due to postcompression, increases the probability to hit a resonance and to produce highly elliptical XUV light.

This scheme produces elliptically polarized XUV pulses with up to 50% ellipticity and is highly intensity dependent as it requires manifestation of dynamical Stark-shifts in HHG. The ellipticities extracted are under the assumption that the generated XUV is fully polarized. The measured quantity is thus only an upper-bound to the ellipticity (ϵ_{max}) of the XUV radiation. Although a fair assumption, but might not be always be true due to depolarization effects that arise from the spatio-temporal inhomogeneities of the HHG process. Indeed, as the process strongly depends on the laser intensity, we expect that the polarization state produced will vary in time during the generating pulse, leading to a partial depolarization of the XUV light. Measurement of a dichroic signal [Barreau 18] [Veyrinas 16] or the use of a XUV quarter-waveplate should be used to characterize the ellipticity of the XUV accurately [Nahon 04].

I. 4. c Bi-Circular Bi-Chromatic HHG

Another way to produce circularly polarized XUV is by using a combination of two counter-rotating fundamental and second harmonic fields, which lead to efficient HHG [Fleischer 14] [Kfir 15] [Kfir 16]. This configuration produces a comb of harmonics with peculiar polarization properties: the harmonics are circularly polarized, but two consecutive harmonics have opposite helicities. In this section we introduce the principle of this technique and show the results obtained using the Blast Beat laser.

Experimental Setup: Figure 2.8 shows the schematics of the beamline to generate circular harmonics using bi-chromatic and bi-circularly polarized laser pulses. The setup is called MAZEL-TOV for MAch-ZEhnder-Less for Threefold Optical Virginia spiderwort. The 1030 nm beam of FWHM 3.7 mm and average power of 50 W was incident on a 1 mm thick BBO crystal to generate 15 W of second harmonic at 515 nm. The two beams, 35 W of 1030 nm and 15 W of 515 nm, are orthogonally polarized relative to each other. The temporal overlap of the two beams is set by propagation through a 1 mm calcite crystal, and finely adjusted by propagating it through a pair of thin fused SiO_2 wedges of about 2 mm in thickness. A superachromatic quarter-waveplate ($300 - 1100$ nm) converts the two orthogonal linear polar-

izations into counter-rotating circular polarizations. The superposition of the two orthogonal counter-rotating circular polarizations can be represented in Lissajous figures as a function of the angle made by the quarter waveplate (α for the fundamental and β for the second harmonic) and is represented in Fig. 2.9. We see that the tree-foil knot field shape is produced when both $\alpha = \beta = 45°$, i.e., the fundamental and its second harmonic are counter-rotating. The resulting Lissajous figure has a 3-fold symmetry. While deviation from this results in the loss of the 3-fold symmetry.

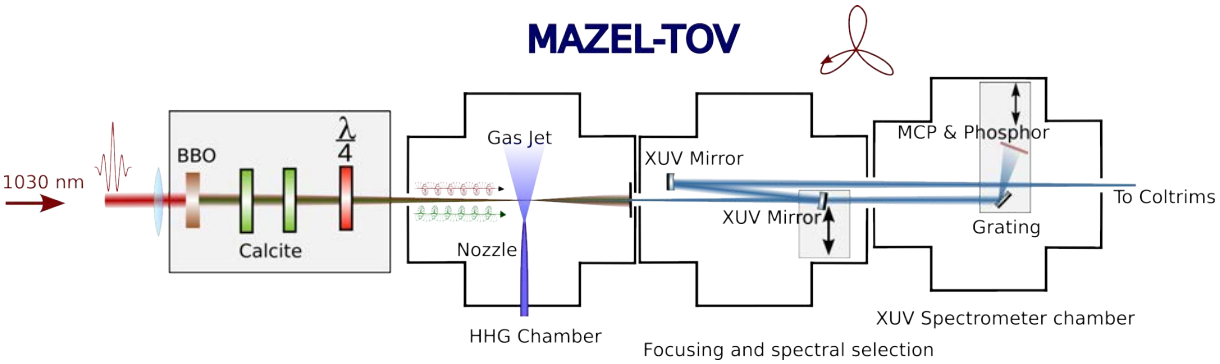

Figure 2.8 – *Schematics of the experimental setup for the generation of circular harmonics in the MAZELTOV configuration.*

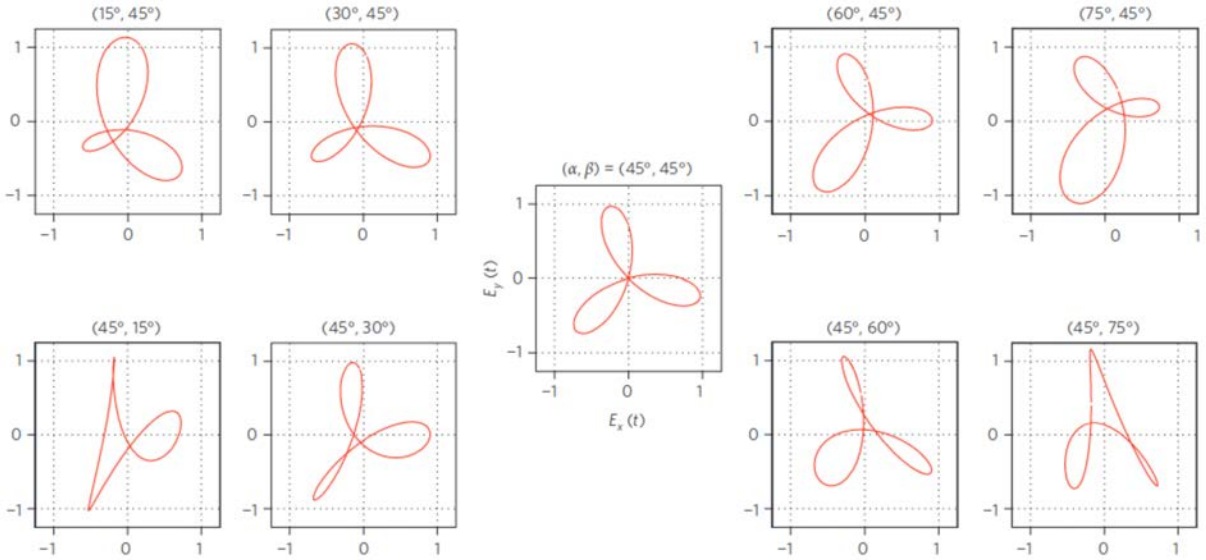

Figure 2.9 – *Lissajous curves of the total electric field experienced by the argon atoms in the jet for several readings of the quarter waveplates. When both waveplates are set at 458, the two colours are counter-rotating circularly polarized and the total electric field has a rosette-like shape with a 2.95-fold rotational symmetry. As the reading of either of the waveplates deviates from 45°, this symmetry is lost. Extracted from [Fleischer 14]*

The bi-circular beam thus produced is them focused on to a motorized gas jet by a pair of dual-band 0° dichroic mirrors to avoid chromatic aberration and preserve the polarization state of the two beams. The intensity at the focus is tuned by changing the focal length of the focusing mirror or by increasing the beam diameter on the quarter-waveplate. A camera

is used to monitor the plasma generated for optimization [Comby 20a]. The HHG interaction chamber is pumped by a 600 m^3/h root pump to pressures of about $\sim 5 \times 10^{-2}$ mbar. The HHG interaction chamber is separated from the focusing and spectral selection chamber by a differential pumping hole of diameter ranging from 0.5 mm to 5 mm over 8 cm and is placed at 3 mm from the laser focus. To prevent loss of the XUV radiation through re-absorption the chambers after the HHG interaction chambers are pumped down to pressures of $\sim 5 \times 10^{-7}$ mbar using turbo-molecular pumps.

The XUV beam is isolated and re-focused into the COLTRIMS using two 0° motorized XUV mirrors (f = 60 and 300 cm) to a focal spot size of ~ 50 μm. With 5% reflectivity of the mirrors, which peaks at 35 eV with a bandwidth of 1.5 eV FWHM, is used to isolate the harmonic 29 (34.9 eV) of the fundamental 1030 nm laser pulse.

The high harmonics generated are characterized using a XUV spectrometer made up of a gold coated grating with a variable spacing (1200 mm^{-1} average). It images the spectrum spatially on a set of chevron-stacked MicroChannel Plates (MCP) (see section II. 3) coupled with a phosphor (P46) screen , with a decay time of < 2 μs, and a CCD camera. The spectrometer has a resolution of > 200 meV at 21.6 eV and is mounted on a translation stage. A calibrated XUV photodiode is used for precise flux measurements which has been calibrated independently by the Physikalisch-Technische Bundesanstalt Berlin.

HHG Spectrum: Figure 2.10 (a) shows the high harmonic spectrum for different intensities of the 515 nm. The spectrum obtained at lower intensities of 2×10^{13} W/cm^2 has a high harmonic cut-off energy at 24 eV, well below 35 eV. Thus successively the intensity is increased to intensities of about 6×10^{14} W/cm^2. At an intensity of 3×10^{14} W/cm^2 the high harmonic cut-off reaches 35 eV but get saturated. This is due to saturation of ionization by 515 nm due to the long pulse width of about 135 fs. Nevertheless a clear signal at 35 eV is observed (see Figure 2.10 (b)).

The harmonic spectrum thus obtained has a three-fold sequence of harmonics, due spin angular momentum conservation, instead of being constituted by only odd order high harmonic spectrum obtained with one color linearly polarized laser pulse. The three-fold high harmonic spectrum consists of a pair of circularly polarized harmonic with opposite helicities with every third harmonic, $q = 3N$ suppressed (harmonics 18, 21, 24, 27 show in the Figure 2.10 (b)). The harmonics $q = 3N + 1$ rotates with the helicity of the fundamental laser field and while the harmonics $q = 3N + 2$ rotates with the helicity of the second harmonic field, where q is the harmonic order given by $q = \lambda_{HHG}/1030$ nm and $N \in \mathbb{Z}$. Figure 2.10 (c) shows the spectrum of the harmonic 29 obtained after two multi-layer mirrors. The signal is clearly dominant with an estimated flux of 10^{10} photons/sec.

Stability: High harmonic generation being a non-linear process any instability in the driving laser field will lead to a magnification of these instabilities in the high order harmonics generated. There can be fast or long term fluctuations in the high harmonics generated due to the driving laser field or the gas jet. To be compatible with data acquisitions of over tens of hours

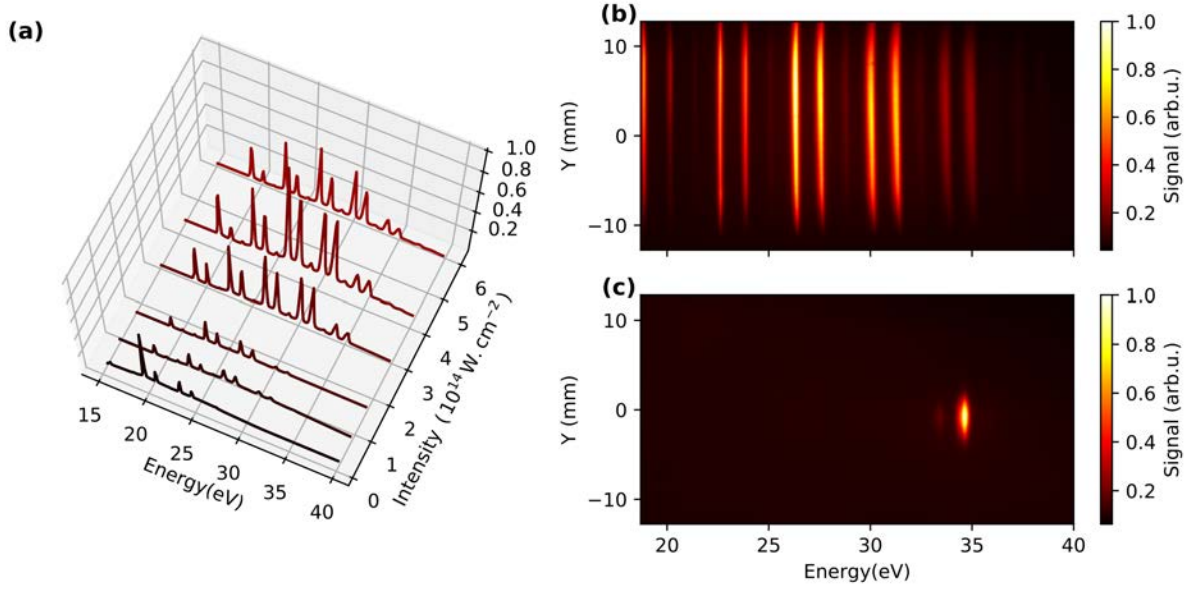

Figure 2.10 – *Circular High order Harmonic Generation using bi-circular bi-chromatic fields. (a) Intensity dependent HHG spectrum. Spatially resolved bi-chromatic bi-circular HHG spectrum before (b) and after (c) multilayer mirrors at 35 eV, showing both the spectral selection and refocusing.*

the XUV source needs to be very stable both in terms of photon flux, pointing and ellipticity. The use of an inline setup to produce the bicircular field should ensure a better stability than a Mach-Zehnder configuration. However, the bottleneck of the experiment in terms of stability is the amount of laser power which falls on the XUV mirrors. Even if these mirrors were designed with a Si substrate, which has very good thermal properties, we observe a clear drift of the pointing of the high harmonics during several hours. The heating up of the mirror could also lead to deformation of the mirror surface leading to reduction in reflectivity, distortion of the XUV wavefront and the polarization state.

To mitigate the aforementioned problem one has to isolate the driving laser field from the HHG generated at the same time preserving the HHG polarization state. In literature there are multiple ways which has been implemented to achieve this with there own pros and cons. The methods are reviewed briefly in the Table 2.1. For example metallic foils (Al, In) can be used as filters to isolate the driving laser field from the HHG with a typical efficiency of $\sim$ 100% while preserving the polarization state of the XUV transmitted [Lee 20]. Although they are highly effective in separating the XUV from the driving laser field while preserving the polarization state, metallic filters have low damage threshold. Thus they cannot directly be implemented on our high power high repetition rate beamline, as they will melt in time. To avoid the problem of low damage threshold one can also use grazing incidence anti reflective plates (fused silica plate coated with Nb_2O_5 under 20° incidence) [Takahashi 04] to reflect the circularly polarized XUV but in this configuration the polarization sate of the reflected XUV is affected. Alternatively, circularly polarized XUV can be generated in a non-collinear setup, which can provide 100% angular separation of the XUV from the driving laser field [Fomichev 02]. But due to the complexity of the experimental setup they are prone to interferometric instabilities and hence are polarization sensitive. Another way to isolate the XUV from the driving laser

field is to use an annular beam to generate XUV in combination with a pinhole [Peatross 94] [Pronin 11]. The driving field is isolated with an efficiency of $\sim 95\%$ while the polarization state of the XUV is preserved. In the coming section we will discuss about the implementation of an HHG beamline using a annular beam and pinhole to generate linearly polarized XUV and then use an all reflective XUV quarter waveplate to convert the linearly polarized XUV to circularly polarized.

Methods	Typical laser rejection	Typical XUV Trans.	Pros	Cons	Reference
Metallic filter	100%	$5\% - 50\%$	Preserves polarization Partial spectral selection	Melts at high power	[Lee 20]
Diffractive MCPs	$> 90\%$	$\sim 25\%$	Preserves polarization	Degrade the spatial profile	[Zhang 14]
Single grating monochromator	100%	$\sim 10\%$	Spectral selection	Spatial and temporal chirp Polarization sensitive	[Mills 12]
Time-compensating monochromator	100%	$2\% - 20\%$	XUV spectral selection	Polarization sensitive	[Frassetto 11] [Poletto 07]
Grazing incidence AR plates	$> 95\%$	$\sim 50\%$	High laser damage threshold	Polarization sensitive	[Takahashi 04]
Annular beam HHG + pinhole	$> 95\%$	$\sim 100\%$	Preserves polarization	Loss of driving laser energy	[Peatross 94] [Pronin 11]
Non-collinear HHG	100%	100%	Angular separation of harmonics	Polarization sensitive	[Fomichev 02]

Table 2.1 – *Methods to remove the driving laser beam in HHG-based XUV beamlines along with theirs pros and cons.*

I. 4. d All Reflective XUV $\lambda/4$ Waveplate

Experimental Setup:

The fundamental 1030 nm laser beam is frequency doubled in a type-I BBO crystal to obtain a 515 nm average power up to 19 W with a conversion efficiency of 38% and ~ 0.9 mm radius at I_{max}/e^2, duration 130 fs FWHM and repetition rate of 250 kHz (see I. 2). Roughly $\sim 35\%$ of the fundamental is used to generate the second harmonic (7 W) while the rest is used to provide power to the pump arm. The 515 nm beam is then expanded using a $\times 4$ telescope ($-75/+300$ mm) before being reflected by a drilled mirror ($\phi = 4$ mm) and then it is reduced by $\times 0.6$ telescope ($+125/-75$ mm). The two telescopes allows to finely adjust inner and outer part of the annular beam. The annular beam is then propagated through a zero-order half waveplate to control the polarization axis direction. The pulses are then focused by a +79 mm aspheric lens down to a focal spot size of $\sim 5 \times 5$ μm FWHM into a thin and dense argon gas jet located

inside a vacuum chamber (see figure 2.11). The gas nozzle is mounted on a 3-axis motorized stage and is 3 mm long with an orifice of ~ 50 μm. A movable gas catcher is placed a few mm above the gas jet so as to minimize XUV re-absorption in the residual gas. Two fixed pinholes are placed ($\sim$ 190 mm and 7 mm) after the gas jet to block the 515 nm beam falling on the XUV mirror, while the XUV beamlet is collimated by an +200 mm focusing SiC/Mg multilayer mirror (NTTAT) located $\sim$ 200 mm away from the HHG source with a 5° angle of incidence. An additional motorized pinhole is used to further remove the driving laser field from the XUV after the XUV mirror.

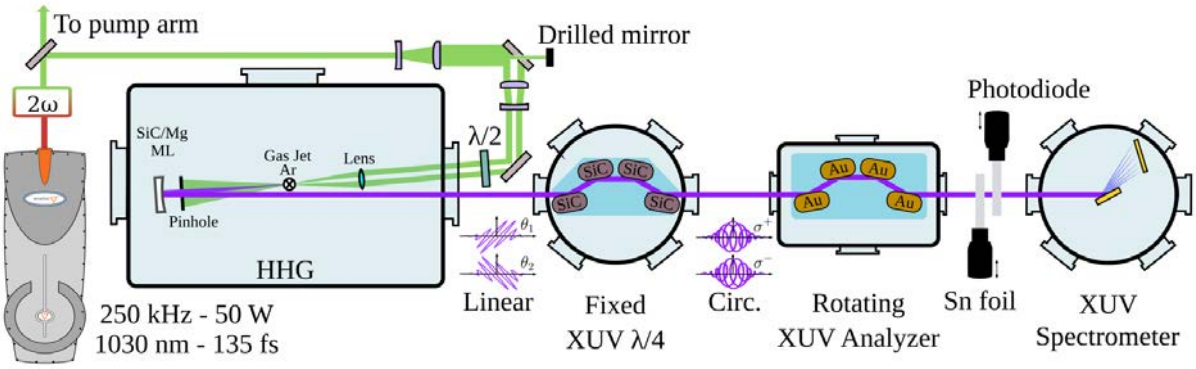

Figure 2.11 – *Schematics of the experimental setup to generate XUV with polarization tunability using annular beam and a XUV QWP. Extracted from [Comby 22]*

Spectral Selection & Refocusing:

The use of annular driving field in combination with a set of two fixed pinholes and a motorized pinhole allows the separation of the XUV beamlet from the driving laser field by a factor of $\sim 10^{-4}$ ($\sim$ 10 mW co-propagating with the XUV). Furthermore, a combination of reflective and transmittive elements are used to isolate the harmonic 9 (H9) at 21.6 eV. Since the high-order harmonics is generated using a linearly polarized light only the odd order harmonics of the driving laser field are generated, thus providing a large spectral spacing of 4.8 eV. A single reflection from a multi-layer mirror (SiC/Mg, NTTAT) followed by transmission from a tin foil allows the mono-chromatization of the XUV source. The reflectivity of the SiC/Mg mirror is of about 40% while Sn foil acts as a narrow band-pass filter $\sim$ 4.75 eV FWHM for 400 nm thickness, around 21 eV (see Figure 2.12).

XUV $\lambda/4$ waveplate:

To generate circularly polarized high harmonics an all reflective quarter-waveplate is used. It is composed of four SiC mirrors. Theoretically, the four reflections of a linearly polarized XUV at 21.6 eV on SiC mirrors at 78° angle of incidence yield a phase-shift of $\lambda/4$ between s- and p-polarization components, while maintaining a high overall transmission. Compared to the standard XUV phase-shifters [Yao 20] where the XUV quarter-waveplate is rotated in a plane perpendicular to the light propagation direction to control the polarization state of the XUV, the linear polarization axis direction impinging on the four SiC mirrors is rotated by rotating the zero-order half-waveplate in front of the HHG interaction chamber. This allows a more precise control the polarization state of the beam without disrupting the beam alignment.

A XUV analyzer is used to measure the degree of polarization of the XUV beam produced.

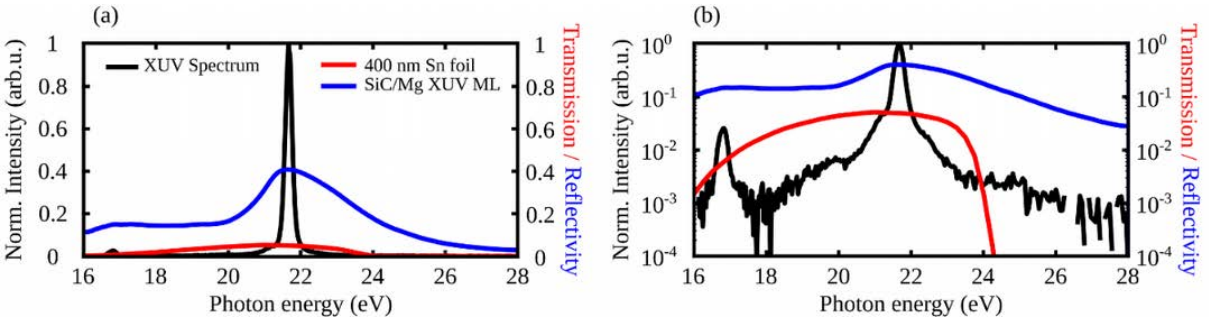

Figure 2.12 – *Mono-chromatization of the XUV source. The theoretical reflectivity of the SiC/Mg mirror (blue), the theoretical transmission of the* 400 *nm thick Sn foil (red) as well as the experimentally measured mono-chromatized XUV spectrum (black) in linear (a) and logarithmic (b) scale. Extracted from [Comby 22]*

The Malus' law curves are recorded by continuously rotating the analyzer by 720°. The XUV signal oscillates with a period of π (see Fig. 2.13). While rotating the polarization axis from $\pm 90°$ to 0° a phase shift of $pi/2$ is observed in the Malus' law curves. This phase shift corresponds to switching from s- to p-linearly polarized XUV radiation. In addition, the maximum XUV intensity is weaker for p-polarization (0°) compared to the s-polarization $\pm 90°$ and is due to s-/p-reflectivity ratio of SiC ~ 1.17 at 21.6 eV, 78° angle of incidence.

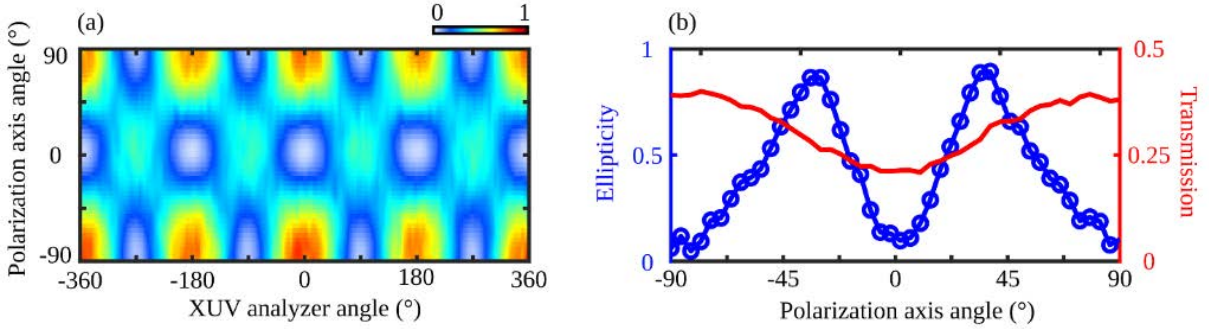

Figure 2.13 – *Mono-chromatization of the XUV source. The theoretical reflectivity of the SiC/Mg mirror (blue), the theoretical transmission of the* 400 *nm thick Sn foil (red) as well as the experimentally measured mono-chromatized XUV spectrum (black) in linear (a) and logarithmic (b) scale. Extracted from [Comby 22]*

Around $\pm 35°$, the ellipticity maximizes to a value around 90%. If the reflectivity of SiC was the same for s- and p-polarization, we would expect the maximum ellipticity for $\pm 45°$, and symmetric behavior when going toward $\pm 90°$ or 0°. The global transmission of the quarter-waveplateis 41% when using s-polarization (80% for each mirror), 21% using p-polarization (68% for each mirror) and 29% for tilt angles generating maximum ellipticities of $\sim 90\%$, resulting in a flux of 5.7×10^{12} photons/sec.

Stability: Despite the active stabilization of the laser beam, a continuous drift of the high harmonic generation is observed for about 12 hours after starting the experiment. We attribute this drift to a heating of the lens under vacuum, which shifts the vertical position of the focus in the jet and induces a loss of HHG efficiency as well as a drift of the pointing of the XUV beam. Past these 12 hours, thermal equilibrium is reached and the XUV becomes stable. The stability

of the quasi-circular XUV source is characterized by measuring the single photon ionization rate of a gas molecule (α-Pinene) over 40 hrs (see Fig. 2.14). The size of the molecular beam is $\sim$ 2.3 mm FWHM and is located $\sim$ 4 m away from the HHG source. The electron count rate measured is stable with 3.6% RMS deviation. The XUV helicity was also changed every 10 min over the acquisition time. This demonstrates that the circular XUV source has a good long-term stability both in terms of photon flux and pointing.

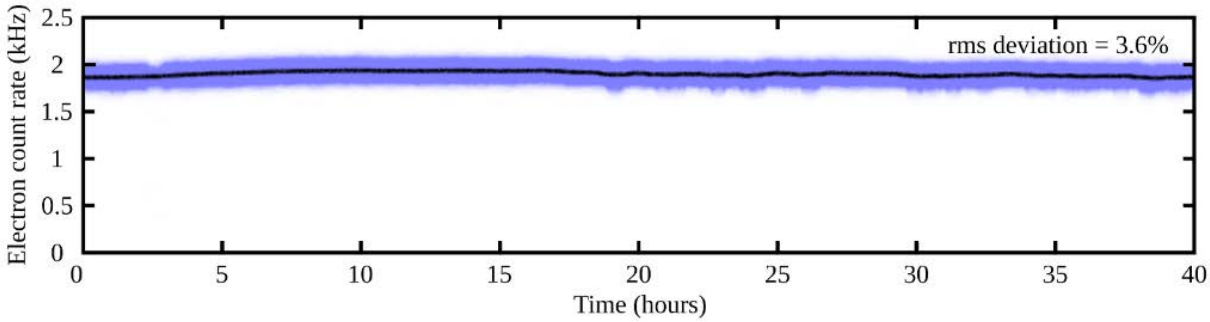

Figure 2.14 – *Long-term stability of the quasi-circular XUV source. The blue dots represent the electron count rate as a function of time, analyzed at 1 Hz sampling rate, over 40 h. The experimental conditions used to measure the electron count rate as a function of time are described in the manuscript. The thick black is a sliding average of the electron yield (width of 1 h). The root means square deviation of the count rate over 40 h is* 3.6%. *Extracted from [Comby 22]*

I. 4. e Conclusion

Fig. 2.15 shows the present day state of the art of quasi-circularly polarized HHG-based XUV sources as a function of the HHG flux generated and the repetition rate of the laser. The color of each dot represents the photon energy. Our work is, to the best of our knowledge, the first beamline combining bright (5.7×10^{12} photons s^{-1} at 21.6 eV—up to 4×10^{11} photons s^{-1} on target, using a 200 nm thick Sn foil) ultrafast high-repetition-rate XUV source with polarization tunability and a maximum ellipticity of 90%.

The polarization tunable XUV source presented along with its stability opens new opportunities for quasi-circular-polarized photon-hungry experiments. Thus, it can be used to perform multi-dimensional photoelectron circular dichroism measurements similar to the ones performed at synchrotrons [Nahon 16].

II Velocity Map Imaging Spectrometer

II. 1 Principle of Operation

Using the versatile XUV polarization tunable source one can perform photoelectron circular dichroism measurements in chiral molecules with attosecond resolution. The chiral molecules used in this thesis have typical ionization potential in the range of $\sim$ 9 eV, and are thus ionized by absorption of XUV light. Structural information about the ionized molecule is encoded in the angular and energy dependence of the the photoelectron, which needs to be resolved experimentally.

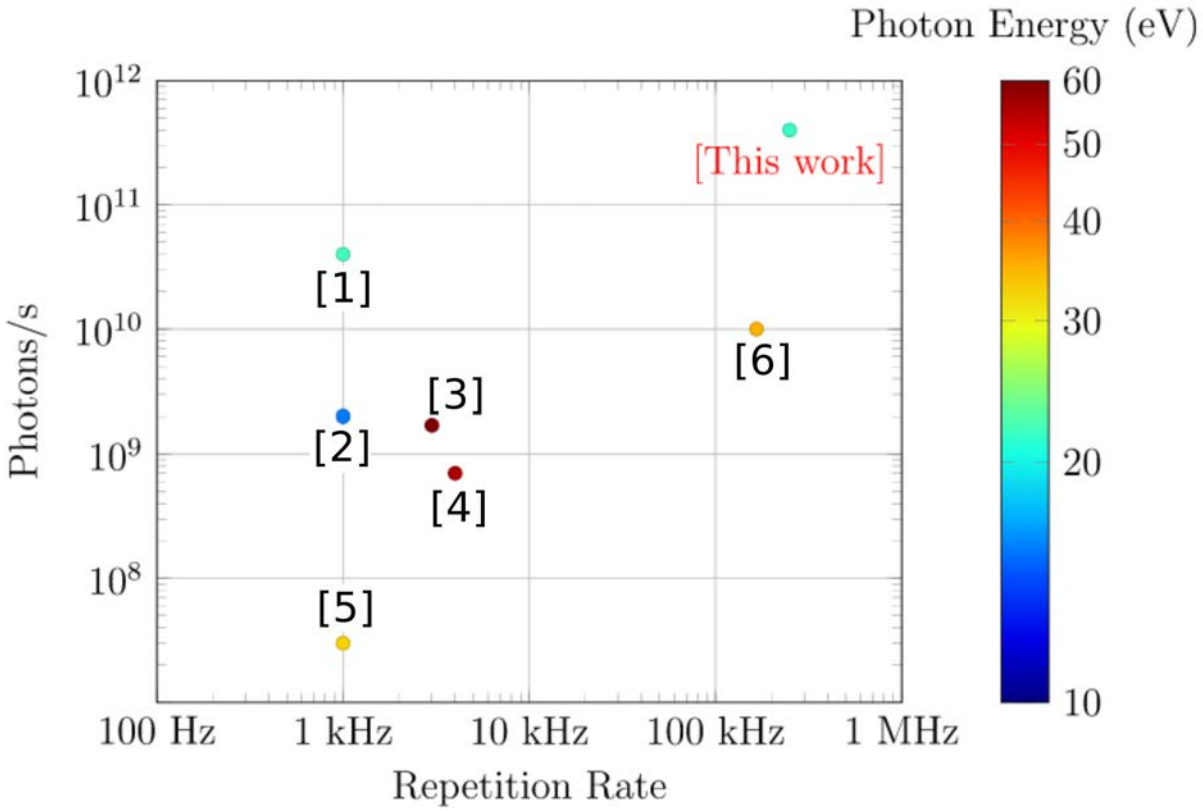

Figure 2.15 – *State-of-the-art of quasi-circularly polarized HHG-based XUV sources. The color of each dot represents the photon energy. The reported flux represents the flux/harmonic available on target. [1] [Hickstein 15], [2] [Ferré 15a], [3] [Yao 20], [4] [Kfir 15], [5] [Huang 18], [6] [Comby 20b]. Extracted from [Comby 22]*

There are many different instruments to measure the photoelectrons emitted during ionization. Early experiments were done using Faraday cup to detect charged particles [Brown 56]. The energy resolution was given by time of flight measurements of the electrons, while their angular distribution was resolved by scanning the polarization direction of the ionizing radiation and using the limited angular acceptance of the instrument. To increase the acceptance angle of the photoelectrons, Magnetic Bottle spectrometers were used, enabling to collect all the emitted electrons but thereby losing the angular resolution [Kothe 13]. Such angular resolution can be achieved with Velocity Map Imaging (VMI) spectrometers, which collect the ejected electrons in all 4π directions and projects them onto a 2-dimensional plane using an array of electrodes to form an electrostatic lens [Eppink 97]. The most simple geometrical configuration, for these array of electrodes, is the Wiley-MacLaren geometry [Wiley 55]. A projection of the 3D distribution can be recorded by microchannel plates, a phosphor screen and a camera. Alternatively, delay line anodes [Strasser 00] [Dinu 02] or a timepix detector [Gademann 09] [Jungmann 10] [Vallance 14] can be used to measure the whole 3-D photoelectron angular distributions. Last, coincidence electron-ion imaging can be used to detect both the 3-D momentum distributions of the electron and ion, thus providing the complete description of the ionization event, for example using a COLTRIMS/REMI [Ullrich 03]. In this section we will describe the working principle of the VMI.

In the Wiley-MacLaren configuration, the spectrometer is divided into three homogeneous field regions, defined by three electrodes (metallic meshes) kept at different static voltages. The first electrostatic mesh voltage is such that it repels the charged particles, generated in the interaction volume and moving away from the detector initially, towards the detector. This is called the repeller electrode. The second electrode extracts all the charged particles created in the interaction region and accelerates them towards the detector. This electrode is called the extractor electrode. The third electrode is kept at ground, and the region after it and up to the detector is the drift-region and is field free. The field strength applied on each of the electrodes along with the length of each of the region needs to be chosen such that the time-of-flight resolution is optimized.

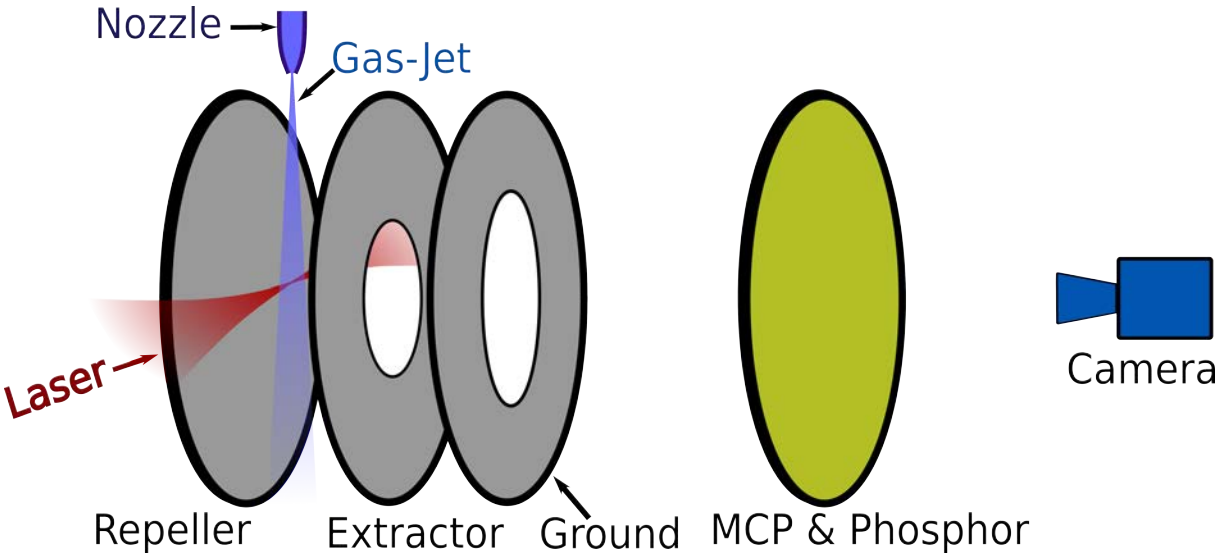

Figure 2.16 – *General schematics of a Velocity Map Imaging spectrometer (VMI). The target molecules are brought into the chamber using a nozzle, forming an effusive gas jet, placed perpendicularly above the plane of the laser-VMI plane. The laser interacts with the effusive gas jet at the center of the repeller and the extractor plates.*

Further improvements were made [Eppink 97] with the use of electrostatic lenses, centrally hollow plates, instead of using meshes (see Fig. 2.16). Although metallic meshes provides homogeneous and isotropic field regions in the spectrometer, using electrostatic lenses produces a gradient of electrostatic field lines. These electrostatic field line gradients behave analogous to the refractive index of a conventional optical lens and hence focuses the charged particles on to the detector. By carefully choosing the electric field strength applied on each of the electrode the charged particles are imaged on to the detector such that the position of the charged particle on the detector is proportional to its initial momentum. Since charged particles are emitted in all 4π directions in the interaction region, the charged particles emitted in the direction away from the detector or in the direction towards the detector and having the same initial magnitude of momentum are mapped on the same point on the detector. Hence the 2-D $\mathcal{P}(p_y, p_z)$ momentum distribution detected on the detector is a projection of the 3-D charged particle momentum distribution $\mathcal{P}(p_x, p_y, p_z)$; where p_x, p_y and p_z are the particles' momentum component along x-axis (plane parallel to the spectrometer axis), y-axis(plane containing the polarization vector

of the incident ionizing radiation) and z-axis (plane parallel to the direction of propagation of the ionizing radiation) respectively. Under perfect imaging conditions the 2-D projections of the charged particles recorded on the detector is not sensitive to the spatial extension of the interaction volume or the momentum of the charged particles along the axis of the spectrometer. But imperfections in the electrode design and the extended size of the source of particles in the interaction region can lead to imaging artifacts.

Depending on the polarity of the voltage applied on the repeller electrode it is possible to extract both the momentum angular distribution $\mathcal{P}(p_y, p_z) = \int \mathcal{P}(p_x, p_y, p_z) dp_x$ of ions (ion mode) and electrons (electron mode). The relationship between the radial position $R = \sqrt{(y^2 + z^2)}$ of the charged particle on the detector repeller voltage is given as:

$$R \propto M \sqrt{\frac{m}{2qV_{rep}}} L_d v_R \tag{2.14}$$

M is the magnification factor of the VMI ($M = V_{ext}/V_{rep}$), m and q are the mass and charge of the particle being measured, L_d is the drift length and $v_R = \sqrt{(v_y^2 + v_z^2)}$. Consequently the radial momentum p_r and the radial energy of the electron $\mathcal{E}_r$ are given as:

$$p_R \propto \sqrt{\frac{qmV_{rep}}{M^2}} R \tag{2.15}$$

$$\mathcal{E}_r \propto \frac{m^2 q V_{rep}}{M^2} R^2 \tag{2.16}$$

Hence radial momentum $p_r = \sqrt{(p_y^2 + p_z^2)}$ varies as $p_r \propto r$ while $\mathcal{E}_r \propto R^2$. From the above equation it is straight forward to find the energy resolution as a function of the radial position on the detector as:

$$\frac{\delta \mathcal{E}_r}{\mathcal{E}_r} = 2 \frac{\delta r}{r} \tag{2.17}$$

II. 2 Tomographic Reconstruction

Abel Inversion

The photoelectron momentum distribution measured in the VMI are 2-D projections of the 3-D distribution. If the 3-D distribution is cylindrically symmetric around an axis parallel to the detector, then it is possible to retrieve it from its 2-D projection. Various approaches can be used to perform this inversion (BASEX, pBASEX oninon peeling, Fourier-Hankel method, etc.) [Heck 95] [Dasch 92] [Dribinski 02] [Manzhos 03]. In our case we use a reconstruction algorithm developed by Baptiste Fabre and based on the pBASEX method [Garcia 04].

Radon Transform

The cylindrical symmetry necessary to reconstruct the 3-D photoelectron angular distribution from its 2-D projection is fulfilled when the ionizing radiation is linearly polarized (the distribution is symmetric around the polarization direction), or when it is circularly polarized (in that case the symmetry axis is the propagation direction of light). When the ionizing radiation is elliptically polarized, or when multiple pulses with different polarizations are used in

an experiment, the cylindrical symmetry of the system is lost and Abel transform cannot be used to reconstruct the 3-D photoelectron angular distribution from the 2-D projections. In that case, the 3-D photoelectron angular distribution from the 2-D projections can be obtained using tomographic reconstruction [Wollenhaupt 13] [Sparling 22].

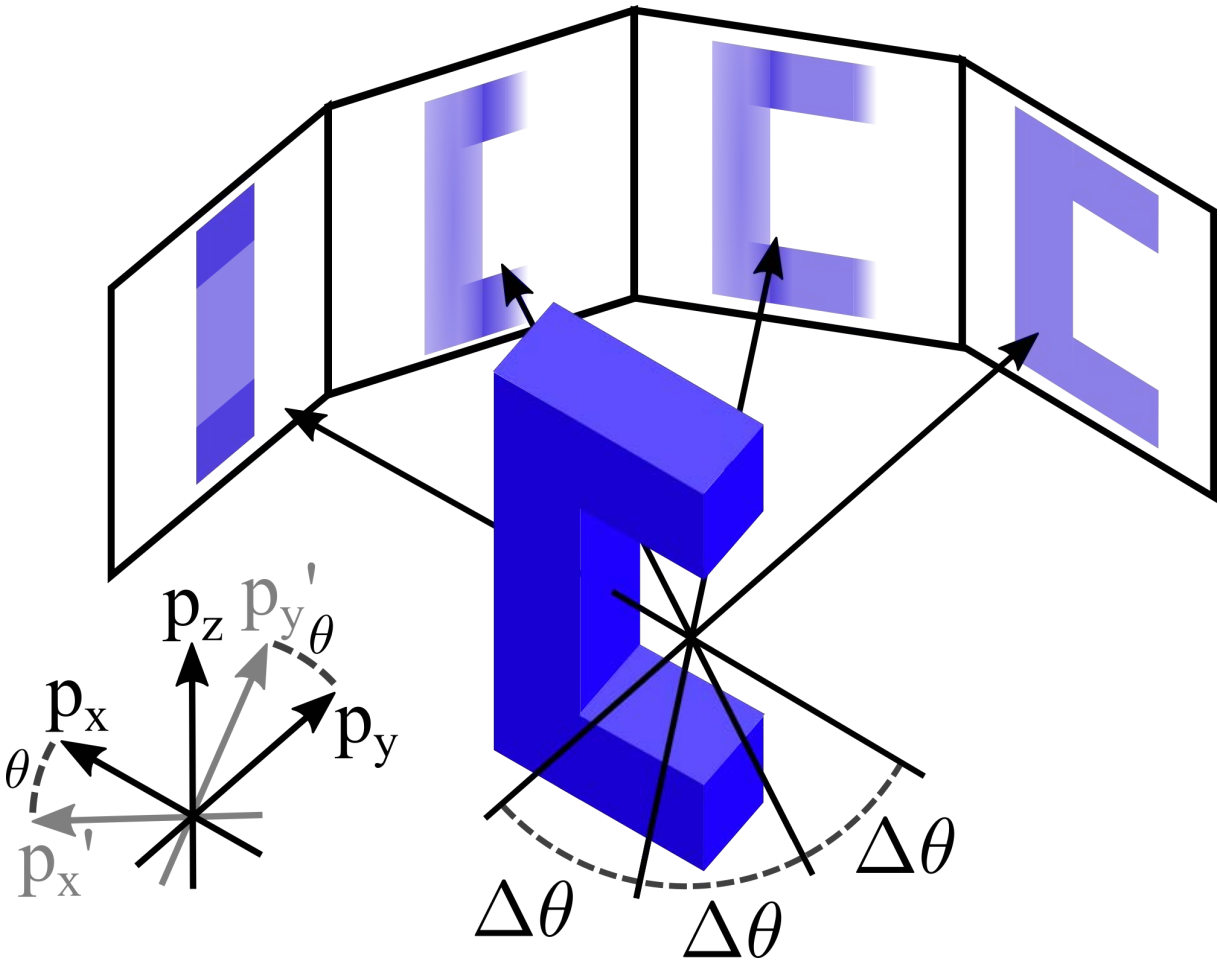

Figure 2.17 – *Schematic principle of the tomographic reconstruction of an arbitrary 3D object from 2D projections along several axis x′ in the polarization plane (x, y). z is the laser propagation axis. Extracted from [Bloch 20]*

In order to reconstruct back the whole 3-D photoelectron angular distribution, $\mathcal{F}(p_x, p_y, p_z)$, n 2-D projections, $P_\theta(p_{x\prime}, p_z)$, are recorded in the velocity map imaging spectrometer. The 2-D electron distribution $P_\theta(p_{x\prime}, p_z)$ is recorded different orientation of the distribution, done by rotating the polarization plane of the laser about the z-axis, for angles θ_i where $\theta_i = \frac{i\pi}{n}$ (see Fig. 2.17). These recorded 2-D projections forms a discrete sinogram (as defined above) and the whole 3-D distribution is obtained by performing an inverse radon transform given by:

$$\mathcal{F}(p_x, p_y, p_z) = \tilde{\mathcal{R}}\left(\frac{\pi}{n}\sum_{i=0}^{n} P_{\theta_i}\right) \tag{2.18}$$

Tomographic imaging requires significantly more acquisition time than simple VMI imaging, because in order to resolve fine structures in the photoelectron angular distribution one has to

make sure that the angular sampling $\delta\theta$ is sufficiently small. Hence, complicated 3-D distribution arising from strong field ionization requires higher angular sampling. We will see that this is not an issue with the high repetition rate laser system.

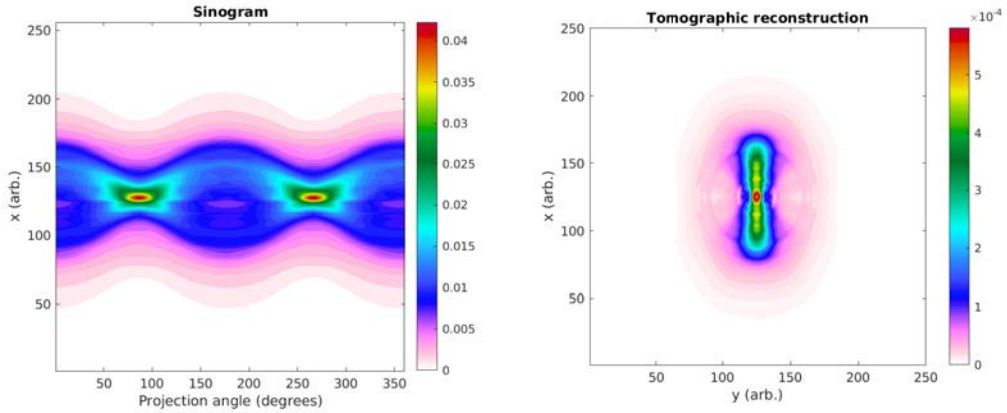

Figure 2.18 – *Tomographic reconstruction. (Left) The sinogram generated by recording a total of 72 2-D projections of the 3-D photoelectron angular distribution with an angular sampling ($\delta\theta$) of 5°. (Right) A cut through the polarization plane of the reconstructed 3-D photoelectron angular distribution.*

As an example, in Fig. 2.18, we show the tomographic reconstruction of the photoelectron angular distribution in strong field ionization of Fenchone. We record 72 2-D projections of the 3-D photoelectron angular distribution with an angular sampling of $\delta\theta = 5°$. The sinogram generated is shown in Fig. 2.18 (on the left) as a function of the projection angle. A inverse radon transform is performed on it to get the 3-D photoelectron angular distribution. A cut in the polarization plane, of the reconstructed 3-D distribution, is show in Fig. 2.18 (on the right).

II. 3 Apparatus Design

Molecular Jet

In velocity map imaging spectrometer the target is generally in a gaseous state. Most chiral molecules exist in either liquid or solid state, so it becomes necessary to convert these solids and liquids in gaseous state before being injected into the spectrometer. To that purpose, a dedicated heating bath and tubes to deliver the vapor in to the spectrometer are required. The chiral molecules of interest are put in test-tubes which are then immersed in a water bath. The temperature of the water bath being controlled by a PID controller. The test-tubes are connected to a KF flange and which are then connected to 1/4 $''$ stainless steel tubes. The stainless steel tubes are connected to the source chamber of the VMI through a CF 40 flange. These tubes are heated to a fixed temperature, to avoid condensation on the interior walls, using a heating strip and the temperature being regulated by an on-off regulation circuit in a feedback loop. The tube inside source chamber of the VMI is connected to a nozzle with a diameter of 200 μm. The nozzle and the tube inside the vacuum chamber are heated to a higher temperature compared to outside, to maintain a temperature gradient and avoid further condensation and unidirectional flow of the vapor.

Depending on the vapor pressure of the chiral molecule being probed and the pressure required in the interaction region to get a high signal-to-noise ratio, one can heat the bath and tubes to different temperature values. The relationship between the vapor pressure and temperature of a pure liquid or solid can be approximated by the Antoine equation:

$$\log P = A - \frac{B}{C+T} \tag{2.19}$$

where P is the absolute vapor pressure T is the temperature, A, B and C are compound specific coefficients. The evolution of vapor pressure of a few compounds used in this thesis is given in the Fig 2.19

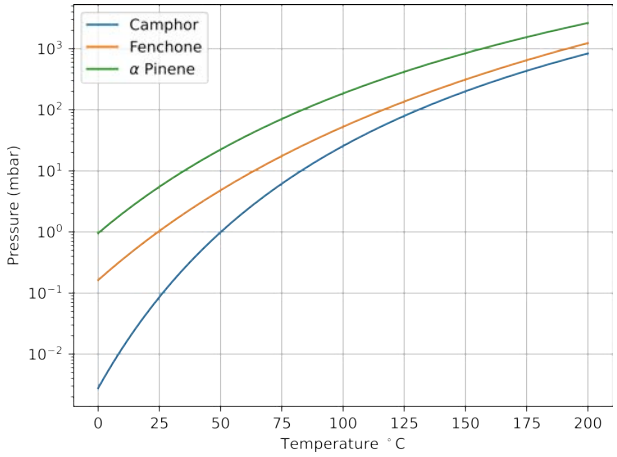

Figure 2.19 – *Variation of the vapor pressure of various chiral molecules as a function of the temperature.*

Typically the pressure in the source chamber is in the order a few 10^{-4} mbar and is pumped by two 2×250 L/s turbo-molecular pumps. The source chamber is separated from the spectrometer chamber by a skimmer of diameter 700 μm which selects the inner part of the molecular jet being formed and ensures differential pumping between the two chambers, as it is necessary to maintain vacuum of $\sim 10^{-7}$ mbars in the interaction chamber. The latter is pumped by 3×500 L/s turbo-molecular pumps, for proper efficient detection and collection of the electrons generated at the interaction region. The skimmer being fixed, the nozzle is mounted on a manipulator with degrees of freedom along the x,y and z axis. The nozzle is aligned with respect to the skimmer so that the molecular jet arrives directly between the extractor and repeller electrodes. The distance between the skimmer and nozzle is maintained at around $5-7$ mm so as to attain a molecular jet with a relatively high molecular density to obtain high signal-to-noise ratio. The size of the skimmer is also chosen wisely so that ionization happens from the smallest possible interaction region. The laser and the effusive molecular jet enters the geomagnetically shielded spectrometer through 10 mm holes in the μ-metal shield.

Spectrometer

Low energy configuration: At the beginning of this thesis, the VMI was in this initial configuration, as built by Charles Handschin in 2012 and shown in Fig. 2.20. The repeller and the extractor electrodes are separated by 23 mm and the ionization volume is located at the

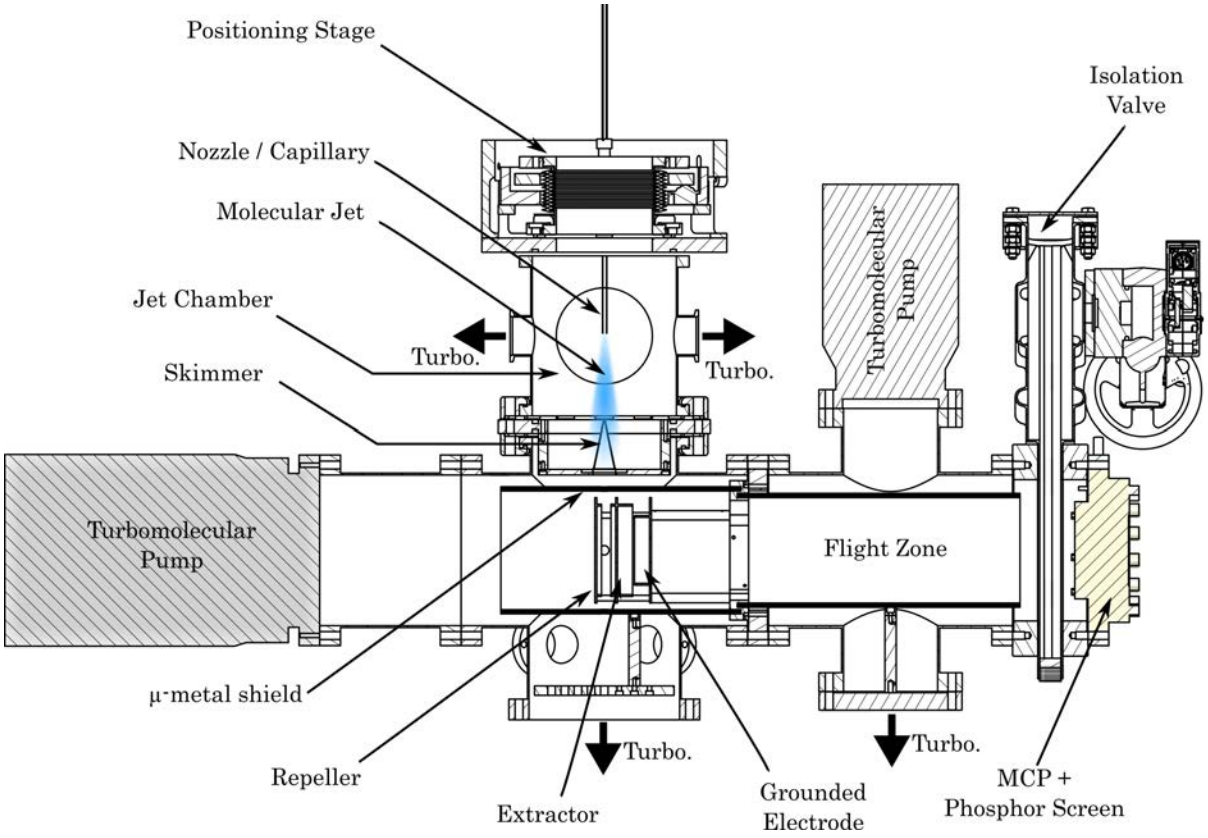

Figure 2.20 – *Schematics of the velocity map imaging spectrometer used to detect low energy electrons up to* 8 *eV [Bloch 20] [Handschin 13].*

center of the two electrodes. The distance between the extractor and the ground electrode is 34 mm. The diameter of the plates is 11 cm and the extractor and the ground electrode has central hole of diameter 2.5 cm each. The drift region is 500 mm long and the whole flight length from the interaction region to the MCP is shielded by a cylindrical μ-metal piece (see Fig 2.20). This geometrical configuration allows to detect low energy electrons with high energy resolution and to minimize aberrations of the electrostatic lens. Each pair of electrodes are separated by three ceramic rods of a dielectric breakdown of 20 kV/mm. This sets a limit to the maximum voltage that can be applied to the electrode before there are electrical discharges. The edges of the electrodes are also rounded to prevent electrical breakdown due to lightning rod effect. The electrodes have a cylindrical hat to minimize aberrations in the electrostatic field lines of the lens. In this configuration of the spectrometer the typical voltage applied on the repeller electrode is $V_{rep} = -2$ kV to detect electron kinetic energies up to 9 eV with a resolution of ~ 100 meV at 5 eV. For good imaging conditions the ratio between the repeller and the extractor voltage is set to $V_{ext}/V_{rep} = 0.714$. The voltages can be scaled accordingly to choose the electron kinetic energies of interest and resolution.

Mid energy configuration: In strong-field ionization of molecules with intensities of 3×10^{13} W/cm^2 and laser wavelength of 1030 nm electrons can gain kinetic energies up to ~ 30 eV. Although theoretically with $V_{rep} = -8$ kV one can detect electron kinetic energies of up to 35

eV, in the above configuration, it generally leads to electric arcs and has a poor electron kinetic energy resolution. One way to avoid electrical breakdown is to provide better ground connection to the whole setup (to remove leak currents and stray charges on the ground plate), switch off all the vacuum gauges (to eliminate any leak current source) and to reduce the molecular density in the interaction region by misaligning the nozzle with respect to the skimmer (to reduce the probability of the very high energy electrons falling on the electrodes and charging up and also to avoid molecules from adhering to the electrodes and getting electrostatically charged and discharging at a latter time). The first two options did not help much but the last one reduced the time interval between the start of the experiment and the appearance of electric arcs on the detector from a minute to $\sim 5 - 10$ minutes. This is however not a long-term viable option for detecting high energy electrons as it could lead to a complete dielectric breakdown of the ceramic spacers and also introduces tons of aberrations in the data recorded.

We thus modified the VMI configuration by shortening the time of flight length, from 500 mm to 150 mm, thus measuring the expanding electron cloud before it exceeds the detection solid angle. This allows to detect high energy electrons up to 50 eV with a repeller voltage of $V_{rep} = -2$ kV hence also eliminating the possibility formation of electric arcs and discharges. Initially, flat electrodes were used but were later replaced with electrodes having cylindrical hats, as this helps in maintaining higher degree of cylindrical symmetry in the electrostatic field lines of the lens and hence reducing aberrations. In this configuration too, to isolate the effects of the geomagnetic field on the trajectory of electrons, a μ-metal shield was used. Although the μ-metal provides shielding through most of the flight length of the electrons, it leaves a portion of ~ 10 mm length uncovered. The seepage of the geomagnetic field through this also caused additional artifacts in the imaging of photoelectrons. A Helmholtz coil was used to negate the effects of the geomagnetic field. In addition to this the distance between the, on-axis, turbo-molecular pump and the repeller electrode was increased to prevent axial magnetic fields of the pump to leak into the spectrometer.

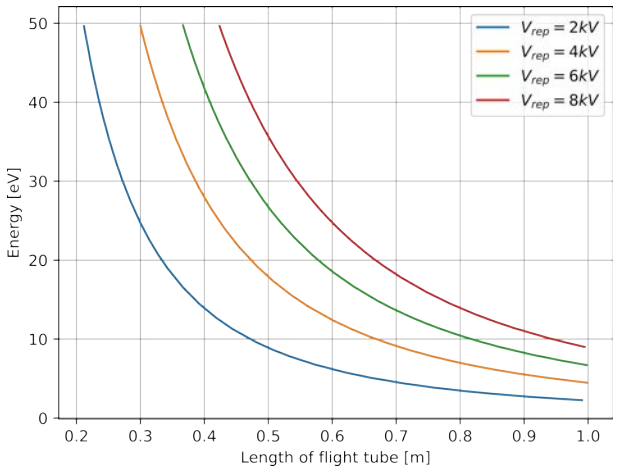

Figure 2.21 – *SIMION simulation results of the evolution of maximum kinetic energy of the phot-electrons detectable by the VMI as a function of the length of flight of the electrons for different repeller voltages (V_{rep}). Images taken from [Handschin 13].*

High energy configuration: The optimized mid-energy configuration was successfully used for experiments involving backscattering electrons in strong 1030 nm fields. The saturation of the molecular ionization prevented us to push the kinetic energy of the detected electrons beyond a few tens of eV. Increasing the laser wavelength would enable us to produce much more energetic electrons. In the perspective of performing experiments at Lidyl with a 3.4 μm source, I have designed a new, high energy configuration for the VMI. To increase the maximum detectable electron energies one can further shorten the length of the time of flight of the photoelectrons or increase the size of the MCP or increase repeller voltage. In the setup of the spectrometer described above, shortening the time of flight axis is not enough to detect electron kinetic energies so high, increasing the size of the MCP is too expensive and increasing the repeller voltages to or higher -8 kV leads to electrical discharges and also causes strong curvatures in the electric field lines which leads to loss of energy resolution. Thus to detect such high energy electrons up to 100's of eV the conventional scheme of using a stack of three electrodes is generally inefficient. To overcome these problems a VMI spectrometer can be combined with an additional Einzel lens [Garcia 05]. Although it allows detection of electrons up to 100's of eV but requires tuning of voltages applied to individual electrodes. The second approach to use additional electrostatic lens of opposite polarities to the reduce curvature of the electrostatic field lines leading to better energy resolution of high energy electrons [Skruszewicz 14]. These modifications help in detecting high energy electrons with good energy and angular resolution but introduce finely tuned voltages to be applied and high degree in complexities in the construction of the spectrometer.

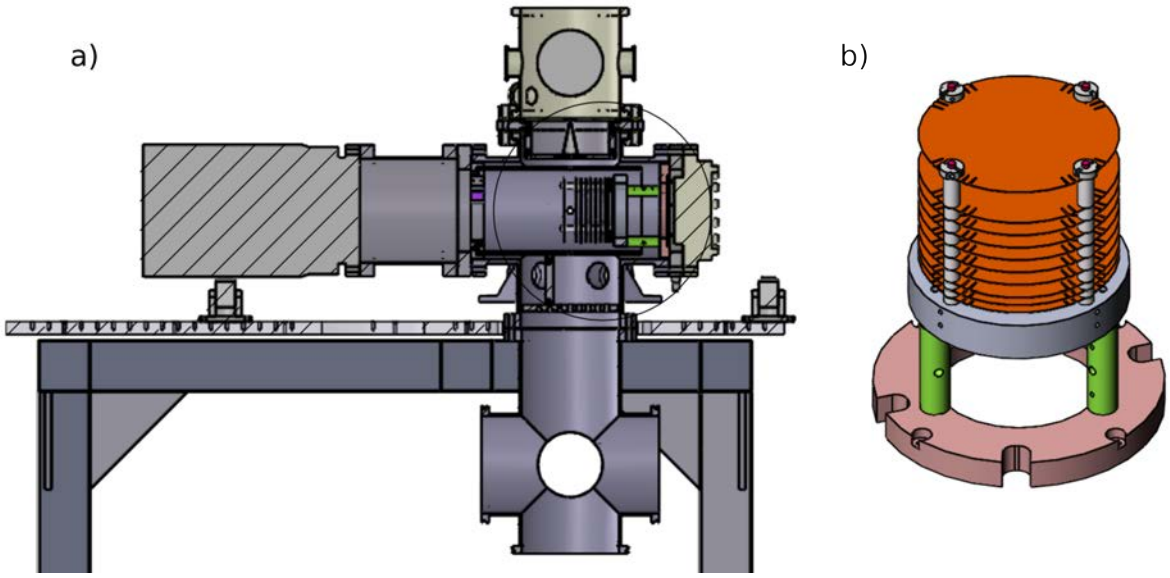

Figure 2.22 – *(a) CAD drawing of the high energy thick lens velocity map imaging spectrometer (TL - VMI). (b) The CAD assembly of the spectrometer.*

A compromise to reduce the degree of complexities without much affecting the energy resolution of the high energy electrons is to use a thick lens velocity map imaging spectrometer (TL - VMI) [Kling 14] [Würzler 18] [Würzler 19]. The TL - VMI developed is similar the one developed by D. Würzler, et. al. [Würzler 19]. Compared to three electrodes in the configuration

of Eppink and Parker, additional electrodes are introduced between the extractor and the ground electrode. This increases the spatial extent of the focusing electrostatic field, making the field lines more homogeneous and reducing the effect of aberration in the imaging of high energy electrons by reducing the curvature of the electrostatic fields when operating at high voltages. In this configuration 11 electrodes are used. The repeller and the extractor are separated by 18 mm and the extractor and the next 6 electrodes are separated by 7 mm from each other the rest is separated by a distance of 4 mm. The ground electrode is separated from the last electrode in the array by 4 mm and the distance between the ground and the detector is 85.8 mm. The electrodes are separated from each other by ceramic glass rods with a DC dielectric strength of 129 kV/mm and volume resistivity of 10^{17} Ω.cm. The first extractor electrode and the electrodes till just before the ground electrode are the connected to each other by 10 MΩ resistors, in series, to provide voltage gradient. The first extractor and the repeller electrode are connected to independent power supplies and hence to achieve good imaging conditions only the ration between the two is to adjusted. The whole spectrometer being enclosed by a μ-metal shield to avoid aberrations due to geomagnetic field. The $\delta E/E$ remains below 0.3% even with an ionization volume of 400×400 μm, which is typically less than the size of the Rayleigh length of ~ 200 μm.

The different spectrometer configurations of the VMI presented here enable us to record the 2-D projections of the 3D photoelectron angular distributions for photoelectrons energies ranging from zero to 100's of eV.

Detector: MCP, Phosphor & Camera

MCP: Micro-channel plates (MCP) are 2-Dimensional array of electron multipliers acting as a chain of dynodes, thus amplifying the detected signal. They provide high spatial and temporal resolution and can detect a wide range of particles from electrons, ions, VUV to X-ray and gamma rays. Typically a potential gradient is applied along the channel. Multiple secondary electrons are emitted when a particle of interest comes and collides with the inner wall of the dynode, leading to cascaded emission of secondary electrons. These secondary electrons are accelerated along the potential gradient applied and follow parabolic trajectories, determined by the initial velocity. This leads them to striking on the opposite wall of the channel, hence creating an avalanche of secondary electrons. The secondary electrons travel in this way till the end of the channel, while hitting its walls repeatedly, resulting in an exponential amplification of the signal detected.

The main parameters that determine the characteristic gain of MCP are the α, the open area ratio and bias angle. The thickness of the MCP is nearly equal to the channel length (L). The ratio of the channel length to the channel diameter (d) $\alpha = L/d$. α determines the gain of the MCP coupled with the secondary emission factor. Typically α is in the range of $40 - 60$. The OAR or the open area ratio is the ratio between the channel open area and the total area of the MCP. This determines the net effective area of the MCP. The bias angle is the angle formed by the channel axis and axis perpendicular to the plate surface. The channels are stacked at an angle to increase the gain of the MCP. It is also chosen carefully to increase the detection efficiency, spatial resolution and to prevent cross-talk between channels. Typically the dead-time of the MCP varies from 450 ps to 1.5 ns thus providing very high temporal resolution. Typically

MCP have resistance of $20 - 700$ M Ω with a dark current of 0.5 p A cm^{-2}.

Phosphor: To image the electron cloud emitted at the exit of the MCP, one can either use a delay line detector or phosphor screen coupled with a camera. Phosphor screens emit photons when accelerated electrons are bombarded on the phosphor. As an electron comes and hits the phosphor it excites an electron from the valence band to the conduction band, thus leaving an associated hole behind in the valence band. They then latter recombine emitting a photon. Typically phosphors have conversion factors between $20 - 200$ photons per electron. The conversion efficiency depends on the phosphor type and the kinetic energy of the photons. Depending on the type of phosphor the emission spectrum changes, typically in the range of $460 - 530$ nm, along with their fluorescence lifetime, ranging from $1\mu s - 100$ ms, and their spatial resolution too. Especially when working with high repetition rate lasers, to avoid ghost images from previous images, phosphors with fast decay times are used.

Camera: A 16-bit cooled scientific-CMOS camera was used (Orca Flash 4.0, Hamamatsu) with an effective number of pixels of 2048×2048, an effective area of 13.312×13.312 mm and cell size of 6.5×6.5 μm. The full well capacity is 30 000 electrons and provides a sufficiently high dynamical range of 33 000 : 1. The quantum efficiency of the camera at 545 nm, the peak emission wavelength of phosphor screen, is $\sim 82\%$. The camera has a low readout noise of 1.5 (RMS) e^- and dark current of 0.6 e^-/pixel/sec thus providing images of high signal-to-noise ratio (SNR):

$$SNR = \frac{signal}{\sqrt{signal + readout\ noise + dark\ current.t}} \tag{2.20}$$

The camera uses a rolling shutter method for exposure and readout. Rolling shutter exposure is achieved by exposing vertical lines slightly offset in time compared to subsequent lines. This enables reducing the dead-time of the camera to zero.

A typical photoelectron spectrum recorded in above threshold ionization by G. Paulus et al. is shown in Fig. 2.23. The dynamic range of the spectrum is in the order of $10^5 - 10^7$. On the other hand, the dynamic range of the camera is limited to 3.3×10^4. This issue can be circumvent by saturating the camera in the area corresponding to low energy electrons, or by acquiring data for different exposure times and then linearly stitching them on top of another to replace the saturated pixels.

II. 4 Energy Calibration

To measure the kinetic energy of the electrons recorded in the VMI one has to calibrate the detector, i.e. to properly assign the energy of the electron that falls at a position (y, z) of the detector. One can simply ionize an atom or a molecule with a known photoelectron kinetic energy spectrum and assign the position on the detector with its corresponding energy of the photoelectrons recorded. The above-threshold ionization process is convenient for energy calibration, because it produces regularly spaced peaks in the photoelectron spectrum, as seen in Fig. 2.23. This process occurs when a molecule or an atom is ionized using an intense laser pulse. The pho-

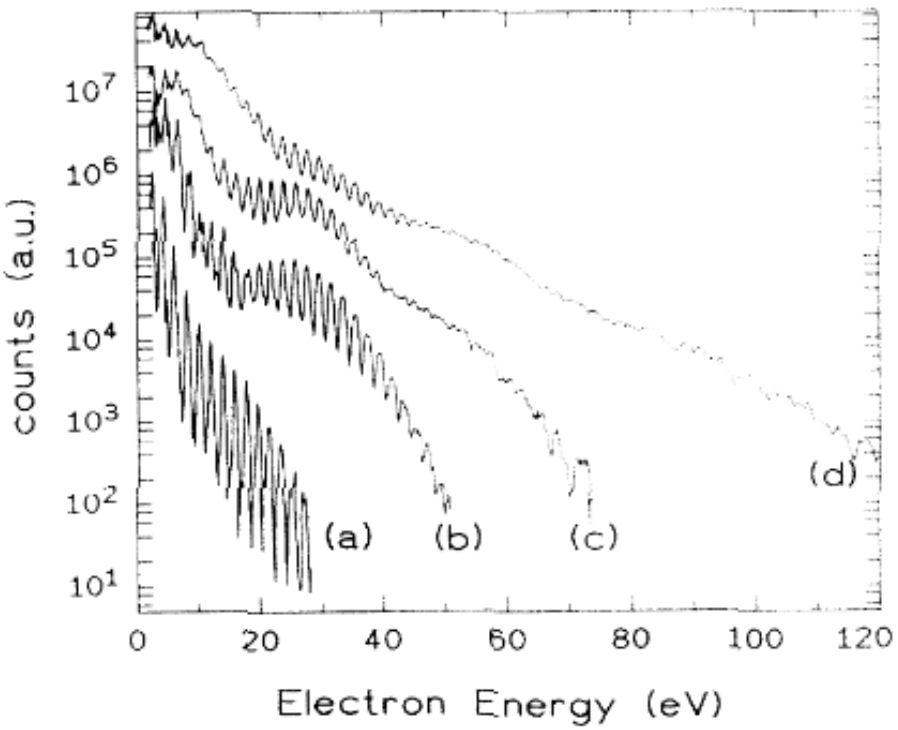

Figure 2.23 – *Typical photoelectron spectrum of above threshold ionization. Extracted from [Paulus 00]*

toelectrons generated can absorb multiple photons beyond the ionization threshold, producing electrons whose kinetic energy can be written as:

$$E_{kin} = n \times h\nu - I_p - U_p \tag{2.21}$$

where I_p is the ionization potential of the molecule or atom, U_p is the ponderomotive energy of the electron gained as a result of the quiver motion in the oscillating electromagnetic field, $\hbar\omega$ is the energy of the photon and n is the number of photons absorbed by the target. Thus the electrons form ATI peaks,separated in energy by $\hbar\omega$. Using the Eqn. (2.21) a calibration curve of energy vs position of the ATI-peaks on the detector can be obtained. The details of the procedure are explained below.

To perform the above calibration, the photoelectron distribution of (+) α-Pinene is recorded in the VMI at an intensity of $\sim 2.5 \times 10^{13}$ W/cm^2. The data acquired is then Fourier filtered and the 2-D photoelectron angular distribution for vertical linear polarization is reconstructed. Calibration of the VMI spectrometer is performed for the vertical linear polarization as it has the highest number of above-threshold ionization peaks. The photoelectron momentum angular distribution is first transformed from Cartesian co-ordinates to polar co-ordinates ($\mathcal{P}(y,z) \Rightarrow \mathcal{P}(r)$, where $r = \sqrt{y^2+z^2}$ corresponds to the pixel number). The 1-D photoelectron spectrum (PES) is extracted from the polar representation of the photoelectron angular distribution by summing over the angular co-ordinate θ $\forall\theta \in [80°, 100°]$ (see Figure 2.24 (a)). Although the ATI peaks are easy to identify on the plateau of the spectrum but it is comparatively hard to identify the exact position of the peaks in the tail of the distribution. One way to identify the

ATI peaks is to manually extract their position but it is lame and it can be automated. The tail of the 1-D photoelectron spectrum can be approximated as an $\exp(r)$ function. One can perform a very crude fit of a straight line to the tail end of the spectrum with the assumption that in the 1^{st}-order approximation an exponential can be expanded into a Taylor series as $\exp(r) = 1 + r + \cdots$. The fitted straight line is then subtracted from the PES, to increase the weight of the peaks, and thus the resultant curve (represented by a function f) have ATI peaks more prominent compared to Figure 2.24 (a) (see Figure 2.24). Each peak thus obtained are local maxima of the function. These peaks can be automatically extracted using the theorem of local maxima, which states that for a given function $f : X \to \mathbb{R}$ then $x_0 \in X$ is a local maxima point of the function f iff $(\exists\ \epsilon > 0)$ such that $f(x_0) \geq f(x)$ for all x in X. The ATI peaks are then extracted from the differential curve obtained by a simple comparison of neighboring values over a high energy interval of the photoelectron spectra where ATI peaks are the only dominant structure present. The extracted position of the peaks are shown in blue in Figure 2.24 (b).

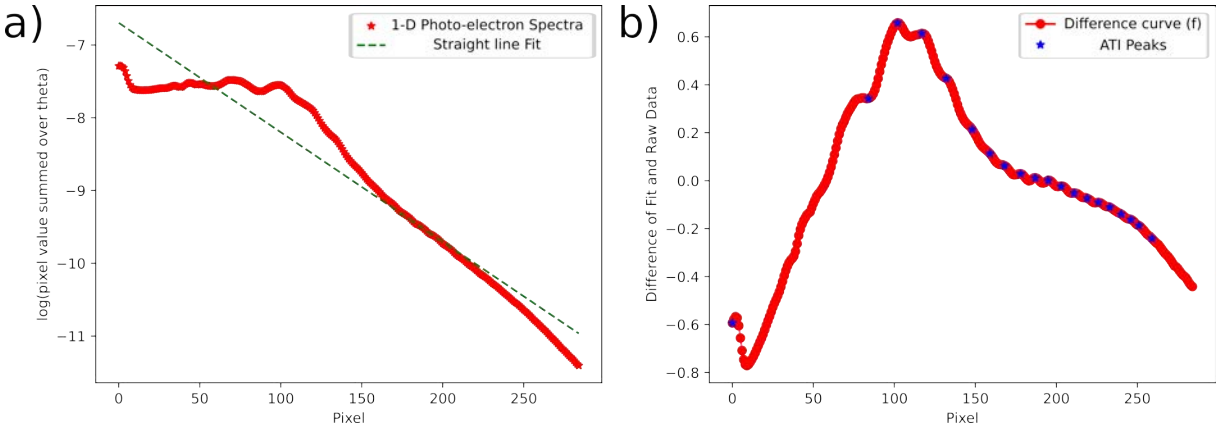

Figure 2.24 – *Figure 2.24 (a) shows 1-D photoelectron spectra (shown in red scatter points in semi-log scale) obtained for (+) α-Pinene at 2×10^{13} W/cm^2 by transforming the 2-D photoelectron angular distribution from Cartesian co-ordinates to polar co-ordinates and then summing over the angular co-ordinate $\theta : \forall\theta \in [80°, 110°]$. A straight line (shown in green dashed line) is then fitted to the 1-D PES. Figure 2.24 (b) shows the difference of the fitted line and the raw signal (shown in red). We see that the difference spectrum (f) shows the ATI peaks in the higher energy part of the spectrum more prominently and thus subsequently the ATI peaks are found out by comparing neighboring values in the difference signal. The ATI peaks thus found out are shown in blue.*

From equation (2.16) we know that $E \propto r^2$ and hence a quadratic fit, expressed by the equation $E = ar^2 + br + c$, is performed with a and b as the fitting parameters; the value of c is set to zero to account for the fact that for $r = 0 \Rightarrow E_{kin} = 0$, the extra term $b\ .\ r$ is used to account for aberrations in the VMI imaging. The fit is done for different values of n (see equation (2.21)) and the value of n is chosen to minimize the fitting error, given by the covariance matrix of the fit. The extracted curve then used as the calibration curve for energy v/s pixel number (see Figure 2.25). The fitting is done using non-linear least square method and the best fit values for the parameter and their respective standard deviation errors, so that the sum of the square of the residuals is minimized, are: $a = 3.62 \times 10^{-4} \pm 0.04 \times 10^{-4}$ and $b = 8.49 \times 10^{-3} \pm 0.82 \times 10^{-3}$.

In the multi-photon regime, since the maximum energy of the electrons detected is sub-

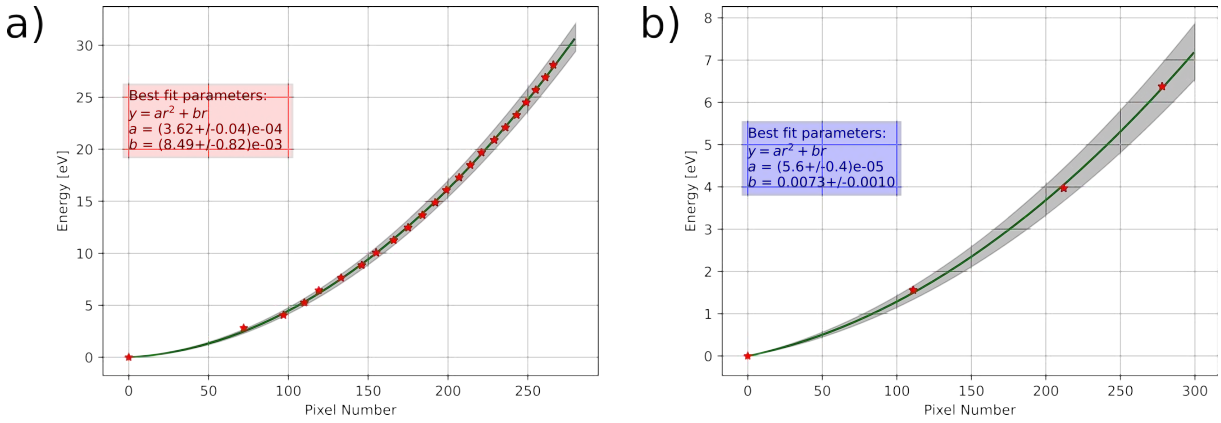

Figure 2.25 – *(a) The energy of the ATI peaks is calculated for different values of n from equn.* (2.21) *(shown in red stars). The ATI peaks are then fitted to a quadratic function ($E = ar^2 + br$) with a and b as the fitting parameters. The fit with the lowest error is then chosen as the energy calibration curve (shown in green). A* 95% *confidence interval of the fit is shown as the grey region. The inset box shows the best fit fitting parameter values and their corresponding error. (b) Shows the calibration curve obtained for a lower repeller voltage V_{rep} to image low energy electrons with higher precision. The grey region is the* 95% *confidence interval of the fit. The inset box shows the best fit fitting parameter values and their corresponding error.*

stantially lower, typically about $5 - 7$ eV, one has to adjust the repeller voltage (V_{rep}) of the VMI accordingly. In doing so one has to re-calibrate the VMI using the above method again, if there is an sufficient number of ATI peaks present, or one can revisit equation (2.16) and find the calibration factor accordingly. For multi-photon ionization of $(-)\alpha$-Pinene with 515 nm at intensities of 2×10^{13} W/cm^2, three ATI peaks are observed. This is enough to perform a meaningful quadratic fit to obtain the energy calibration curve. We follow the fitting procedure as described above. The best fit values for the parameter and their respective standard deviation errors, so that the sum of the square of the residuals is minimized, are: $a = 5.6 \times 10^{-4} \pm 0.4 \times 10^{-4}$ and $b = 7.3 \times 10^{-3} \pm 1.0 \times 10^{-3}$. The 95% confidence interval of the fit is comparatively larger, than for high energy VMI setting, and is due to comparatively less number of ATI peaks used to perform the quadratic fit.

III COLTRIMS

We have seen that velocity map imaging is a powerful technique to measure the angular distribution of photoelectrons. The 3D distribution can be retrieved from its projection if symmetry conditions are fulfilled, and otherwise a tomographic procedure can be used. However the information provided by a VMI can be insufficient in many situations. For instance, when a polyatomic molecule is photoionized by XUV light, many ionization channels are open. In other words, electrons can be removed from many different orbitals. The resulting photoelectron spectrum is constituted of the incoherent superposition of these different channels and it can be difficult to assign spectroscopic features in it. This issue can be partially solved by measuring not only the photoelectrons, but also the ions which they originate from. This requires a coincidence electron-ion detection, which can be performed using a COLTRIMS (COld Target Recoil Ion Momentum Spectrometer) [Ullrich 03]. The COLTRIMS allows to simultaneously detect

3-D angular distribution of photoelectrons and photoions. This provides a multi-dimensional picture of the interaction, enabling for instance to disentangle multiple ionization channels or retrieve molecular-frame photoelectron angular distributions.

The COLTRIMS detector consists of:

- Gas jet
- Ultra-High Vacuum chamber
- Helmholtz coils
- Spectrometer
- Detector:
  - Micro-channel Plates (MCP)
  - Delay line detector
- Electronics for signal amplification and differentiation

III. 1 Vacuum & Molecular Jet

Supersonic Jet

As most chiral molecules exist in liquid or solid state, at room temperature, it becomes necessary to convert them into gaseous phase to produce a supersonic gas jet. Thus the chiral molecule of interest is kept in a bubbler and heated to temperature of about $50 - 100$ °C. This enables reaching pressures of a few 10 mbar (see Fig. 2.19), which is too low to generate a supersonic flow. To solve this issue, a carrier gas, typically Ar, N_2 and He, is fed into the bubbler at pressures of 2.5 bars. The chiral molecules along with the carrier gas are then connected to the nozzle through a series of stainless steel tubes. The tubes are heated to higher temperatures than the bubbler to avoid condensation and unidirectional flow of the gas. The nozzle can be heated up to temperatures of 120°C. As set of two metallic mesh filters with mesh hole diameters of 6 μm is placed in the gas line before the nozzle to avoid clogging. The nozzle is mounted on a $X - Z$ manipulator to align the supersonic flow with the skimmer (fixed) in vacuum.

Supersonic gas jets of atoms and molecules are a common tool in ultrahigh-resolution spectroscopy, laser-induced fluorescence spectroscopy and laser-induced atomic and molecular spectroscopy. The high translational velocity of the molecules and atoms in the gas jet results in the cooling of the internal degrees of freedom and thus provides ultrahigh-resolution images. A supersonic gas jet is produced by expansion of gas through a small nozzle into an evacuated chamber. In the COLTRIMS a supersonic jet is produced by expanding the gas molecules of interest from a high backing pressure region (typically > 2 bar above absolute zero) to an evacuated region (typically in the range of $\sim 10^{-5}$ mbar) through a nozzle of 30 μm resulting in a supersonic expansion. The expansion profile of a supersonic jet is shown in Fig. 2.26. The center zone of the gas expansion is supersonic and it is selected using a 200 μm skimmer placed 12.8 mm from the nozzle.

Vacuum System

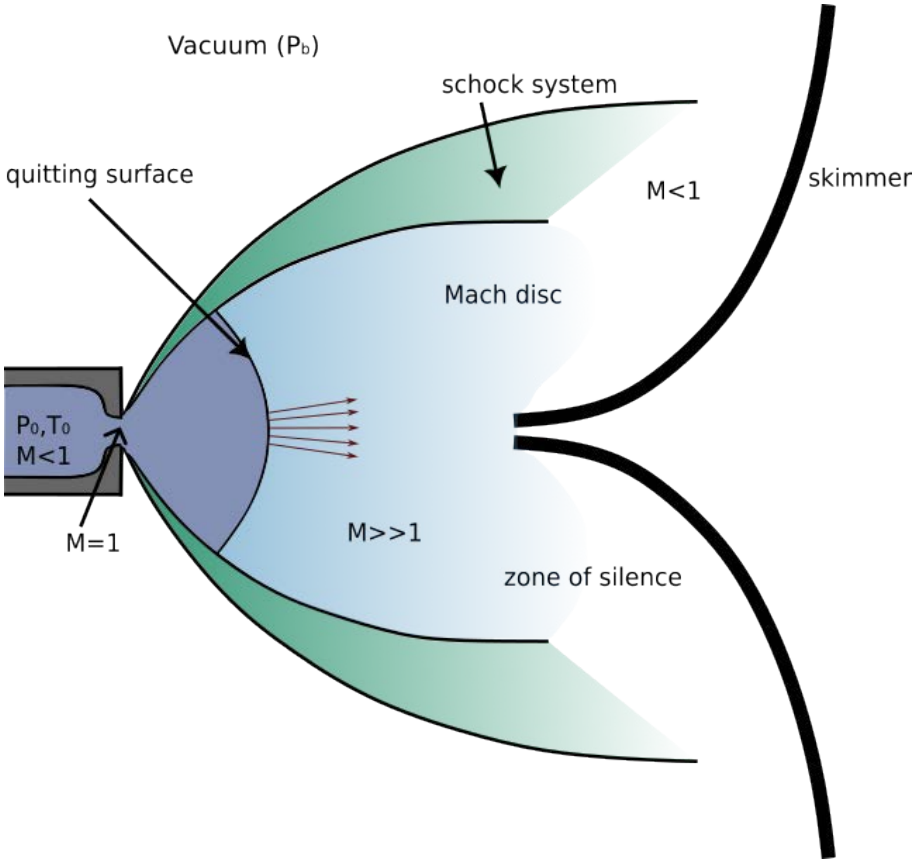

Figure 2.26 – *Profile of the supersonic flow produced at the nozzle. The central part of the zone of silence is selected using a skimmer to produce a supersonic molecular jet.*

The vacuum system of the COLTRIMS can be divided into three parts: Jet, Spectrometer and the Dump chambers. In the jet chamber the molecular gas jet is formed. The jet chamber is pumped down to pressures of $10^{-4} - 10^{-5}$ mbar using a 1800 L/s turbo-molecular pump to obtain a supersonic jet. A skimmer is used to skim the molecular jet into the spectrometer chamber. The spectrometer chamber is kept at pressures of $\sim 10^{-7}$ mbar for nominal operations of MCPsn high voltage operation without electrical discharges, and to reduce background signal produced by ionization of the residual gas. The spectrometer chamber is pumped using two 700 L/s turbo-molecular pumps backed by a 33 L/s turbo pump connected to a diaphragm pump. Pressures of about low 10^{-9} mbars is obtained, after two weeks of pumping, without molecular jet and 5×10^{-8} mbar is obtained with the jet. To extract the molecular jet efficiently without polluting the spectrometer chamber a two-stage dump is used. The first part of the dump stage consists of a catcher, of internal diameter of 9.5 mm, which is used to extract the molecular jet efficiently and thus minimizing the backflow. The catcher is placed 155.5 mm from the interaction volume. The catcher of the second dump stage is 15 mm in diameter and is placed 88 mm away from the first catcher (it must be placed at a distance of 5 times the diameter of the second catcher from the first catcher). The first dump stage is pumped by a 80 L/s while the second stage is pumped by a 300 L/s turbo-molecular pump. The residual pressure in the dump stage is about $\sim 10^{-6}$ mbar. All the turbo-molecular pumps are backed by a 600 m^3/h root pump.

Laser Coupling

A EUV-grade fused silica window is installed perpendicularly to the molecular jet to couple the fundamental, second and third harmonic of the laser. Two optical skimmers with diameters of 9 and 4 mm are placed after the window to reduce scattered light falling on the MCP. An optical skimmer of 9 mm in diameter is further placed at the exit of the COLTRIMS to prevent back reflections from the expanding beam. The expanding beam is then reflected using a 45° mirror down into a dump.

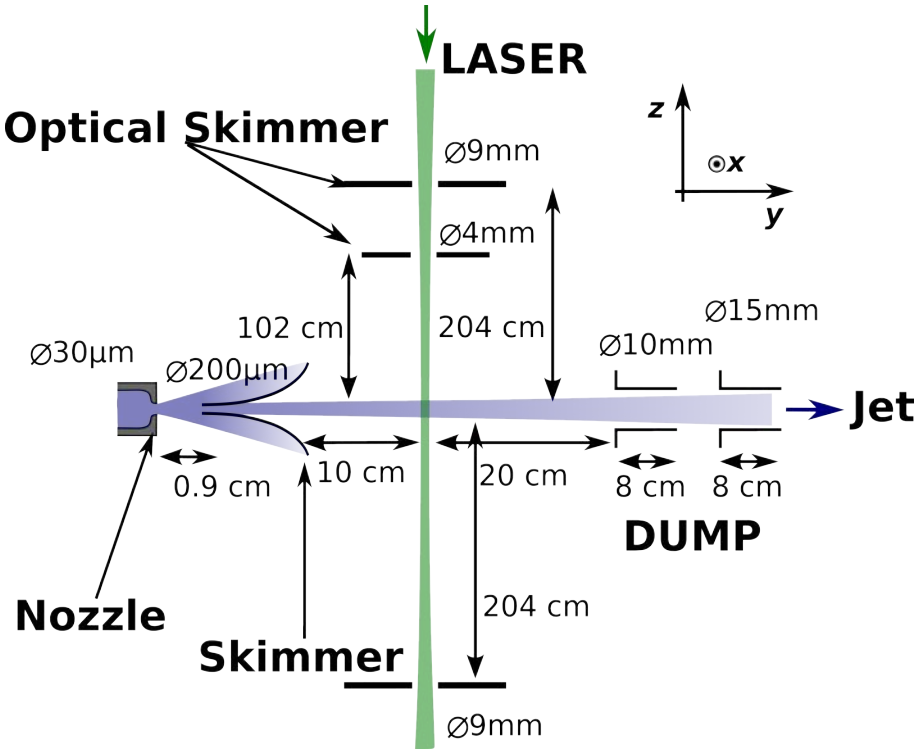

Figure 2.27 – *Schematics of the jet and optical elements. A 200 µm skimmer is used and is placed 9 mm from the nozzle of diameter 30 µm to produce a supersonic jet. See text for details.*

Measurement of molecular beam size

To extract the size of molecular beam, the fundamental laser beam ($\lambda_L = 1030$ nm) is expanded using a $\times 3.33$ telescope ($-75/+250$ mm). The expanded beam is frequency doubled in a type-I BBO crystal to obtain a 515 nm beam which in turn is further expanded using a $\times 3$ 0° reflective telescope ($-100/+300$ mm). The second harmonic ($\lambda_L = 515$ nm) is filtered using two 45° dichroic mirrors ($R = 99.9\%$ at $\lambda = 515$ nm and $T = 99.9\%$ at $\lambda = 1030$ nm). The second harmonic is then focused on to the molecular gas jet, in the COLTRIMS, using a 500 mm CaF_2 plano-convex lens. The Rayleigh length of the laser beam is experimentally found out by measuring the diameter of the laser beam at different positions around the focus and fitting them to Eq. 3. The FWHM focal spot of the laser beam is determined to be 16 μm and a Rayleigh range of 1.56 mm (see Fig. 2.28 (a)).

The focused second harmonic beam is intense enough to only ionize the chiral molecules in the molecular jet and not the carrier gas. The chiral molecule used is (+) Methyl Lactate, with ionization energy of 9 eV, which undergoes multi-photon ionization following a power

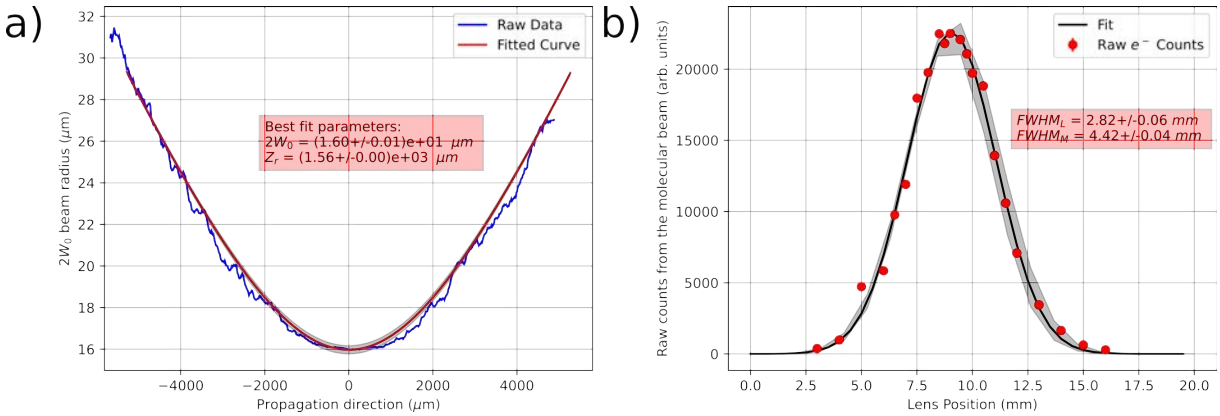

Figure 2.28 – *Determination of the size of molecular beam. (a) The laser beam profile of the focused second harmonic. (b) Electron counts per minute as a function of lens position. A Gaussian fit is made to the convolution of the molecular beam and the laser beam. $FWHM_M$ is the full width at half maxima of the Gaussian fit to the convolution and $FWHM_L$ is the molecular beam width extracted from the Equn. 15. A 95% confidence interval of the fit is shown by the region shaded in gray.*

law dictated by $I^{3.66}$. The number of photoelectrons generated is recorded per minute as a function of the focal spot position relative to the molecular beam (electrons produced from the thermal part of the molecular jet is not taken into account). The effective length of ionization is calculated from Eqn. 10 (see Appendix III) $z_{Reff} = z_R\sqrt{1/3.66} = 522$ μm. Assuming that the interaction of the molecular beam and the laser to be a convolution of two Gaussian functions, the number of photoelectrons generated per minute as a function of the focal spot position relative to the molecular beam is fitted to a Gaussian function. The FWHM of the convoluted Gaussian calculated is 4.42 ± 0.06 mm (see Fig 2.28 (b)). The molecular beam width (FWHM_L) is calculated using Equn. 15 (see Appendix IV) to be 2.82 ± 0.04 mm.

III. 2 Spectrometer

The spectrometer is designed to measure electrons with energies ranging from $0 - 20$ eV as photoelectron circular dichroism decreases with an increase in the energy of electrons. On contrary to VMI, position sensitive detectors are used in COLTRIMS to perform spatial imaging of the photoelectron angular distribution. To guide the electrons and ions on to the position sensitive detector a series of copper electrodes are used to generate a homogeneous and isotropic field along the spectrometer axis. A total of 65 electrodes have been used and are separated from each other by ceramic spacers. The electrodes are connected to each other in series by 100 kΩ resistors, with a total resistance of 6.4 MΩ across the whole spectrometer. The spectrometer is held by ceramic rods and supported to the vacuum flange using stainless steel rods.

The spectrometer can be divided into two sides: ion and the electron side. The length of ion side of the spectrometer is 46 mm. An additional mesh is added on the ion side to prevent electron feedback and is placed 4 mm from the ion MCP. Thus the total ion length of the spectrometer is 50 mm. The shorter ion side reduces the time of flight of ions to help collect more events in coincidence. The length of the electron side is 295 mm, the larger distance helps in providing higher resolution for the photoelectron distribution. The electric field in the

spectrometer is 8 Vcm^{-1}. Such small electric fields are not sufficient enough to detect electrons as the efficiency of the MCP decreases with the energy of the electrons. Hence the electrons and ions are accelerated in a length of 6 mm between the mesh and the MCP. The voltage difference between the mesh-front MCP acceleration potentials of -2127 V for the ions and $+111$ V for the electrons is used. The mesh has a 80% transmission efficiency.

Voltages to the spectrometer are supplied by 6 independent high voltage supplies with passive voltage adjusters (HVZ's) to distribute voltages to the detectors. The voltage configuration of the spectrometer is shown in Fig. 2.29.

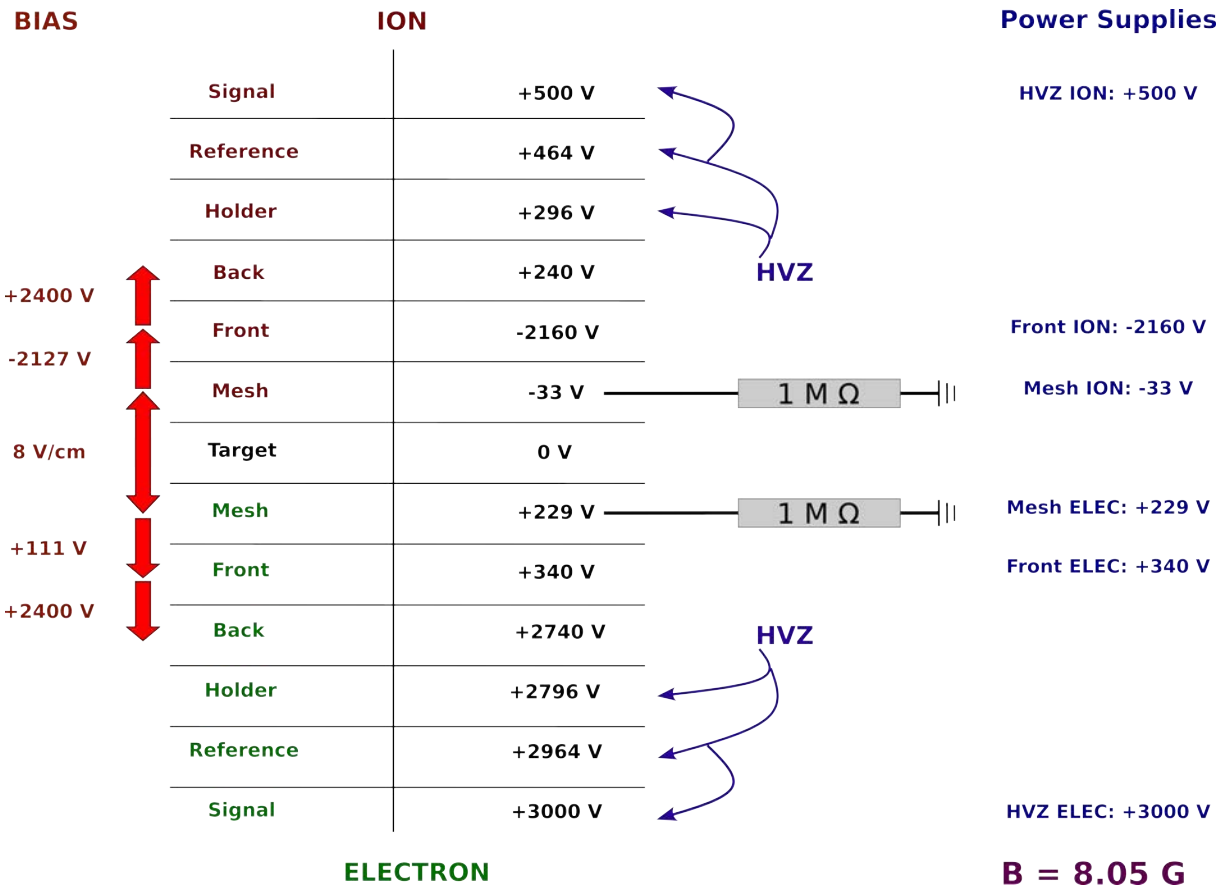

Figure 2.29 – *Voltage configuration of the spectrometer. Six high voltage supplies along with HVZ modules are used to distribute the voltages.*

Magnetic Fields

The electric field geometry of the spectrometer is insufficient to collect all electrons over a 4π solid angle. To circumvent this issue, a homogeneous magnetic field B is generated along the spectrometer axis, using Helmholtz coils, to confine the electrons in the spectrometer. The Helmholtz coils is 60 cm in radius with 60 cm spacing and 60 windings. Due to the presence of the magnetic field, the electrons follow a cycloid trajectory, performing a helical motion along the detector plane while their momentum component along the spectrometer axis, i.e. the TOF, remains unaffected. The radius of the helix (R_{helix}) and the angular frequency of the electrons

about the helix (ω_{helix}) is given as:

$$R_{helix} = \frac{p_r}{eB} \tag{2.22}$$

$$\omega_{helix} = \frac{eB}{m_e} \tag{2.23}$$

where p_r is the initial photoelectron radial momentum component in the (r, θ) plane, e is the electronic charge and m_e is the mass of the electron. Equn. 2.22 is valid for all charged particles in a constant magnetic field but the ions remains unaffected due to their high mass rendering the helical motion negligible. The radius of the photoelectrons from the center of the detector, r_{wiggle}, oscillates, or wiggles, expressed by the formula:

$$r_{wiggle} = 2R_{helix}|\sin(\omega_{helix}TOF/2)| \tag{2.24}$$

From equn. 2.24, all the electrons whose TOF is a multiple of $2/\omega_{helix}$ end up at the center of the detector, regardless of their initial momentum in this plane p_r. This completely erases the momentum resolution and thus must be avoided as much as possible. In practice, the magnetic field B has to be set such that the electrons ejected with zero momentum along the spectrometer axis reach the detector at the maximum r_{wiggle} and one has to make sure that the rest of the electrons, within a certain kinetic energy range, does not spread too much in TOF from this value. For this reason the chosen magnetic field strength is 8.05 G as the first node of the wiggle $r_{wiggle} = 0$ happens at 44.4 ns and the second at 88.8 ns which is in between the TOF of 63. ns for the electrons.

To compensate for the effect of the geomagnetic field, an additional Helmholtz coil is added along the laser (z) and jet (y) axis. The currents on the coil is adjusted to center the photoelectron distribution on the detector.

III. 3 Detector

In COLTRIMS, photo-fragments are detected in coincidence, such that both the measured electrons and ions originate from the same photoionization event. Pairs of microchannel plates are used to detect the charged particles guided by the spectrometer. The pair of MCPs is stacked in chevron configuration (see II. 3) to amplify the signal. They have a thickness of 1.5 mm each, pore size of 20 μm, 8° bias angle, with a diameter of 80 mm and 70% OAR. The MCPs have a spatial and temporal resolution of < 0.1 mm and < 100 ps and multi-hit dead time of ~ 20 ns. To make the detection single particle sensitive, the MCPs works in the saturated regime (see II. 3) with a bias voltage of +2400 V for both electrons and ion side. The amplified signal is then detected by a set of delay line anodes, placed ~ 7 mm away from the MCP back. To guide the electron cloud from the exit of MCP to the delay line anode, a potential difference of +260 V is applied.

Delay Line Anodes

Delay lines anodes are composed of multiple layers of conducting copper wires, with each layer made of a single wire and a resistance measured to be of 14Ω and 19Ω for electrons and

ion side respectively. The wire is wound around in such a away that with each turn of the wire is parallel to the previous one and with a spatial offset (see Figure 2.30 (a)), with a pitch of 1 mm. The amplified electron cloud, at the exit of the MCP, is driven to the delay line anode and is captured partially. The captured electrons produces a bell-shaped/Gaussian pulse which propagates along the wire in opposite directions. The two resulting pulses are detected electronically and are discriminated with respect to each other. For a given layer the arrival times of the two pulses, at the end of the wire, are denoted by t_1 and t_2. The position and time of origin of the pulses encode the spatial information of the photoelectron and hence can be determined using the following set of relations:

$$x_{hit} = (t_1 - t_2)/2 \tag{2.25}$$

$$t_{hit} = t_1 + t_2 \tag{2.26}$$

From Equn. 2.25 it is important to note that both x_{hit} and t_{hit} are independent of each other and depend on the time of arrival of the two pulses. The calibration factors are conveniently ignored. Each layer provides a one-dimensional spatial resolution perpendicularly to the winding, the spatial resolution parallel to the winding is not possible to resolve. It is important to note that the spatial resolution can look limited here by the grid spacing (1 mm) and the cloud of electrons ejected from the MCP shines across several winding of the wire. Thus the parallel spacing of the wire, in each layer, is much smaller than the size of the electron cloud falling on it, thus the electron could falls across multiple windings of the wire. Thus multiple pulses are generated and they smear out into a single pulse, during the signal propagation. The position is then reconstructed from the center of mass of the pulse. Thus the spatial resolution is proportional to the temporal resolution in the pulse discrimination, equivalent to ~ 100 μm.

As mentioned above, a single layer of delay line anode provides only a 1-D spatial information about the photoelectron angular distribution. To extract the 2-D photoelectron distribution another layer of delay line anode is used orthogonal to each other. The transmittance of the first layer is enough to produce a signal on the other delay line. The arrival times of the two pulses, at the end of the wire, are denoted by t_3 and t_4:

$$y_{hit} = (t_3 - t_4)/2 \tag{2.27}$$

$$t_{hit} = t_3 + t_4 \tag{2.28}$$

Thus providing the set of observable (x_{hit}, y_{hit}, t_{hit}). The difference between the signal arrival times at the adjacent ends of each delay line is proportional to the position on the MCP in the respective dimension.

Another set of delay line can be used too, called a hexanode. In this configuration the three layers are placed 120° with respect to each other in a hexagonal fashion. The signals from the third layer serve as a redundant source of information for cases when signals are lost due to electronic dead-time occurring from multiple hit events or imperfect electronic threshold. With

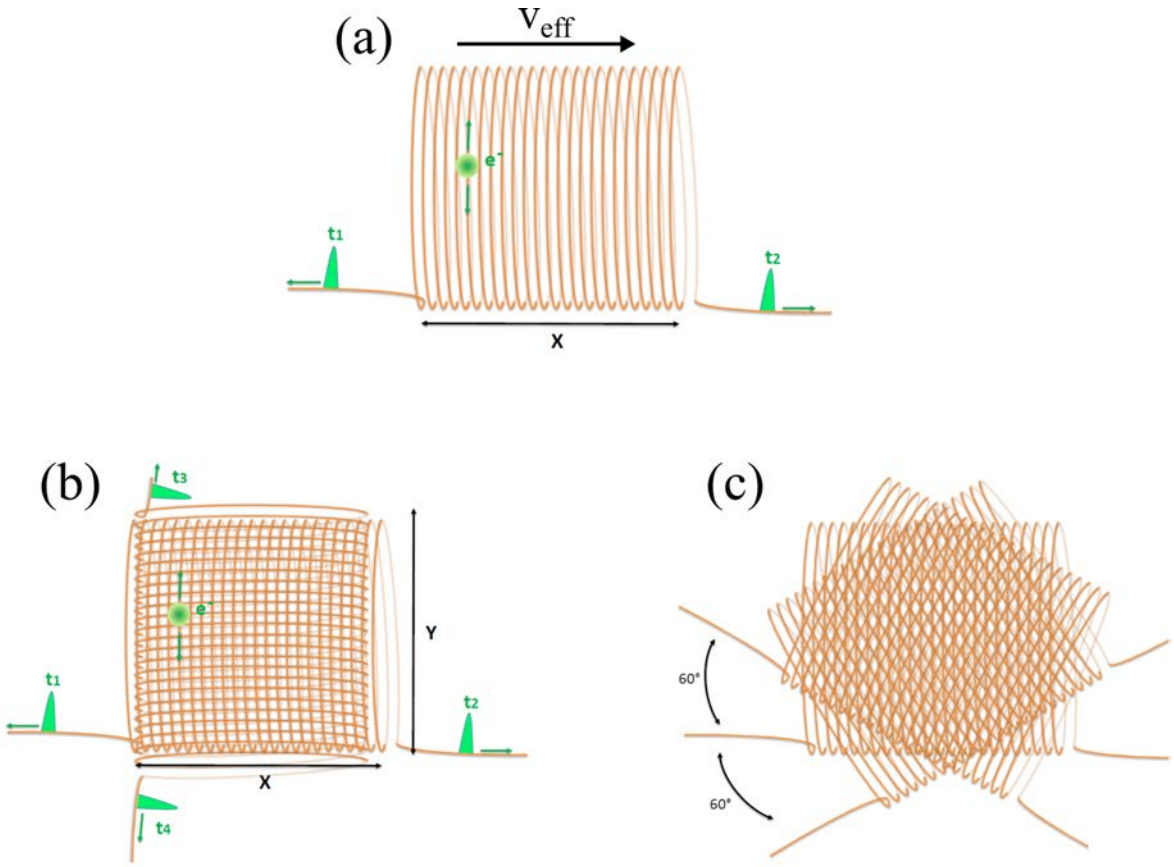

Figure 2.30 – *Schematics of the delay line detector. (a) Operating principle of a delay line. The electron cloud from the MCP generates a signal that propagates in opposite directions along the wire. The position and time-of-flight are calculated from the timings of these signals. (b) Typical delay line configuration, where* 2 *layers are used and are arranged orthogonal to each other. (c) Hexagonal delay line configuration.*

the additional layer it is possible to control the delay-lines' intrinsic resolution and linearity an thus improving the overall imaging performance.

In our case, the ion detector is made of two layers (DLD80, Roentdek GmbH) and the electron detector has the hexagonal configuration (HEX75, Roentdek GmbH). The wire in each layer of the delay line is doubled and has a spacing of 0.5 mm. The first wire (SIG for signal) has a bias voltage of $V_{SIG} = +260$ V with respect to the MCP back. The other wire serves as a reference (REF for reference) to the signal and has a bias voltage of $V_{REF} = V_{SIG} - 36$ V. Thus allowing them to be sensitive to the local electromagnetic noise while not measuring the signal. Thus the signal for the i^{th} layer of the delay line is measured as:

$$S_i = S_{i,SIG} - S_{i,REF} \tag{2.29}$$

Additional timing information is measured from the ion (t_i) and electron MCPs (t_e) along with the timing from the oscillator of the laser (t_L). Thus there are a total of $4+6+2+1 = 13$ timings are recorded.

Electronics

The signals are extracted from the DC line using high pass filters. These filters, as well

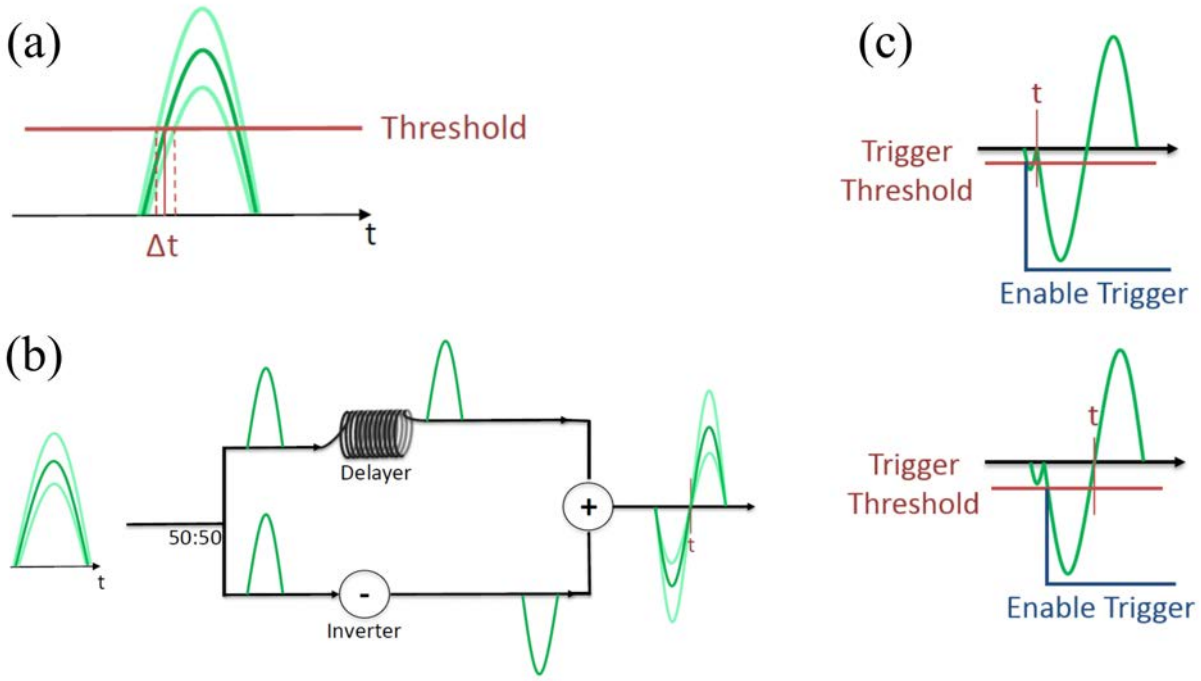

Figure 2.31 – *Schematics of the principle of timing measurement. (a) A threshold is set to measure the time of arrival of the pulse but is dependent to the signal amplitude. (b) Principle of operation of a constant fraction discriminator (CFD). The time of arrival of the pulse is determined when the signal changes sign i.e. the signal crosses* $0\,V$ *and thus the time information is not sensitive to the signal amplitude. (c) Setting of the threshold of the CFD. The threshold is set such that it is high enough to avoid the noise in the leading edge but low enough to not miss an real count*

as the SIG-REF subtractors are housed in two FT12-TP, Roentdek GmbH modules. The MCP signal is isolated using HFSD decouplers. The extracted signal is amplified from $0.2 - 2$ mV to $\sim$ 100's mV using fast amplifiers. The signals from the electron side is amplified using FAMP8 whereas two ATR19-2 and FAMP1+ is used for the ion signals. Each pulse in the signal corresponds to a single particle hit and can have different amplitudes due to the inhomogeneous gain of the detector along with delay line collection fluctuations. These amplitude fluctuations would introduce substantial errors in the timing (see Fig. 2.31). Thus to circumvent this issue a constant fraction discriminator (CFD) is used. CFD7x is used for the electron signal and MCP, FAMP1+ and CFD1c are used for the ions, Roentdek GmbH.

To find the time of arrival of the electronic pulse, the signal ($S(t)$) is split into two pulses with a ratio of R. One of the split pulses is delayed in time by an amount τ while the other pulse is inverted. The two pulse are then added. The resulting signal is $S_{CFD} = RS(t-\tau)-(1-R)S(t)$. Its profile is a function that goes from negative to positive value. The time at which the S_{CFD} crosses the zero defines the time of arrival of the pulse. This method is not sensitive to any modulations in the amplitude, as they will affect both the split signals equally. Typically $R = 0.5$ and $\tau = \text{FWHM}/2$ is used as it provides the maximum slope at the zero point crossing. As most electronic signals are plagued with random noise or pre-pulses, a threshold is set to prevent CFD from triggering from the noise in the early rising edge of the signal (see Fig 2.31 (c)). The output signal from the CFD is fed to the time-to-digital converter TDC8HP along with the

signal from laser oscillator. Although the TDC8HP has a temporal resolution of < 35 ps the overall temporal resolution is about 100 ps.

III. 4 Reconstruction Algorithm

The COLTRIMS is used to detect photo-induced fragments and reconstruct the momentum distribution of the electrons together with the mass spectrum and momentum distribution of the ions with a single-particle sensitivity. To retrieve the spatial and temporal information from the delay line anodes they have to be calibrated. To make sure that the delay lines works in the optimal condition and maximum events are recorded per hit, the gas jet is ionized using the XUV beam. A histogram is plotted for each of the delay line along with the number of counts detected on the delay line per hit on the electron MCP. The threshold of the CFD along with the gain of the MCP is adjusted such that the number of counts per time window is almost zero. Although one must make sure that the threshold is not too low such that CFD gets triggered by noise and also that it is not too high such that events with a small signal doesn't gets triggered.

Calibration

To extract the temporal and spatial information from each hit each wire of the delay line anode needs to be calibrated across the spatial resolved dimension. To extract the time-of-flight (TOF) of the charged particle firstly the temporal offset (Δt_l) between different layers of the delay line is found out such that the total time ($t_l + t'_l$) for the pulses to reach the ends of the wire is the same for all layers. Thus Δt_l accounts for the differences in the length of the wires in each layer. Additionally a temporal offset (Δt_0) is obtained from the reference signal, given by the master clock of the laser t_{laser}. Thus the position and TOF can be calculated as:

$$X_l = \frac{t_l + t'_l}{2v_l} - \Delta x_l \tag{2.30}$$

$$TOF_l = t_l + t'_l - \Delta t_l - \Delta t_0 - t_{laser} \tag{2.31}$$

where v_l is the velocity of the signal and Δx_l is proportional to the relative offset between the two ends of the wire in each layer l.

The mass spectrum of the ions can be extracted by the following equation:

$$\frac{m}{q} = \frac{E}{2L_{ion}} TOF_{ion}^2 \tag{2.32}$$

where E is the electric field of the spectrometer and L_{ion} is the length of the ion side and TOF_{ion} is the ion time of flight.

On the other hand, the reconstruction of the 3D photoelectron angular distribution is complicated by the presence of the magnetic field. As the magnetic field is along the TOF of the electrons, they are not affected by the magnetic field along the x axis or the axis of the spectrometer. Thus the photoelectron momentum (p_x^{elec}) along x can be reconstructed from the following equation:

$$p_x^{elec} = m_e v_x^{elec} = m_e \frac{L_e}{TOF^{elec}} - \frac{eE}{2} TOF^{elec} \tag{2.33}$$

where L_e is the electron acceleration length and TOF^{elec} is the time of flight of the electron. The electron detector global time offset Δt_0^{elec}, in Eq. 2.30, can be precisely adjusted here to get the zero kinetic energy electrons time-of-flight by centering the p_x^{elec} to zero.

The magnetic field B introduces a helical trajectories of the electrons in the detector plane. The helix is characterized by the angular frequency $\omega_{helix} = eB/m_e$ of the electrons and the radius $R_{helix} = p_r/eB = r/2|\sin(\omega_{helix}TOF/2)|$. A coordinate transform from the radial momentum p_r and emission angle ϕ can be made to Cartesian coordinates (y, z) detected r, θ and TOF, given as:

$$p_r = \frac{eBr}{2}|\sin(\omega_{helix}TOF/2)| \tag{2.34}$$

$$p_\phi = \theta - \frac{\omega_{helix}TOF}{2} \tag{2.35}$$

where,

$$p_x = p_r\cos(\phi) \tag{2.36}$$

$$p_y = p_r\sin(\phi) \tag{2.37}$$

To tune the magnetic field a plot of the electron position (r,x,y) as a function of the time-of-flight is made. To obtain the best spatial resolution the TOF of the zero kinetic energy electrons matches the maximum radius of the wiggle.

Coincidence Measurements

COLTRIMS is used to record photo-fragments in coincidence i.e. the electron and the ions fragments produced from the same photo-ionization event is recorded. Thus it becomes imperative that a single photo-ionization event happens per laser pulse. To do so the energy per pulse can be adjusted, by tuning the laser intensity and repetition rate, along with the gas jet density, by adjusting the backing pressure, temperature of the bubbler or with different skimmer configurations. The coincidence condition requires that the number of photo-ionization events per shot is about 1/10 to allow the slow ions to reach the detector and be detected. This condition reduces the number of counts i.e. for a laser operating at 250 kHz the maximum counts that can be measured with the coincidence condition in place is just $\sim$ 25 kHz. Although this reduces the number of multiple photo-ionization events per shot but it is not completely eliminated. To eliminate them further set of filters are used.

To assign the photo-ionization events in coincidence, the COLTRIMS works in a window mode. In this mode a time window is opened during which the photo-fragments are collected and any detected event in the time window is labeled as coming from the same ionization event. To open the time window a trigger event is required. There are two main triggers to be used as a trigger to open the time window for acquisition. Firstly, an acquisition window can be opened either by using the electron signal from the detector as a trigger (see Fig. 2.32 (a)). Secondly, an ion signal from the detector can also be used as a trigger to open the acquisition window (see Fig. 2.32 (b)). The advantage of using the ion signal as a trigger to open the acquisition window is that as the detection efficiency of ions is much less compared to that of electrons thus for a given ion detected it is less likely to not find a corresponding electron. The disadvantage of this

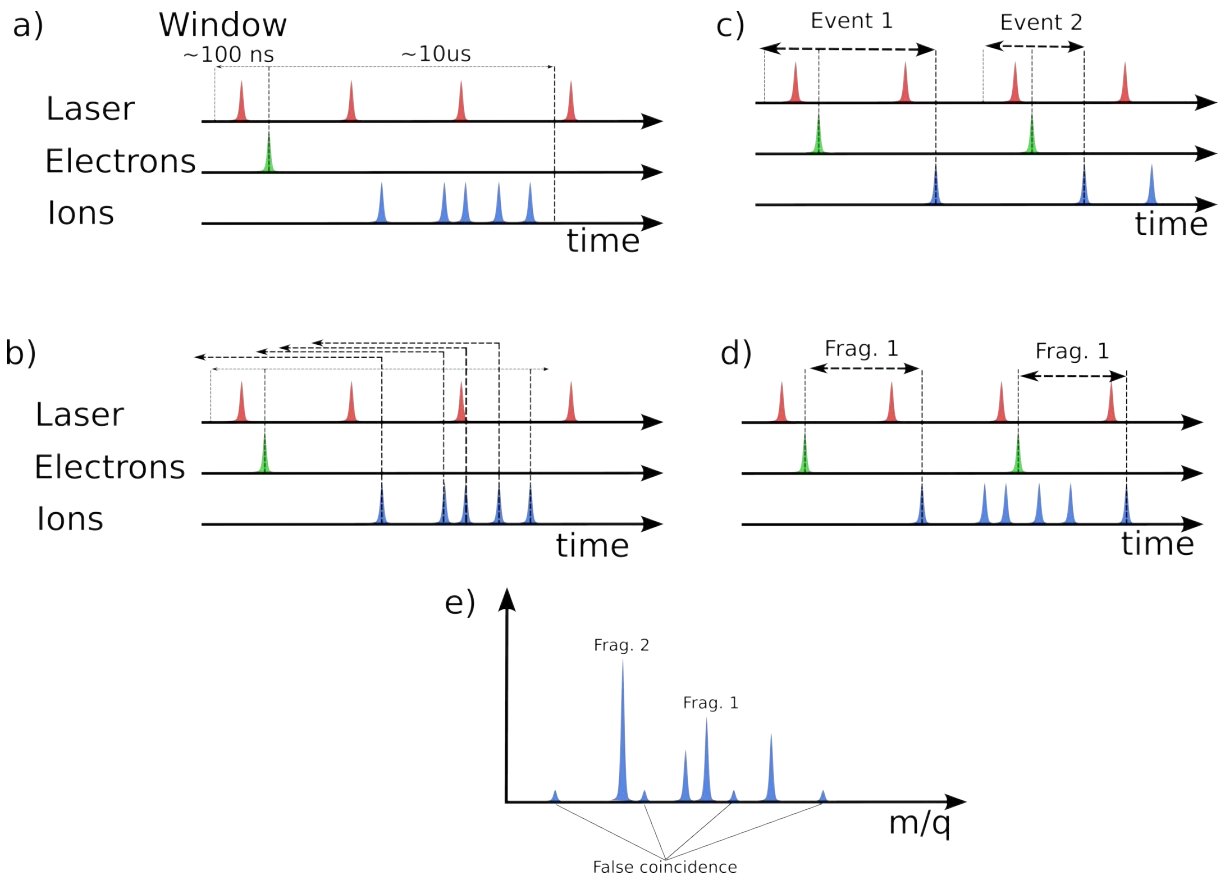

Figure 2.32 – *Schematics of the operation of window acquisition mode in COLTRIMS. (a) The window is triggered on the electrons. The acquisition window opens* $\sim$ 100 *ns before the electron is detected to get the laser pulse and is open for* $\sim$ 10 μs *to get the ions in coincidence i.e. from the same photo-ionization event. (b) The window is triggered on the ions, where the acquisition window is opened backwards in time to get the corresponding electron and laser pulse in coincidence. (c) Issue with triggering the acquisition window on the ion signal, where the electron from the previous window is counted. (d) Principle of continuous acquisition mode, wherein the coincidence events are determined in the post-analysis. (e) Appearance of false coincidence peaks, which appears as unreasonable masses in the mass spectrum.*

method of triggering the window on ion signal is that an electron could be wrongly assigned to the previous window (see Fig. 2.32 (c)). Thus leading to false coincidence events.

In our case, the signal from the electron detector is considered as the trigger to open the window. The window is opened 500 ns before and 10's of μs forward in time to collect the ions. To avoid background electrons from triggering the acquisition window the window is not triggered if there is no laser shot found just before the electron detected (see Fig. 2.32 (a)). This method of operation reduces the number of false coincidences recorded.

Although acquiring coincidence events through the window mode is robust, it suffers from a few limitations. Firstly one can only open one window at a time. Thus the counting rate is limited to $1/T_{win}$, where T_{win} is the temporal duration of the window. To collect all ion fragments generated from the photo-ionization event the T_{win} must be at least be equal to the TOF of the heaviest ions. As chiral molecules are large and the parent ion has the highest mass of 100's amu thus it becomes imperative to have long T_{win} of around $\sim$ 12 μs to collect the

parent ions in coincidence. This severely reduces the number of events that can be recorded in coincidence. Secondly, since the Blast beat laser system has a minimum of 166 kHz repetition rate which accounts to a temporal separation of two consequetive pulse of 6 μs. This is less than the typical ion TOF (see Fig. 2.32 (c)). This not only leads to loss of events as ionization events from the immediate second laser pulse has to neglected but also the ionization events from this second laser pulse gets mixed with the first photo-ionization event. Thus although the laser repetition rates can go up to 2 MHz the COLTRIMS acquisition rate in coincidence is limited to about $\sim$ 20 kHz.

To reconstruct more coincidence events, one can operate the COLTRIMS in a continuous acquisition mode. In that case, all the photo-ionization events are recorded and the coincidence assignment is performed afterwards (see Fig. 2.32 (e)). A time dependent electric field can be applied in the ion side of the spectrometer to deflect the ions. The detected ion position then depends on the time at which the ionization was performed. Combined with the time-of-flight, one can retrieve the original laser shot without the electron information. Thus the electrons and ions can be tagged in coincidence unambiguously.

We use a software named COBOLD to perform data acquisition from the COLTRIMS. The software can reconstruct coincidence events at a rate of $>$ 100 kHz, and it works in the window mode where the acquisition window is triggered using the electron signal. It could be modified to perform acquisition in continuous mode also. This would result in a significant increase the number of coincidence events by a factor of $\sim$ 5. This would definitely increase the statistics of the photoelectron angular distributions acquired as PECD is a weak signal of about few %.

III. 5 Modifications

The number of ions detected in coincidence with the electrons is far less compared to the number of electrons observed within the coincidence condition. This is due to the reduced efficiency in the detection of ions ($<$ 5% at 0.5 keV) compared to that of electrons ($\sim$ 60% at 0.5 keV). To increase the efficiency of the detection of ions, higher acceleration voltages can be applied on the ion side as the detection efficiency increases to about $\sim$ 60% for ions energies of about 2 keV. But increasing the voltages leads to electrical discharges. To increase the number of ions detected one can also increase the effective area of the detector. To do so funnel MCP's, where the channels in the MCP has a shape of funnel compared to that of a cylinder in a conventional MCP, are used. This leads to an increase in the effective detector area from 60% to 90%. The voltage difference between the electron MCP front and back is increased. The Voltages are still supplied by 6 independent high voltage supplies with passive voltage adjusters (HVZ's) to distribute voltage to the detector. With the use of funnel type MCP an addition HVZ is used to supply voltage to the shim between the MCP front and back, on the ion side. The distribution of voltages are shown in Fig. 2.33.

The above discussed configuration of the COLTRIMS is very suitable for multi-photon ionization of chiral molecules using fundamental and the second harmonic of the laser. But it is not suitable to couple XUV to the COLTRIMS. The use of 200 μm skimmer creates a significant thermal part in the jet, i.e. a part of the shock wave still exists after the skimmer.

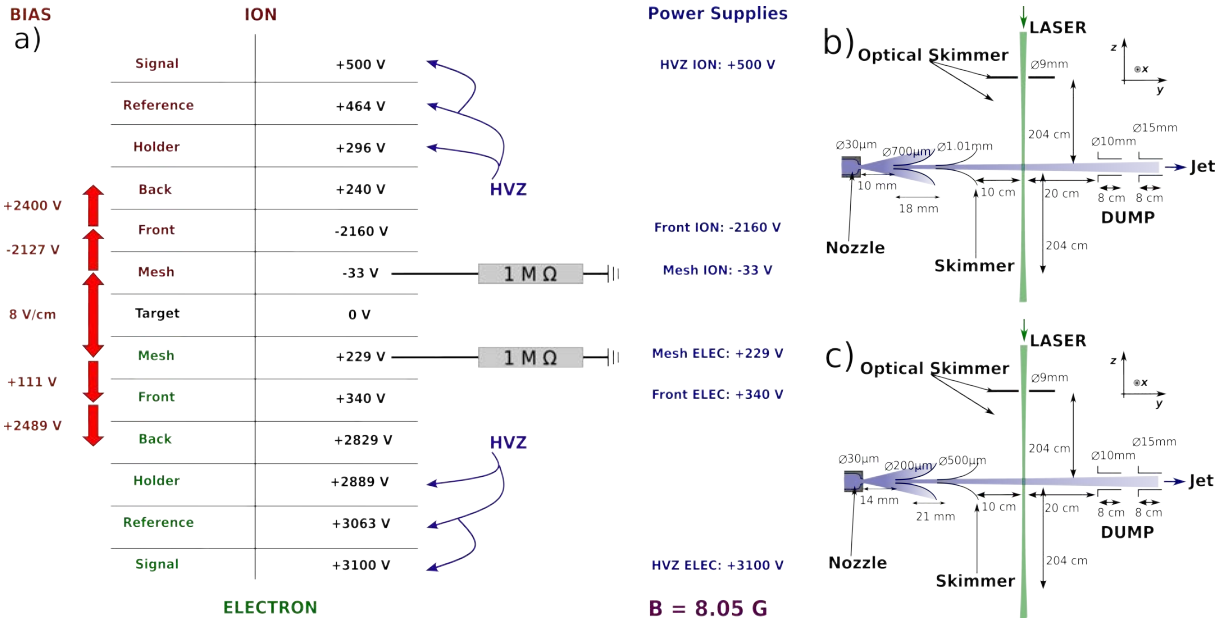

Figure 2.33 – *(a) Voltage configuration of the spectrometer. Six high voltage supplies along with HVZ modules are used to distribute the voltages. (b) & (c) Schematic of the modified jet and optical elements to provide efficient coupling of the XUV and reduce the thermal part of the supersonic jet. See text for details.*

This thermal part of the jet gets spread over in the COLTRIMS and thus the base pressure in the spectrometer is considerably higher. Thus on coupling the XUV beam with the COLTRIMS all these background gas is ionized before the XUV hits the molecular gas jet. This reduces the percentage of ionization events from the molecular gas jet thus resulting a loss in the coincidence events and improper reconstruction of the photoelectron angular distribution. The corresponding broadening in the mass spectra (m/q) and photoelectron momentum (p_x) is given as:

$$\Delta(m/q) = \frac{E}{2L_i} TOF_i^2 \Delta L_i \tag{2.38}$$

$$\Delta p_x = \frac{m_e}{TOF_e} \Delta L_e \tag{2.39}$$

where E is the electric field applied in the spectrometer L_i & L_e is the ion and electron length of the spectrometer and $\Delta L_i = \Delta L_e$ is the total increase in the ionization length.

To reduce the thermal part of the molecular jet there are two approaches. Firstly one can add an additional skimmer to select the supersonic part of the jet more efficiently. Secondly, the distance between the nozzle and the first skimmer can be increased so that only the center of the Mach disk (see Fig. 2.26) is skimmed more efficiently and the shock wave is eliminated. We tried two configuration of the double skimmer arrangement. Initially, a 700 μm skimmer was placed before a 1.01 mm skimmer (see Fig. 2.33 (b)). And the distance between the nozzle and the first skimmer (700 μm skimmer) is increased from 9 mm to 10 mm while the distance between the first and the second skimmer is kept at 18 mm. This indeed reduces the thermal part in the molecular jet compared to that of a single skimmer of 200 μm. But the size of the molecular beam is significantly larger (see Fig. 2.34 (b)). This increased size of the molecular

beam still leads to a broadening in the the mass spectra and photoelectron momentum.

Thus one still needs to reduce the size of the molecular beam without compromising on the thermal part of the jet. To do so the distance between the skimmer and the nozzle is increased to 14 mm. The 700 μm and 1.01 mm skimmer are replaced by a 200 μm and 500 μm skimmers respectively (see Fig. 2.33). This further decreases the thermal part of the molecular jet while significantly reducing the size of the molecular beam compared to the previous two skimmer configurations employed (see Fig. 2.34). This reduction in the thermal part of the molecular jet at the interaction region reduces the number of ionization events coming from it. And about $70 - 80\%$ of the total photoelectrons recorded comes directly from the molecular beam. Thus resulting in an efficient reconstruction of the photoelectron and mass spectrum.

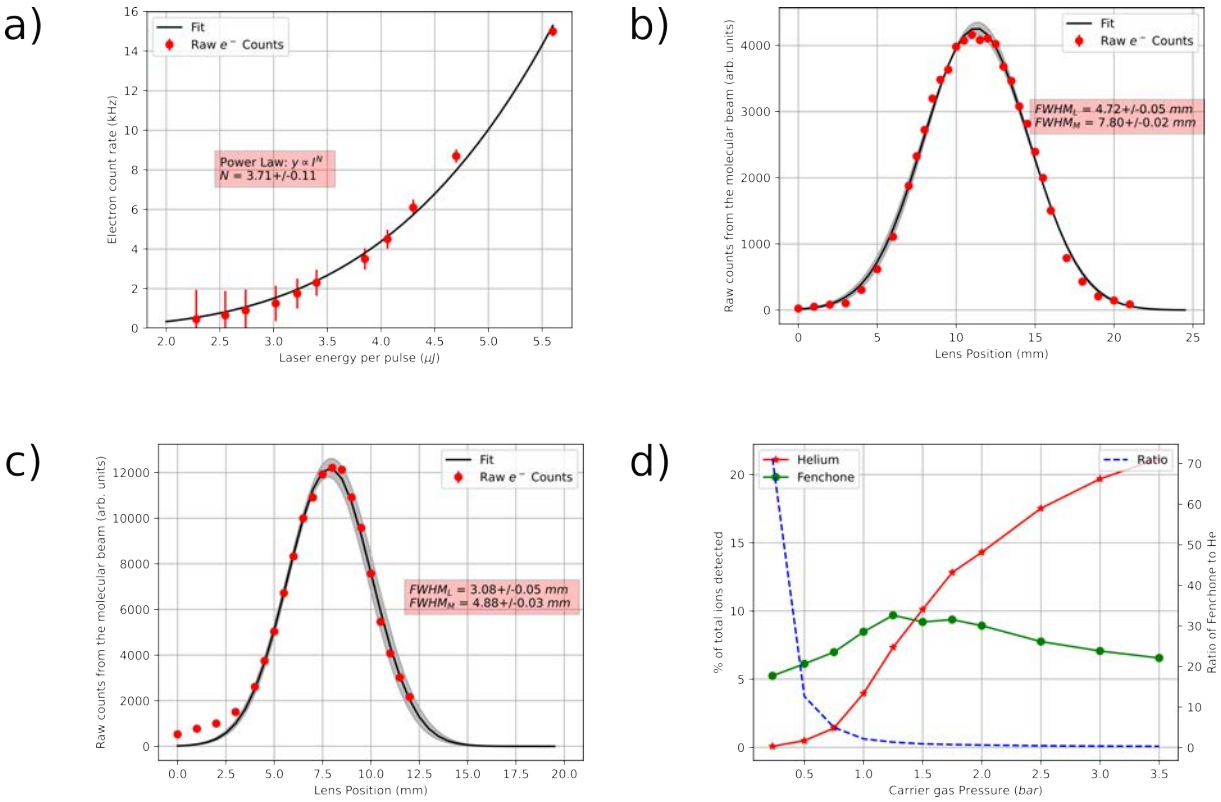

Figure 2.34 – *Determination of the size of molecular beam. (b) Electron counts per minute as a function of lens position for the molecular jet generated using the configuration shown in 2.33 (b). A Gaussian fit is made to the convolution of the molecular beam and the laser beam. $FWHM_M$ is the full width at half maxima of the Gaussian fit to the convolution and $FWHM_L$ is extracted from the Equn. 15. (c) Electron counts per minute as a function of lens position for the molecular jet generated using the configuration shown in 2.33 (c). (d) Percentage of ions detected in coincidence for (+) α-Pinene (shown in green) and for He (shown in red). The fraction of (+) α-Pinene ions to that of the He ions detected in coincidence (shown in blue).*

To extract the size of molecular beam we use the experimental setup described in III. 1. The focused second harmonic beam is used to ionize Acetone which is pushed into the COLTRIMS using Helium as the carrier gas. Acetone (IP = 9.7 eV) undergoes multiphoton ionization and follows a power law dictated by $I^{3.71}$ (see Fig 2.34 (a)) which is similar to (+) Methyl Lactate (IP $\sim$ 9 eV) of $I^{3.66}$. The molecular beam size is determined as discussed in sec. III. 1. For the configuration of skimmers of 700 μm and 1.01 mm the experimentally observed FWHM of the

convoluted Gaussian is 7.80±0.05 mm (see Fig 2.34 (b)). The molecular beam width is calculated using Equn. 15 to be 4.72 ± 0.02 mm. Whereas for the configuration of skimmers of 200 μm and 500 μm the experimentally observed FWHM of the convoluted Gaussian is 4.88 ± 0.05 mm (see Fig 2.34 (c)). The molecular beam width is calculated using Equn. 15 to be 3.08 ± 0.03 mm. To extract the percentage of chiral molecules present in the molecular beam (+) α-Pinene is used with the bubbler heat to 70°C, the external tube heated to 80°C and the nozzle heated up to 110°C and is pushed into the COLTRIMS with Helium as the carrier gas. The percentage of detected ions from the ionization of (+) α-Pinene and Helium is obtained as a function of the absolute carrier gas pressure of Helium (see Fig. 2.34 (d)). The % of total ions detected with respect to the number of ions detected from (+) α-Pinene increases with an increase of the carrier gas pressure and then saturates at around 1.75 bar. Then it starts to decreases with a further increase in the pressure of carrier gas as the number of He atoms increases and is ionized more compared to the chiral molecule while the number of chiral molecules doesn't increase considerably with an increase in the carrier gas pressure. A maximum of $\sim$ 10% of the total ions detected are from (+) α-Pinene with an absolute carrier gas pressure of 1.5 bar. With an increase in the carrier gas pressure the photo-fragments of (+) α-Pinene are more finely resolved in the $p_y - p_z$ plane but the percentage of (+) α-Pinene decreases in the molecular beam. As a result a compromise if found at 2.5 bars of carrier gas pressure.

IV Conclusion

The experiments presented in the following of this thesis all rely on two key elements: well-controlled light sources and optimized photoelectron imaging.

The light sources are based on the Blast Beat laser system, which provides laser pulses with a high repetition rate and high stability. Together with the capability to perform frequency up-conversion, it acts as a versatile laser source. The problems of generation of elliptically polarized XUV light have been mitigated using the XUV quarter waveplate. Even if this Yb-doped fiber laser provides a unprecedented signal acquisition rate, its main drawback is its pulse duration of 135 fs, which is longer than the widely used Ti:Sa lasers of about $\sim$ 20 fs. This leads to the saturation of ionization the strong field regime and hence the effective intensities in the strong field ionization of molecules cannot be increased higher than typically $\sim 3 \times 10^{13}$ W/cm^2. A post-compression setup is available to reach pulse width down to 20 fs, but it operates at 515 nm which is not optimal to achieve strong field ionization regime due to the influence of multi-photon resonances. The global stability of the beamline is quite good and very long acquisition over several weeks (24/24) have been performed, especially with the XUV in COLTRIMS. The ability to measure and control the polarization state of the laser for both the fundamental, second harmonic and the XUV is unprecedented.

In parallel to the development of these light sources, an important work has been performed regarding the photoelectron imaging. The VMI spectrometer has been optimized and its kinetic energy range has been increased significantly to perform strong field experiments. The COLTRIMS has also been optimized for XUV photoionization and to improve the detection efficiency. As a result, we have two complementary detectors which can be used in different types

of experiments. The VMI will be used for fast acquisitions in which the polarization state of the light is continuously modulated while the photoelectrons images are filmed on the fly. This lock-in type detection enables recording high quality 3D photoelectron angular distributions in a few minutes, and is very useful in the strong field regime, where a single molecular orbital is ionized. By contrast, the XUV ionization regime requires a multidimensional acquisition, in which the COLTRIMS acquires 3D photoelectron angular distributions in coincidence with the corresponding mass spectra. The acquisition times then reach several days, but provide information that could up to now only be accessed using synchrotrons, with the additional possibilities offered by the ultrashort nature of the source and its natural synchronization with laser pulses.

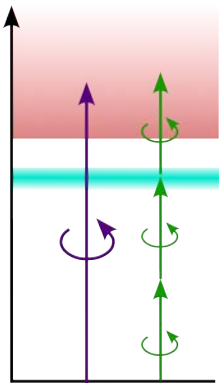

Chapter 3

Multiphoton Regime

In the previous chapter we have described our state of the art ultrashort high power high repetition rate photon sources and the methods required to characterize them. We have also described the two main detectors, namely velocity map imaging spectrometer (VMI) and COLTRIMS, to detect photoelectrons. In this chapter, we will be using them to study ultrafast chiral light-matter interactions.

The chapter is organized as follows: In section 1 we give a brief motivation of our work. Section 2 introduces photoelectron circular dichroism (PECD) and a brief state of the art of PECD in both single and multiphoton regime. Section 3 shows our work on multidimensional chiral response using wavelength and ellipticity dependence of dichroism. Our experimental setup, data analysis procedures and our results on photoelectron elliptical dichroism (PEELD) of Methyl Lactate are discussed in section 4. In section section 5 we discuss our results on coincidence measurements of PECD. Finally, in section 6 we provide our conclusion and future perspectives.

I Introduction

Distinguishing the two enantiomers of a chiral molecules has been the subject of many investigations for decades. A broad variety of experimental techniques have been developed, from chiral chromatography to X-ray diffraction or Nuclear Magnetic Resonance. The tool of choice for physicists is light-matter interaction, which gives rise to chiroptical processes. Indeed, chiral molecules can interact differently with right and left handed circularly polarized light. For instance, circularly polarized light of opposite helicities travel with different velocities through an optically active medium, giving rise to circular birefringence and optical activity. Also circularly polarized light of opposite helicities can be absorbed differently while propagating through a chiral medium, leading to absorption Circular Dichroism (CD). Typically these chiroptical processes arise from magnetic dipole and electric quadrupole interactions with the electromagnetic wave and hence are weak interactions, typically in the order of 10^{-4} . In this chapter we will use a different chiroptical phenomenon, in which circularly polarized light is energetic enough to ionize the chiral molecules. The detection of the ejection direction of the emitted

electrons enables observing a very strong dichroic effect, from pure electric dipole interaction: PhotoElectron Circular Dichroism (PECD).

II PhotoElectron Circular Dichroism

It was first predicted in 1976 [Ritchie 76], accurately simulated in 2000 [Powis 00] and first experimentally observed in 2001 [Böwering 01] that when a distribution of randomly oriented chiral molecule is ionized using a circularly polarized electromagnetic wave the photoelectrons are asymmetrically emitted in the direction relative to the propagation axis of the electromagnetic wave. This is called PhotoElectron Circular Dichroism (PECD). Unlike other chiroptical effects PECD is an electric dipole effect and hence the dichroism observed is stronger and in the range of several %s.

II. 1 Single photon Ionization

PECD has been initially studied in the single photoionization regime using synchrotron radiation. It was observed that PECD is sensitive to the whole dynamics of the single photoionization process: PECD is strongly dependent on the ionized orbital, molecular structure, kinetic energy, vibrational excitation and molecular orientation.

Influence of Initial Orbital

The initial orbital, from which the electron is ejected into the continuum, plays a pivotal role in the asymmetric emission of electrons [Nahon 06] [Turchini 13]. For instance, it was experimentally observed [Nahon 06] that photoelectrons emitted from HOMO and HOMO-1 orbitals of Camphor showed opposite signs in PECD. These two orbitals have different shapes, but also different locations in the molecule, as can be seen in Fig. 3.1. The photoelectron angular distribution is shown in Fig. 3.1 (1) and the measured dichroism in Fig. 3.1 (1) of Camphor when ionized with $\hbar\omega = 10.3$ eV photons. The angularly integrated PES and PECD is shown in Fig. 3.1 (2) where the spectrum can be cut into four regions, assigned to different orbitals ionized. Regions I and II correspond to ionization form HOMO and HOMO-1. It clearly appears that the PECD changes sign between these regions (see Fig. 3.1 (2)). The influence of the orbital shape was investigated in another experiment, where a significant amount of PECD was observed upon single-photon ionization from a spherically symmetric inner orbital [Hergenhahn 04]. This indicates that PECD is sensitive to the localization of the electronic density of the molecular orbital rather than to the chirality of the orbital, because it is a non-local effect accumulated during the electron scattering in the molecular potential before ejection into the continuum.

Influence of Molecular Structure

The non-local character of PECD was confirmed by measurement demonstrating its sensitivity to the whole structure of the chiral molecular potential [Nahon 16]. (-) Camphor and (-) Fenchone are isomers of each other and have very similar structures, the only difference between them being the substitution of two methyl groups which are not bonded to asymmetric carbons (see Fig. 3.2 (a)). Upon single photoionization being performed from the HOMO, which is not located at the substituted methyl groups, it was experimentally observed that they showed a

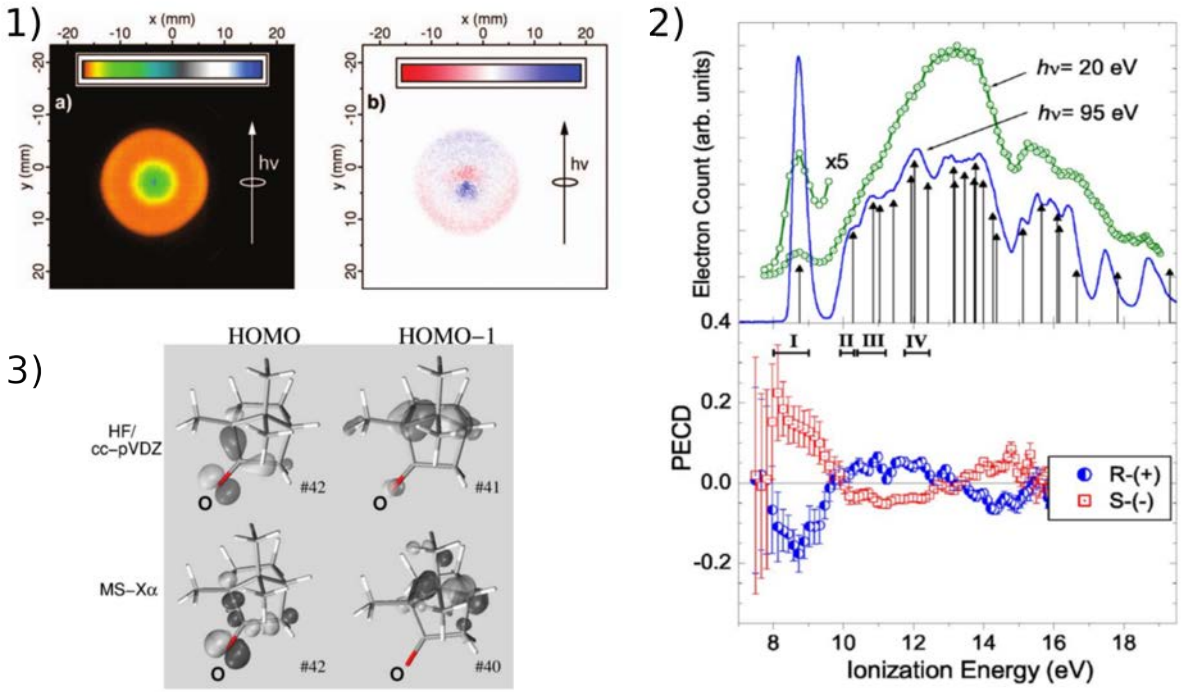

Figure 3.1 – *(1) (a) Raw photoelectron angular distribution (PAD) produced in one-photon ionization of Camphor at $\hbar\omega = 10.3$ eV. (b) Corresponding subtraction between the signals obtained with left circular polarization and right circular polarization, in the (+) enantiomer. The PECD clearly appears as a forward/backward asymmetry along the laser propagation axis. (2) Angularly-integrated photoelectron spectrum (PES) and PECD as a function of the photoelectron kinetic energy in Camphor. (Top) PES obtained at $\hbar\omega = 95$ eV (blue line), compared to a reference at 20 eV (green line). (Bottom) Corresponding PECD measured for the two enantiomers. (3)Electron density of the HOMO and HOMO-1 obtained using two types of calculation. Extracted from [Nahon 06].*

similar photoelectron spectra (PES) as it can be seen in Fig. 3.2 (b). While their PECD showed opposite signs as it can be seen in Fig. 3.2 (c). Thus showing PECD is extremely sensitive to the whole chiral molecular structure itself.

Further studies have been performed to investigate the effects of substitution and orbital dependency on PECD [Stener 04]. In [Garcia 14] (-)-Methyloxirane and (+)-Trifluoromethyloxirane, where the terminal hydrogen atoms were substituted by Fluorine atoms, were compared. Although the electronic density of the HOMO is completely away from substituted Florine atoms the PECD is drastically different in both. Furthermore, effects of conformational geometry were studied [Turchini 09] (as illustrated in Fig. 3.3). It was shown [Turchini 13] that the PECD for the two conformers of 3-Methylcyclopentanone, whose calculated structure is shown in Fig. 3.3 (left), showed opposite sign as shown in Fig. 3.3 (right).

Influence of the Kinetic Energy

It was shown in [Powis 08] that electrons emitted from the same orbital and differing in energies of about few eV can show opposite signs in PECD. Also as the energy of the photelectron, emitted from the same orbital, increases, the PECD starts decreasing and vanishes at high kinetic energies. This can be understood as higher kinetic energy electrons spend less time in the chiral molecular potential and thus is less scattered by it, showing lower or no PECD. Note that the

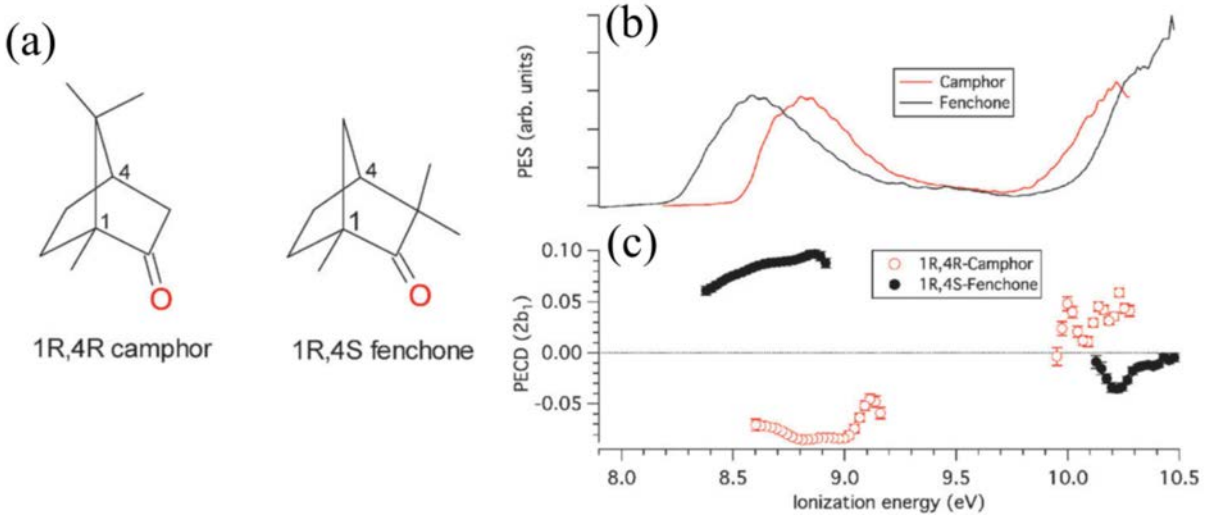

Figure 3.2 – *(a) Structure of (+)-Camphor and (-)-Fenchone, two similarly-structured isomers with the same asymmetric carbon configuration (labeled 1 and 4 here). (b) PES of Camphor and Fenchone, recorded respectively at* $\sim \omega = 10.3$ *eV and* 10.5 *eV. (c) Corresponding measurement of the PECD of (+)-Camphor and (-)-Fenchone [Nahon 16].*

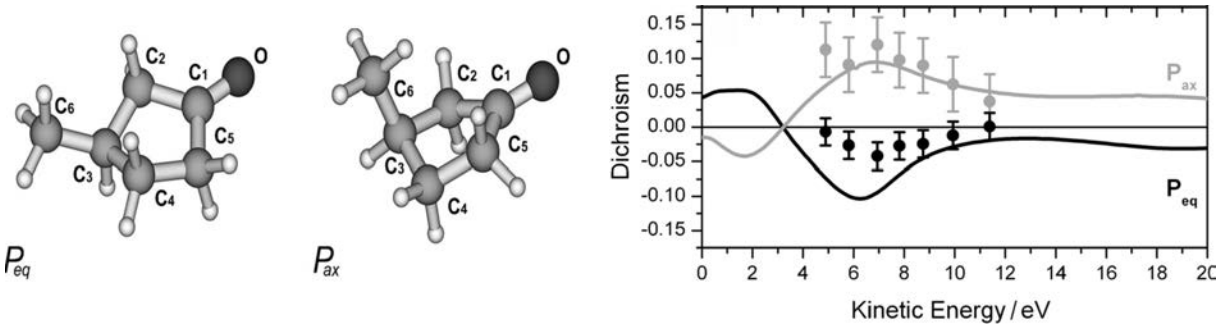

Figure 3.3 – *The calculated structure of the two conformers* P_{eq} *and* P_{ax} *of (+)-3- Methylcyclopentanone is shown on the left. The measured experimental dichroism* D_{eq} *(black dots) and* D_{ax} *(grey dots) for the HOMO state, together with the theoretical dispersions for* P_{eq} *and* P_{ax} *(black and grey solid curves), are respectively shown on the right. Extracted from [Turchini 13]*

presence of autoionizing states in the continuum can also play a role and lead to locally strong PECD at high electron kinetic energy [Hartmann 19] [Ganjitabar 20].

Influence of Vibrational Excitation

According to the Born-Oppenheimer approximation [Born 27] the molecular wavefunctions can be disentangled into its corresponding nuclear and electronic part in molecules. This is a result of the fact that the nuclei is much heavier than the electrons and hence the timescale of electronic motion is much faster than that of the nucleus, hence the nucleus is frozen in time. Furthermore, from Franck-Condon approximation the electronic transition matrix elements are assumed to vary negligibly with the nuclear motion [Franck 26] [Condon 26]. Thus, effectively the nuclear and electronic motion are decoupled in a molecule. If this was the case, then PECD which arises from electronic transitions should be insensitive to the vibrational excitation of the neutral molecule or ion.

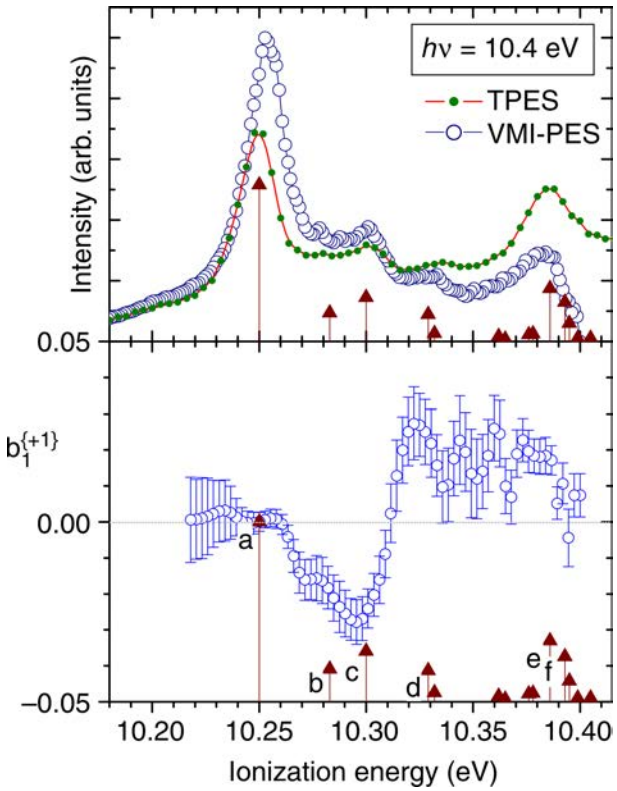

Figure 3.4 – *On the top PES associated with the HOMO of (-)-Methyloxirane measured at* $\sim \hbar\omega =$ 10.4 *eV where the red arrows correspond to the calculated vibrational spectrum. The corresponding PECD is shown in the bottom [Garcia 13].*

It was experimentally observed [Garcia 13] that PECD is in fact sensitive to the vibrational excitation [Powis 14]. Where the PECD associated with the ionization from two consecutive vibrational states of HOMO of (-)-Methyloxirane at $\hbar\omega = 10.4$ eV shows an opposite sign, as shown in Fig. 3.4. This was also observed for terpenes [Ganjitabar 18a] [Ganjitabar 20].

Influence of Molecular Orientations

In general PECD experiments are performed in a distribution of randomly oriented chiral molecules as produced in a molecular beam. However, PECD is expected to depend on the molecular orientation.In fact, even achiral molecules produce anisotropic angular distributions when oriented, leading to the CDAD (Circular Dichroism in Angular Distributions) effect[Dowek 07]. This two effects can thus be combined in oriented chiral molecules [Tia 17].

II. 2 Multiphoton Ionization

Single photoionization, using XUV radiation, provides a wealth of information on the electronic dynamics involved in PECD. Most single-photon PECD experiments have been carried out using synchrotron radiation, because of the lack of table-top sources of circularly polarized XUV radiation. We have seen in the previous chapter that high-order harmonic generation can solve this issue, enabling table-top single photon PECD experiments [Ferré 15b]. Another possible path consists in using femtosecond laser pulses to perform multiphoton ionization PECD [Lux 12] [Lehmann 13].

Perturbative Regime of Multiphoton Ionization

The quantum mechanical treatment of the single and multiphoton ionization event is treated in the perturbative regime, i.e. the incident electromagnetic field perturbs the molecular potential. In this regime the interaction Hamiltonian can be expressed as:

$$\hat{\mathcal{H}}(t) = \hat{\mathcal{H}}_0 + \hat{\mathcal{V}}(t) \tag{3.1}$$

where $\hat{\mathcal{H}}_0$ is the field free Hamiltonian of the molecular system and $\hat{\mathcal{V}}(t)$ is the perturbation or in this case the incident electromagnetic field. For Hydrogen like atoms the eigenstates and eigenvalues of $\mathcal{H}_0$ are known. In general the laser wavelength is several orders of magnitude larger than the size of the atom or molecule under study and hence one can apply the electric dipole approximation and hence the perturbative part of the Hamiltonian can be expressed as:

$$\hat{\mathcal{V}}(t) = \hat{\mathcal{V}}_0 \cos(\omega t) \tag{3.2}$$

where $\mathcal{V}_0$ is interaction field amplitude and ω is the frequency. With the assumption that $\hat{\mathcal{V}}_0 \ll \mathcal{H}_0$ and applying time-dependent perturbation theory the transition amplitude from an initial state $|\psi_i\rangle$, with energy eigen value of E_i, to a final state $|\psi_f\rangle$, with energy eigen value of E_f, can be calculated as different order of the perturbations to the $\hat{\mathcal{H}}_0$. The first order perturbation is expressed as:

$$\Gamma^{(1)}_{i\to f} \propto |\, \langle\psi_f|\hat{\mathcal{V}}_0|\psi_i\rangle \,|^2 \delta(E_f - E_i - \hbar\omega) \tag{3.3}$$

This transition amplitude describes the probability of an electron in the ground sate ($|\psi_i\rangle$) of a molecule/atom to absorb a photon of energy $\hbar\omega$ and reach the final state $|\psi_f\rangle$. To describe a single photon ionization from an initial state $|\psi_i\rangle$ the final state is replaced with the continuum. For events where the perturbative field is stronger i.e. at higher intensities of the laser electromagnetic field (but still in the regime $\mathcal{V}_0 \ll \mathcal{H}_0$) multiple photons can be absorbed by the electron in the ground state and reach a final state $|\psi_f\rangle$. In this case, higher order perturbations have to be taken into account and thus a generalized transition amplitude for an event where the electron absorbs N photons to reach the final state $|\psi_f\rangle$ from the state $|\psi_i\rangle$ is given by the N^{th} order perturbation and can be expressed as:

$$\begin{aligned}\Gamma^{(N)}_{i\to f} \propto & |\, \langle\psi_f|\, \hat{\mathcal{V}}_0\, |\psi_{k_1}\rangle\, \langle\psi_{k_1}|\, \hat{\mathcal{V}}_0\, |\psi_{k_2}\rangle \ldots \langle\psi_{k_{N-1}}|\, \hat{\mathcal{V}}_0\, |\psi_i\rangle \,|^2 \\ & \times \delta(E_f - E_{k_1} - \hbar\omega)\delta(E_{k_1} - E_{k_2} - \hbar\omega)\ldots\delta(E_{k_{N-1}} - E_i - \hbar\omega)\end{aligned} \tag{3.4}$$

where $k_1, k_2 \ldots k_{N-2}, k_{N-1} \ldots$ are all the possible intermediate (real or virtual) states. From the expression of the transition amplitude describing a N photon process it is evident that the field couples states separated by $\hbar\omega$ with each other and hence the electron density can jumps several times in a multiphoton processes passing though intermediate states. Thus making multiphotoionization much more sensitive and angularly structured compared to single photionization as multiple intermediate states are involved in the ionization process. Together with the fact that $\hat{\mathcal{V}}_0$ scales linearly with the electric field, a N-photon process efficiency scales as $\Gamma^{(N)} \propto E_0^{2N} \propto I^N$ with E_0 the electric field amplitude and I the laser intensity.

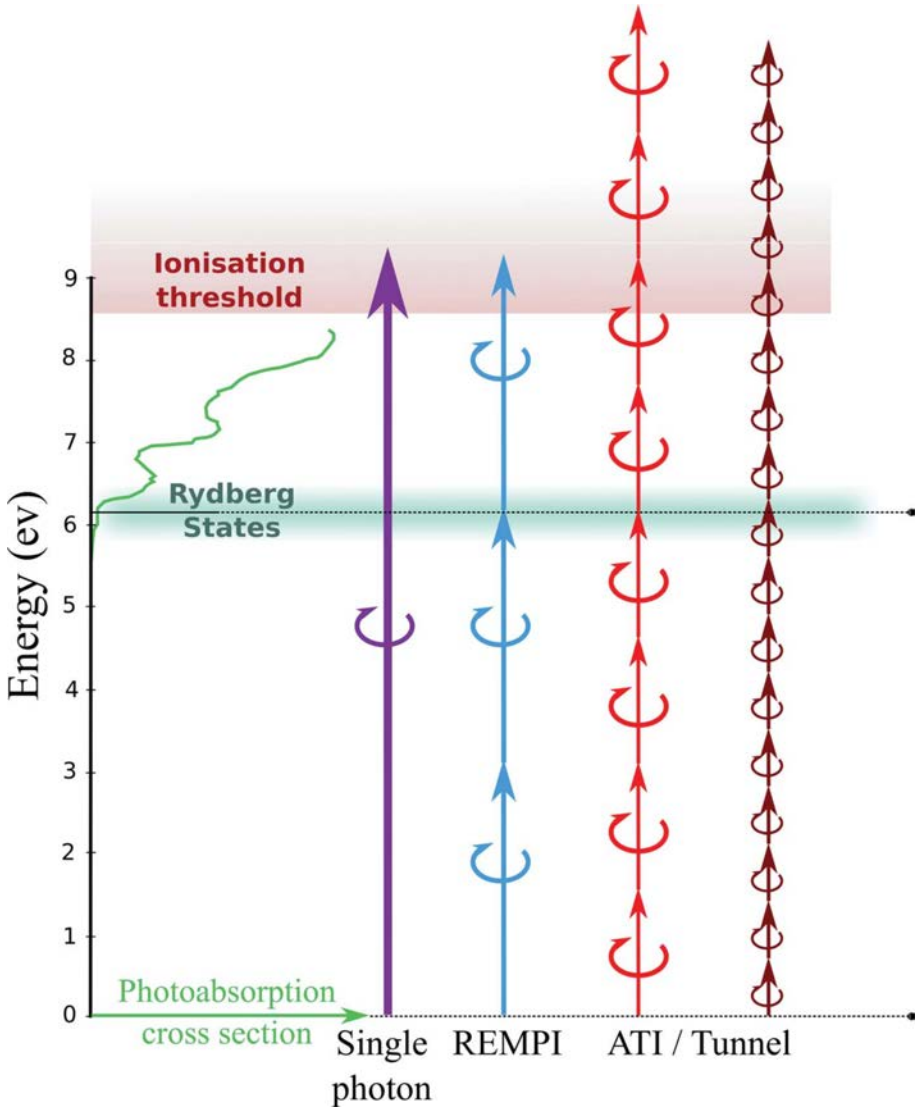

Figure 3.5 – *Illustration of the different ionization regimes at which the PECD arises. In particular in the resonance-enhanced multiphoton ionization (REMPI), the intermediate excited states can play an important role, in this chapter mainly through the anisotropy of excitation that they induce. The Rydberg states absorption spectrum of Fenchone (shown in green) is depicted here as an example [Beaulieu 16]*

II. 3 MultiPhoton PECD

Replacing XUV with femtosecond laser pulses allows one to reach the multiphoton ionization regime. In the multiphoton ionization of atoms or molecules intermediate excited states can indeed be reached and drastically affect the process. Transitions to excited states the ionization yield is enhanced and this is called Resonance-Enhanced MultiPhoton Ionization (REMPI). Chiral molecules have an ionization potential below ~ 10 eV with a high density of states above $6-7$ eV typically Rydberg series, which can be easily reached by absorption of a few photons of the fundamental laser at 1030nm (1.2 eV) or its higher harmonics. These processes are usually denoted as $[n+m]$ REMPI, where n is the number of photons required to reach the resonance and m is the number of photons from this resonance to the continuum (see Fig. 3.5).

MP-PECD was first measured in Fenchone and Camphor using 400 nm circularly polarized femtosecond pulse in a [2+1] REMPI scheme [Lux 12] [Lehmann 13]. A strong forward-backward emission of electrons was observed, reaching more than 10%. Measurements were then performed in other compounds [Rafiee Fanood 14] [Rafiee Fanood 15] [Beaulieu 18]. Like single-photon PECD, MP-PECD shows sensitivity to molecular structure [Lux 12] [Lux 15], the orbital ionized [Rafiee Fanood 14] and the excited vibrational state [Beaulieu 16]. A specificity of MP-PECD is its sensitivity to the intermediate excited states which can be reached resonantly during the multiphoton ionization process [Beaulieu 16] [Kastner 17]. This REMPI scheme can be decoupled using two ultrashort laser pulses in pump-probe configuration. This enables one to access the relaxation dynamics of the photoexcited states on the femtosecond and timescale [Comby 16]. Last, since MP-PECD is enantiomer-specific it has also been used to determine the enantiomeric excess of samples [Rafiee Fanood 15] [Kastner 16] [Miles 17] [Comby 18].

Quantification of Dichroism

The structure of the photoelectron angular distribution recorded for multiphoton ionization is in general completely different from those obtained in the single photoionization case. As multiple photons are involved in the process, sharper structures appear in the angular distributions. The photoelectron angular distribution ($\mathcal{S}_p(E,\theta)$), generally recorded in a Velocity Map Imaging spectrometer, can be expanded on a basis of Legendre polynomials P_i^0 as:

$$\mathcal{S}_p(E,\theta) = \sum_{i=0}^{2N} b_i^l(E) P_i^0(\cos(\theta)) \tag{3.5}$$

where N is the number of photons involved in the ionization, E is the photoelectron kinetic energy, θ is the photoelectron ejection angle, $l = \pm 1$ corresponds to the light helicity and i corresponds to the order of the polynomial. The maximum number of polynomials required to describe the distribution is $2N$ [Reid 12]. It is important to note that the even order polynomials are symmetric while the odd order polynomials are antisymmetric along the laser propagation axis. The odd order polynomials vanish for linearly polarized light or achiral molecules and they change sign with the incident light helicity.

The symmetric part of the photoelectron angular distribution for single photoionization can be described by P_0^0 and P_2^0 while the P_1^0 describes the chiral response. With the decomposition of the photoelectron angular distribution into Legendre polynomials it becomes possible to define an angularly integrated quantity to define the overall asymmetry. Where the asymmetric emission of the electrons along the laser propagation direction, defined as MP-PECD, can be expressed as a linear combination of Legendre polynomial coefficients as:

$$MP - PECD(E) = \frac{4}{b_0(E)} \sum_{l=odd} p_l b_l(E) \tag{3.6}$$

where,

$$p_l = \int_0^{\frac{\pi}{2}} P_l(\cos\theta) \sin\theta d\theta \tag{3.7}$$

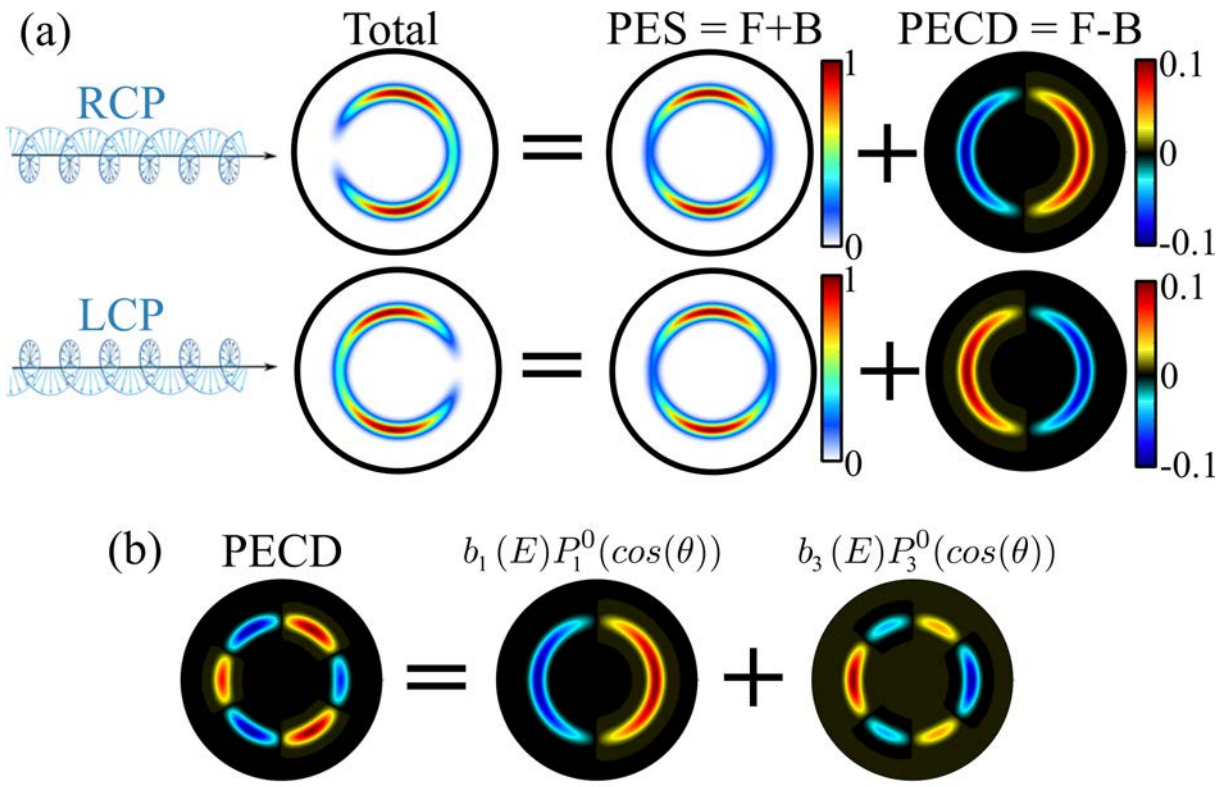

Figure 3.6 – *a) Schematic of the decomposition of the photoelectron angular distributions on a basis of Legendre polynomial. The total distribution has a symmetric and antisymmetric part along the laser propagation axis (horizontal). The antisymmetric part reverses with the light helicity while the symmetric one remains unchanged. Note that the distribution is fully symmetric if the light is linearly polarized or if the molecule is achiral. The PECD depicted is typical of a single-photon ionization, where the first order Legendre polynomial fully described the antisymmetric part. (b) Decomposition of a typical multiphoton PECD, where higher Legendre polynomial orders are reached (here for a two-photon ionization). Extracted from [Bloch 20]*

where $p_l = 1$ for $l = 0$, $p_l = 0$ for l even and

$$p_l = (-1)^{\frac{l-1}{2}} \frac{l!!}{l(l+1)(l-1)!!}$$

where b_0 defines the total number of electrons. The MP-PECD is normalized by the total number of electrons or the number of electrons emitted by hemisphere. This expression is valid $m = 0$, implying that a cylindrical symmetry is maintained in the ionization process i.e. the molecules are randomly oriented and the incident laser polarization is circular.

II. 4 PhotoElectron Elliptical Dichroism

Photoelectron dichroism has been studied in chiral molecules using circularly polarized light because it is an excellent chiral probe. A question which naturally arises is whether elliptically polarized light can be used to probe chiral molecules? In the single photoionization regime it has been established that the PECD obtained with elliptical polarization is simply proportional to the amount of circularly polarized photons, characterized by the third Stokes parameter ($S3$) [Nahon 06]. Thus there is not much of physical interest to study the influence of ellipticity of the

light on the dichroism. However, in the case of REMPI scheme, the intermediate resonances can significantly modify the chiral response of the molecules. It has been experimentally observed that the slope of the curve, dichroism v/s S3, increases at higher ellipticities [Lux 15]. Also sharp changes in the slope have been observed at $|S3| = 0.4$ [Miles 17].

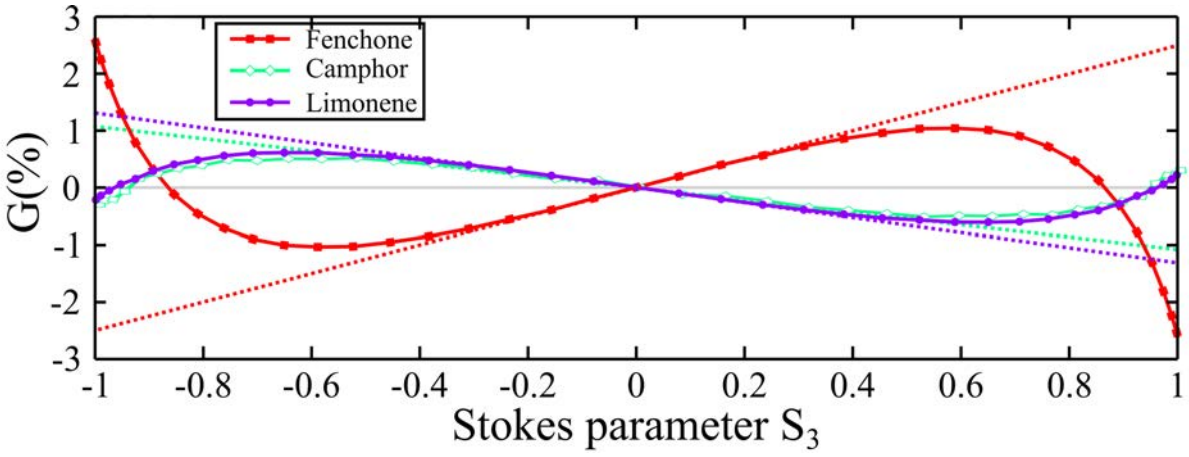

Figure 3.7 – *Evolution of the forward/backward asymmetry G as a function of S3 , in (+)-Fenchone (red squares), (+)-Camphor (green diamonds) and (+)-Limonene (purple circles), at* 5×10^{12} *W.cm*^{2} *. The dotted lines are a linear extrapolation of the low-S3 behavior. Extracted from [Comby 18]*

Thus an asymmetry factor of the 2-D photoelectron angular distribution recorded in the VMI, called the G-function, is defined as follows:

$$G(S3) = \frac{4(F - B)}{F + B} \tag{3.8}$$

where F and B are respectively the integrated signal on the forward and backward hemispheres with respect to the laser propagation direction. The evolution of the G-function has been studied extensively for Fenchone, Camphor and Limonene [Comby 18].

The evolution of G-Function for Fenchone, Camphor and Limonene at an intensity of $I_{515nm} = 5 \times 10^{12}$ W/cm^2 is shown in Fig 3.7. It is observed that G-Function has a linear dependency with S3 at low ellipticity, as depicted with the dotted lines. As the ellipticity of the incident electromagnetic wave increases the G-Function starts to deviate from it linear behavior at around $|S3| \sim 0.6$. The G-Function evolves non-linearly and non-monotonically with S3 and even changes sign at $|S3| = 0.9$. Finally, the G-Function shows a strong molecular dependency, especially between Fenchone and Camphor/Limonene, where the G-Function is maximizes for Fenchone in circular polarization while it almost vanishes for the other Camphor/Limonene. Even by reducing the dimensionality of the observable (G-function compared to the angularly structured PECD) a clear difference is observed between Fenchone and Camphor, which are isomers of each other.

The complex behavior of the chirosensitive asymmetry in the multiphoton ionization by elliptically polarized laser pulses leads to the redefinition of the dichroic effect as PhotoElectron Elliptical Dichroism (PEELD). The question now arises about the physical processes responsible for this non-linear and non-monotonic behavior of the PEELD.

Bound-Bound and Bound-Continuum Transitions

Multiphoton ionization of Fenchone using 515nm (2.21 eV) occurs in a $[3+1]$ REMPI scheme, where the intermediate states lie in the Rydberg state manifold at $3 \times 2.41 = 7.22$ eV, just below the ionization threshold (See Fig. 3.8), where the ionization potential of Fenchone is 8.72 eV [Comby 18]. At lower ellipticities the resonant excitation will starts to be due to the linear polarization component of the field. Thus in the case of lower ellipticities the excitation will preferentially occurs along the polarization axis whereas for circular and higher ellipticities the excitation preferentially occurs for the molecules whose transition dipole moments are in the polarization plane. It is important to note that, in most of the cases multiphoton excitation is more efficient for linear photons than for circular photons. Together with the non-linearity of the ionization, where the efficiency of a three-photon process scales with the cube of the laser intensity, makes the anisotropy of the excitation extremely sensitive to the linear polarized component of the laser as a linear field has an amplitude greater than that of a circular one. Thus a preferential excitation is observed in the bound-bound transitions involved during the multiphoton ionization process and varies non-linearly as schematically shown in Fig. 3.8.

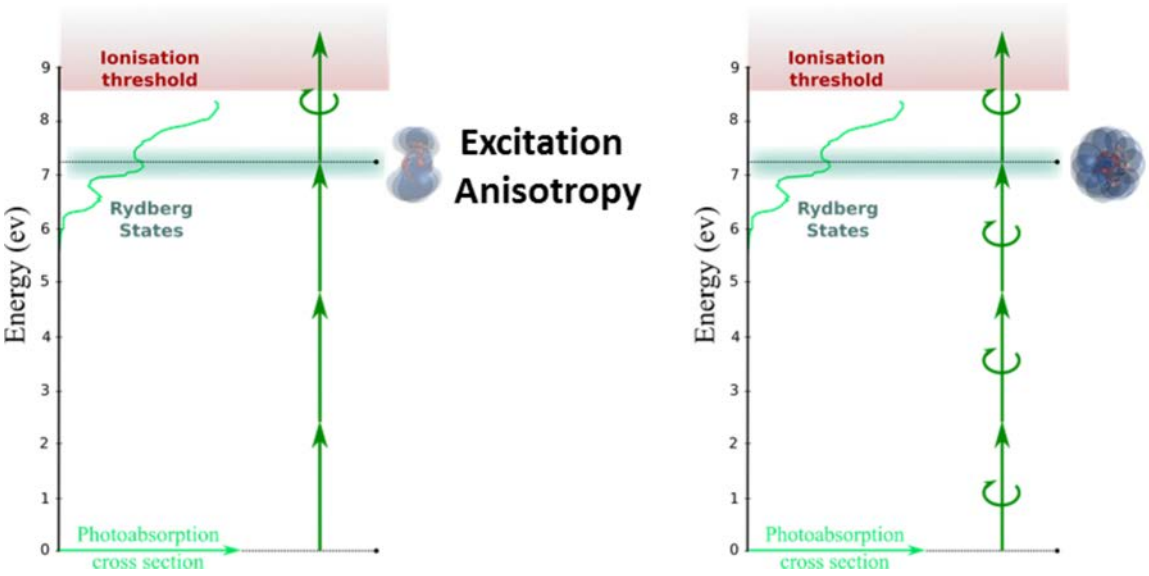

Figure 3.8 – *PEELD effect in the REMPI scheme of the Fenchone at a wavelength of 515 nm ([3+1] REMPI). (left) At low field ellipticity, the excitation to the intermediate states is preferentially performed by the linearly polarized photons. This induces an anisotropy of excitation in the randomly aligned sample, as the molecules having a transition dipole along the polarization axis are preferentially excited. The dichroic response only comes from the part ionized from the excited states with circularly polarized photons. (right) At high ellipticity, the excitation is performed mainly by circularly polarized photons, selecting all the molecules in the polarization plane.*

In the final step of the $[3+1]$ REMPI process the electron in the excited state absorbs a single photon and reaches the continuum. The competition between circular and linear photons does not take place in this final ionization step. An asymmetric emission in the photoelectrons is due to circularly polarized photons only. Thus, the final step, which is essentially a single photon ionization event, and thus the dichroism can be considered to vary linearly with S3, as observed between $S3 = \pm 0.4$ in Fig. 3.7. Or in other words bound-continuum transitions vary linearly with the S3.

II. 5 Wavelength Dependence

So far we have seen how varying the ellipticity of the ionizing light enabled manipulating the bound-bound and bound-continuum transitions, inducing drastic changes on the PEELD signal. Another way to manipulate the REMPI process is to to vary the wavelength of the ionizing radiation to select different resonances. The role of the Rydberg state in the [2+1] photoionization of Fenchone have been investigated by scanning the excitation wavelength from 359 to 431 nm and simultaneously excite up to three electronically distinct resonances [Kastner 17]. Using high-resolution spectroscopy two of the resonances as belonging to the B- and C-bands, which involve excitation to states with 3s and 3p Rydberg character, respectively were identified. A sign change was ob- served in the PECD signal, depending on which electronic state is used as an intermediate states. Thus two differently behaving contributions were identified. Scanning the laser wavelength also showed a decrease in the magnitude of the PECD with increasing photoelectron energy for the 3s state. These studies revealed the crucial role of the intermediate states in the multiphoton PECD.

III Multidimensional chiral response: wavelength- and ellipticity- dependent dichroism

So far we have seen how the intermediate states play a role in the PECD. There are two ways to disentangle the role of bound-bound and bound-continuum transitions. Either by changing the excitation wavelength or by changing the ellipticity of the ionizing electromagnetic wave. The high repetition rate of our laser system gives us the possibility to perform multidimensional investigations in a reasonable amount of time (typically a PEELD measurement takes < 30 min for a set of parameters). We thus investigated the combined influence of the laser wavelength and ellipticity in the photoionization of Fenchone molecules. I have been involved in this experiment partially and was involved in the preliminary data analysis. The results being already published [Beauvarlet 22], the publication is enclosed. The main conclusion of this investigation is that PEELD provides a wealth of information with higher degree of sensitivity than PECD by revealing states that were dark (did not participate) in PECD. The coefficient b_3 (in Eqn. (3.6)) is mainly associated to selectivity in the molecular orientation induced by resonances. Through the variation of b_3 as a function of S3, ultrafast coupling between electronic states have been revealed. In a nutshell, varying S3 in a $[m + n']$, for $m > 2$, photoionization allows to vary the electronic content of the wavepacket created by the pump, providing an additional easy way to test ab initio simulations of TR-PES and its consecutive assignments of specific spectro-temporal features. In a more general context than chirality, our work illustrates how continuous variation of S3 with Fourier filtering could be used as an additional dimensionality in time-resolved photoelectron imaging, usually used in femtochemistry.

PCCP

PAPER

View Article Online
View Journal

Cite this: DOI: 10.1039/d1cp05618b

Photoelectron elliptical dichroism spectroscopy of resonance-enhanced multiphoton ionization *via* the 3s, 3p and 3d Rydberg series in fenchone

Sandra Beauvarlet, Etienne Bloch, Debobrata Rajak, Dominique Descamps, Baptiste Fabre, Stéphane Petit, Bernard Pons, Yann Mairesse and Valérie Blanchet *

Received 9th December 2021,
Accepted 26th January 2022

DOI: 10.1039/d1cp05618b

rsc.li/pccp

The resonance-enhanced multiphoton ionization of chiral molecules by elliptically polarized laser pulses produces photoelectron angular distributions that are forward/backward asymmetric with respect to the light propagation axis. We investigate this photoelectron elliptical dichroism in the (2 + 1)-photon ionization of fenchone molecules, using wavelength tunable femtosecond UV pulses. We show that the photoelectron elliptical asymmetry is extremely sensitive to the intermediate resonant states involved in the ionization process, and enables electronic couplings to be revealed that do not show up so clearly when using circularly polarized light.

1 Introduction

Chiral molecules are of particular interest in a broad range of scientific fields, from fundamental physics to biology. The two non-superimposable mirror forms of a chiral molecule, called enantiomers, interact differently with other chiral objects. Since all living organisms are formed of chiral building blocks, enantio-specificity is at the heart of biological processes and plays a fundamental role in pharmacology. From a spectroscopic point of view, the interaction between chiral molecules and circularly polarized light gives rise to a broad variety of phenomena referred to as Circular Dichroisms (CDs). These chiroptical processes are extensively used to distinguish enantiomers. Absorption CDs extend from the microwave to the ultraviolet range of the spectrum, probing rotational, vibrational and electronic transitions. They rely on the combination of magnetic dipole and electric quadrupole transitions and as such provide rather weak differential absorption, around 10^{-4} in relative. In 1976, Ritchie *et al.* predicted a purely electric-dipole effect giving chiral signals in the range of 1–10% when chiral molecules are photoionized by circularly polarized radiation.[1] This PhotoElectron Circular Dichroism (PECD), confirmed in 2000 by theoretical calculations done by I. Powis,[2] would manifest as a forward/backward asymmetry in the photoelectron yield with respect to the light propagation. Bowering *et al.* measured the first PECD in 2001, as a 3% asymmetry in the one-photon ionization of bromocamphor by vacuum ultraviolet radiation.[3] Since then, this effect has been extensively investigated on different chiral targets ionized by Vacuum UltraViolet (VUV) or extreme-UV (XUV) synchrotron light, showing remarkable spectroscopic sensitivity to molecular orbitals, vibrations, chemical substitution and conformation.[4–6]

One decade later, table-top PECD experiments arose, using resonance-enhanced multiphoton ionization (REMPI) by femtosecond UV laser pulses.[7,8] They revealed a strong REMPI-PECD in camphor and fenchone molecules, in the 10% range, which could exceed the PECD observed in single photon ionization at the same electron kinetic energy.[9] These pioneering experiments opened the way to the time-resolved investigation of chiral dynamics by PECD,[10,11] as well as to the spectroscopic investigation of PECD in the multiphoton and strong-field ionization regimes.[9,12]

Compared to single-photon PECD, REMPI-PECD signals show two important additional features. First, increasing the number of photons N involved in the photoionization process produces more structured angular distributions. Indeed, as stated by Yang's theorem, the absorption of N photons produces a photoelectron distribution P that can be decomposed as a sum of Legendre polynomials – within the assumption of a cylindrical symmetry of the interaction – up to $2N$:

$$P(E_k, \theta) = \sum_{i=0}^{2N} b_i(E_k) P_i(\cos(\theta)) \quad (1)$$

where θ is the ejection angle of the photoelectron in the (y,z) detection plane, z is the propagation axis of the light and x is the time-of-flight axis of the Velocity Map Imaging Spectrometer (VMIS)

Université de Bordeaux - CNRS - CEA, CELIA, UMR 5107, F33405 Talence, France. E-mail: valerie.blanchet@u-bordeaux.fr

used to characterize the momenta of photoelectrons. In this distribution, all the odd polynomials encode the photoelectron asymmetry relative to the light propagation axis, while the even terms describe symmetric, non-enantiosensitive interaction. Thus, while single-photon PECD at a given electron energy can be described by a single parameter b_1, the REMPI-PECD is characterized by a series of parameters $b_{1,3,5\ldots}$, which enriches its spectroscopic content and its sensitivity.

The second additional feature of REMPI-PECD is the impact of an intermediate resonance in the photoionization process. The $M + K$ REMPI stands for a resonant excitation of electronic states by absorption of M photons, followed by absorption of K additional photons to overcome the ionization potential. In the present study, the resonant electronic states are Rydberg states populated with $M = 2$ and ionized with $K = 1$. Goetz *et al.*[13] introduced a theoretical treatment of REMPI-PECD that decoupled the excitation and ionization. They showed that the anisotropic distribution of photoexcited molecules strongly affects the PECD, in particular by increasing the contributions of higher Legendre polynomials in the angular decomposition. This was confirmed experimentally by decoupling photoexcitation and photoionization in a two-color pump–probe scheme.[10,11] These measurements showed that photoexciting molecules with linearly or circularly polarized light produces different PECDs, mainly due to the different subset of molecular orientations selected by the excitation process from an initial isotropic unexcited sample.

Indeed for $M = 2$, the anisotropy resulting from the photoexcitation of a molecular ensemble by linearly polarized light is expected to differ from that obtained by photoexciting with circularly polarized radiation. Controlling the proportion of circularly polarized photons, quantified by the third Stokes parameter S_3 of the incoming light, thus offers a way to select the class of molecular orientations that is excited.

As important, the polarization state of the light is also expected to modify the two-photon absorption cross section (TPA). As a consequence, while in single-photon ionization the forward/backward photoelectron asymmetry is known to scale linearly with $|S_3|$,[4] in (2 + 1) REMPI, it can increase non-linearly with $|S_3|$[8,14] and even evolve non-monotonically.[15,16] The sensitivity of this PhotoElectron Elliptical Dichroism (PEELD) to the anisotropy of excitation should make it very sensitive to the intermediate state, specifically revealing information about the excitation process.

In this paper, we investigate the (2 + 1)-REMPI of fenchone molecules by elliptically polarized 60–70 fs laser pulses tuned between 415 nm to 343 nm. We show that the angle- and energy-resolved PEELD maps, as well as their evolution with the polarization state and wavelength of the ionizing radiation, produce a multidimensional spectroscopy highlighting the importance of electronic couplings between excited states.

The paper is structured as follows: Section 2 summarizes our *ab initio* calculations and the Rydberg spectroscopy of fenchone. Section 3 describes the experimental set-up and the data processing. The data are presented in Section 4. Finally, we summarize our findings in Section 5.

2 State of the art

2.1 Rydberg spectroscopy of fenchone and *ab initio* calculations

Most of the electronic excitation of fenchone above 6 eV results from the promotion of an electron from the highest occupied molecular orbital (HOMO), localized on the carbonyl bond (n orbital) to virtual orbitals building Rydberg states. In the 5.9–7.22 eV energy range investigated here, the first three Rydberg series have to be considered. They are characterized by their principal quantum number $n = 3$ and their respective angular momentum $l = 0, 1, 2$. Their first assignment was performed by Pulm *et al.* relying on one-photon absorption CD measurements and DFT/SCI calculations.[17] More recent calculations using TDDFT and an improved basis, d-Aug-cc-pDVZ,[18–20] were performed by Singh *et al.*[21] Note that the latter focused their attention on the $n = 3$ Rydberg states without considering the second valence state that was predicted to lie between the 3p and 3d Rydberg bands according to Pulm *et al.*[17] We thus used the same method and basis of Singh *et al.* and calculated the state energies up to the 12th state, including the second valence state. The energies of the first excited states are in good agreement with the latest calculations (see Table 1). The second valence state, which mainly results from the excitation of the HOMO−1 σ-orbital located on the bicyclic part to a π unoccupied orbital located on the carbonyl group, is found to lie at 7.45 eV, just above the 4s Rydberg state. This is significantly higher than the predictions of previous calculations.[17] The shape of the excited states are displayed in Fig. 1 in terms of 3D isodensity plots. Zooming on the nuclear structure reveals that the $3p_3$ and $3d_5$ states exhibit a π sizeable component on C═O. This indicates a mixing of Rydberg and second valence states, as already noted by Singh *et al.*[21] This valence mixing is presently also noticeable in the structure of the $3p_2$ and $3d_{2,3}$ states. In this respect, the strong one-photon absorption CD observed around 7.2 eV has been assigned to the mixing of this second valence state and the 3d band.[17]

We have also calculated the oscillator strengths and Two-Photon Absorption cross sections (TPA) of these excited states at the equilibrium geometry of neutral fenchone. The TPA are inherently different in linear ($S_3 = 0$) and circular ($|S_3| = 1$) polarizations. Fig. 2 shows how the electronic excitation is expected to change significantly by varying S_3. For instance, it is expected that the $3d_1$ state should be preferentially populated through the absorption of two circularly polarized photons while the $3d_2$ state largely dominates its neighbours in the case of linear polarization. Varying S_3 at the same time as the driving wavelength should thus allow us to turn on or off an intermediate resonance within the (2 + 1)-ionization process.

2.2 Photoelectron spectroscopy

In 2017, Kastner *et al.* investigated the role of Rydberg states of fenchone in a (2 + 1)-REMPI scheme using tunable 45–60 fs pulses centered between 431 nm to 360 nm, reaching a two-photon excitation in the 5.75–6.9 eV range.[23] They identified up to three distinct contributions in the Photoelectron Angular

Table 1 Measured and calculated E_R binding energies of the states belonging to the Rydberg series involved in our PEELD spectroscopy. The energy of the $\sigma \rightarrow \pi^*$ valence state is also given

		Pulm *et al.*[17]		Kastner *et al.*		Singh *et al.*			This work	
		Absorption		(2 + 1) REMPI		(2 + 1) REMPI			(2 + 1) REMPI	
State		Meas.	Calc.	Meas. ns[22]	Meas. fs[23]	Meas. ns[21]	Meas. ps[24]	Calc.[21]	Meas. fs	Calc.
$n \rightarrow 3s$	Ryd.	6.10	6.28	5.953 ± 0.001	6.10	5.95	5.965	6.26	5.95	6.25
$n \rightarrow 3p_z$			6.67			6.4	6.403	6.69		6.67
$n \rightarrow 3p_y(b_2)$	Ryd.	6.58	6.68	6.37	6.50	6.46		6.72	6.43	6.70
$n \rightarrow 3p_x(b_1)$			6.77					6.76		6.74
$n \rightarrow 3d_1$			7.18					7.16		7.14
$n \rightarrow 3d_2$								7.25		7.23
$n \rightarrow 3d_3$	Ryd.				6.94[a]			7.27	6.93[a]	7.24
$n \rightarrow 3d_4$								7.29		7.26
$n \rightarrow 3d_5$			7.45					7.31		7.28
$\sigma \rightarrow \pi^*$	Val.	7.21	7.05–7.23		6.94[a]					7.45

[a] Indicates the possible mixing character of a pure Rydberg state with a valence one. All energies are expressed in eV and the calculations employ TDDFT[25] with CAMB3LYP functional[26] and underlying d-aug-cc-pVDZ Gaussian basis.[18–20]

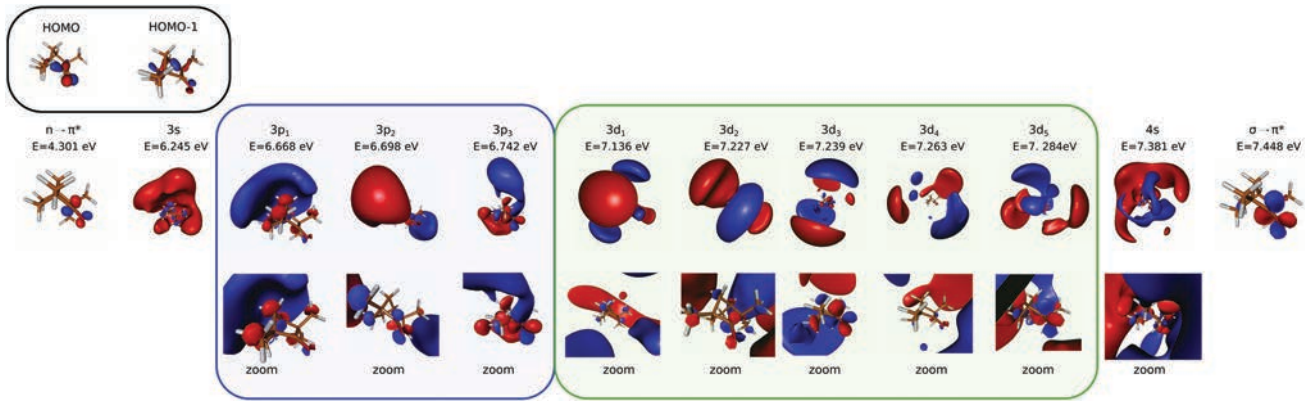

Fig. 1 Shapes of the orbitals and excited states of fenchone, resulting from TDDFT[25] with CAMB3LYP functional[26] and underlying d-aug-cc-pVDZ Gaussian basis.[18–20] For some of the Rydberg states, we zoom on the molecular structure to elicit possible mixing with the $\sigma \rightarrow \pi^*$ valence state (lower row).

Distribution (PAD), progressively appearing with increasing two-photon excitation energy. These all presented a significant PECD signal, with different signs and amplitudes. The 3s and 3p channels, respectively located at 5.95 eV and 6.37 eV excitation energies, gave a negative sign of PECD for (*S*)-(+)-fenchone corresponding to a backward asymmetry. The third channel, appearing at 6.94 eV, was tentatively assigned to the $\pi^* \leftarrow \sigma$ valence state, from which a positive PECD-forward asymmetry was observed for the same enantiomer. These PECD measurements further enabled separating two components arising from the 3p states, which were barely visible in the non-chiral part of the PAD. These measurements established that the sign of the PECD can switch depending on which intermediate electronic state is involved in the REMPI.

Three years later, the same group conducted a higher energy resolution study, with nanosecond pulses between 420 and 375 nm, leading to an investigation of resonances lying between 5.9 to 6.62 eV.[22] From this first high-resolution ns-REMPI spectra, they assigned the three dominant peaks lying between 6.37–6.55 eV to the 3p Rydberg states. They resolved the PECD associated with different vibrational levels of the 3s Rydberg state, and found a smooth decrease of the magnitude of the PECD with increasing vibrational excitation energy. The ns-REMPI-PECD of the 3p states were so weak that no reliable values were provided.

The comparison of the PES recorded in fs-REMPI and ns-REMPI reveals that the 3s/3p branching ratio in the PES strongly increases with the pulse duration. This drastic increase was assigned to an internal conversion taking place from the 3p and resulting in an increase of the 3s population. This population transfer to the 3s state was also confirmed at higher energy (6.9 eV).[27] The bandwidths of the 3p components measured on the ns-REMPI spectra lead to an estimated lifetime of 30 fs for each of these sub-states.

In 2020, Singh *et al.*[21] performed a joint experimental and theoretical investigation of the low-lying Rydberg states of fenchone. They measured the (2 + 1)-REMPI photoionization yield with a 1.3 ps pulse at wavelengths between 450 and 350 nm and determined an adiabatic ionization energy of $IP_a = (8.495 \pm 0.01)$ eV. The results of their TDDFT calculations

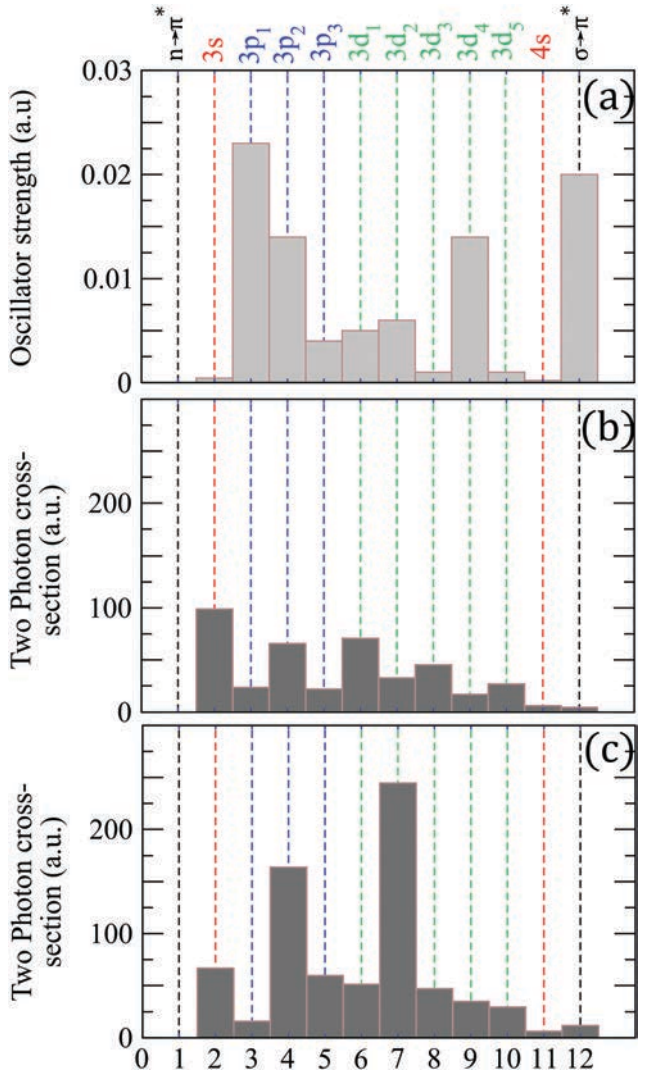

Fig. 2 (a) Oscillator strengths to the first excited states of fenchone. Two-photon absorption cross sections (TPA) calculated (b) in circular and (c) linear polarizations. The $3p_{1,2,3}$ are the $3p_{z,y,x}$ identified by Singh *et al.* The axis are defined relatively to the local C_{2v} (planar) geometry of the carbonyl group: *x*-axis normal to the plane of the C–CO–C group, and *z*-axis parallel to the C=O bond. The calculations employ TDDFT[25] with CAMB3LYP functional[26] and underlying d-aug-cc-pVDZ Gaussian basis.[18–20]

are presented in Table 1, together with the experimentally determined energies of the Rydberg states. These energies globally lie ~0.3 eV below their computed ones. They also measured the dependency of the two-photon transitions as a function of the polarization state of the ionizing radiation. They found that for the 3s band, the absorption was ~1.2–1.5 stronger in circular than in linear polarization, consistently with the TPA shown in Fig. 2. By contrast, the absorption of the 3p band was reduced by a factor of ~2 from linear to circular, which is again consistent with our TPA calculation. Both the ns-REMPI and ps-REMPI schemes show an enhancement of the 3s state component in the photoelectron spectrum. This was attributed again to the prevalent internal conversion from the 3p series. In 2021, Singh *et al.*[24] have investigated the (2 + 1) REMPI-PECD with a 17 cm^{-1}–1.3 ps-UV pulse reaching the 5.95–6.75 eV two-photon energies. They concluded that the internal conversion from the 3p to the 3s state induced a switch of the PECD sign.

An important question which arises whenever Rydberg states are involved in the photoionization process is the influence of fast relaxation dynamics on the outcome of the measurement. An experimental time-resolved photoionization study in (1 + 1′)-configuration showed that the 3s state of fenchone relaxed in 3.3 ps, significantly affecting the PECD.[10] While such measurements provide a straightforward insight into the process, they are not the only way to obtain information on the presence of relaxation dynamics. Indeed, several signatures of internal conversion from the 3p to 3s Rydberg states were observed in the investigation listed above. First, the increasing 3s/3p ratio with increasing pulse duration definitely provides a hint as to the relaxation dynamics. A second interesting observation reflecting the relaxation dynamics is the breakdown of the $\Delta v = 0$ propensity rule: when the 3s is populated through non-adiabatic coupling from the 3p, some photoelectrons appear at lower kinetic energies than expected for ionization of Rydberg states.[21,24] In the following, we show that single-color (2 + 1)-fs-REMPI spectroscopy based on PEELD[15] gives access to additional signatures of the internal conversion.

3 Experimental set-up and data processing

Our experiment was performed with the BlastBeat laser system (Tangerine SP from Amplitude) delivering 130 fs pulses at 1030 nm, with 300 μJ $pulse^{-1}$ at 166 kHz (50 W average power). The second harmonic was used to pump an Optical Parametric Amplifier (OPA, Mango SP from APE). The prism-compressed OPA output was frequency doubled in a 100 μm BBO crystal. Typically, fs-REMPI was achieved with 500 nJ p^{-1} to 1 μJ p^{-1} and pulse durations between 55 to 75 fs, with a pulse bandwidth of ~40 meV (corresponding to a Fourier-limited duration of ~45 fs).

We used 11 wavelengths ranging from 343 nm to 420 nm to photoionize fenchone molecules. The photon energy (from 2.9 to 3.6 eV) allowed us to proceed with two-photon excitation of Rydberg states lying between 5.9 and 7.2 eV followed by ionization using a third photon. The laser pulses were focused by a CaF_2 lens with 300 mm focal length at an intensity around 4×10^{11} W cm^{-2} into the interaction chamber of a VMIS, which recorded a 2D projection of the 3D photoelectron momentum distribution. Enantiopure (1*S*,4*R*)-(+)-fenchone molecules (Sigma Aldrich, further called *S*-(+)-fenchone) were introduced by a 200 μm nozzle heated at 90 °C, leading to a pressure in the interaction chamber of 2×10^{-6} mbar (with a background pressure of 7×10^{-8} mbar). To record the 2D projection (*y*,*z*) of the PAD, we used a set of two Micro-Channel Plates (MCP) coupled to a fast phosphor screen whose luminescence was recorded by an sCMOS camera with an exposure time of 1 s (166 000 laser shots) and no dead time between images. Each image was binned by 2 × 2. The laser polarization state was

controlled by rotating a superachromatic quarter waveplate (B. Halle) while continuously recording the VMIS images.

The PEELD analysis has been already fully described in ref. 15 and 16. The data were collected by rotating the quarter waveplate at the speed of $4^\circ\ s^{-1}$ and recording movies of 1200 frames, covering 13 full waveplate rotations. Per turn of the quarter waveplate, S_3 reaches zero value four times, twice $S_3 = 1$ and twice $S_3 = -1$. In the 13 full rotations of the quarter waveplate that builds the 1200-frame movie, 26 repetitions of the PEELD S_3 features are expected.[15] To mimick the (Left-Right) subtraction of the VMIS images that is usually done in the PECD studies, the paired images with the same $|S_3|$ but opposite helicities are subtracted to each other. The resulting differential image was (anti-)symmetrized along the z axis, symmetrized along y. Fourier analysis of the evolution of the images as a function of waveplate rotation was used to filter pixel per pixel the projections of PAD and PEELD varying as a function of S_3. Finally, these projections were decomposed as a sum of Legendre polynomials P_i as follows:

$$\mathrm{PAD}(E_\mathrm{k},\theta) = \sum_{i=0}^{N} b_{2i}(E_\mathrm{k}) P_{2i}(\cos(\theta)) \quad (2)$$

$$\mathrm{PEELD}(E_\mathrm{k},\theta) = \sum_{i=0}^{N} b_{2i+1}(E_\mathrm{k}) P_{2i+1}(\cos(\theta)) \quad (3)$$

where E_k is the kinetic energy of the emitted photoelectrons, θ the ejection angle in the (y,z) detection plane, N is the number of absorbed photons and b_i the Legendre coefficients. When the ionizing radiation is linearly ($S_3 = 0$) or circularly ($|S_3 = 1|$) polarized, the cylindrical symmetry of the interaction ensures that the Legendre decomposition of the 2D projection enables retrieving the 3D photoelectron angular distribution (Abel inversion[28]). For intermediate values of S_3, the correspondence between the Legendre decomposition and the Abel inversion is lost. We will nevertheless rely on the Legendre decomposition while keeping in mind that they do not reflect the full 3D structure of the momentum distribution of the emitted photoelectrons.

Fig. 3 shows the electron distributions obtained when S-(+)-fenchone is photoionized at 3×358 nm with resonances reached around 6.92 eV. We show the raw and fitted images for two polarizations: circular ($S_3 = -1$, Fig. 3(a and c)) and elliptical close to linear ($S_3 = -0.2$, Fig. 3(b and d)). In both cases, we observe three contributions in the PAD. The two inner ones result from the ionization from 3s and 3p Rydberg states. The third, weaker component at higher photoelectron kinetic energy was previously observed but not further discussed.[23] Whereas the PADs recorded in circular and elliptical lights are very similar, the PEELDs are remarkably different. With $S_3 = -1$, the PECD displays two contributions of opposite signs, reaching a few percents ($\sim$2%). When the ionizing field is elliptically polarized with $S_3 = -0.2$, additional contributions and very different angular distributions clearly appear in the PEELD image. This example illustrates the spectroscopic interest of PEELD investigation and its potential to reveal features that are not showcased by the usual PECD. In the following, we pursue this comparison between PECD and PEELD images by

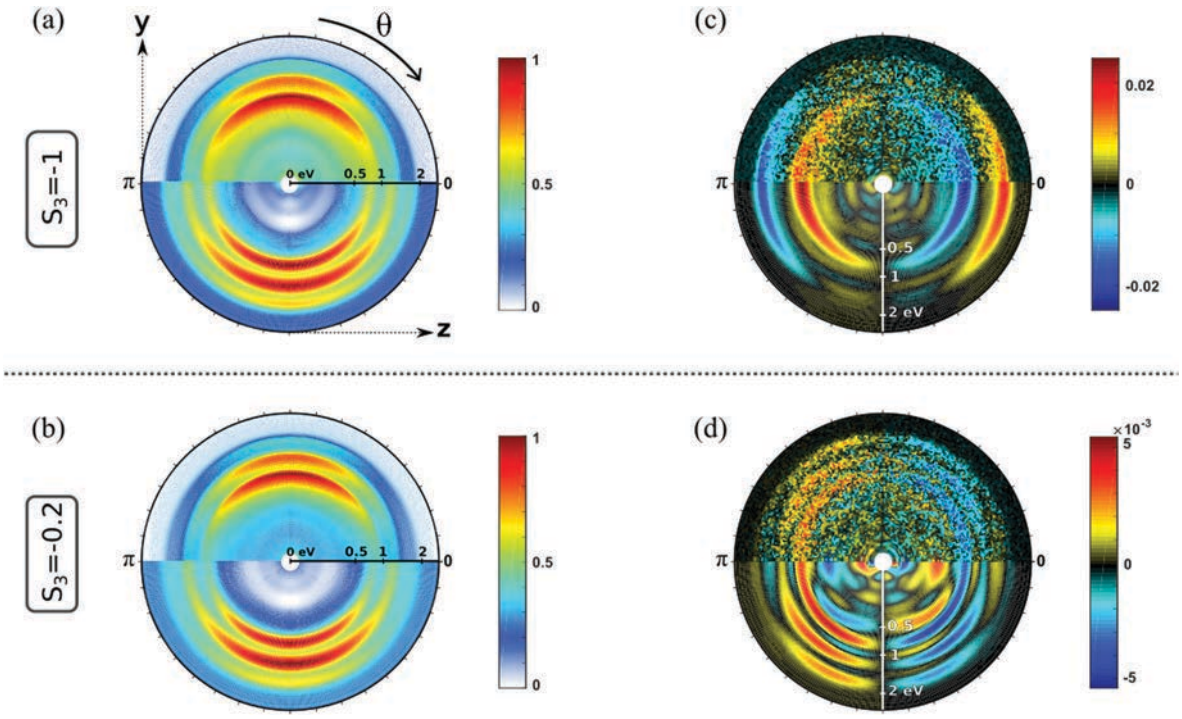

Fig. 3 Normalized photoelectron angular distribution (PAD) of S-(+)-fenchone photoionized at 358 nm by (a) a circularly polarized field ($S_3 = -1$) and (c) its corresponding antisymmetric signal, *i.e.* PECD. Upper half of each image is raw experimental data, that have been antisymmetrized with respect to the light propagation direction z. Lower half of each image is Abel inverted image. (b and d) are the same as (a and c) for a lower ellipticity ($S_3 = -0.2$). The PAD are normalized by their maximal amplitudes (pixel value) which are also employed to normalize the PECD and PEELD images.

analyzing their evolution as a function of the ionizing laser wavelength.

4 The PEELD spectroscopy

4.1 Wavelength scan

The sensitivity of REMPI-PEELD to the intermediate electronic state is better visualized through the evolution of the Legendre coefficients b_i as a function of the two-photon energy and the ionization energy, as shown on Fig. 4. The ionization energy is defined as IE = $3 \times \hbar\omega_0 - E_k$, where ω_0 is the angular frequency of the ionizing photon and E_k is the kinetic energy of the photoelectron. The absorption of two photons leads to the population of a Rydberg state, with binding energy E_R, which can be vibrationally excited with energy E_{vib} such that $2\hbar\omega_0 = E_R + E_{vib}$. Assuming that the Rydberg and ion potential energy surfaces are parallel, the absorption of a third photon produces an ion whose vibrational energy is also E_{vib}. This assumption is often called the $\Delta v = 0$ ionization propensity rule of Rydberg states. The expected ionization energy from a given Rydberg state then evolves as $IE = IP_a - E_R + 2\hbar\omega_0$. The 2D-maps of Fig. 4 allows to highlight these $\Delta v = 0$ propensity rules for each Rydberg channel, represented by the white continuous lines. We further superimpose to the maps white dashed lines which correspond to E_R listed in Table 1 and determined by Kastner *et al.*[22,23] The identification of sub-states within 3p and 3d series is restrained by the driving laser bandwidth and the energy resolution of our VMIS.

The first striking observation that can be drawn from the evolution of the PES(b_0) in Fig. 4 is the validity of the $\Delta v = 0$ Rydberg ionization propensity rule. The local extrema appearing in the $b_{1,3}$ maps are slightly shifted in energy with respect to the maxima of the PES, depending on the ionization channel and S_3. Such an energy shift is common in PECD measurements, and usually assigned to the kinetic energy dependency of the phase shifts of the ionization partial waves defining the photoelectron asymmetry.[29]

We start by analyzing the case of photoionization by circularly polarized light ($S_3 = -1$, Fig. 4(a–c)). At low photon energy, only the 3s Rydberg state is accessible and shows a negative asymmetry. When the two-photon energy reaches $\sim$6.4 eV, photoelectrons associated with ionization from the 3p band appear at lower ionization energy. The 3s contribution remains important until the two-photon energy reaches $\sim$7 eV. At this third threshold, the 3d intermediate states take the lead of the PES(b_0). The ratio between the contributions from the 3s and 3p states in our measurements differs from that of Kastner *et al.*[23] who observed a larger photoelectron yield from the 3p states than from the 3s using $\sim$50 fs laser pulses. On the other hand, our results are more consistent with the ones recorded with picosecond[21,24] or nanosecond pulses.[22] This underscores that the few additional tens of femtoseconds of our pulses (70 fs) compared to those of Kastner *et al.*[23] (50 fs) are enough to

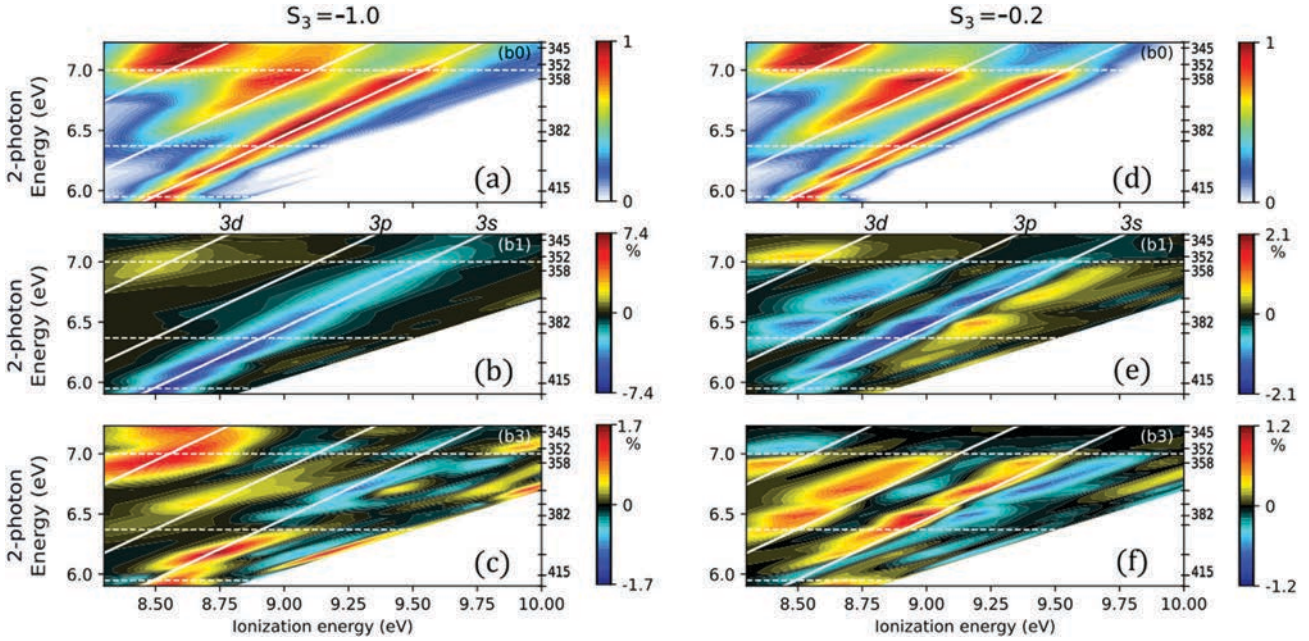

Fig. 4 Legendre decomposition of the REMPI photoelectron signal as a function of the two-photon excitation energy and the ionization energy ($IE = 3 \times \hbar\omega_0 - E_k = Ip_a - E_R + 2\hbar\omega_0$), for (a–c) a circular polarization with $S_3 = -1$ and (d–f) an elliptical polarization with $S_3 = -0.2$. (a and d) refers to b_0, while (b and e) correspond to b_1, and (c and f) to b_3. The 11 excitation wavelengths used in this study are indicated on the right side of each graph and the five ones leading to remarkable transitions in the ionization dynamics are mentioned in nm. For each excitation wavelength, the coefficients are normalized to the maximum of b_0. The 3s, 3p and 3d Rydberg series are identified by the continuous diagonal white lines corresponding to the $\Delta v = 0$ propensity rules of ionization with binding energies E_R = 5.95 eV, 6.37 eV and 6.94 eV, respectively (see Table 1). The horizontal dashed lines indicate the thresholds of appearance of 3s, 3p and 3d bands on the PEELD maps. Note that the Legendre decomposition of (2 + 1)-REMPI PAD also involves a b_5 coefficient which has been found negligible in all cases.

induce a larger sensitivity to non-adiabatic couplings (NAC) at play between the Rydberg states. Focusing on the forward/backward asymmetric signal, decomposed in the b_1 and b_3 maps (Fig. 4(b and c)), it is clear that the chiral response is dominated by the contribution of the 3s state for $S_3 = -1$, throughout the whole range of photon energies scanned. As already observed in the ref. 22 and 23, we confirm that b_1(3s) does not change sign as a function of vibrational excitation but experiences a smooth decay. As we will discuss further, the sign change of the b_3(3s) coefficient in Fig. 4(c) above $\sim$6.5 eV is related to the change of the anisotropy of excitation that is then imposed by the 3p electronic transition. The asymmetric signatures of the 3p or 3d states are more noticeable through the b_3 map (Fig. 4(c)) than through the b_1 map (Fig. 4(b)).

We have seen in Fig. 3 that chiral photoionization by circularly and elliptically polarized light could produce dramatically different angular distributions. To evaluate the generality of this statement, we now turn our attention to the b_0, b_1 and b_3 maps recorded at $S_3 = -0.2$ (Fig. 4(d–f)). The overall evolution of the b_0 map closely resembles the one measured in circular polarization, but the relative weight of the contributions from the different Rydberg states differs: the 3p state is stronger, and as soon as the 3d state is energetically accessible, this latter band dominates the whole spectrum. This is consistent with the two-photon absorption probabilities shown in Fig. 2. The TPA to the 3p and 3d bands are indeed expected to strongly increase when going from circular to (quasi-)linear polarization. Regarding the chirosensitive b_1 and b_3 coefficients, the most striking difference with respect to the circular case is the appearance of a strong b_1 contribution from the 3p state. Above 6.2 eV excitation energy, the b_1 and b_3 components from the 3s state split in two parts of opposite signs. A clear transition also lies within the 3d region around 7 eV, showing a sharp sign switch of b_1 and b_3, and almost no more signal from the other channels.

The evolution of the chiral signal from the three intermediate states can be further studied by spectral integration over respectively 450 meV, 630 meV and 830 meV around the white continuous lines depicted in Fig. 4 for 3s, 3p and 3d bands. The PECD, defined as twice the difference between the number of electrons emitted in the forward and backward hemispheres, normalized by the mean signal per hemisphere,[30] is given by:[7,31]

$$\mathrm{PECD} = \frac{1}{b_0}\left(2b_1 - \frac{b_3}{2} + \frac{b_5}{4}\right) \quad (4)$$

The PEELD recorded with $S_3 = -0.2$ can be defined similarly with an extra normalization to take into account the amount of circularly polarized photon $|S_3|$. Here we assume that only the last absorbed photon defines the amount of photoelectron asymmetry, yielding:

$$\mathrm{PEELD}_{\mathrm{norm}} = \frac{\mathrm{PEELD}}{|S_3|} = \frac{1}{|S_3|b_0}\left(2b_1 - \frac{b_3}{2} + \frac{b_5}{4}\right) \quad (5)$$

The result of these spectral integrations are shown in Fig. 5. As already mentioned, in the single-photon ionization case, the chiroptical response evolves linearly with S_3 such that the normalized $b_i/|S_3|$ is expected to be constant if no anisotropy of excitation enhances the photoelectron asymmetry. In other words, the S_3 dependency of these normalized coefficients is able to highlight deviations induced by the anisotropy of excitation of the resonant states.

With $S_3 = -1$, the PECD from the three channels shows an overall monotonous trend with the excitation energy. At 5.9 eV, the PECD from the 3s state reaches -13.2%, in agreement with the previous PECD investigations.[22–24] The 3s PECD reaches a maximum amplitude of -16% at 6.17 eV two-photon energy (402 nm driving wavelength) before progressively decreasing down to $-$ 3%. The PECD from the 3p channel remains between $\pm 2\%$ on the whole two-photon energy range, which

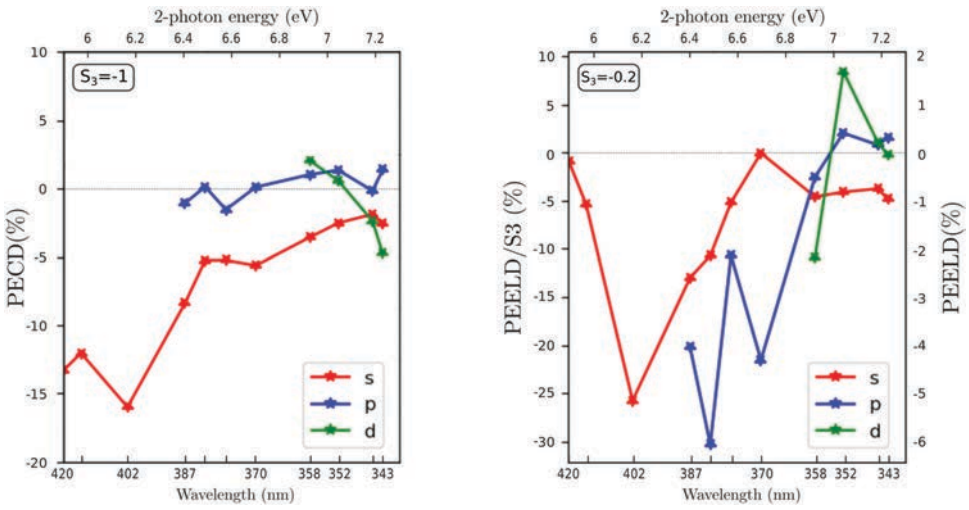

Fig. 5 Observed values of forward/backward dichroism spectrally integrated over 450 meV, 630 meV and 830 meV over each of the three ionization bands, related each to populations in the Rydberg states 3s, 3p and 3d (called s, p, d). The photoelectron dichroism is displayed as a function of the two-photon excitation energy for two specific ellipticities $S_3 = -1$ (on the left) and $S_3 = -0.2$ (on the right). The lines joining the stars are just guidelines.

is also in accordance with the values reported by Kastner *et al.*[23] but slightly lower than the ones recorded in ps-(2 + 1) REMPI.[24] Regarding the 3d state contribution, we observe a sign change of the PECD, starting from 2% at 6.92 eV (358 nm) and reaching −4.6% at 7.23 eV (343 nm).

When the ionizing radiation is elliptically polarized with $S_3 = -0.2$, the evolution of the PEELD with excitation energy shows an overall similar trend for the 3s band, but also displays some sharp features especially for the 3p and the 3d bands. For the 3s channel, the PEELD is very weak at 5.9 eV, reaching about −1% after normalization by $|S_3|$ whereas it was −13.3% in circular polarization. Increasing the photon energy results in an abrupt increase of the magnitude of $\text{PEELD}_{\text{norm}}$ which reaches −26.3% at 6.17 eV (402 nm). Even more impressive is the $\text{PEELD}_{\text{norm}}$ recorded for the 3p band, which shows a huge enhancement with respect to the PECD. Indeed, the raw PEELD reaches ∼−6% at 6.5 eV (382 nm), more than five times the value of the PECD at this photon energy. This is remarkable since the light producing the PEELD contains five times less circularly polarized photons than the one producing the PECD. The $\text{PEELD}_{\text{norm}}$ reaches thus −30%. This enhancement underscores how the ensemble of aligned molecules selected by the quasi-linearly polarized pulses from the original isotropic distribution is very different from the one selected in a circular radiation, and how this anisotropy results in a very strong chiroptical response in ionization. Last, the PEELD from the 3d state reaches high values and is very sensitive to the excitation wavelength, showing abrupt variations and changes of sign.

To get a deeper insight into the transitions in this REMPI regime investigated by PEELD, we focus on a few specific photon energies in the following sections to show the kinetic energy dependencies of the b_1 and b_3 parameters with $|S_3|$.

4.2 Transition between 3s and 3s–3p excitation

We start by investigating the influence of the 3p threshold in the REMPI process. Fig. 6(a) shows the photoelectron angular distributions and PEELD recorded when only the 3s state is

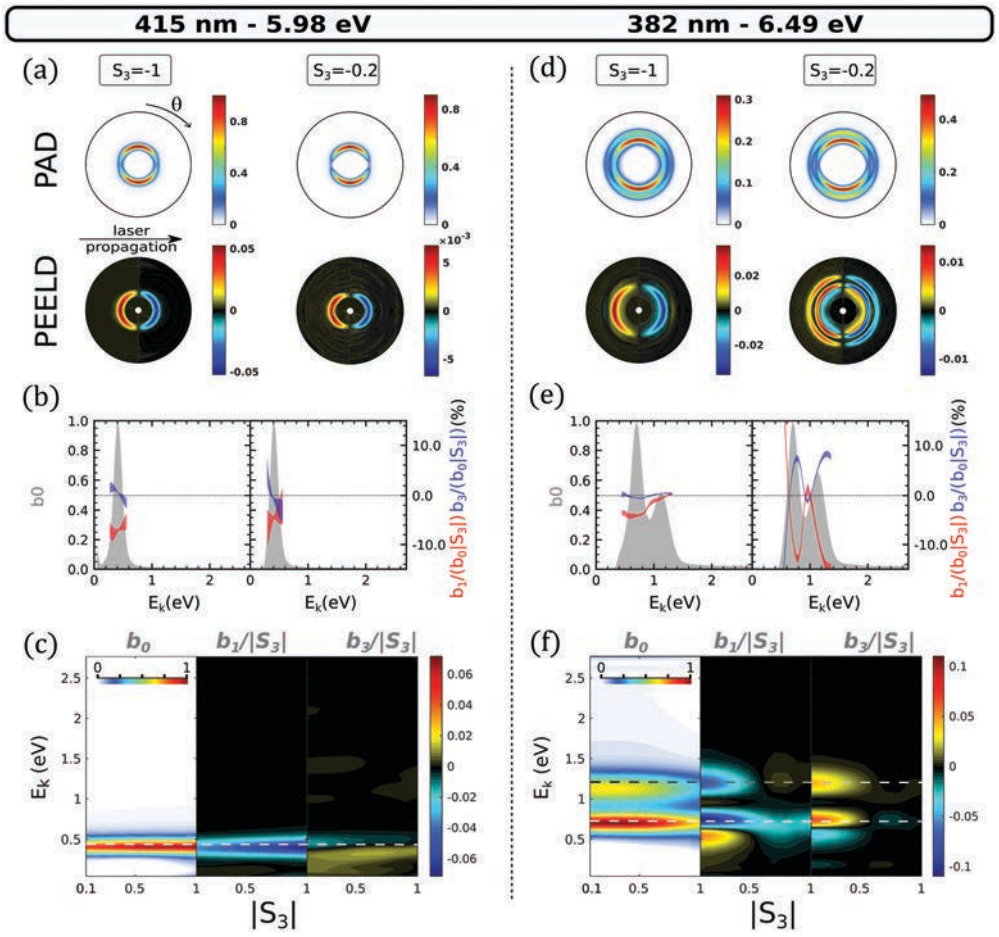

Fig. 6 2D PAD and PEELD recorded in (2 + 1) REMPI at 415 nm (a–c) and 382 nm (d–f). (a and d) Abel-inverted PAD and PEELD images recorded with $S_3 = -1$ and $S_3 = -0.2$. The PAD is normalized to its own maximum and the PEELD to the PAD maximum. (b and e) Kinetic energy distributions of the Legendre coefficients b_0 (in grey), $b_1/|S_3|$ (in red) and $b_3/|S_3|$ (blue) for these two ellipticities. The $b_{1,3}(E)/|S_3|$ coefficients are normalized to $b_0(E,|S_3|)$. (c and f) $b_i/|S_3|$ parameters as a function of $|S_3|$ and the kinetic energy. Both $b_{1,3}(E,S_3)/|S_3|$ are normalized to the maximum value of $b_0(E,|S_3|)$. $b_0(E,S_3)$ is normalized to its own maximum over all the S_3 recording. In the (c and f) panels, the horizontal lines indicate the kinetic energies expected from $E_k = \hbar\omega_0 - \text{IP}_a + E_R$ for 3s and 3p bands using the E_R binding energies listed in Table 1. The white dashed line is for 3s and the white-gray one for the 3p band.

accessible at 5.98 eV two-photon excitation energy, using circularly ($S_3 = -1$) or elliptically ($S_3 = -0.2$) polarized light. A single kinetic energy component characterizes the ionization. The angular distributions can be analyzed by plotting their decomposition onto the first Legendre polynomials (Fig. 6(b)). The analysis of the raw data includes Legendre polynomials up to 6, but we focus here on the first dominant terms $b_{0,1,3}$. To extract error bars on the $b_{1,3}$, we used a series of 6 to 21 consecutive measurements, each of them corresponding to 100 images with 1 second exposure time. We Fourier-filtered these measurements to extract the PAD and PEELD, and used pBasex[4] to extract the $b_{0,1,3}(E,|S_3|)$. We then conducted a statistical analysis of the results of the pBasex fittings, to extract 68% confidence intervals using Student's statistics. These confidence intervals are used to define the error bars in Fig. 6(b).

At that wavelength, switching the ellipticity from circular ($S_3 = -1$) to $S_3 = -0.2$ does not drastically affect the PAD and PEELD. The continuous evolution of the Legendre coefficients as a function of $|S_3|$ is shown in Fig. 6(c). The ionization yield, visible through b_0, maximizes when the ionizing pulses are circularly polarized. This is due to a favored TPA in circular polarization as shown in Fig. 2 and as already observed by Singh *et al.*[21]

With an isotropic excitation as stemmed for a s state, we expect the $b_{1,3}/|S_3|$ ratios to be constant with respect to S_3. In a previous investigation of (1 + 1′) TR-PECD in fenchone, the time-dependency of the b_3 was found to follow the decay of the anisotropy of excitation.[10] In Fig. 6(c), for a 3s excitation, $b_1/|S_3|$ maximizes slightly in circular polarization and $b_3/|S_3|$ is rather weak. This very weak $b_3/|S_3|$ observed for all S_3 values thus likely results from the very weak anisotropy of excitation to the 3s state.

As soon as the 3p state is energetically accessible, as illustrated in Fig. 6(d) for 382 nm laser wavelength, the angular distributions recorded with $S_3 = -0.2$ are characterized by a rather strong PEELD asymmetry from the 3p contribution. We further observe a splitting of the 3s asymmetry into two components of opposite sign. Both features disappear in circular polarization with a single contribution from the 3s state, leading to PECD pictures quite similar to the ones recorded at lower two-photon energy. In Fig. 6(f), the evolution of the Legendre coefficients with $|S_3|$ reveals the complexity of the underlying mechanisms which are at play in this excitation range. For instance, the photoionization yield b_0 is now stronger in linear polarization for both 3s and 3p ionization channels. This is expected from the TPA calculations for the 3p states, but not for the 3s (see Fig. 2). The asymmetry coefficients follow the same trend, also maximizing close to linear polarization. The kinetic energy splitting of the b_1(3s) coefficient in two opposite components appears as soon as $|S_3| < 0.5$, which matches the appearance of an asymmetry in the 3p band. This similarity of the S_3 dependencies of both $b_1/|S_3|$ and $b_3/|S_3|$ for the 3s and 3p channels reveals that a decay of some of the 3p sub-states into the 3s state occurs before the absorption of the third (ionizing) photon.

In an adiabatic picture, all these Rydberg states are not coupled to each other. Non-adiabatic coupling(s) are thus at play, and are sufficiently strong to get an efficient population transfer from the 3p band to the 3s state within the 70 fs pulse duration. One has to underscore that in the past, the presence of this 3p–3s NAC had not been drawn from PECD measurements but by comparing the PES(b_0) recorded with different pulse duration (ns *versus* fs).[22] Here, the PEELD maps of Fig. 6(f) shows a clear signature of such 3p–3s NAC at low $|S_3|$, which is not revealed with circularly polarized ionizing radiation.

The importance of the NAC in the experiment can be quantified by using the calculations performed by Singh *et al.*[21] They show that at 6.5 eV, the direct excitation of the 3s state induced by the absorption of linearly polarized photons is only ∼17%, due to small Franck–Condon factors. The indirect population of the 3s state through intermediate 3p states is thus of paramount importance. This indirectly populated 3s state has an anisotropy of excitation fixed then by the 3p band. On the other hand, the $3p_1$ TPA cross section is smaller than its $3p_{2,3}$ counterparts, especially when $S_3 = 0$ (see Fig. 2), so that the $3p_1$ state can be depreciated within the 3p manifold. By combining our TPA cross-sections moments with the $3p_2$ and $3p_3$ Franck–Condon profiles calculated by Singh *et al.*, we find that the $3p_2$/3p absorption ratio is ∼90% for both $|S_3| = 0$ and 1. This indicates that the $3p_2$ state should play the major role among all the 3p states. It probably monitors the indirect population of the 3s state at small $|S_3|$ through the associated $3p_2$–3s NAC coupling. Meanwhile the $3s/3p_2$ TPA ratio is ∼17% in linear polarization and increases to ∼42% in the case of circular radiation. The relative weight of direct and indirect 3s population pathways thus significantly varies with $|S_3|$, which explains the variations of $b_1/|S_3|$ and $b_3/|S_3|$ associated to the 3s state around $|S_3| = 0.5$ in Fig. 6(f). These asymmetry patterns are stronger at small $|S_3|$, where the indirect pathway is dominant and involves an intermediate 3p state whose anisotropy of excitation enhances the asymmetry.

Importantly, the variation of the 3s-state population with $|S_3|$ clearly depends on the occurrence of 3p–3s NAC: we can expect that ionisation taking place from the 3s channel involves two different vibrational wavepackets, one created from a direct TPA to the 3s dominant at large $|S_3|$ and another one created by the ultrafast NAC from the 3p band dominant at low $|S_3|$. The different vibrational content of the 3s-wavepacket has been very recently investigated in the ps-REMPI-PECD.[24] On that ps timescale proper to a more complete vibrational relaxation, the photoelectrons breaking the $\Delta v = 0$ propensity rule of photoionization show a reversed PECD compared to the ones fulfiling it. The possible eventual interference between these two vibrational wavepackets could explain the feature observed on $b_1/|S_3|$ around $|S_3| = 0.7$ in Fig. 6(f). This opens the door to femtochemistry with elliptical fields, aiming at picturing the role and dynamics of NAC.

The signal recorded at 6.7 eV excitation energy is shown in Fig. 7(a–c). It is very similar to the one obtained at 6.49 eV (Fig. 6(d–f)), apart from a slightly stronger b_0 contribution in the 3p ionization channel and a splitting of its b_3 parameter. This shows that the kinetic energy of the ejected electrons does

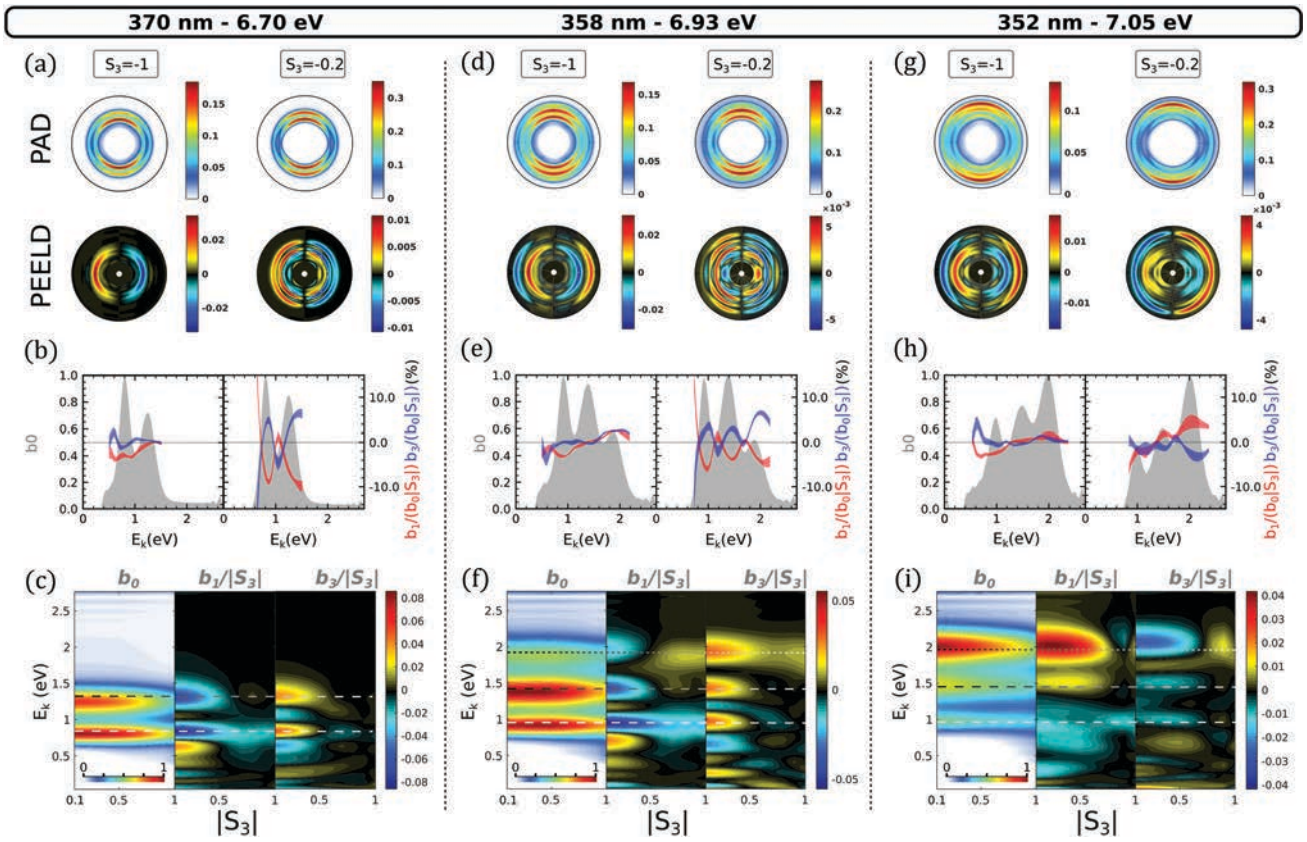

Fig. 7 Same as Fig. 6 but for two-photon excitation energies reaching the 3d band. A (2 + 1) REMPI at (a-c) 370 nm, (d-f) 358 nm, (g-i) 352 nm. In the (c, f and i) panels, the horizontal lines indicate the kinetic energy expected from $E_k = \hbar\omega - IP_a + E_R$ for 3s, 3p and 3d bands using the E_R binding energies listed in Table 1. The white dashed line is for 3s state, the white-gray one for the 3p band and the dot white-gray line for the 3d band.

not significantly affect the PECD and PEELD in this excitation range.

4.3 Reaching the 3d excitation threshold

The second transition focuses on the appearance of the 3d states in the photoelectron spectrum. When the excitation energy reaches 6.93 eV, an additional photoelectron peak appears around 1.9 eV kinetic energy. We assign this third contribution to the 3d Rydberg band since its kinetic energy follows nicely the $\Delta v = 0$ propensity rule shown in Fig. 4. Its E_R = 6.93 eV is also in agreement with the (2 + 1)-fs-REMPI spectra recorded by Kastner *et al.* The signal from this peak slightly increases as $|S_3|$ increases from 0 to 0.5 as shown in Fig. 8, before slightly decaying. This is consistent with our TPA calculations (Fig. 2): the only 3d substate whose population maximizes in circular polarization is $3d_1$ which also presents the lowest E_R. We thus assign this peak to this sub-state.

In circular polarization, the 3d peak shows weak positive b_1 and b_3 asymmetry parameters. At $S_3 = -0.2$, b_1 is negative, reaching a value of $b_1/|S_3| \sim -5\%$, while b_3 remains positive. The PEELD map shown on Fig. 7(f) reveals that the sign change in b_1 occurs around $|S_3| = 0.5$ for the $3d_1$ state and is associated with a slight shift in kinetic energy. The two lower photoelectron components, associated to the 3s and 3p ionization channels, show asymmetry parameters which behave as a function of $|S_3|$ similarly as at lower excitation energy. The only change that is observed concerns the 3s/3p branching ratio in the PES(b_0) which does not vary as drastically as before as a function of $|S_3|$. These results demonstrate that the 3p and 3s channels are not significantly affected by the population of $3d_1$ state. This suggests that no NAC from the $3d_1$ to the 3s or 3p

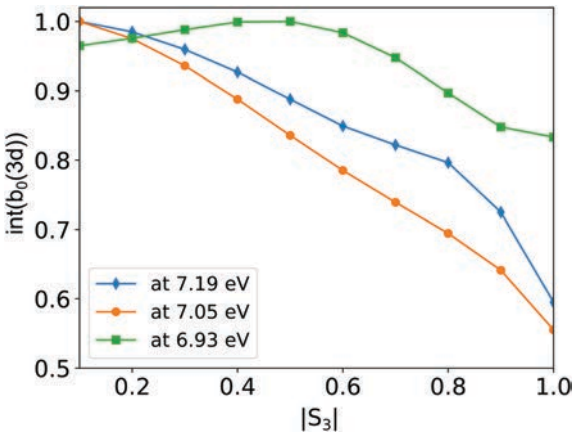

Fig. 8 The PES is fitted by three Gaussian in order to extract the electron yield in the 3d channel as a function of $|S_3|$, for different two-photon excitation energies. For each energy, the electron yield is normalized to its own maximum.

bands takes place in this energy range over the 70 fs timescale of the experiment.

4.4 Excitation above the 3d threshold

As the excitation energy increases to 7.05 eV (352 nm pulses, Fig. 7(g–i)), which represents only a 120 meV increase with respect to the case of Fig. 7(d–f), the photoelectron spectrum drastically changes, showing an inversion of the excited state balance. The 3s channel becomes the weakest band while the 3d one dominates, especially at low $|S_3|$ (Fig. 7(h)). Interestingly, the ellipticity dependence of the PES also changes across this transition: while it was maximizing with $S_3 = 0.5$ at 6.93 eV, the signal is maximum in linear polarization at 7.05 eV as shown in Fig. 8. This behavior is consistent with our TPA calculations, where the absorption to the $3d_2$ state, predicted about 100 meV above the $3d_1$ state, becomes very strong in linear polarization (Fig. 2(c)). We thus propose that the $3d_1$ state is populated at 6.93 eV, while the $3d_2$ state is reached at 7.05 eV and dominates the absorption, in particular close to linear polarization.

At 7.05 eV two-photon energy, the PEELD maps are dominated by the 3d contribution (Fig. 7(i)). Interestingly, for this component we observe a sign inversion of b_1 and b_3 at low $|S_3|$ compared to the 6.93 eV excitation case. This inversion is also present for the signal originating from the 3p. The transition along $|S_3|$ now occurs beyond $|S_3| = 0.7$ for the three ionization channels. This behavior suggests that while the $3d_1$ state was showing no sign of non-adiabatic coupling to 3s and 3p, the $3d_2$ state is significantly coupled to the 3p band.

As the excitation energy further increases, higher 3d states can be reached. The measurements show that exciting at 7.19 eV (343 nm pulses) does not significantly modify the ratio between the different components of the photoelectron spectrum, but strongly affects the chiroptical response, as shown in Fig. 9(f and i). The asymmetry is drastically lower (6×10^{-3} *versus* 4×10^{-2}) and does not show any clear transitions as a function of S_3. We attribute this effect to the simultaneous excitation of the different 3d states, whose dichroisms could cancel each other. The PEELD from the 3p band almost completely vanishes at all $|S_3|$, while the 3s band shows an almost constant, pure b_1 contribution. This raises the question of the origin of this 3s band. Indeed, at such high excitation energy, direct excitation to the 3s and 3p is extremely unlikely.

We have identified at lower excitation energies the $3d_2 \rightarrow 3p$ and $3p_2 \rightarrow 3s$ NACs. Therefore, the $3d \rightarrow 3p \rightarrow 3s$ NAC cascade is a highly probable route to 3s population at high excitation energies. On the other hand, transitions from the 3d states to the excited $\sigma \rightarrow \pi^*$ valence should also operate in this high energy range – Pulm *et al.*[17] have demonstrated that this valence state efficiently mix with the 3d band. Internal conversion from this valence state to the 3s state, mediated by NACs,

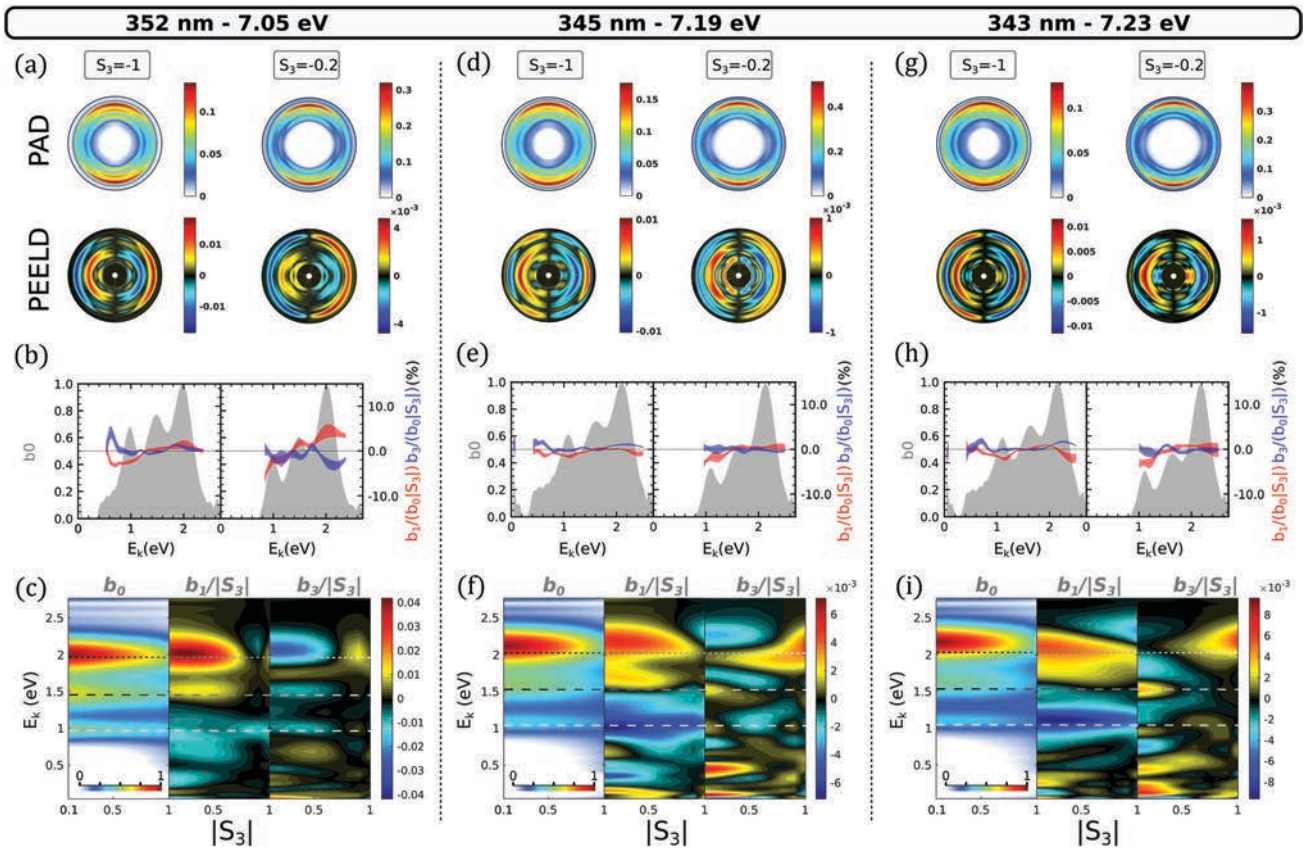

Fig. 9 Same as Fig. 6 for two-photon excitation energies within the 3d band.

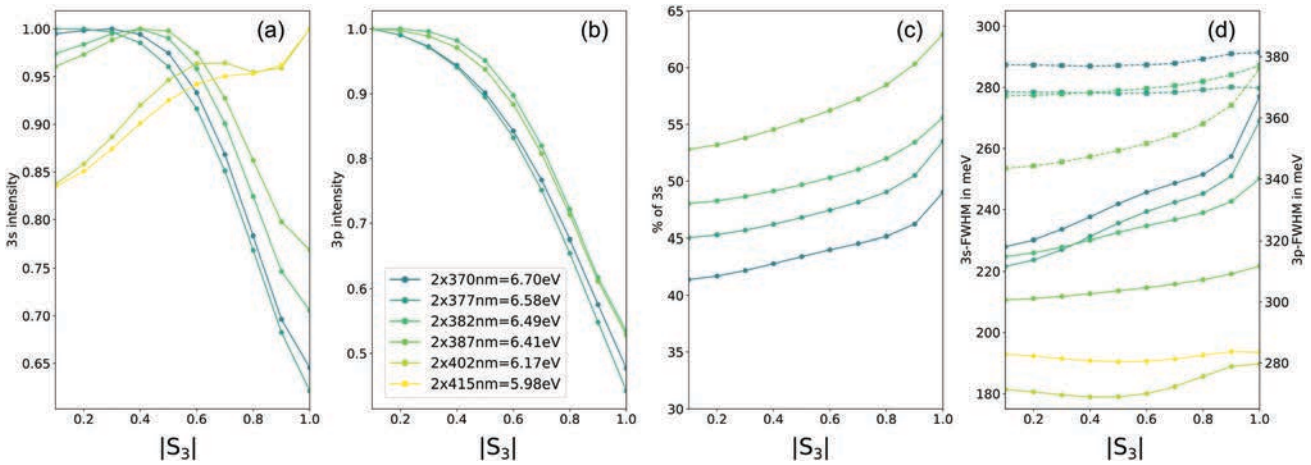

Fig. 10 The PES(b_0) has been fitted by a sum of Gaussians for each $|S_3|$ and wavelength to monitor at which $|S_3|$ the electron yield of (a) the 3s channel maximizes, (b) the 3p channel, or (c) the percentage of the 3s/(3s + 3p) in the PES, as well as (d) Bandwidths of 3s-mediated (full lines, left scale) and 3p-mediated (dashed lines, right scale) of these photoelectron bands.

could also contribute to the present observations. Disentangling the contributions of each initial state and subsequent dynamics is difficult in this dense energy range and requires further experimental measurements with high resolution.

4.5 Usefulness of a continuously varied $|S_3|$ for fs-REMPI with $M \geq 2$

Beyond the investigation of excitation and relaxation in chiral molecules, we think that a measured photoelectron spectra as a function of the ellipticity of the light as done in the present experiment could alleviate many of the challenges faced when several electronic states enter in the wavepacket composition created by the pump pulse. Indeed varying $|S_3|$ in a $M \geq 2$ pump transition allows to vary the electronic content of the wavepacket, providing an additional easy way to test *ab initio* simulations of TR-PES and its consecutive assignments of specific spectral-temporal features. Fig. 10 that shows the variation of the PES(b_0)-an achiral observable- as a function of the excitation energy in the 3s–3p range illustrates this point. The PES have been fitted by several Gaussian functions to extract the $|S_3|$ dependency of each channel as well as their bandwidth variation. The impact of the TPA dependency with $|S_3|$ for the 3p channel is apparent on Fig. 10(b), while the one for a direct excitation of the 3s is only visible for an excitation taking place below 6.4 eV (Fig. 10(a)). At higher energy, the $|S_3|$ dependency of the 3s channel reveals again the 3p–3s NAC at play. As the excitation energy increases, the 3s contribution shown in Fig. 10(c) is clearly decreasing, showing that the 3p–3s NAC efficiency is energy dependent. The NAC impact is also apparent on the bandwidth of the 3s that is more dependent on $|S_3|$ once the 3p band is resonant. In a more general context than chirality, Fig. 10 as well as Fig. 8 illustrate both how a $|S_3|$ continuous variation with Fourier-filtering could be used as an additional dimensionality in time-resolved photoelectron imaging used usually in femtochemistry. This constitutes a continuous and enriched version of the circular-linear dichroism, whose interest was recently pointed out by Singh *et al.*[21]

5 Conclusions

Using elliptically polarized laser pulses in resonance-enhanced multiphoton ionization enables modifying the anisotropy of excitation as well as the multiphoton absorption probabilities. Scanning the ellipticity thus considerably enriches the photoelectron spectroscopy. By revisiting the (2 + 1)-REMPI of fenchone molecules, we have shown that PEELD provides a higher sensitivity, revealing states that were almost dark in PECD signals. We have confirmed through the wealth of PEELD information that the 3s and 3p Rydberg states are strongly dynamically coupled, which results in the appearance of a second component of the 3s band in the photoelectron asymmetry. This effect could not be revealed in circularly polarized light. Several estimates of the duration of this process come from previous high-resolution work. We have taken a step further by experimentally reducing the upper bound of the time scale over which the non-adiabatic coupling takes place – it occurs in less than 70 fs. In the 3d band, the PEELD technique allowed us to highlight the role of different intermediate states in the asymmetry separated by only 120 meV. The forward/backward asymmetry in the electrons ejected through the $3d_1$ and $3d_2$ states are of opposite signs in elliptically polarized light, while they are of the same sign in circularly polarized light. Higher excitation of the 3d states leads to more complex relaxation dynamics, which cannot be safely assigned using the current results. Extending this study to higher photon energy could help us to better understand which states and couplings are involved. Performing time-resolved PEELD would provide a complete picture of the relaxation process. The use of high repetition rate Yb-based laser systems makes this goal achievable in a reasonable

acquisition times. We thus believe that TR-PEELD could become a standard pump–probe technique to investigate chiral femtochemistry.

Conflicts of interest

There are no conflicts to declare.

Acknowledgements

We acknowledge Florent Guichard – Amplitude et Marcus Buetler – APE Angewandte Physik & Elektronik GmbH for experimental assistance, and Rodrigue Bouillaud, Nikita Fedorov and Laurent Merzeau for technical assistance. This project has received funding from the European Research Council (ERC) under the European Union's Horizon 2020 research and innovation program no. 682978 – EXCITERS and from 871124 – Laserlab-Europe. We acknowledge the financial support of the Région Nouvelle Aquitaine (RECHIRAM).

Notes and references

1 B. Ritchie, *Phys. Rev. A: At., Mol., Opt. Phys.*, 1976, **13**, 1411–1415.
2 I. Powis, *J. Chem. Phys.*, 2000, **112**, 301–310.
3 N. Böwering, T. Lischke, B. Schmidtke, N. Müller, T. Khalil and U. Heinzmann, *Phys. Rev. Lett.*, 2001, **86**, 1187–1190.
4 G. A. Garcia, L. Nahon, M. Lebech, J.-C. Houver, D. Dowek and I. Powis, *J. Chem. Phys.*, 2003, **119**, 8781–8784.
5 U. Hergenhahn, E. E. Rennie, O. Kugeler, S. Marburger, T. Lischke, I. Powis and G. Garcia, *J. Chem. Phys.*, 2004, **120**, 4553–4556.
6 L. Nahon, G. A. Garcia and I. Powis, *J. Electron Spectrosc. Relat. Phenom.*, 2015, **204**, 322–334.
7 C. S. Lehmann, N. B. Ram, I. Powis and M. H. M. Janssen, *J. Chem. Phys.*, 2013, **139**, 234307.
8 C. Lux, M. Wollenhaupt, C. Sarpe and T. Baumert, *ChemPhysChem*, 2014, **16**, 115–137.
9 S. Beaulieu, A. Comby, B. Fabre, D. Descamps, A. Ferré, G. Garcia, R. Géneaux, F. Légaré, L. Nahon, S. Petit, T. Ruchon, B. Pons, V. Blanchet and Y. Mairesse, *Faraday Discuss.*, 2016, **194**, 325–348.
10 A. Comby, S. Beaulieu, M. Boggio-Pasqua, D. Descamps, F. Légaré, L. Nahon, S. Petit, B. Pons, B. Fabre, Y. Mairesse and V. Blanchet, *J. Phys. Chem. Lett.*, 2016, **7**, 4514–4519.
11 V. Blanchet, D. Descamps, Y. Petit, S. Mairesse, B. Pons and B. Fabre, *Phys. Chem. Chem. Phys.*, 2021, **23**, 25612–25628.
12 C. Lux, M. Wollenhaupt, C. Sarpe and T. Baumert, *ChemPhysChem*, 2015, **16**, 115–137.
13 R. E. Goetz, C. P. Koch and L. Greenman, *Phys. Rev. Lett.*, 2019, **122**, 013204.
14 J. Miles, D. Fernandes, A. Young, C. Bond, S. Crane, O. Ghafur, D. Townsend, J. Sá and J. Greenwood, *Anal. Chim. Acta*, 2017, **984**, 134–139.
15 A. Comby, E. Bloch, C. M. M. Bond, D. Descamps, J. Miles, S. Petit, S. Rozen, J. B. Greenwood, V. Blanchet and Y. Mairesse, *Nat. Commun.*, 2018, **9**, 5212.
16 A. Comby, C. M. Bond, E. Bloch, D. Descamps, B. Fabre, S. Petit, Y. Mairesse, J. B. Greenwood and V. Blanchet, *Chirality*, 2020, **32**, 1225–1233.
17 F. Pulm, J. Schramm, J. Hormes, S. Grimme and S. D. Peyerimhoff, *Chem. Phys.*, 1997, **224**, 143–155.
18 T. H. Dunning, *J. Chem. Phys.*, 1989, **90**, 1007–1023.
19 R. A. Kendall, T. H. Dunning and R. J. Harrison, *J. Chem. Phys.*, 1992, **96**, 6796–6806.
20 D. E. Woon and T. H. Dunning, *J. Chem. Phys.*, 1994, **100**, 2975–2988.
21 D. P. Singh, N. De Oliveira, G. A. Garcia, A. Vredenborg and I. Powis, *ChemPhysChem*, 2020, **21**, 2468–2483.
22 A. Kastner, G. Koumarianou, P. Glodic, P. C. Samartzis, N. Ladda, S. T. Ranecky, T. Ring, S. Vasudevan, C. Witte, H. Braun, H.-G. Lee, A. Senftleben, R. Berger, G. B. Park, T. Schäfer and T. Baumert, *Phys. Chem. Chem. Phys.*, 2020, **22**, 7404–7411.
23 A. Kastner, T. Ring, B. C. Krüger, G. B. Park, T. Schäfer, A. Senftleben and T. Baumert, *J. Chem. Phys.*, 2017, **147**, 013926.
24 D. P. Singh, J. O. F. Thompson, K. L. Reid and I. Powis, *J. Phys. Chem. Lett.*, 2021, 11438–11443.
25 E. Runge and E. K. U. Gross, *Phys. Rev. Lett.*, 1984, **52**, 997–1000.
26 T. Yanai, D. P. Tew and N. C. Handy, *Chem. Phys. Lett.*, 2004, **393**, 51–57.
27 A. Kastner, T. Ring, H. Braun, A. Senftleben and T. Baumert, *ChemPhysChem*, 2019, **20**, 1–5.
28 G. A. Garcia, L. Nahon and I. Powis, *Rev. Sci. Instrum.*, 2004, **75**, 4989–4996.
29 H. Ganjitabar, G. A. Garcia, L. Nahon and I. Powis, *J. Chem. Phys.*, 2020, **153**, 034302.
30 L. Nahon, G. A. Garcia, C. J. Harding, E. Mikajlo and I. Powis, *J. Chem. Phys.*, 2006, **125**, 114309.
31 C. Lux, M. Wollenhaupt, T. Bolze, Q. Liang, J. Köhler, C. Sarpe and T. Baumert, *Angew. Chem., Int. Ed.*, 2012, **51**, 5001–5005.

IV PhotoElectron Elliptical Dichroism in Methyl Lactate

Most PECD and PEELD studies on chiral molecules have been done on Fenchone [Comby 18] [Beauvarlet 22], Camphor [Comby 18], Limonene [Comby 18], Methy-Oxirane. Similar studies on the PECD of terpenes (carene, α-Pinene, etc.), as they are rigid molecules without any distribution of conformers and high volatility, have also been performed [Singh] [Ganjitabar 21] [Ganjitabar 18b]. Now the question arises that how is the PECD or PEELD gets affected or the mechanisms involved in the way chiral molecules interact with each other. Thus a time-resolved photodissociation of homodimers and heterodimers of chiral molecules becomes interesting to observe and study the mechanisms involved. To simplify the problem at hand we start with homodimers. Where for an efficient creation of homodimers of chiral molecules with a high permanent dipole must be used. For this reason we start to investigate Methyl-Lactate ($C_4H_8O_3$), which has a permanent dipole moment as high as 3 Debye and a capacity to create a variety of H-bonded network through its flexibility [Hong 18] [Schrøder 15].

IV. 1 Absorption Spectra and Power Scaling Law

Since no literature was found on Methyl-Lactate the energy levels of the molecules have to be determined experimentally. We asked our colleague Nelson De Oliveira from Synchrotron Soleil to measure the absorption spectrum of these molecules. The absorption spectra was recorded in gas phase by VUV-Fourier Transform absorption [De Oliveira 11], in the range of 6 eV to 11 eV at 1 mbar pressure and a photon resolution of 0.45 meV. The results are shown in Fig. 3.9. It is observed that there are three main humps in the spectrum at $\sim$ 8.3 eV, $\sim$ 9 and a broad hump around 10 eV, where the absorption around 10 eV is 2 times larger than that at $\sim$ 8.3 eV and $\sim$ 9 eV.

Although the absorption spectrum is a result of a one-photon process and thus cannot be used quantitatively to describe the dynamics in a multiphoton process but it still provides a wealth of valuable information. Firstly, it gives us with the position of the broad level of energy manifolds present in the molecule. Secondly it can be used to calibrate and asses the reliability of the theoretical simulations of the underlying states. We also see tiny regularly spaced contributions from 8 eV to above correspond to the vibrational levels of the $A1\Pi \leftarrow X1\sum$ transition in CO molecules produces during the gas phase expansion of ML in the cell.

The next step required to study molecules in the multiphoton regime is to identify the resonances at play in the multiphoton ionization. To determine it experimentally we measure the photoelectron yield S as a function of the laser intensity I. In a non-resonant regime the photoelectron yield is given as $S \propto I^n$, where $n \in \mathbb{R}^+$ and is the number of photons required for ionization. However if there are intermediate resonances involved the photoelectron yield can be expressed as:

$$S = \sum_{m=1}^{n} A_m I^m \tag{3.9}$$

where weight of the integer polynomial orders A_m are to be determined. Equn. 3.9 is used to fit the photoelectron yield of Methyl-Lactate. It is important to note that the equation is valid

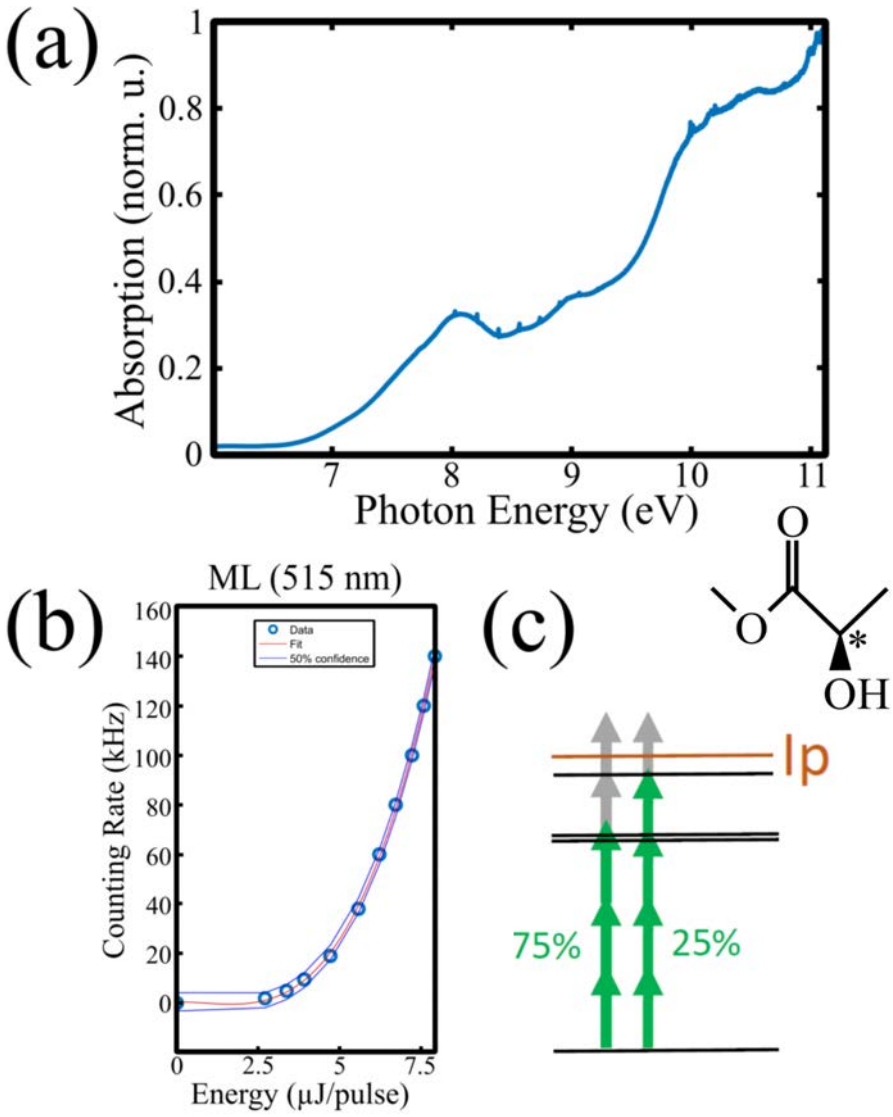

Figure 3.9 – *(a) Absorption spectra recorded for Methyl-Lactate between 6-11 eV at synchrotron SOLEIL on the VUV-Fourier Transform beamline. (b) Shows the power scaling law fit at 515 nm. The experimental data, is recorded using a COLTRIMS and a 500 kHz repetition rate laser with a counting rate of the photoelectrons as a function of the energy per pulse as shown in circles, the fit is shown in red and the 50% confidence interval is shown in blue. (c) Shows the resonant contributions during multiphoton ionization of Methyl-Lactate by a 125 fs pulse centered at 515 nm.*

only for ionization below the saturation. The photoelectron yield, is measured in COLTRIMS, as a function of laser energy and a laser wavelength of 515 nm is shown in Fig. 3.9 (b). The experimentally measured data is shown in blue circles, the red solid line is the fit which is bounded by a 50% confidence interval. The power scaling law indicates a decomposition into two processes: a 3+2 ionization and a 4+1 ionization. This enables us to conclude that the intermediate states involved lie at 7.2 eV ($\sim$ 75%) and 9.2 eV ($\sim$ 25%) just below the ionization threshold (see Fig. 3.9 (c)).

IV. 2 Lock in Detection

In order to measure the PEELD one has to record several sets of the photoelectron angular distributions for opposite ellipticities and for multiple polarizations. Although the method is straightforward to perform, it is cumbersome and is exposed to various fluctuations and drifts, like the laser intensity, alignment, target density, etc. Thus, to mitigate the effects of such fluctuations, several measurements have to be carried out and average the results. This makes the overall acquisition very cumbersome, slow and prone to artifacts resulting from fluctuations.

In order to overcome such fluctuations while at the same time performing fast data acquisition, we use a lock-in detection scheme. In this scheme the ellipticity of the incident electromagnetic radiation is varied continuously by rotating a quarter-wave plate at a fixed angular velocity. This results in a periodic and continuous modulation of the third Stokes parameter (S3) of the second harmonic of the laser. The corresponding photoelectron angular distribution is recorded in a velocity map imaging spectrometer using a camera with no deadtime.

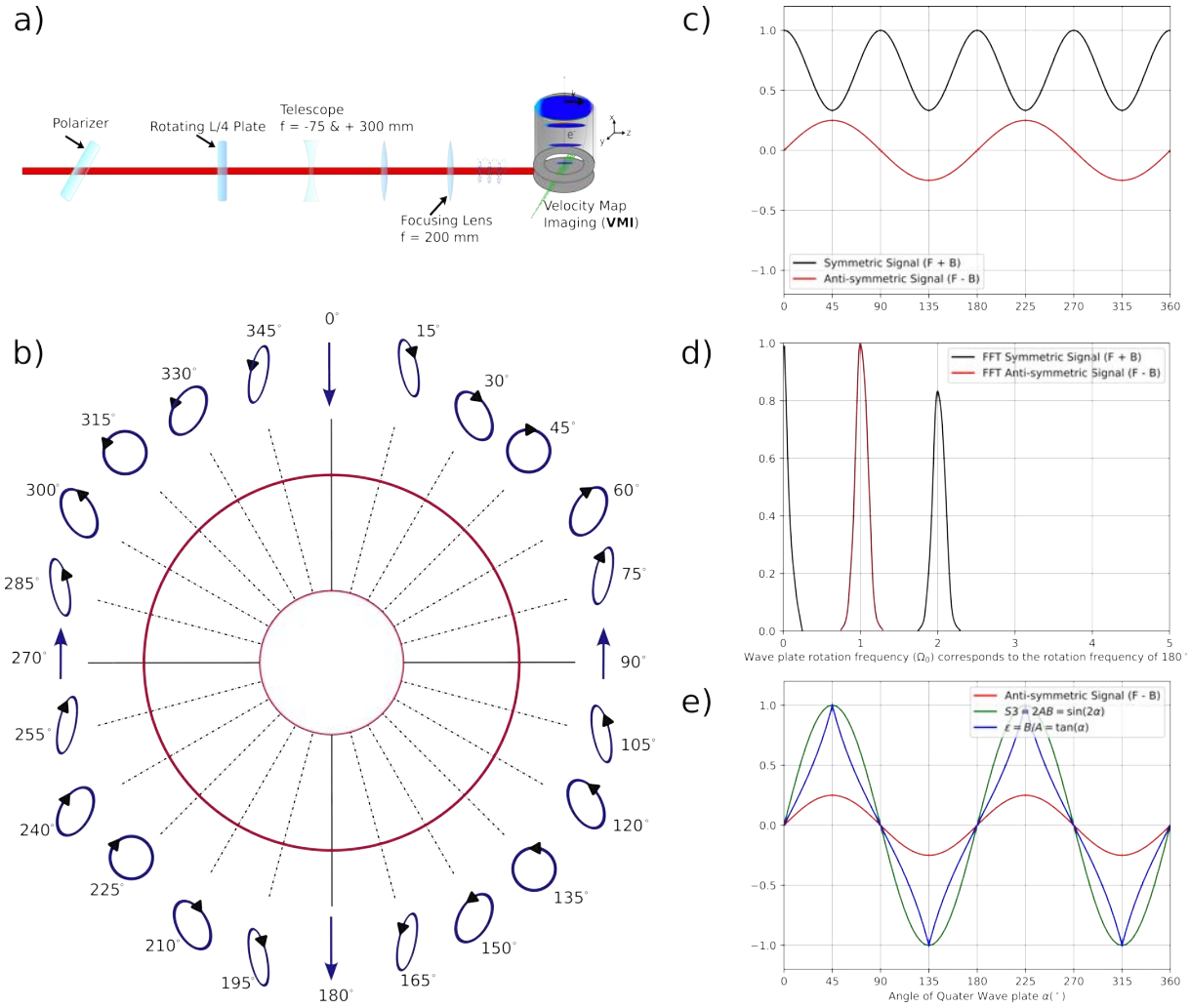

Figure 3.10 – *(a) Shows the schematics of the setup to measure the PEELD using the lock-in detection method. (b) Evolution of the ellipticity as a function of the quarter-wave plate. (c) Evolution of the total photoelectron yield (shown in black) and the dichroism (shown in red) as a function of the QWP angle. (d) Corresponding Fourier domain spectra. (e) Evolution of the third Stoke's parameter and the ellipticity of the laser beam as a function of the QWP angle*

The experimental setup, to realize such a lock-in detection mechanism to measure PEELD, is shown in Fig. 3.10 (a). The fundamental laser (50W, 1030 nm and beam size of 1.3 mm at $I_{max}/\exp^2$) is frequency doubled in a 1mm thick β-barium borate (BBO) crystal ($\theta = 23.4°, \phi = 90°$) to obtain a 515 nm average power up to 19 W (38% conversion efficiency, ~ 0.9 mm radius at $I_{max}/\exp^2$, and a pulse duration 130 fs FWHM). The second harmonic produced is then isolated from the fundamental laser beam using two dichroic mirrors. For more details on second harmonics generation setup see Sec. I. 2. A thin film polarizer is used to clean any polarization artifacts present in the laser. The laser beam is then incident on a continuously rotating quarter-wave plate. The quarter-wave plate used to modulate the polarization is mounted on a fast direct-drive rotation stage capable of a rotation speed of up to 720 °/s (RGV100BL, Newport). The beam is expanded using $-75/+300$ mm $\times 4$ telescope. The expanded beam is then focused into into the VMI using a focusing lens of focal length f= +200 mm, reaching an intensity of about 1×10^{13} W/cm^2. The photoelectron angular distribution is recorded using a SCMOS camera (without any deadtime between two consecutive images) coupled with a velocity map imaging spectrometer. The camera is triggered by the rotation stage such that the initial phase is known and is the same for all consecutive scans. The exposure time of the camera is set to 50 ms per image and 3000 images are recorded. The quarter-wave plate is rotated at an angular speed of 45 °/sec. The symmetric part of the photoelectron angular distribution evolves with a periodicity of 90° with a time period of 2 sec and is described by 40 images (see Fig 3.10 (c)). While the full periodicity of the asymmetry is 180° with a time period of 4 sec and is described by 80 images, where each image is averaged over 2.25°, on which the PEELD doesn't evolve too rapidly, of the quarter-wave plate angle (see Fig 3.10 (c)). This is good enough for performing a fast Fourier transform.

The temporal evolution of the polarization state is given in Fig. 3.10. On rotating a quarter-wave plate the polarization state of the resultant laser beam goes from linearly polarized to next linearly polarized one with a rotation of 90° of the quarter-wave plate. Thus the symmetric part of the signal should evolves with a period of 90° and in the frequency domain with a frequency of $2\Omega_0$ (see Fig. 3.10 (d) (shown in black)). It also takes a 90° rotation of the quarter-wave plate to go from a circularly polarized light of one helicity to that of the other. Thus the asymmetry of the 2-D photoelectron distribution oscillates with a period of 180° and in the frequency domain with a frequency of Ω_0 (see Fig. 3.10 (d) (shown in red)). The evolution of the ellipticity and the third Stokes' parameter of the laser is shown in Fig. 3.10 (e).

It is important to note that with the rotation of the quarter-wave plate the polarization ellipse gets tilted (see Fig. 3.10 (b)). This lead to the projection angle relatively to the ellipse varies with the ellipticity. This issue can be avoided completely by using a fixed quarter-wave plate in front of a continuously rotating half-wave plate (see Chapter 4 Section III). However, this rotation of the polarization ellipse with ellipticity is almost inconsequential to the measurements in the multiphoton ionization regime. This is so because, the VMI records the 2-D projections of the 3-D photoelectron angular distributions and is thus insensitive to the momentum component along the spectrometer axis (p_x). The only effect is in the slight displacement of the features along p_y.

In the following section, we show how the Fourier analysis of the measured signal enables

filtering out the experimental fluctuations and providing a noise free signal.

IV. 3 Results & Discussions

Measurement of G-Function

To measure the continuous evolution of the PEELD we first reduce the dimensionality of the measurements conducted. The 2-D VMI photoelectron angular distribution, $\mathcal{P}(p_z, p_y, t) = \int \mathcal{P}(p_z, p_y, p_x, t)dp_x$, recorded is summed over in both p_z and p_y, for each image, mathematically expressed as:

$$S(t) = \int \mathcal{P}(p_z, p_y, p_x, t)dp_x dp_y dp_z \tag{3.10}$$

Where the $\hat{\mathbf{x}}$ is the VMI axis, $x - y$ is the polarization plane as shown in Fig. 3.10 and $\hat{\mathbf{z}}$ is the light propagation direction along which the photoelectron asymmetry appears.

The resultant is the photoelectron yield as a function of the quarter-wave plate angle or the ellipticity. A fast-Fourier Transform is performed on this 1-D photoelectron yield as a function of the continuously modulating quarter-wave angle. The resultant 1-D Fourier spectrum is shown in Fig. 3.11 (a) in green. We see that the photoelectron yield evolves with a frequency of $2\Omega_0$.

To calculate the evolution of photoelectron asymmetry as a function of the quarter-wave plate angle we Equn. 3.8. The asymmetry factor $G(t)$, defined in Eqn. 3.8, is determined for every image. To remove artifacts introduced in the 2-D photoelectron angular distribution, due to spatial inhomogeneity of the detector or imaging artifacts in the VMI, the calculated G for a given helicity is subtracted from that of the opposite helicity. Thus the G-function is expressed as:

$$G(t) = \frac{1}{2}\Big(G(t) - G(t + T_0/2)\Big) \tag{3.11}$$

where $T_0/2$ is the time taken for a 90° rotation of the quarter waveplate. The measured $G(t)$ for (-)-Methyl Lactate is plotted as a function of the quarter-wave plate angle in red and the photoelectron yield in green (see Fig. 3.11 (a)). A fast-Fourier Transform is performed $\mathcal{F}|G(t)| = G(\Omega)$. The $G(\Omega)$ is shown in Fig. 3.11 (a) in red. We see that the g-function of Methyl-Lactate oscillates at Ω_0, $3\Omega_0$ and $5\Omega_0$. The dichroic signal oscillates at odd multiples of Ω_0 and this arises from the fact that the helicity of the light changes with a period of $T_0 = 1/\Omega_0$. The presence of multiple harmonics in the spectrum of G reflect a non-sinusoidal evolution with the wave plate angle, i.e a non-linear and non-monotonic evolution of the dichroism with S3; as already observed in Fencone, Camphor and Limonene (see Fig. 3.7) [Comby 18]. The amplitude of the frequency components keeps decreasing with an increase in the frequency. We see that $A_{\Omega_0}/A_{3\Omega_0} \approx 3$ and $A_{\Omega_0}/A_{5\Omega_0} \approx 12$, where $A_{i\Omega_0}$ is the amplitude of the i^{th} frequency component. On the other hand we see that the photoelectron signal oscillates at only $2\Omega_0$ (see Fig. 3.11 (b)).

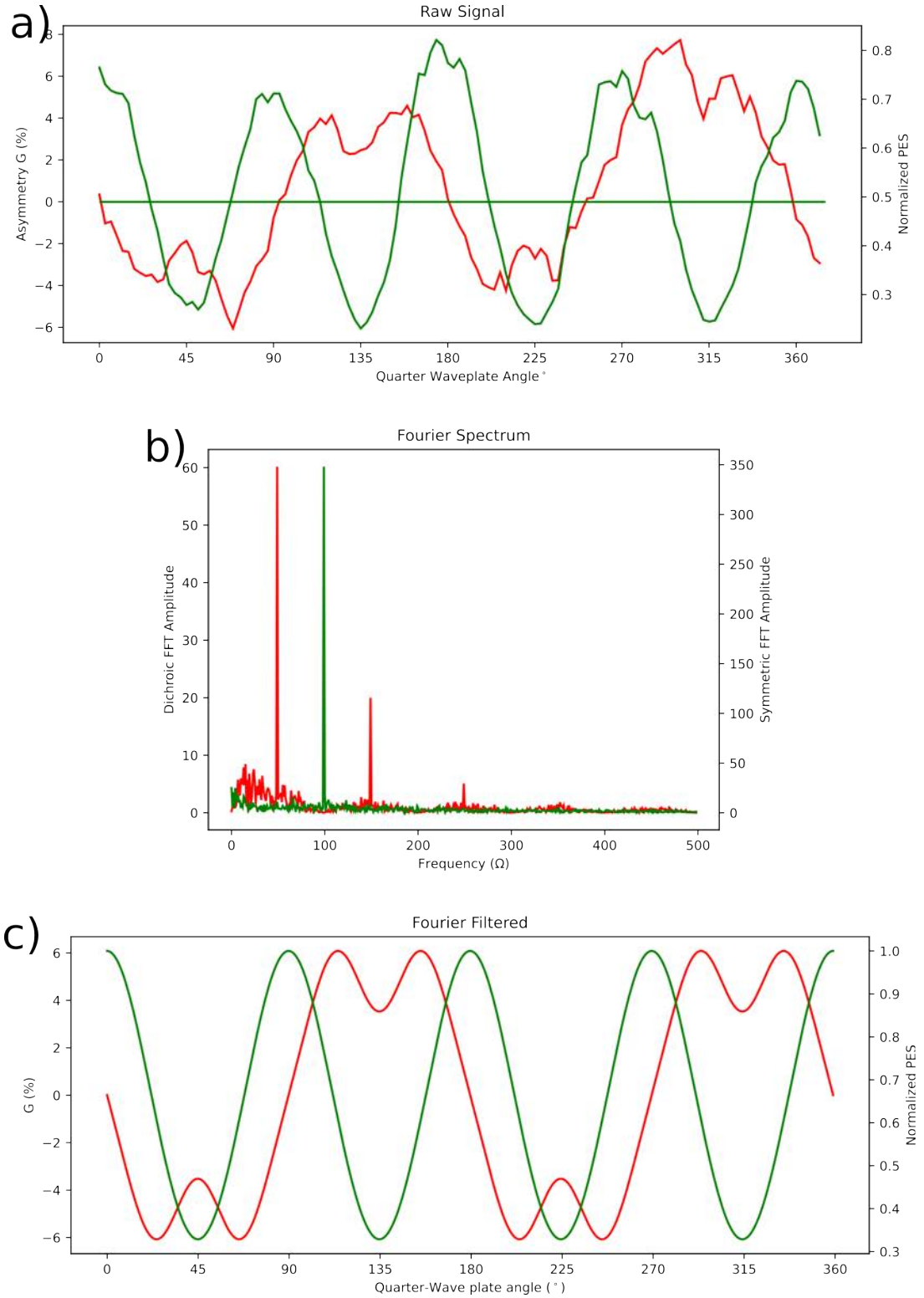

Figure 3.11 – *(a) Evolution of the measured G-Function (shown in red) and photoelectron yield (shown in green) as a function of the quarter-wave plate angle for Methyl-Lactate. The data is shown for one full rotation of the quarter waveplate. 18.75 consecutive rotations were recorded for this scan, corresponding to a total of 3000 photoelectron images. (b) The 1-D Fourier spectrum, performed on 3000 images, of the symmetric (shown in green) and the asymmetric part (shown in red) of the PAD recorded for Methyl-Lactate. (c) The Fourier reconstructed G-Function (shown in red) and photoelectron yield (shown in green) as a function of the quarter-wave plate angle for Methyl-Lactate.*

The relative phase and the amplitude of the frequency components of the dichroic signal is enantio-specific and molecular sensitive [Boesl 13] [Comby 18]. Since G is a normalized quantity, the absolute amplitude of the oscillating frequencies is proportional to the enantiomeric excess. The enantiomeric excess in a unknown sample, ee, can be calculated using a known sample with an ee_{ref} and is expressed as:

$$ee = \pm \frac{|G(3\Omega_0)|}{|G_{ref}(3\Omega_0)|} ee_{ref} \tag{3.12}$$

where the $\pm$ is given by the phase of $G(3\Omega_0)$.

The Fourier analysis conducted here can be used to retrieve the noise-free evolution of the G-function. This is done by reconstructing the oscillation of G(t) from the amplitude and phases of the Fourier peaks using discrete inverse Fourier Transform. Figure 3.11 (c) shows the reconstructed G as a function of quater-wave plate angle in red and the photoelectron yield in green. As it was observed previously in other molecules, we find that the asymmetry does not scale linearly with S3. Upon comparison of the raw G-function measured (see Fig. 3.11 (a)) and the Fourier filtered (see Fig. 3.11 (c)) we also see that Fourier filtering helps in acquiring a noise free G-function along with the photoelectron yield as a function of S3 or the quarter-wave plate angle.

From the reconstructed photoelectron yield we see that it maximizes for linear polarization and minimizes for circular. This is due to the fact that the intensity at the focus for circular polarization is less by a factor of $\sqrt{2}$ compared to that of the linear polarized laser. From the reconstructed G-function of Methyl Lactate we see that for linear polarization the G-Function is zero, as expected. The asymmetry parameter then increases almost linearly and maximizes for $\theta_{qwp} = 24°; |S3| = 0.74$, reaching an asymmetry value of $G = 6\%$. With a further increase in the ellipticity the asymmetry (G) starts decreasing and reaches to an asymmetric value of $G =\sim 4\%$ for circular polarization. Also we see that the G-function reverse sign when the helicity of the incident electromagnetic wave is reversed.

Higher Dimensional Fourier Component Analysis

The 1-D dichroic signal obtained by reducing the dimensionality of the 2-D photoelectron angular distribution ($\mathcal{P}(p_z, p_y)$) provides a first information on the overall influence of the intermediate resonances in the REMPI process. However it is clear that much more detailed information could be obtained from the 2D images recorded by the VMI.

Hence to increase the dimensionality of the measurement we perform a fast-Fourier Transform on the 2-D image of the photoelectron angular distribution pixel by pixel. The symmetric ($\mathcal{P}_{sym}$) part 2-D photoelectron angular distribution (PAD) and the asymmetric ($\mathcal{P}_{asym}$) part of the PAD (PEELD) is given as:

$$\mathcal{P}_{sym}(p_z, p_y, t) = \frac{1}{2}\Big(\mathcal{P}_{sym}(p_z, p_y, t) + \mathcal{P}_{sym}(-p_z, p_y, t)\Big) \tag{3.13}$$

$$\mathcal{P}_{asym}(p_z, p_y, t) = \frac{1}{2}\Big(\mathcal{P}_{sym}(p_z, p_y, t) - \mathcal{P}_{sym}(-p_z, p_y, t)\Big) \tag{3.14}$$

A fast-Fourier Transform is performed per pixel on the symmetric and asymmetric 2-D distributions to get $\mathcal{P}_{sym}(p_z, p_y, \Omega)$ and $\mathcal{P}_{asym}(p_z, p_y, \Omega)$ in the frequency domain respectively.

The symmetric and asymmetric 2-D distributions oscillate at the same frequencies as that of the photoelectron yield ($S(\Omega)$) and g-Function ($G(\Omega)$). The 2-D distribution of the amplitude for the symmetric part of the PAD is shown in Fig. 3.12 at even multiples of the fundamental frequency Ω_0 . The spectral decomposition of the antisymmetric part over the odd harmonics of Ω_0 are shown in Fig. 3.13. The Fourier transform provides complex quantities.

Figure 3.12 and 3.13 show that the Fourier components of the symmetric part of the signal are mostly real, while those of the antisymmetric part are mostly imaginary. This can be explained by the fact that the origin of time in our experiment was chosen when the polarization state of the laser is linear. The total signal is thus expected to be even with respect to this origin, while the chirosensitive signal, which changes sign with the light helicity, is expected to be odd. The imaginary component of the symmetric signal and the real component of the antisymmetric signal are thus noise, which can be disregarded.

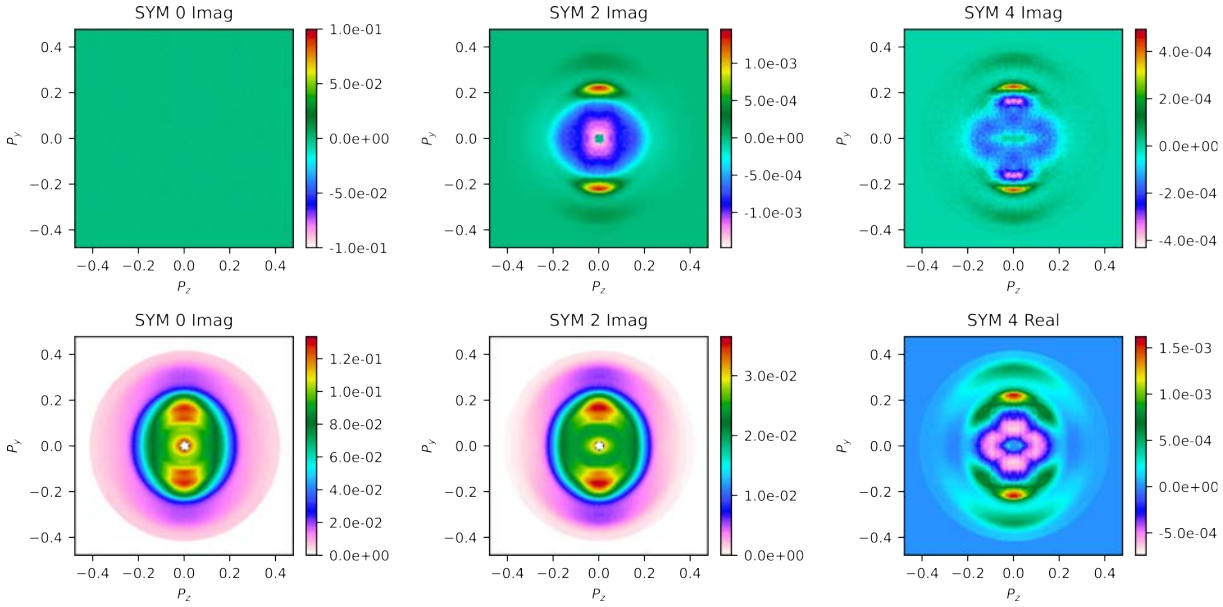

Figure 3.12 – *The 2-D maps of the FFT components of the symmetric part of the PAD oscillating at even multiples of* Ω_0*. The top panel shows the imaginary part while the bottom panel shows the real part. We can see that majority of the signal is contained in the real part as expected.*

Spectroscopically speaking, the symmetric 2-D amplitude maps are unique for a given molecule and the asymmetric ones change sign for the enantiomers. They are also structurally rich and hence contain information about the molecular energy levels and the dichroism respectively.

The $\mathcal{P}_{sym}(p_z, p_y, 0\Omega_0)$ describes the continuous component of the PAD. While $\mathcal{P}_{sym}(p_z, p_y, 2\Omega_0)$ and $\mathcal{P}_{sym}(p_z, p_y, 4\Omega_0)$ is related to the variation of the PAD with S3 at $2\Omega_0$ and $4\Omega_0$ respectively. The $\mathcal{P}_{sym}(p_z, p_y, 2\Omega_0)$ component maximizes at linear polarization (see Fig. 3.12). The change in sign of the $\mathcal{P}_{sym}(p_z, p_y, 4\Omega_0)$ map does not point to any interesting physics but is rather related to the rotation of the field ellipse axis relatively to the projection axis. The 2-D frequency maps of the asymmetric part of the PAD is much richer. Although we don't see a change of sign of the dichroic signal in the spectral maps corresponding to Ω_0 and $3\Omega_0$ but we see a sign change in $5\Omega_0$ distribution (see Fig. 3.13). It is important to note that

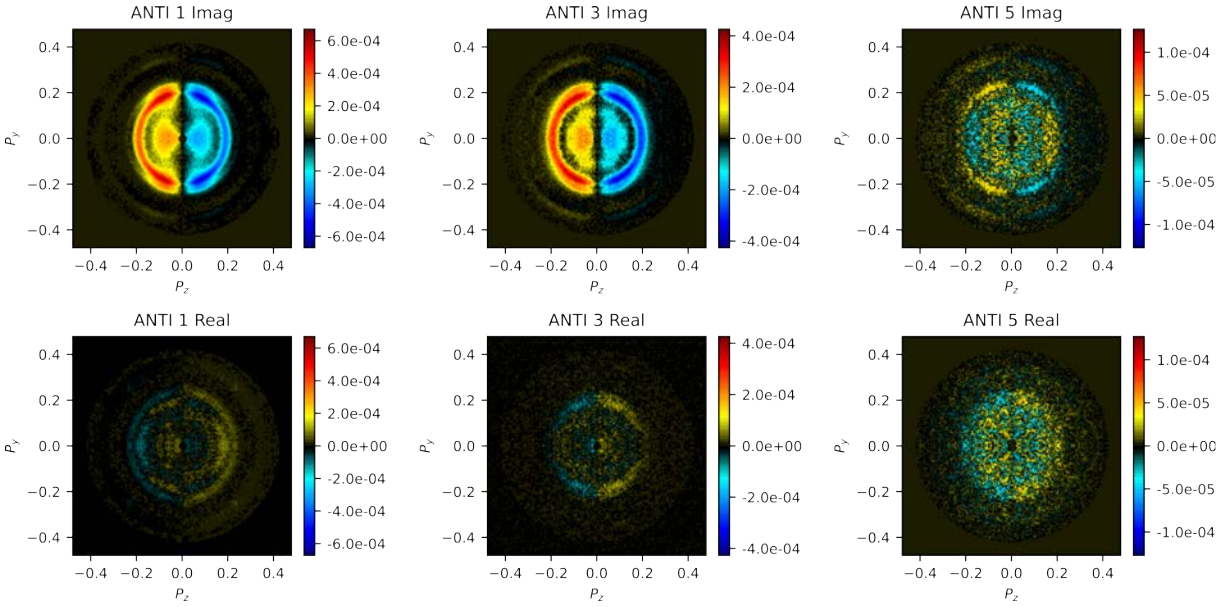

Figure 3.13 – *The 2-D maps of the FFT components of the asymmetric part of the PAD oscillating at odd multiples of* Ω_0*. The top panel shows the imaginary part while the bottom panel shows the real part. We can see that majority of the signal is contained in the imaginary part as expected.*

for a given hemisphere two different areas can have opposite sign and hence the integrated 1-D dichroic signal ($G(t)$) will have a reduced sensitivity.

PAD & PEELD of Methyl-Lactate

The complete 2-D photoelectron angular distribution can be reconstructed for all the ellipticities from the 2-D frequency amplitude maps by using discrete inverse Fourier transform. Where the symmetric PAD ($\mathcal{P}_{PAD}(p_z, p_y, S3)$) and the asymmetric PAD of PEELD $\mathcal{P}_{PEELD}(p_z, p_y, S3)$ is expressed as:

$$\mathcal{P}_{PAD}(p_z, p_y, S3) = \mathcal{IF}(\mathcal{P}_{sym}(p_z, p_y, 2n\Omega)) \tag{3.15}$$

$$\mathcal{P}_{PEELD}(p_z, p_y, S3) = \mathcal{IF}(\mathcal{P}_{asym}(p_z, p_y, (2n+1)\Omega)) \tag{3.16}$$

The 2-D photoelectron angular distribution reconstructed using discrete inverse Fourier Transform for quasi linear polarization $|S3| = 0.03$ are shown on the right in Fig. 3.14. We see two main peaks in the photoelectron kinetic energy distribution at 0.86 eV and 1.35 eV (shown in red circles). The peak in the photoelectron kinetic energy of 3.26 eV corresponds to the first ATI of 0.86 eV. The corresponding reconstructed PEELD is shown on the left in Fig. 3.14. We see that $\sim$ 87% of the photoelectrons have a kinetic energy lower than 2.4 eV, in full agreement with the 5 photons ionisation expected and the power law of ionisation. The remaining 13% at 3.26 eV, corresponds to the first ATI peak of the 0.86 eV component. Thus we can conclude that most of the ionisation takes place via a [3+2] and/or [4+1] REMPI (as shown in Fig. 3.9). The reconstructed PEELD is normalized per pixel with that of the photoelectron angular distribution and the corresponding S3. Even for a small ellipticity, we see a significant PEELD of $\sim$ 20% corresponding to the photoelectron kinetic energies of 0.86 and 1.35 eV. In the PEELD distribution we can clearly see a PEELD of about $\sim$ 15% for the ATI.

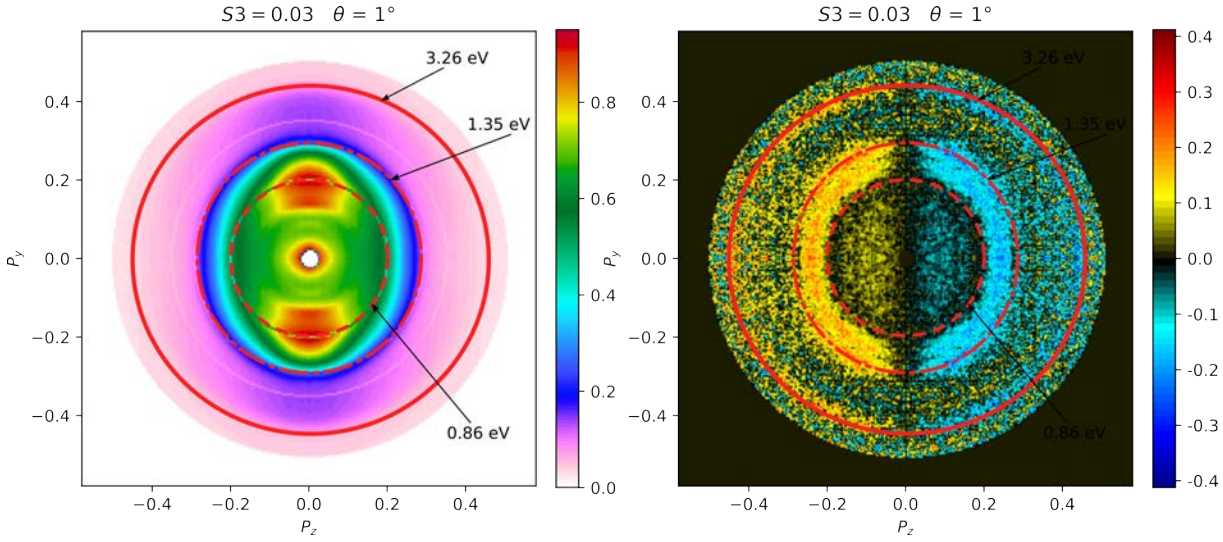

Figure 3.14 – *The 2-D distribution of the PES measured in Methyl-Lactate using a VMI for quasi linearly polarization shown in left. The corresponding PEELD distribution is shown on the right. Red circles indicates photoelectron with kinetic energies of 0.86, 1.35 and 3.26 eV respectively.*

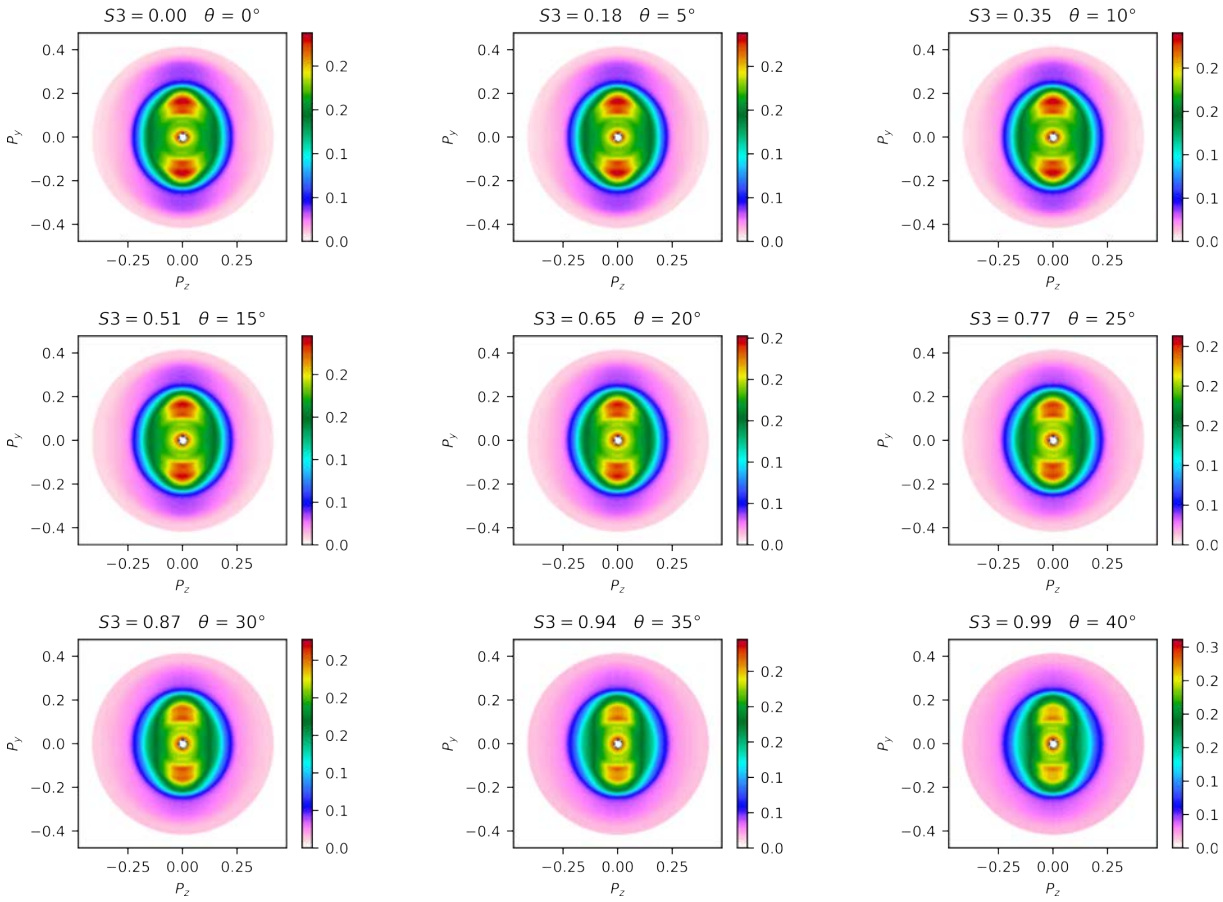

Figure 3.15 – *The 2-D distribution of the PES measured in Methyl-Lactate using a VMI.*

The 2-D PAD is reconstructed for all ellipticities and are shown for 9 different ellipticities in Fig. 3.15. We clearly see the photoelectrons corresponding to the kinetic energies of 0.86 eV and 1.35 eV along with the ATI of 0.86 eV. The proximity of the energy levels of 0.86 eV and

1.35 eV is attributed to ionization onto HOMO and HOMO-1. Furthermore, we clearly see that the structure of the PAD doesn't change significantly. Except a decrease in the photoelectron yield which is attributed to the fact the intensity for circular polarization is $\sqrt{2}$ times less than that for linear.

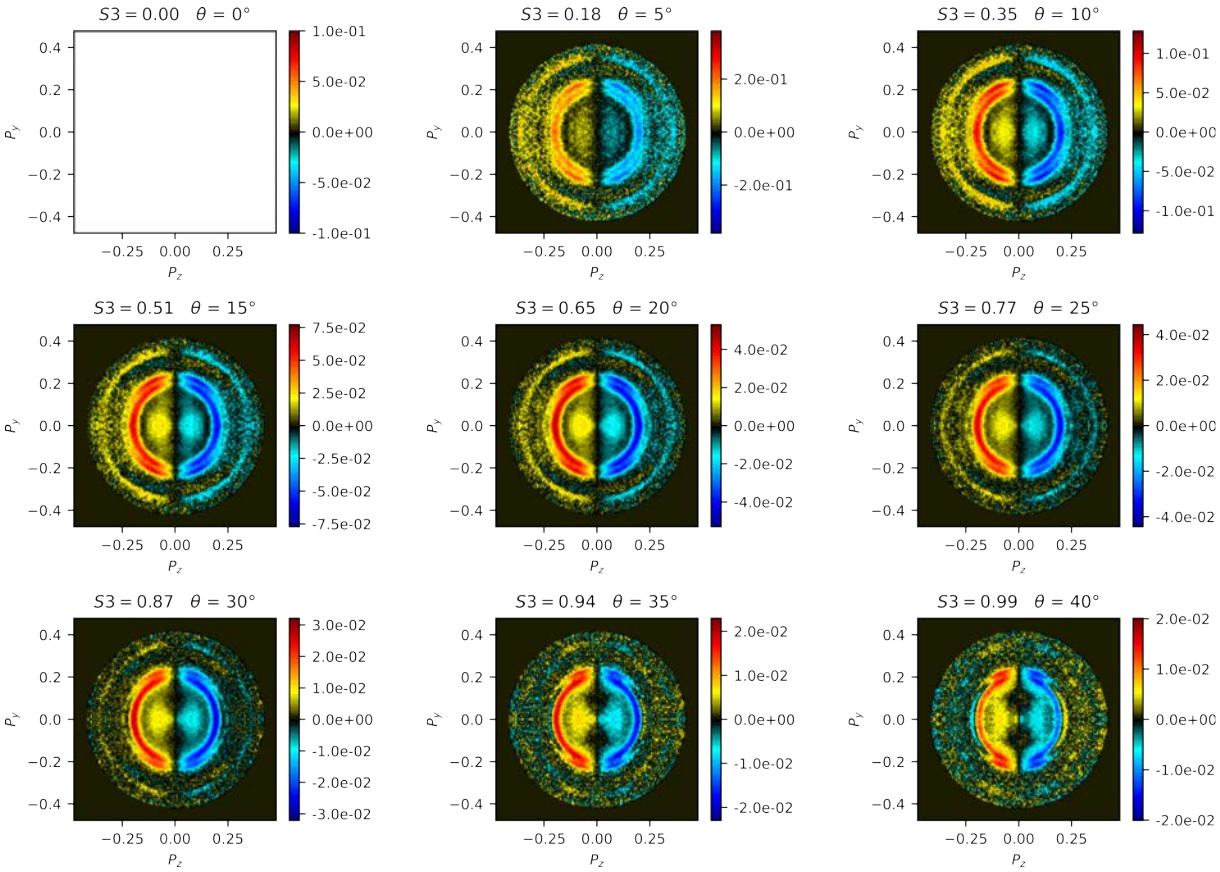

Figure 3.16 – *The 2-D distribution of the PEELD measured in Methyl-Lactate using a VMI.*

The corresponding 2-D PEELD distribution are shown in Fig. 3.16 for the same 9 ellipticities. We see a strong dichroic response in Methyl-Lactate. The PEELD shown in Fig. 3.16 is normalized by the PAD per pixel and by the corresponding S3. We see a very strong dichroic response of about $\sim 20\%$ for small ellipticities of $S3 = 0.18$ and about $\sim 2\%$ for $S3 = 0.99$. The 2-D PEELD distribution is structurally rich and most of the dichroism comes from the photoelectron kinetic energy corresponding to 0.86 and 1.35 eV. They both show the same sign of dichroism but have a different angular structure. While for the PEELD at 0.86 eV has a more uniform angular structure, i.e., the PEELD throughout $p_\theta[-\pi/2, +\pi/2]$ is more or less constant but for the PEELD at 1.35 eV the PEELD maximizes at $p_\theta \pm \pi/2$ but minimizes and reaches zero for $p_\theta[-\pi/4, +\pi/4]$. The structural distribution of the PEELD remains the same for $|S3| < 0.90$. With a further increase in the S3 the PEELD at photoelectron kinetic energy of 1.35 eV starts to show changes in its angular structure. The PEELD at 1.35 eV maximizes at $p_\theta \pm \pi/2$, with an asymmetry of 2%, then it minimizes and reaches zero for $p_\theta \pm \pi/4$ and then changes sign for $p_\theta[-\pi/4, +\pi/4]$, reaching an asymmetry of $\sim 1\%$. The ATI of 0.86 eV at 3.26 eV also show a significant dichroism and has the same sign as that of the 0.86 eV. The

dichroism from this ATI peak starts to decrease with the increase in ellipticity and is negligible for $|S3| > 0.9$.

These results show several interesting features in the PEELD angular distributions of Methyl-Lactate. TDDFT simulations are to be performed to identify the energy levels which participate in the REMPI process. Some of the observations could be due to the presence of different ionization pathways, which could be associated with different fragmentations of the associated ions. To investigate these effects, we study in the following the photoelectron elliptical dichroism in electron-ion coincidence using a COLTRIMS.

V Influence of Fragmentation on PECD

When a molecule is ionized it can fragment into different ionic species. Molecules can also fragment through multiple fragmentation pathways with different branching ratios. In general fragmentation of a molecule depends on several factors. Firstly, it can depend on the molecular orbital from which ionization occurs for example upon ionization from a bonding orbital can lead to the fragmentation of the molecule. Secondly, upon ionization the cation can be left in an exited state from which it can dissociate. Finally, fragmentation can depend on the molecular orientation.

It has been observed that in general PECD depends on all these factors and hence fragmentation can be linked to PECD and vice-versa. IT has been experimentally observed that upon single photoionization of Methyl-Oxirane and that the PECD can vary depending on the molecular orbital ionized and the fragmentation pathway [Garcia 14]. It has also been observed that upon strong-field ionization of Methyl-Oxirane, where ionization happens only from the HOMO in the regime, a dependency of the PECD on the fragments is observed [Fehre 19]. Where the results have been interpreted as a result of alignment, involving preferential transitions to excited states, which have been known to affect PECD [Tia 17] and fragmentation. It has also been observed, in the multiphoton regime, that the kinetic energy spectra and their angular dependency are not sensitive to the coincident ion as the fragmentation happens post-ionization [Lehmann 13] [Rafiee Fanood 16]. On the other hand, it has been observed in Methyl-Oxirane that the amplitude of the PES varies with the fragment and hence so does the amplitude of the PECD [Rafiee Fanood 18]. These results tell us that indeed there maybe a dependence of fragmentation on the PECD.

V. 1 Coincidence Measurements

Removal of false coincidence events

To investigate the effects of fragmentation on the PECD we use the COLTRIMS to record the photoelectrons ejected in coincidence with the ions. To do so we use the electron signal to open a time window for acquisition in which all the ions arriving at the ion side are marked as arising from the same photoionization event. But this can also lead to false coincidence measurements due to multiple factors discussed in the previous Chapter. The solution chosen, to discard these false coincidence events, uses the spatial resolution of the ion detector. The

ions are spread along the detector axis corresponding to the molecular jet axis, as shown in Fig. 3.17 (a). Since the species carried in the jet have approximately the same velocity, this position is proportional to their time-of-flight. A relevant representation is $Y = f(TOF)$, displayed in Fig. 3.17 (b), where the slope α corresponding to the jet velocity clearly appears. This is a precise manner to determine the velocity, that depends on the carrier gas and the backing pressure (1500 m/s in the example given, with 1 bar of helium). Importantly in this plot, the position is proportional to the actual TOF, while the abscissa is the reconstructed TOF. These two quantities match along the $TOF = \alpha Y$ line, meaning that any count along this axis are ions with a good TOF reference (within a certain margin to account for the velocity dispersion and the recoil of the fragments). On the contrary, any count outside of this range has a wrong reference and can be discarded. One can identify the features due to the previous or next laser shots along the $TOF = \alpha Y + nT$ where $T = 1/(rep.rate)$ and $n \in \mathbb{Z}$, as highlighted in Fig. 3.17 (c). By selecting the green area only, the cleaned mass spectrum, devoid of any false coincidence peaks, can be safely obtained.

PES, Mass Spectrum and Fragmentation Pathways

To investigate the effects of fragmentation on the PECD we ionize Methyl-Lactate using 515 nm circularly polarized electromagnetic wave at an intensity of 4.5 μJ/pulse. The corresponding photoelectrons emitted are recorded in coincidence with the ions using a COLTRIMS. The helicity is changed every 5 mins between left and right polarization. A total of $\sim 4 \times 10^8$ counts are recorded in coincidence over a period of 56 hrs at 700 kHz laser repetition rate. The photoelectrons are recorded for different S3 namely $|S3| = 0.75, 0.90, 0.95, 1.00$. This time window to measure the events in coincidence is fixed at 13.5 μs to collect the parent ion. Methyl-Lactate is introduced into the COTRIMS using a carrier gas of N_2 at a pressure of 2 bars and the nozzle is heated to a temperature of 110°C to avoid dimer formation. The photoelectron spectrum recorded in the COLTRIMS is shown in Fig. 3.18 (b) and the corresponding mass spectrum, resulting from the fragmentation of methyl-lactate, is shown in Fig. 3.18 (a) with the subtraction of the replicas using the method discussed above.

The structure of the PES observed on ionization of Methy-Lactate show three main peaks at 0.86 eV, 1.35 eV and 3.26 eV which is the same as that observed in the VMI (shown in Fig. 3.18 (b)). The mass spectrum shows a rich fragmentation behavior and we observe masses corresponding to 15, 32, 45, 61, 89, 102 and 104 amu (shown in Fig. 3.18 (c)). For the mass 32 we observe a broad peak whereas. The whole fragmentation is dominated by a broad peak at the mass corresponding to 45 amu. The width of the features correspond to the recoil momenta acquired during the fragmentation process. The sharp peak at 104 amu corresponds to the parent ion peak.

Fragmentation pathways of Methyl-Lactate has been studied using electron impact [Tajima 95]. The various fragmentation pathways are described in figure 3.19. The 15 amu mass is most probably CH_3^+ and can appear from two fragmentation pathways leading to two different neutrals at 89 amu. The 31 amu mass probably comes from the deprotonation of the methanol group whereas the 32 amu mass corresponds to the detachment of the methanol group. The mass at 61 amu comes from the so-called McLaffertie rearrangement. The mass at 102 amu comes from the deprotonation of the parent molecule.

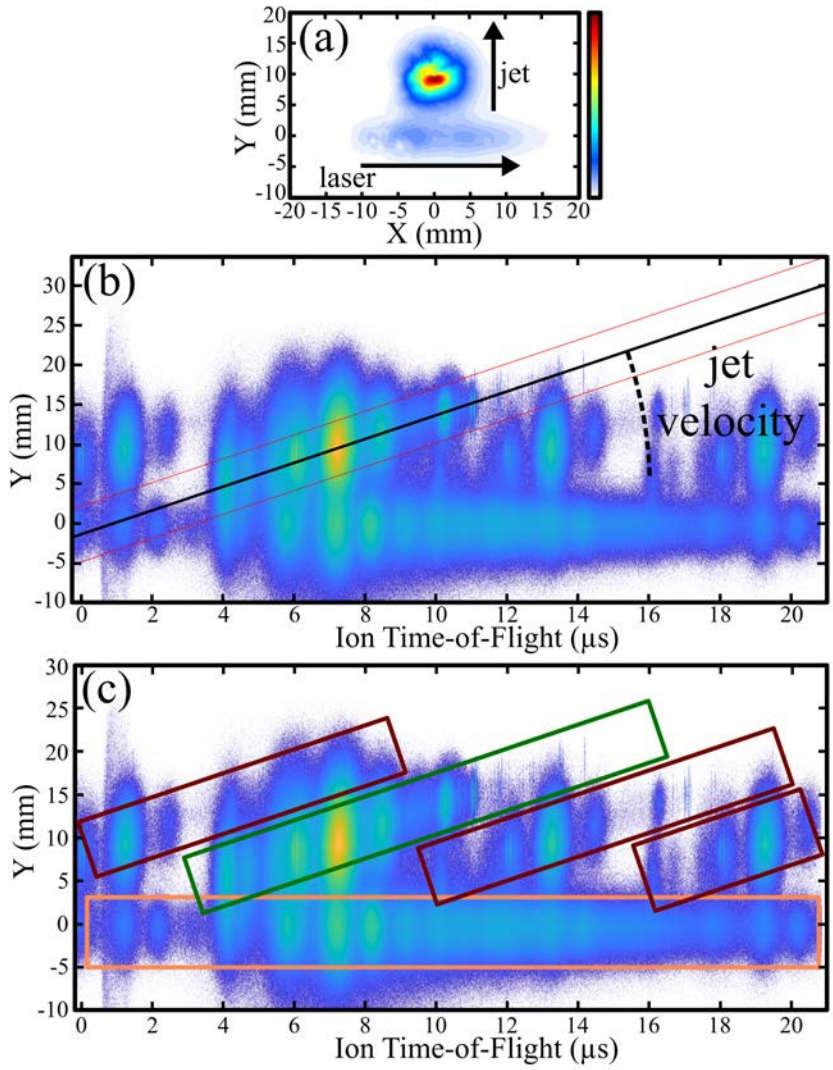

Figure 3.17 – *(a) Spatial ion distribution. The signal along the laser axis comes from the residual pressure while the one along the jet axis comes from it. (b) Corresponding spatially-resolved time-of-flight spectrum, along the jet axis. The jet velocity is visible in the slope indicated. (c) Same as (b) where areas of interest are indicated. The signal that comes from the jet and the right laser shot is in the green box, while the signal that has a wrong laser shot reference is highlighted in red and the signal from the residual pressure is in orange. Extracted from [Bloch 20]*

PECD in coincidence

The PECDs associated with all the main fragments are shown in Fig. 3.20 & 3.21. The photoelectrons detected in coincidence with the masses at 15, 32, 60 and 89 amu. do not show any PECD. On the other hand, the photoelectrons detected in coincidence with the fragment at 45 amu show a significant PECD of about $\sim 1\%$, and the parent shows a PECD of 0.5%. The PECD distribution of both are similar in structure. We see that the PECD changes sign along the laser propagation direction in a given hemisphere and is similar to that observed using a VMI, changing sign at 0.86 and again at 1.35 eV. The PECD measured in coincidence with the fragment with a mass of 45 amu is probably due to selection of differently oriented non-isotropic sub-samples from the randomly oriented molecules. PEELD for $|S3| = 0.75, 0.90, 0.95$ shows

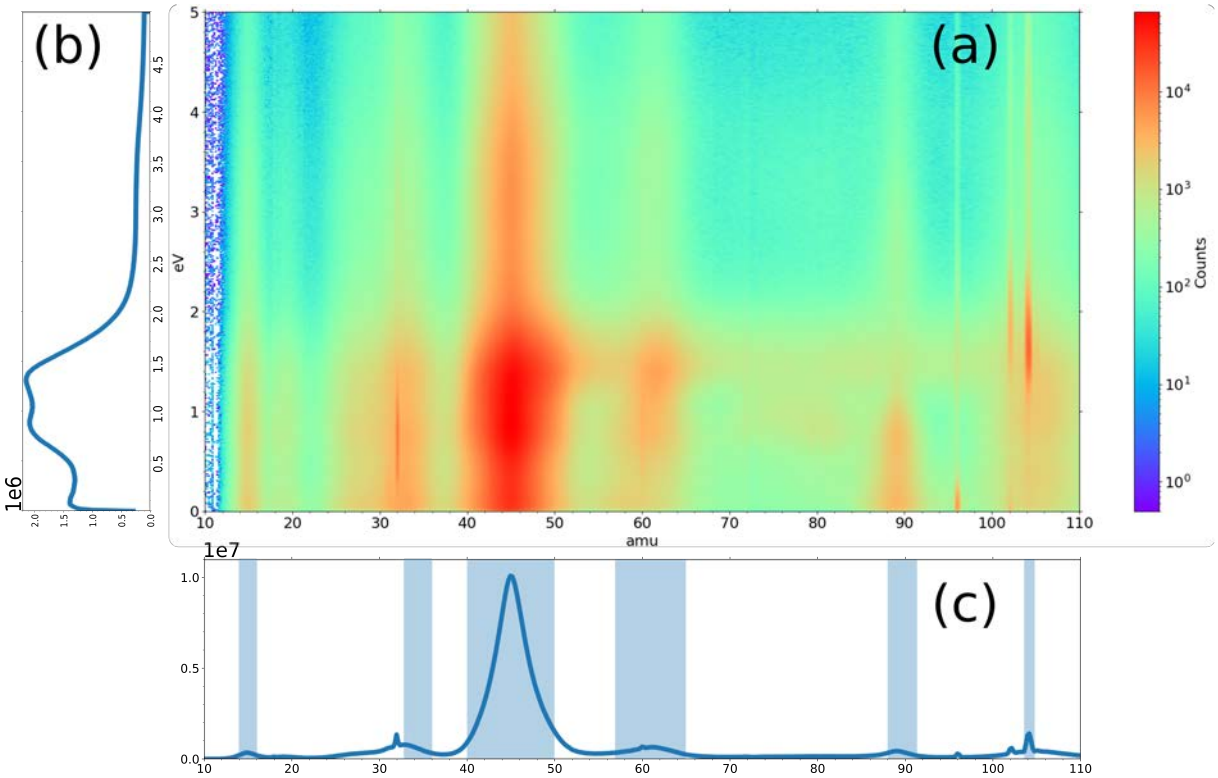

Figure 3.18 – *Photoelectron spectrum in log scale as a function of the mass spectrum with* $|S3| = 0.95$. *(b) photoelectron spectrum integrated over the masses, while (c) mass spectrum integrated over the electron kinetic energies. This 2D map has been recorded over 56 hours at 700 kHz repetition rate and corresponds to* $\sim 3.7 \times 10^8$ *ionization events. Note that the* 12% *replica of ionization appearing within the* 13.5 μs *has been subtracted.*

an asymmetry of $\sim 1\%$, $\sim 2\%$ and $\sim 0.5\%$ respectively for both the masses and has a similar angular structure.

Similar to the PEELD observed in VMI we see that the PEELD at 1.35 eV the PEELD maximizes at $p_\theta \pm \pi/2$ then it minimizes and reaches zero for $p_\theta \pm \pi/4$ and then changes sign for $p_\theta[-\pi/4, +\pi/4]$ for $|S3| = 0.90, 0.95\&1.0$. While the angular structure remains similar to that observed in VMI, this measurement reveals that the fragments 15, 32, 60 and 89 amu. do not show any PEELD. An additional sign change is observed at 0.75 eV which was previously not observed in VMI. This can be attributed to the the different laser intensity in the two experiments, since PEELD is known to be very sensitive to intensity [Comby 16].

VI Conclusion and Perspectives

Throughout the chapter we have seen that PEELD provides a wealth of information with a higher sensitivity than PECD, revealing states which did not participate in PECD. The use of a lock-in ellipticity modulation scheme provides an enrichment of the dichroic response of chiral molecules, and has been implemented for continuous isomeric and enantiomeric content monitoring. We have also seen that the coefficient (b_3) of the Legendre Polynomial, used to describe the PAD, is associated to the selectivity in the molecular orientation induced by resonances. Thus, the continuous variation of $|S3|$ combined with Fourier filtering could be used as an additional

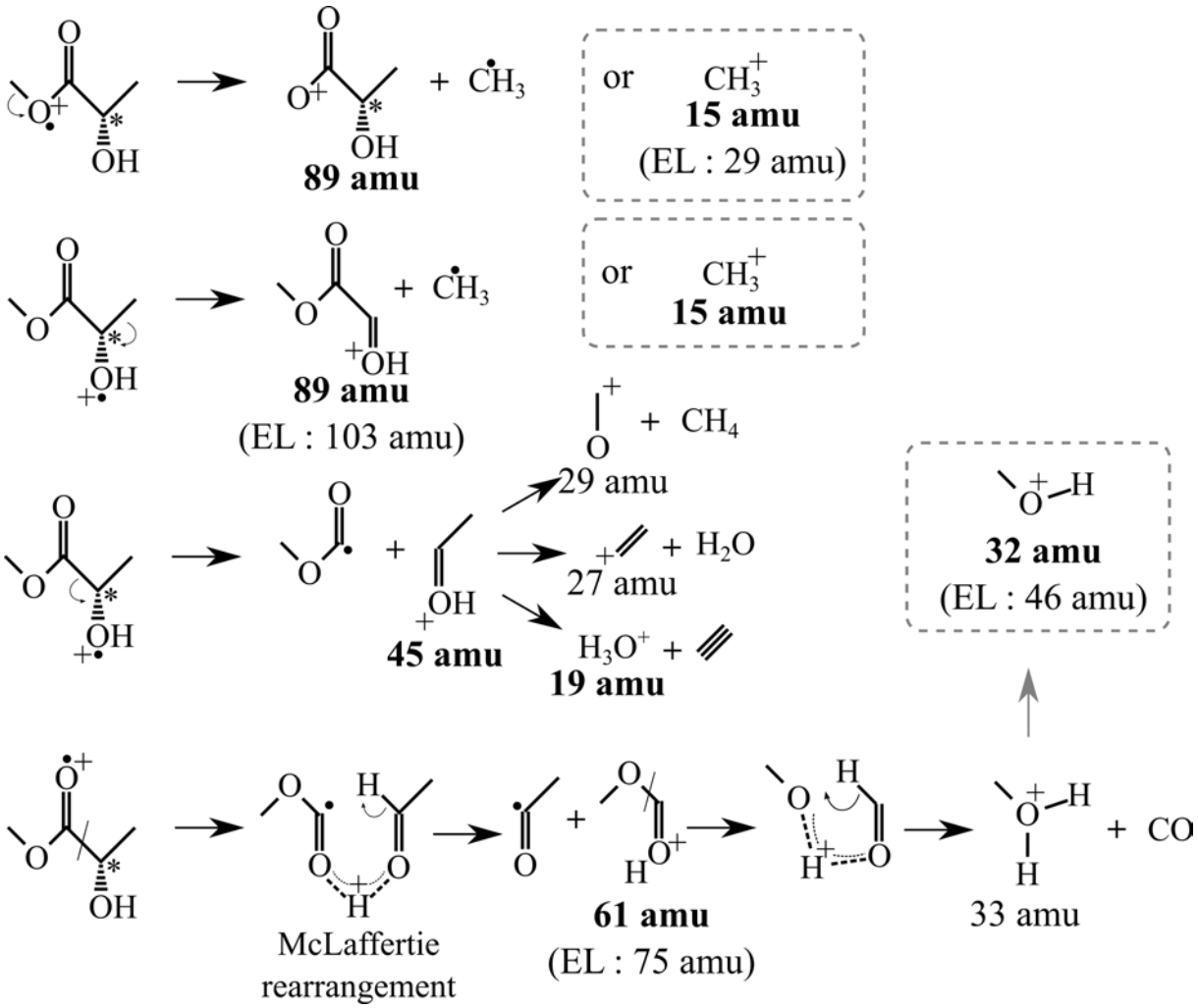

Figure 3.19 – *Plausible fragmentation mechanisms of the Methyl-Lactate, adapted from [Tajima 95]. The masses indicated in bold are the one observed in our conditions. The mass shifts that are visible by replacing the methyl by an ethyl group (in Ethyl-Lactate, EL) are indicated.*

dimensionality in time-resolved photoelectron imaging. Furthermore, variation with S3 and the wavelength provides a multi-dimensional approach to decouple the bound-bound and bound-continuum transitions. Thus the question also arises how is the PECD affected in continuum-continuum transitions? We will see in the overall Conclusion chapter that we have initiated an experiment to investigate this question.

From the experiments performed on Methyl-Lactate, strong fragmentation reveals interesting characteristics. We see that only the photoelectrons recorded in coincidence with the fragment 45 amu shows PEELD, apart from the parent, while all others fragments show no PEELD. Furthermore, these molecules should efficiently form dimers due to there high permanent dipole moment. And thus can be used to address the question that how is the PECD or PEELD affected if several chiral molecules interact with each other. An additional structure in the PEELD was observed due to a change in the intensity of the incident electromagnetic wave. Thus the question arises what happens if we keep on increasing the intensity and reach a regime where $\mathcal{H}_0 < \mathcal{V}$, does PECD still survive in these conditions? Also, for the regime where

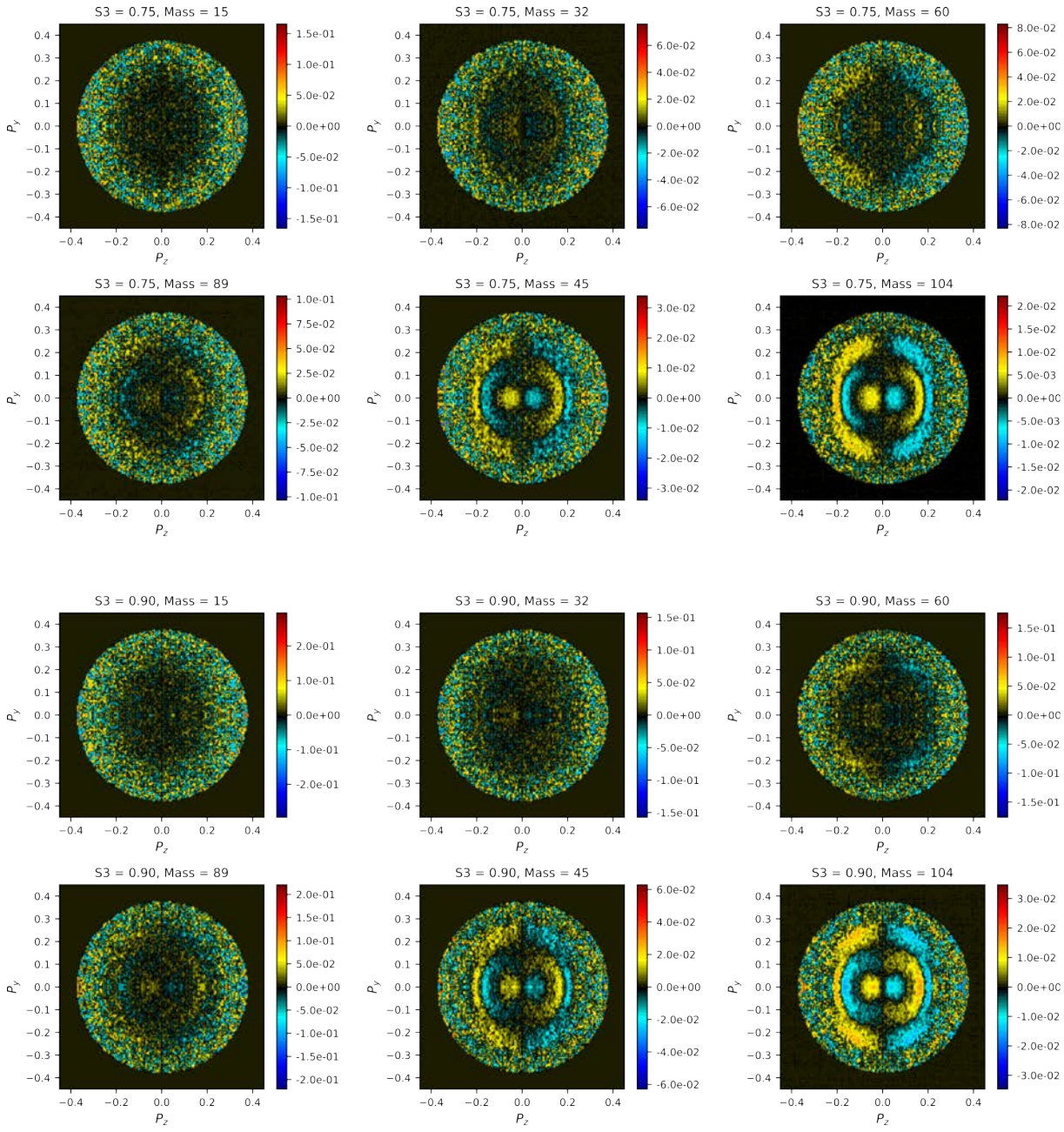

Figure 3.20 – *2-D distribution of the measured PhotoElectron Elliptical Dichroism for different ellipticities ($|S3| = 0.75, 0.90, 0.95, 1.00$) measured in coincidence with the Methyl-Lactate fragments. We see that the photoelectron angular distribution doesn't show any PEELD for the fragment 15, 32, 60 and 89 amu. While for a significant PEELD is observed in the photoelectron angular distribution measured in coincidence with fragment 45 amu and the parent with a mass of 104 amu.*

$\mathcal{H}_0 < \mathcal{V}$, the dynamics of the electrons will be dictated by the electromagnetic field. Now as the electromagnetic wave goes from its maximum to zero in about $\sim$ 600 as, for a 1030 nm wavelength light, can we exploit this property to investigate chiral light-matter interactions in attosecond time scales?

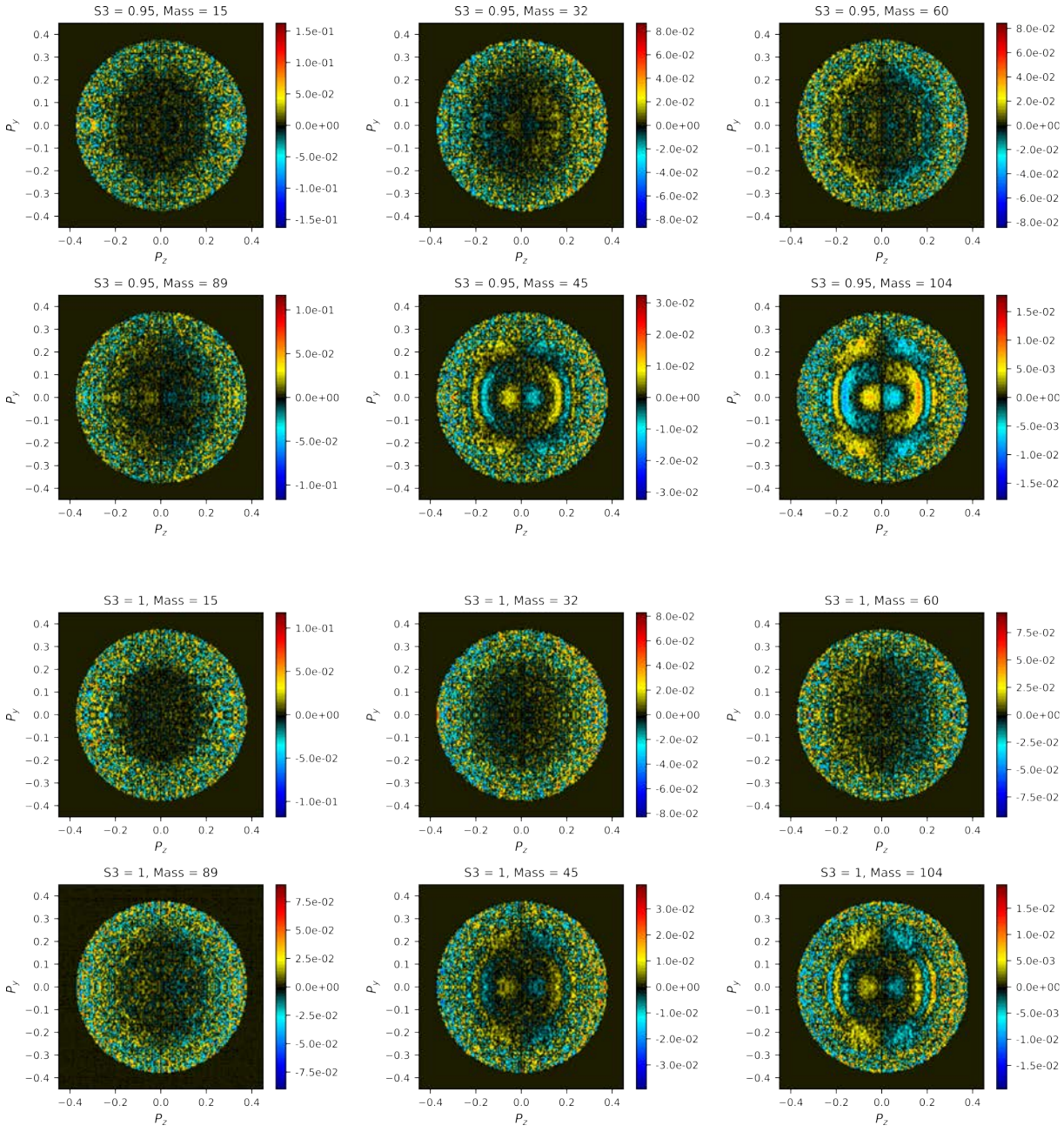

Figure 3.21 – *2-D distribution of the measured PhotoElectron Elliptical Dichroism for different ellipticities ($|S3| = 0.95, 1.00$) measured in coincidence with the Methyl-Lactate fragments. We see that the photoelectron angular distribution doesn't show any PEELD for the fragment 15, 32, 60 and 89 amu. While for a significant PEELD is observed in the photoelectron angular distribution measured in coincidence with fragment 45 amu and the parent with a mass of 104 amu.*

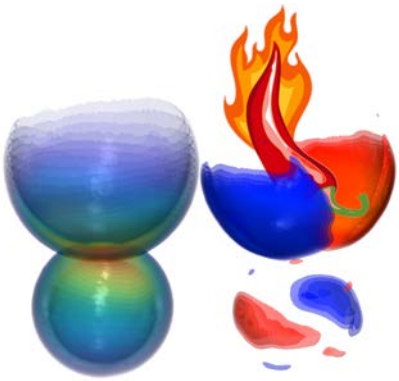

Chapter 4

Strong Field Regime

In the previous chapter, we have seen that using moderately intense laser pulses enabled ionizing chiral molecules by multiphoton absorption. In this chapter we increase the laser intensity to reach the strong-field regime. This could at first sight look like a bad idea because in this regime the laser field often dominates the electronic dynamics, so that the molecular potential only has a very weak impact on the motion of the outgoing electron. However in elliptical polarization, electrons can be driven back to recollide with their parent ion. We find that the angular distribution of these high energy photo-electrons shows a strong forward-backward asymmetry, resulting from their rescattering on the chiral ionic potential. The rescattering electrons can penetrate deep inside the molecular potential, thus encoding structural chirosensitive information in laser induced electron diffraction. Furthermore, the interference between direct and indirect electrons opens the way to chiral photo-electron holography.

In a second experiment, we use linearly polarized strong fields to ionize chiral molecules. This could at first sight look like an even worse idea. It is indeed generally assumed that circularly polarized light is needed to reveal chirality. However, we observe a rotation of the photoelectron angular distribution, about the laser propagation axis, depending on the handedness of the molecule. This new effect, conceptually similar to optical rotation, produces surprisingly strong signatures of the interaction between the laser magnetic field and the chiral potential.

The chapter is organized as follows: In section 1 we give a brief motivation of work. Section 2 introduces strong field interaction. Our experimental setup and data analysis procedures are explained in section 3. The results obtained in strong field photoelectron elliptical dichroism and our interpretations are discussed in section 4. Section 5 presents our motivation for the experiment on interaction of chiral molecules with linearly polarized light, along with the experimental setup, data analysis procedure, results and interpretation. Finally, in section 6 we

provide our conclusion and future perspectives.

I Introduction

Light induced chemical processes are mediated by electronic interactions, which happen on the attosecond timescale and are sensitive to the molecular structure. To probe these electronic dynamics in chiral molecules requires dedicated ultrafast spectroscopic methods to isolate and study the characteristic response of the molecules. The most commonly used experimental technique is pump-probe spectroscopy, in which two ultrashort light pulses are used, one to trigger the dynamics and a delayed one to probe it. We will see in this chapter that strong laser fields offer an alternative way to study and manipulate light induced process at attosecond timescales [Uiberacker 07] [Smirnova 09] [Sansone 10] and with sub-angstrom spatial [Blaga 12] resolution.

With advances in femtosecond laser technology it has become possible to reach electric field values similar to the atomic/molecular binding potential. When an atom/molecule is exposed to such intense electromagnetic fields the potential barrier of the atom/molecule is considerably modified by the electromagnetic field. This modification is a dynamical process (see Fig 4.1), occurring as the electromagnetic field oscillates, i.e. on the attosecond timescale (it takes only $\sim$ 860 as for the electric field of a radiation at 1030 nm to go from its peak to zero). At the maximum of the laser field (Fig 4.1 (a)), the molecular potential barrier is lowered significantly

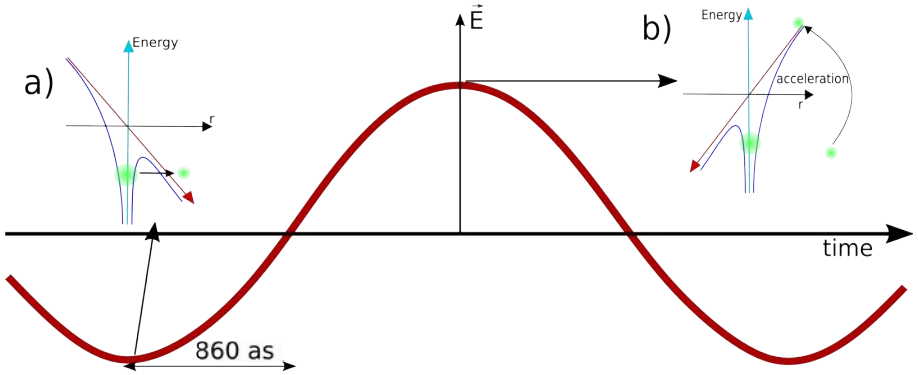

Figure 4.1 – *A quarter oscillation of the electric field, from its peak to zero, of an electromagnetic wave at* $1030nm$ *wavelength takes about* $\sim 860as$. *The electric field strength is strong enough to deform the molecular potential barrier. The Dynamical processes involved in strong-field ionization: a) At peak electric field the electrons tunnels out of the modified potential barrier, b) when the electric field reverses sign in the next half cycle these electrons maybe driven back to ionic core leading to rescattering, recombination or diffraction.*

and the electrons can tunnel out of this reduced barrier into the continuum. These tunneled electrons are then driven by the oscillating laser field and can follow different trajectories. Some of them can be driven back to the ionic core, leading to a variety of processes: rescattering [Paulus 94][Paulus 98], radiative recombination [McPherson 87] back to the ion emitting an XUV photon, or even diffraction from the molecular potential itself (Fig 4.1 (b)). These phenomena, referred to as "self-imaging" [Itatani 04][Meckel 08a] [Lin 10] [Haessler 11] [Blaga 12] [Amini 20], enable measuring structural and dynamics information with unprecedented resolu-

tions – Angstroms spatial resolution determined by the de Broglie wavelength of the recolliding electron, and attosecond temporal resolution set by the duration of the recolliding wavepacket.

The majority of self-imaging measurements have up to now been restricted to small systems (diatomics, triatomics). Indeed, retrieving structural information for polyatomic molecules is challenging due to the complexity of the molecular potential, the possible involvement of many molecular orbitals, and the averaging over various the molecular orientations [Lin 12] [Liu 21]. In this chapter we propose a novel approach to retrieve these structural and temporal information using a symmetry property that survives random orientation of molecules – molecular chirality, and an associated observable –Photo-Electron Circular Dichroism (PECD) [Powis 00] [Böwering 01] [Garcia 03].

II Strong Field Ionization

II. 1 Classical electronic trajectories

Once they have been released from the attraction of the ionic core by tunnel ionization, the electrons are accelerated by the strong laser field and their dynamics can be described in very good approximation from a purely classical viewpoint. Within the single active electron approximation one assumes that a single electron oscillates in the incident ionizing field while the remaining non-ejected electrons act as frozen spectators [Lewenstein 94] [Awasthi 08] [Hertel 08]. A second approximation, the strong-field approximation [Lewenstein 94], further simplifies the interaction. It consists in neglecting the influence of the ionic core on the motion of the released electron. Within this framework, the motion of the electron is purely driven by the oscillating linearly polarized electromagnetic field $E(t) = E_0 \cos \omega_0 t$, and can can be described via the classical Newton's equation of motion :

$$m\ddot{x}(t) = -eE_0 \cos \omega_0 t \tag{4.1}$$

where m is the electron mass and e its charge. The equation can be reformulated in atomic units:

$$\ddot{x}(t) = -E_0 \cos \omega_0 t \tag{4.2}$$

and integrated to obtain the electron trajectories. The electron is assumed to have lost all its energy going through the tunnel, such that its initial velocity at the time of ionization is $\dot{x}(t_i) = 0$. We will also assume that the tunnel extent is negligible, such that the electron arrives in the continuum at $x(t_i) = 0$. These initial conditions provide the following equation of the electron trajectories:

$$x(t) = \frac{E_0}{\omega_0^2}(\cos(\omega_0 t) - \cos(\omega_0 t_i)) + \frac{E_0}{\omega_0} \sin(\omega_0 t_i)(t - t_i) \tag{4.3}$$

It can be shown that these classical trajectories are a good approximation of quantum paths describing the motion of the electrons in the continuum in a quantum mechanical description of the interaction [Salières 01].

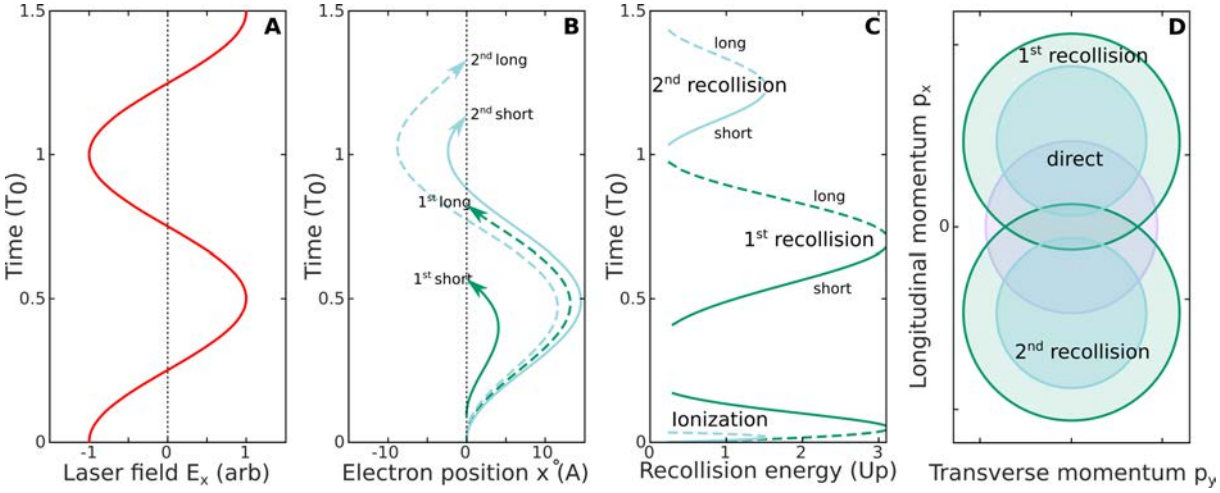

Figure 4.2 – *Semi-classical electron dynamics in a linearly polarized strong laser field.* ***A*** *Temporal evolution the electric field.* ***B*** *Typical electron trajectories in a 1030 nm laser field at* 3×10^{13} $W.cm^{-2}$. *The depicted green trajectories recollide with a kinetic energy of* $2U_P$. *The blue trajectories recollide upon second return with a kinetic energy of* U_P. ***C*** *Ionization and recollision times as a function of the kinetic energy of the recolliding electron, for first (green) and second (blue) recollisions, and short (continuous) and long (dashed) trajectories.* ***E*** *Final momentum of direct (purple) and indirect electrons after recollision upon first (green) and second (blue) return.*

Figure 4.2 shows a few trajectories corresponding to different ionization times t_i of an electron in a laser field at 1030 nm with 3×10^{13} W.cm^{-2}. The electrons released slightly before the maximum of the laser field (purple) drift away from their ionic core, gaining a maximum kinetic energy $2U_P$, where $U_P = E_0^2/4\omega_0^2$ is the ponderomotive potential determined by the intensity E_0^2 and frequency ω_0 of the driving laser. This process repeats every laser period, resulting in the formation of above-threshold ionization peaks in the photoelectron spectra [Agostini 79]. On the other hand, the electrons released slightly after the maximum of the field are subsequently driven back to the core as the laser field changes sign. They can recombine radiatively and emit attosecond bursts of extreme ultraviolet (XUV) light, forming high-order harmonic generation (HHG) [McPherson 87, Ferray 88]. Alternatively, the electrons can experience a collision with the ion and be scattered off by the ionic potential [Paulus 94].

Some electrons recollide with their parent ion upon their first return to their starting point. They are depicted in green in Fig. 4.2. Other electrons keep on moving and recollide during their second return to the ionic core (light blue in Fig. 4.2). We will neglect the influence of subsequent returns because their recollision is less probable due to the expansion of the electronic wavefunction. Remarkably, for both first and second returns, two different electron trajectories lead to the same recolliding kinetic energy. The two green trajectories in Fig. 4.2 recollide with $2U_P$ energy, and the two blue trajectories recollide with U_P energy. These two families of electron trajectories, associated with two sets of quantum paths in the quantum mechanical description of the interaction [Salières 01], are labeled short and long. Repeating the trajectory calculation for different ionization times enables us to extract the electron recollision energy for each family (Fig. 4.2 C). For the first recollision, the maximum kinetic energy the electrons can gain in the continuum is $3.17U_P$. The electrons recolliding at their second return are ionized within a much sharper time interval and their maximum kinetic energy is twice smaller.

The electron-ion collisions considered here are elastic collisions, in which the electron momentum is conserved but its direction can be reoriented as a result of the scattering. Conservation of momentum ensures that the final momentum of the electron is given by $\mathbf{p_{final}} = |\mathbf{p_{rec}}|\,\mathbf{u} + \mathbf{A}(t_{rec})$, where $\mathbf{u}$ is the direction of the scattered electron and $\mathbf{A}(t_{rec})$ is the value of the laser vector potential at the time of recollision [Amini 20]. For each recolliding energy, the electrons end up on a sphere of radius$|\mathbf{p_{rec}}|$ centered on $\mathbf{A}(t_{rec})$. For both first and second returns, the highest energy electrons recollide around the zeros of the laser field (Fig. 4.2 C), i.e. when the vector potential is at its maximum value A_0. Their recollision thus produces spheres in momentum space, centered around $\pm A_0$, with respective radii $\sqrt{2 \times 3.17U_P}$ and $\sqrt{3.17U_P}$. Cuts in these spheres are represented in Fig. 4.2 D, for electrons ionized around $t = 0$. The electrons ionized around the next maximum of the laser field ($t = T_0/2$) end up with the opposite longitudinal momentum p_y.

While the direct electrons end up with a maximum kinetic energy of $2U_P$, the electrons which backscatter upon recollision gain a much higher kinetic energy: $10U_P$ for first recollisions and $7U_P$ for second recollisions. A typical photoelectron angular distribution thus looks like the one presented in Fig. 4.3. However this picture only takes into account the classical aspect of the dynamics. Since the electrons are quantum objects, their wavefunctions will produce interference patterns in the areas where several quantum paths lead to the same final momentum. We discuss this in the next section.

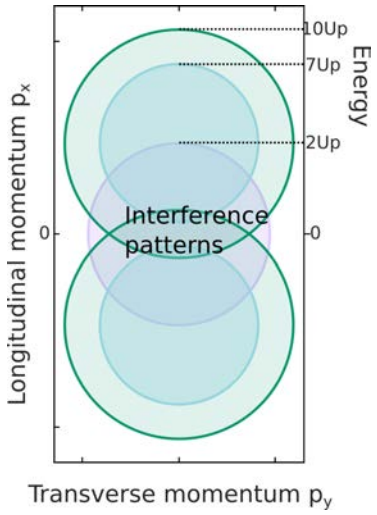

Figure 4.3 – *Schematic of the photoelectron angular distribution in strong-field ionization, with direct electrons (purple), electrons recolliding upon first returns (green) and second returns (blue).*

II. 2 PhotoElectron Holography

Our classical calculations have shown that several trajectories could lead to the same final momentum of the electron. Quantum mechanically, these different trajectories can interfere with each other leading to interference patterns, encoding the different phase accumulated between different trajectories. This interference can be used in the same manner as in holography, where we have an interference between an object beam, which scatters from the object of interest, and

a reference beam. Here the electron direct trajectories play the role of reference beam, and the forward scattered electrons, which end up with similar momentum but see their phase affected by the ionic potential, are the object beam. However the multiplicity of electron trajectories and interference processes makes this analogy a bit more complicated.

Interferences of direct electron trajectories:

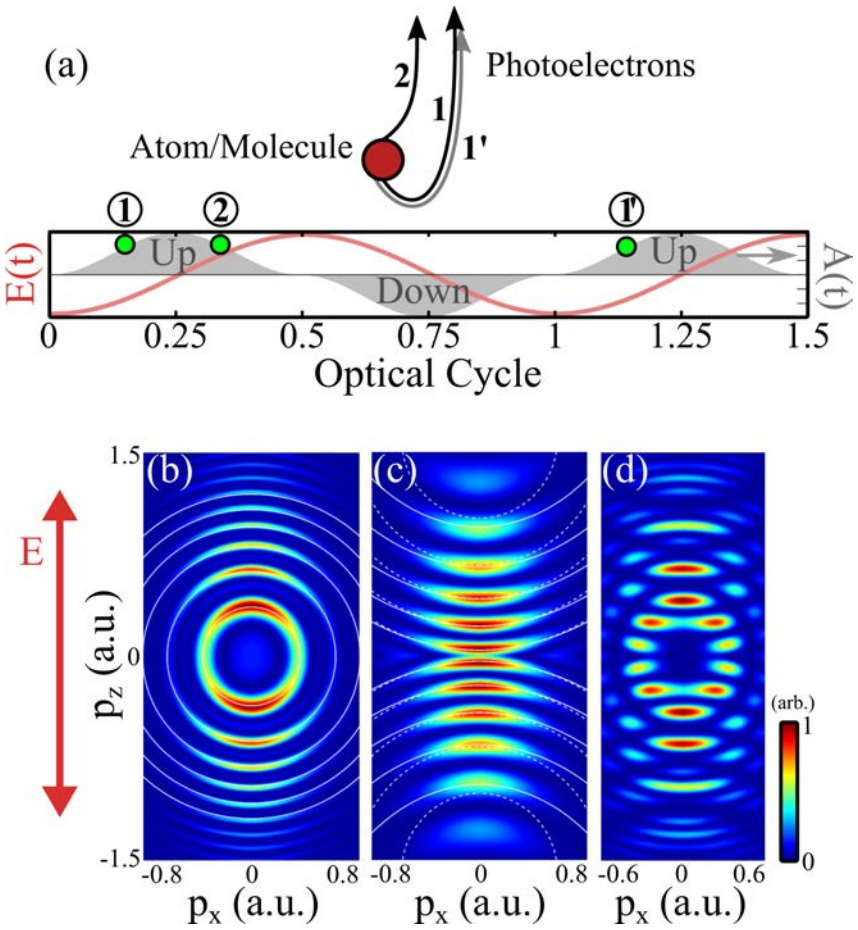

Figure 4.4 – *Scheme of the direct photoelectron trajectories with the same final momentum, ionized at different times. The ionization time of the three trajectory examples, with a final momentum upwards, are reported on the temporal panel. The interference can occur between two optical cycles (e.g. between trajectories 1 and 1'), yielding the ATI pattern presented in (b). It can also originate from ionization times within half an optical cycle (1 and 2), yielding the pattern on (c). The white lines in (b) and (c) correspond respectively to the solutions of the analytical expression 4.11 and 4.12. The combination of the two effects gives the modulation shown in (d). (b,c,d) are adapted from [Maxwell 17]. Reproduced from [Bloch 20].*

The most obvious interference pattern in photoelectron angular distributions is the formation of above-threshold ionization rings, separated by one photon energy of the ionizing field. Their emergence is explained in Fig. 4.4. The electrons 1 emitted during a given laser half cycle, e.g. between 0 and 0.5 optical cycles, end up with the exact same momentum as the electrons $1'$ emitted one laser cycle later. This produces a spectral interference pattern, whose fringe spacing is determined by the delay between the two electron wavepackets, which is one laser period (Fig.

4.4 (b)). The resultant interference patterns happens at electron kinetic energies given by:

$$E_{kin}^{1-1'} = n\omega - I_p - U_P \tag{4.4}$$

where $n \in \mathbb{N} \mid n\omega - I_p - U_P > 0$. Solutions to the Eqn. 4.4 are concentric rings, separated by $\Delta E = n\hbar\omega$, centered at $E_{kin} = 0$. These are basically the ATI rings.

Together with intercycle interference of electronic trajectories electronic trajectories originating from the same optical cycle but from the opposite edges of the optical cycle also end up with the same kinetic energies and thus interfere with each other, i.e. trajectory 1 and 2 (see Fig. 4.4 (a) (c)). The interference patterns thus generated are called intracycle interferences. The kinetic energies of these electrons, for a given electric field along y, are obtained from the equation:

$$\left(p_y - \frac{4\sqrt{U_P}}{\pi}\right)^2 + p_x^2 + p_z^2 = 2n\omega - 2I_p - 2U_P + \left(\frac{4\sqrt{U_P}}{\pi}\right)^2 \tag{4.5}$$

where $n \in \mathbb{N} \mid 2n\omega - 2I_p - 2U_P + (4\sqrt{U_P}/\pi)^2 > 0$. The solutions to the Equn. 4.5 are concentric circles with the rings centered at $p_y = \pm 4\sqrt{U_P}/\pi$.

The final interference pattern observed in the experiment is an interference of both the intra and intercycle interference pattern(see Fig. 4.4 (d)).

Other interference patterns:

The rescattered electron trajectories in one half cycle of the laser can further interfere with the direct electrons to produce more holographic patterns on the photoelectron angular distributions. Such interference patterns can be used to access the phase accumulated by the electronic wavepacket during the rescattering process. Since the direct electrons dominates in the low energy part of the photoelectron angular distribution (maximum energy obtained by them is $2U_P$) the photoelectron holographic patterns are localized in this energies. Furthermore, forward-scattered electrons from the same cyle of the laser can interefere with each other to form spider like interference patterns and the direct electrons can also interfere with the back-scattered electrons to form fish-bone like interference patterns [Huismans 11] [Hickstein 12].

As the rescattered electrons can penetrate deep inside the ionic core and scatter from it, the ionic potential significantly influences their trajectories. To take into account the influence of the coulombic ionic potential, to correctly reproduce their behavior, the Coulomb potential of the ion is perturbatively taken into account in the SFA action. This is called the Coulomb Corrected SFA (CCSFA). These advances are comprehensively summarized in [Figueira de Morisson Faria 20].

Manipulating holographic patterns:

Although these interferences encodes a lot of information about the molecular potential, it is difficult to extract it because of the superoposition of several sets of holographic patterns. A solution consists in selectively manipulating the electron trajectories using a weak second harmonic field [Porat 18] [Shafir 12]. This can be done in two ways, using either parallel or orthogonal polarizations of the fundamental and second harmonic. In the first case, the second harmonic leads to subtle modifications of the potential barrier through which the electrons tunnel out. This induces the suppression or enhancement of the holographic interference signal depending on the relative phase of the two harmonics. The subtle modifications in the potential barrier

results in different time of release of electrons into the continuum which results in a change in the position of the holographic fringes. When the second harmonic is polarized orthogonally to the strong fundamental field, it imparts a lateral velocity component to electrons, perturbing their trajectories. The indirect electrons thus rescatters with the ionic potential at a different spatial position. This provides a spatial resolution of the molecular potential at the Angstrom scale, which is again encoded in the holographic interferogram. Last, let us mention that synthetic laser fields can be used to further manipulate the electronic trajectories, for instance by using bi-color and bi-circular fields. The relative helicities of the field and their relative intensities can be used to tailor the electron trajectories leading to other exotic shapes in the photoelectron angular distribution [Mancuso 16] . This also allows to control the instantaneous polarization state of the light within the optical period [Bloch 21].

II. 3 Laser-induced electron diffraction

The presence of interference and holographic patterns in the low energy region of the photoelectron distributions makes this area very sensitive to the molecular structure. However the superposition of multiple patterns originating from different sets of quantum paths makes it difficult to retrieve the structural information. By contrast, in the high energy region of the spectrum, beyond $7U_P$, a single set of electron trajectories contribute to the signal: the long trajectories from first return recollisions (since the short trajectories are unfavored due to their late ionization in the optical cycle and therefore low ionization probability). The structural information can be straightforwardly extracted from these electrons, in a scheme called laser-induced electron diffraction.

Laser induced electron diffraction (LIED) is a strong-field process in which the recolliding electronic wavepacket have enough kinetic energy such that the de-Broglie wavelength of the electron is comparable to the size of the molecular bonds. This returning electronic wavepacket can diffract off these molecular bonds thus forming diffraction patterns encoded on the photoelectron angular distribution. Being a strong field process the influence of the strong laser field on the electron momentum has to be isolated to retrieve the field-free elastic electron-ion differential cross-section (DCS) from the measured electron momentum distribution. From strong field approximation the observed electron momentum $\boldsymbol{p}$ is given as the sum of momentum after re-collision $\boldsymbol{p_r}$ and the electromagnetic vector potential at the time (t_r) of re-collision $\boldsymbol{A_r}$, given as $\boldsymbol{p} = \boldsymbol{p_r} - \boldsymbol{A_r}$ (see Figs. 4.3 and 4.5). Thus the field free electron-ion differential cross-section (DCS) is given by measuring the signal of the electrons detected along the circumference of a circle whose radius is defined by $\mid \boldsymbol{p_r} \mid$. At low scattering angles, DCS is heavily polluted by the direct electrons from the ionization process. This restricts the angular range in which the DCS can faithfully be extracted.

Laser induced electron diffraction was initially performed in simple diatomic molecules like N_2 [Blaga 12] where the bond length of the neutral molecule was found in accordance to the calculated one of 1.12. However, the experiment was unable to resolve the small N–N bond motion of 0.02 during the 4–6-fs time interval after tunnel ionization, as the experimental error was 0.05. LIED has also been performed in O_2 [Meckel 08b], Neon dimers [Kunitski 19], CS_2[Amini 20]

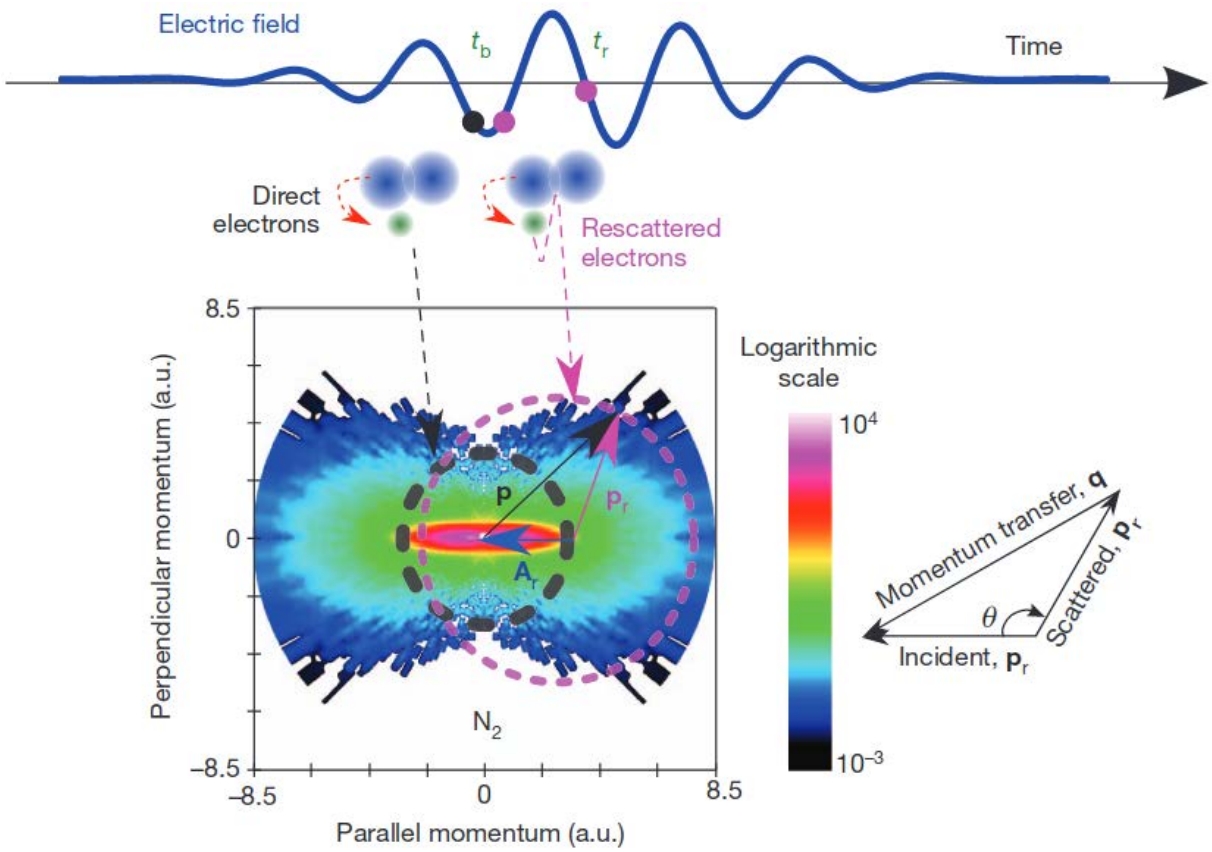

Figure 4.5 – *Strong-field rescattering. An electron is released at time t_b in the electric field (solid blue line) of an intense mid-infrared laser. For certain initial times t_b, 'direct' electrons drift away from the core (solid blue), detected with momenta inside the dashed black circle. At other birth times, the electron returns roughly an optical cycle later back to the core (magenta trajectory). After elastic backscattering the electron gains additional momentum from the field, resulting in a larger detected momentum and separability from the direct ones (magenta dashed circle). A quasi-classical analysis allows one to deconstruct the detected momentum* $\mathbf{p}$ *into the momentum during rescattering* $\mathbf{p}_r$*, using the vector relationship* $\mathbf{p} = \mathbf{p} - \mathbf{A}_r$ *(atomic units), where* $\mathbf{A}_r = \mathbf{A}(t_r)$ *is the field's vector potential at* t_r*. The inset defines the incident momentum* $\mathbf{p}$*, the scattered momentum* $\mathbf{p}_r$*, the rescattering angle* θ *and the momentum transfer* $\mathbf{q}$*. Extracted from [Blaga 12]*

and OCS with a precision of $< \pm 5$ pm [Karamatskos 19]. LIED has been performed in aligned molecules [Pullen 15]. LIED has also been performed in poly-atomic molecules like ammonia [Belsa 21] and Fenchone [Liu 21], where machine learning techniques has been used to extract the molecular structure from the DCS.

II. 4 Chirality in Strong field Ionization

In the strong field approximation picture, the influence of the ionic potential on the departing electron is neglected. In this framework, the strong-field ionization process is thus not expected to be sensitive to molecular chirality [Dreissigacker 14]. However, measurements of the photoionization of Fenchone molecule by a strong circularly polarized laser field have revealed the existence of a significant ($\sim 2\%$) forward/backward asymmetry (PECD) in the photoelectron angular distribution (see Fig. 4.6) [Beaulieu 16].

Several experimental and theoretical studies have in fact established that molecular chirality

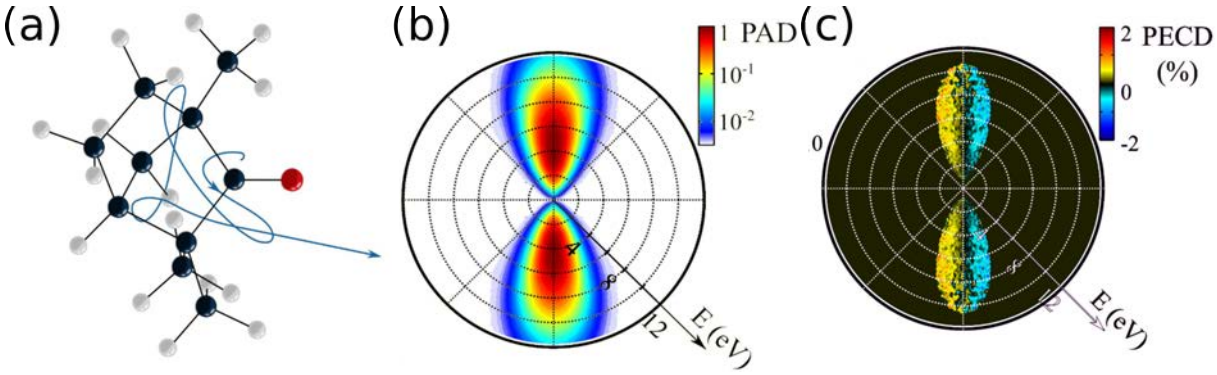

Figure 4.6 – *(a) CTMC electron trajectory in Fenchone when ionized by a circularly polarized laser pulse at a 800 nm wavelength and $I = 10^{14}$ Wcm^{-2} . (b) - (C) The raw 2-D projection of the PAD and its corresponding PECD is shown for $\lambda = 1850$ nm pulses with an intensity of $I \sim 4 \times 10^{13}$ Wcm^{-2}. Reproduced from [Beaulieu 16]*

could play a crucial role in several steps of the strong-field ionization process. Most obviously, the chiral ionic potential can affect the propagation of the electron in the continuum. In other words, the electron not only oscillates in the ionizing field but also scatters from the chiral ionic core [Dreissigacker 14, Beaulieu 16]. Second, the tunneling process, which is the first step of strong-field ionization, can also be sensitive to molecular chirality. The electronic wavepacket emerging from the tunnel in a rotating electric field will be different in a chiral molecule and its mirror image [Bloch 21]. Here we aim at examining the influence of the third step of the strong-field ionization process: the rescattering of the electrons onto their parent ion. The rescattering electrons, which are driven back by laser field and penetrate deep into the chiral molecular potential, interact more with the chiral potential and hence should show more PECD. On the other hand, observing PECD requires a circularly polarized ionizing field, but there is no rescattering in circular polarization because the electrons are not driven back to their parent ion.

There are two main ways of circumventing the problem of closed electronic trajectories. Firstly, with the use of synthetically polarized fields. One can use bi-linear or bi-circular fields to generate closed electronic trajectories of these rescattering electrons [Kfir 16] [Fleischer 14] [Neufeld 18] [Mancuso 16]. Interestingly such fields can also reveal sub-optical cycle chiral light matter interactions [Bloch 21]. Secondly and more simply, one can use elliptically polarized light. The probability of recollision decays exponentially with laser ellipticity [Budil 93], but a significant signal from backscattered electrons can still be observed using significant ellipticities. It should thus be possible to find a trade-off between the necessary rotation of the laser field, giving rise to a dichroic signal, and the existence of recolliding electron trajectories.

III Experimental Setup and Data Analysis

III. 1 Experimental Setup

Strong field photoionization of Fenchone, α-Pinene, Camphor and Limonene was conducted in the VMI using the 2^{nd} arm (TG2) of the Blast Beat fiber laser system as described in Section I.

The 50 W output of the TG2 amplifier, delivers pulses with a pulse width of 130 fs wavelength centered at 1030 nm and working at 1 MHz, is incident onto a thin film polarizer associated with a half waveplate, used as a variable attenuator. The polarization state of the laser is further cleaned using another thin film polarizer (see Fig. 4.7). The linearly polarized light is then incident onto a B. Halle zero order $\lambda/2$ waveplate which is mounted on a continuously rotating mount (Newport RGV100BL). The polarization state of the laser beam after the $\lambda/2$ waveplate is measured using a continuously rotating quarter-wave polarimeter (see Fig. 2.6 (c)), and is purely linear. The linearly polarized light after the $\lambda/2$ waveplate is incident on a fixed B.Halle $\lambda/4$ waveplate. The polarization state of the laser beam after the $\lambda/4$ waveplate is measured for different orientation of the laser polarization with respect to the fast axis of $\lambda/4$-the waveplate (see Fig. 2.6 (d-g)). The third Stokes parameter is extracted using Py-pol library and is 0.00 for the linear polarizations and $|S3| = 0.99$ for both left and right circular polarizations. The beam is then expanded using a $\times 4$ telescope $(-75/+300$ mm) before being focused into the VMI using a +200 mm focusing lens. The focal spot-size is measured using a CCD camera with a FWHM of 17.94 μm. Thus reaching intensities of $1-3\times10^{13}$ W/cm^2. This corresponds to an ponderomotive potential energy gained by an electron of $\sim 1-3$ eV and a Keldysh parameter $\gamma \approx 2-1.2$ indicating that the experiment takes place in the non-adiabatic tunneling regime. The schematics of the experimental setup is shown in Fig. 4.7.

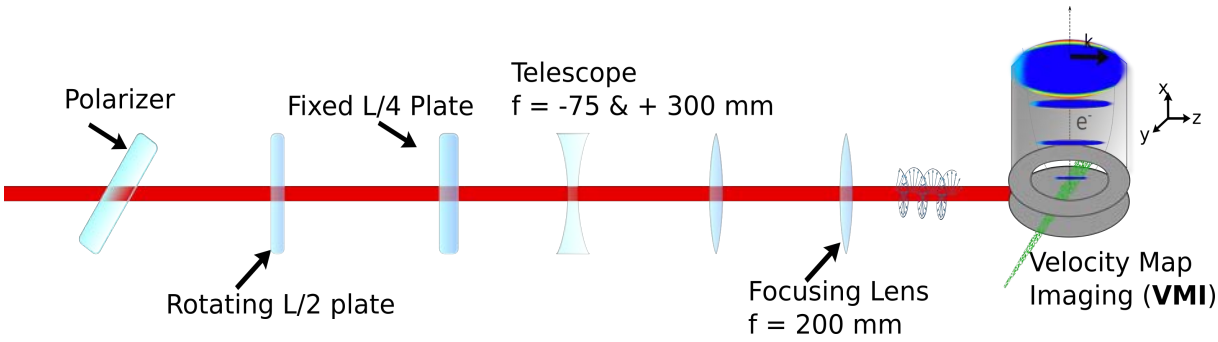

Figure 4.7 – *A schematics of the experimental setup is shown to measure the photoelectron electron angular distributions in a lock-in mechanism. A high contrast polarizer is used to clean any reaming polarization artifacts in the laser beam. A continuously rotating $\lambda/2$ waveplate is placed before a fixed $\lambda/4$ waveplate to change the ellipticity of the beam while keeping the orientation of the polarizing ellipse constant. A telescope is used to enlarge the laser beam by a factor of 4 and the laser beam is focused into the velocity map imaging spectrometer using a focusing lens of focal length $f = +200mm$. The target chiral molecules are introduced into the VMI spectrometer in a direction perpendicular to the propagation of the laser beam and the VMI spectrometer axis. The co-ordinates are shown in the inset and is used throughout the chapter unless otherwise mentioned.*

III. 2 Fourier Reconstruction

The cross-sectional probability of rescattering electrons in strong field ionization is generally $10^{-2}-10^{-4}$ times lower than that of the direct electrons. To increase the number of rescattering events detected in the VMI the laser repetition rate is increased to 1 MHz and the gas pressure in the VMI is also increased, the limitation being the appearance of space charge effects in the VMI. An additional difficulty of the experiment comes from the fact that we aim at detecting forward-

backward asymmetries in the emission of the electrons, which are generally in the range of a few %. Thus one needs to perform a noise free detection of the photoelectron angular distribution. One such way is to perform a lock-in detection of the PAD for different ellipticities, as we have seen in the previous chapter. In the setup we were using to investigate multiphoton ionization, the polarization state of the light was modulated by rotating a $\lambda/4$ waveplate. This means that the orientation of the ellipse was rotating as the ellipticity was varied. For the current experiment, we aim at working with a fixed polarization ellipse. The optical configuration is thus slightly different.

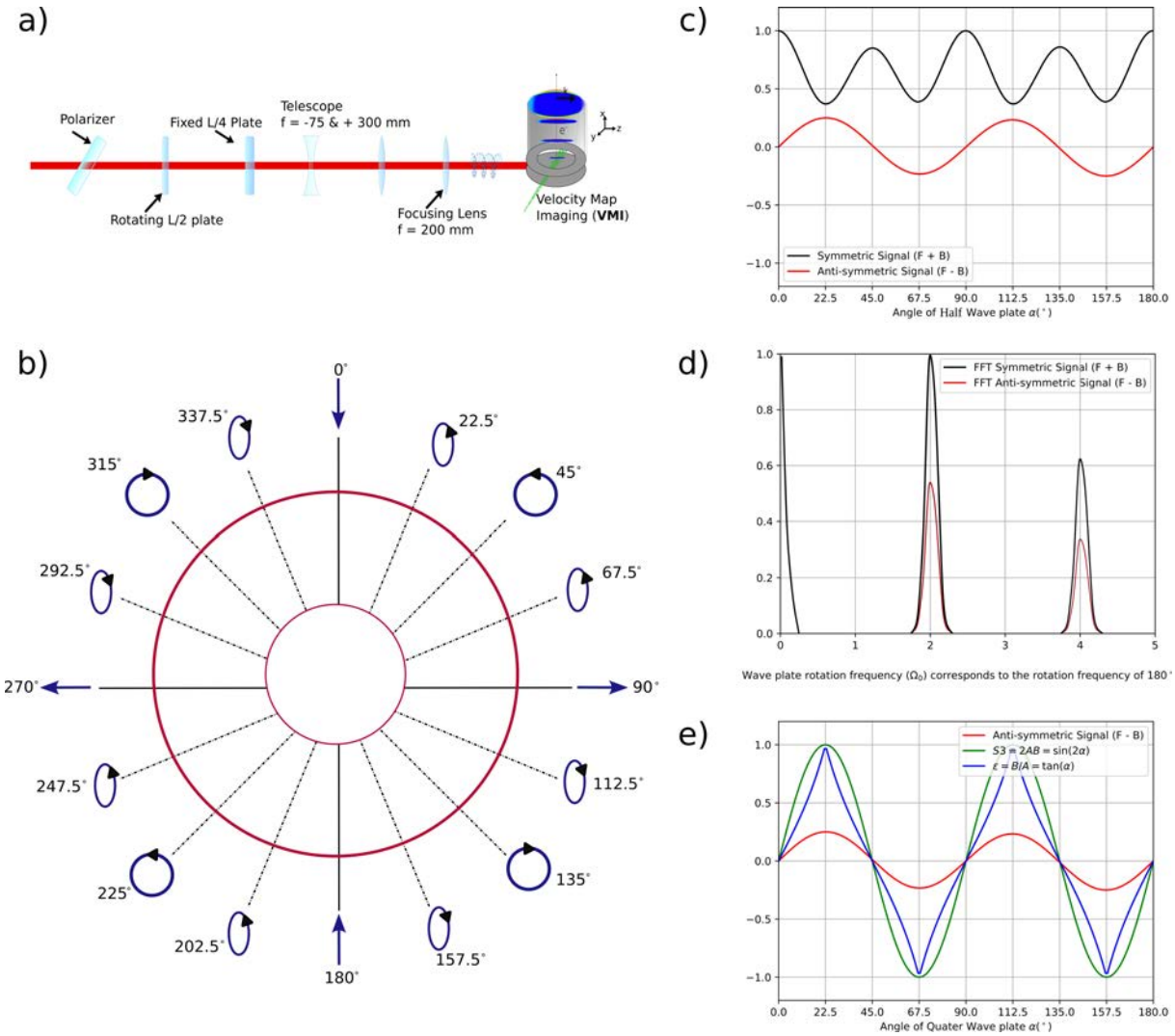

Figure 4.8 – *The principle of working of a lock-in measurement of the photoelectron angular distribution is depicted. (a) Shows a typical setup to perform a lock-in detection of the PAD. (b) Shows the evolution of the laser ellipticity in the lab frame as a function of the angle (α) made by the neutral axis of the half waveplate, placed in front, with respect to the fast axis of a fixed quarter waveplate. Note the angle shown in the figure is 2α. (c) Shows the schematic evolution of the total photoelectron yield and the antisymmetric part of the signal of the VMI images with respect to the angle (α) made by the neutral axis of the half waveplate with respect to the fast axis of a fixed quarter waveplate. (d) Shows the corresponding Fourier transform of the periodic symmetric and antisymmetric signal. (e) Shows the variation of the ellipticity and the third stokes parameter with the angle α.*

The initial polarization is linear horizontal. The rotating $\lambda/2$ waveplate induces a rotation

of this polarization. At any given instant of time the linear horizontally polarized laser beam makes an angle α with respect to the neutral axis of the $\lambda/2$ waveplate. After passing through the $\lambda/2$ waveplate the linearly polarized laser beam gets rotated by an angle 2α. This beam is then incident onto a fixed $\lambda/4$ waveplate, i.e. the neutral axis of the $\lambda/4$ waveplate is fixed in the lab frame. As the $\lambda/2$ waveplate rotates continuously ($22.5°/s$) the polarization axis of the electromagnetic wave rotates continuously. When α increases from 0 to 22.5°, the polarization state of the light emerging from the $\lambda/4$ waveplate goes from linear horizontal to circular (Fig. 4.8). Further rotation of the $\lambda/2$ waveplate brings the pulse back from circular to linear, but along the other neutral axis of the $\lambda/4$ waveplate, i.e. horizontal. This schemes thus enables recording two orthogonal projections of the photoelectron angular distribution for each ellipticity.

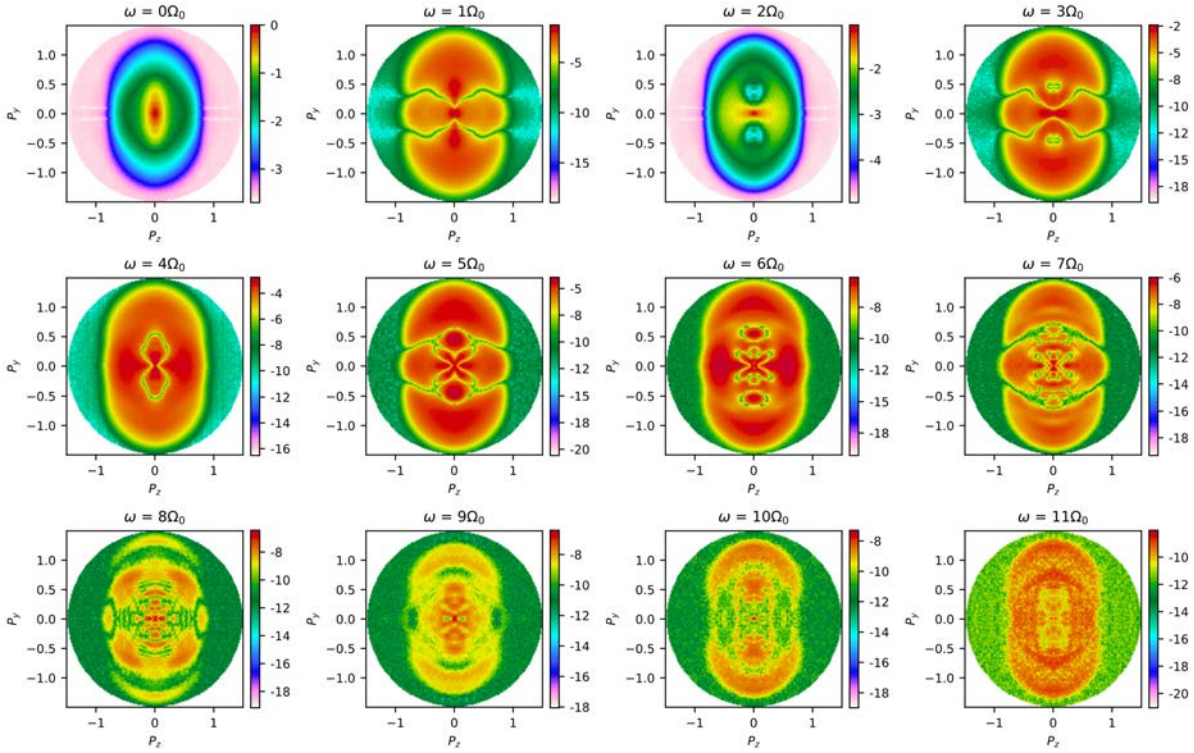

Figure 4.9 – *The 2-D maps of the FFT components of the symmetric part of the PAD oscillating at $k\Omega_0$ (where $n \in \mathbb{W}$).*

As the ellipticity is continuously scanned the images obtained on the camera of the VMI are 2-D projections of the 3-D photoelectron angular distribution given as $\mathcal{P}(p_x, p_z, S3) = \int P(p_x, p_y, p_z, S3)dp_y$ ($S3$ being the third Stoke's parameter). From these 2-D projections of the PAD a forward-backward symmetrized and anti-symmetrized images are constructed which are defined as $\mathcal{P}_{\text{sym}}(p_x, p_z, S3) = (\mathcal{P}(p_x, p_z, S3) + \mathcal{P}(p_x, -p_z, S3))/2$ and $\mathcal{P}_{\text{asym}}(p_x, p_z, S3) = (\mathcal{P}(p_x, p_z, S3) - \mathcal{P}(p_x, -p_z, S3))/2$ respectively. Physically, $\mathcal{P}_{\text{sym}}(p_x, p_z, S3)$ corresponds to the photoelectron angular spectra (PES) and $\mathcal{P}_{\text{asym}}(p_x, p_z, S3)$ correspond to the chiral response spectra as a function of ellipticity or photoelectron elliptical dichroism (PEELD). Each of the 2-D images thus obtained are fast Fourier transformed along $S3$, pixel per pixel, described as $\mathcal{P}_{\text{sym}}(p_x, p_z, \Omega)$ and $\mathcal{P}_{\text{asym}}(p_x, p_z, \Omega)$. This spectra in the $S3$ Fourier space shows peaks at $k\Omega_0$, where $2\Omega_0$ is the frequency of the change in $S3$ and $k \in \mathbb{W}$. By construction $\mathcal{P}_{\text{sym}}(p_x, p_z, S3)$

(PES) and $\mathcal{P}_{\text{asym}}(p_x, p_z, S3)$ (PEELD) are even and odd functions respectively. Hence, they are purely real or imaginary and thus they can be reconstructed using inverse discrete Fourier transform, with frequencies $f \in k$. This reconstruction method helps us to isolate the oscillatory signal pixel per pixel form noise.

On contrast to the frequency components seen in the Fourier filtering method discussed in chapter 3 section IV. 2, where the symmetric part of the PAD oscillated at even frequencies and asymmetric part of the PAD oscillates at odd frequencies, in this scheme both of the symmetric and asymmetric parts of the PAD oscillate at the same frequencies $k\Omega_0$ (where $k \in \mathbb{W}$). Fig. 4.9 and 4.10 shows the symmetric and asymmetric 2-D spectra oscillating at $k\Omega_0$. For the symmetric part of the PAD we see that frequencies as high as $12\Omega_0$ show significant structures. This is due to the structurally rich PAD in the strong field regime compared to the PAD for multiphoton ionization. Spectroscopically speaking both the 2-D symmetric and asymmetric frequency maps are unique to the molecule and the asymmetric maps change sign as a function of the enantiomers, similar to that observed in the multiphoton regime. In other words the phase of the 2-D spectral map of the asymmetric component is sensitive to the handedness of the enantiomer. These 2-D spectral maps encode information about the structural dependence of the PAD and PEELD on the ellipticity of the ionizing laser field, which can be retrieved by Fourier reconstruction.

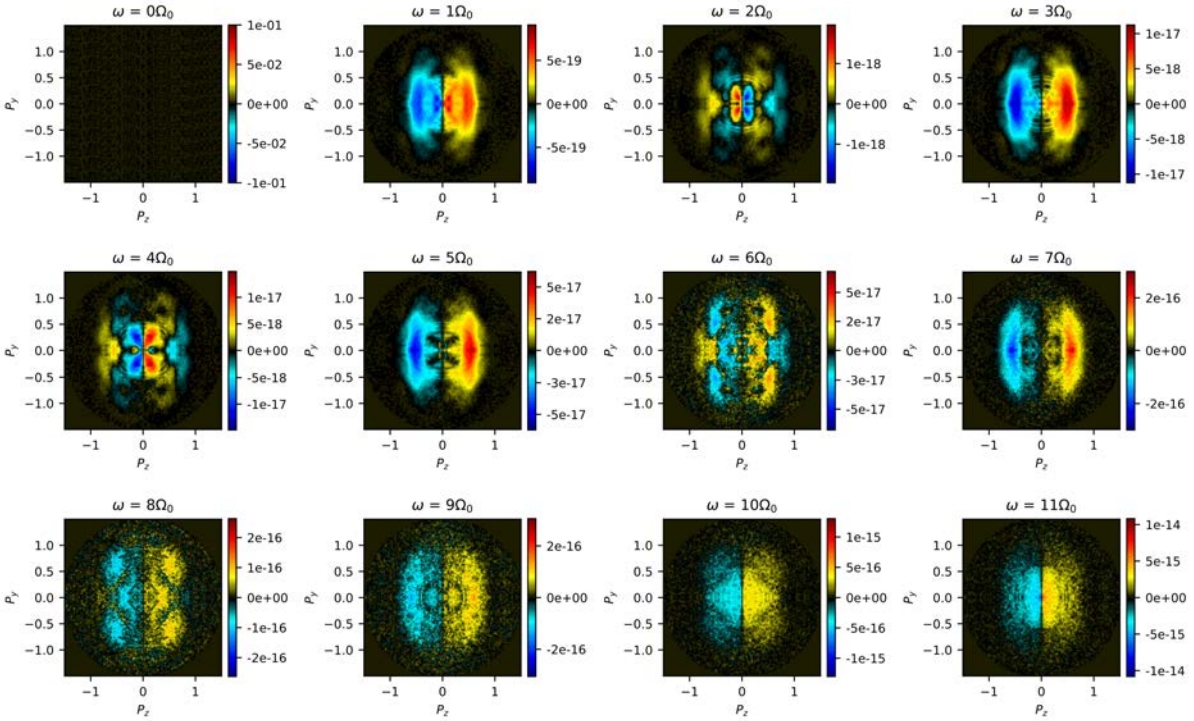

Figure 4.10 – *The 2-D maps of the FFT components of the asymmetric part of the PAD oscillating at $k\Omega_0$ (where $n \in \mathbb{W}$).*

IV Results and Discussion

Figure 4.11 shows the reconstructed 2D projection of the 3D PAD obtained by photoionizing Fenchone molecules at an intensity of 3×10^{13} W/cm^2, with a linear vertical polarization. The laser propagation direction is horizontal. At the laser intensity used here, the ponderomotive potential energy gained by an electron is about 3 eV. The direct electrons are expected to extend up to about $2U_P \approx 6$ eV, and the backscattered electrons could extend up to $10U_P \approx 30$ eV. The circles drawn in Fig. 4.11 correspond to these two energies. We can clearly see spider patterns appearing in the 2-D PAD along with holographic interference patterns due to the interference of direct and indirect electron trajectories. These patterns have been discussed in more details in Section IV. 5.

The Fourier reconstruction provides the 2D projections for different ellipticities. Due to the optical configuration used here, as the half waveplate is rotated, 2-D PAD's for both the horizontal and vertical orientation of the polarization ellipse are recorded in the VMI. The evolution of the reconstructed VMI images as a function of the position of this half waveplate is shown in Fig. 4.12. The top left panel corresponds to the image already shown in Fig 4.11. The laser ellipticity increases moving to the next panels, until circular polarization is reached at the end of the third row. The first three rows thus depict the evolution of the projection of the 3-D PAD along the short axis of the laser ellipse. The next three rows correspond to projections of the 3-D PAD along the long axis of the laser ellipse, from circular to linear polarization. The last (bottom right) pannel corresponds to a linear polarization pointing along the time-of-flight axis of the VMI. This schemes thus enables recording two orthogonal projections of the 3-D PAD, along the two axis of the $\lambda/4$ waveplate. Repeating this measurement for different orientations of the $\lambda/4$ waveplate provides all the data necessary to reconstruct the 3D PAD by tomographic reconstruction.

When the Fenchone molecule is strong field ionized using circularly polarized light $|S3| = 1$ we see that the photoelectron angular distribution is confined inside the $2U_P$ circle. Now since the direct electrons have maximum kinetic energies up to $2U_P$, the electronic trajectories present in the strong field ionization using circularly polarized light are direct electrons. Thus there are no rescattering electronic trajectories as the circularly polarized light drives the electrons away from the ionic core thus inhibiting rescattering.

As the third Stokes parameter of the incident electromagnetic wave is decreased (for $|S3| < 0.75$) we start to see that electrons gain kinetic energies higher than $2U_P$. Thus indicating the presence of indirect electronic trajectories as the tunneled out electronic wavepacket is partly driven back to the ionic core and they rescatter from it thus gaining kinetic energies higher than $2U_P$. As the third Stokes' parameter is reduced the transverse component of the electric field is weaker and hence the tunneled out electrons are driven less and less away from the ionic core. This increases the probability of re-collision of the electronic wavepackets. Together with the fact that as the transverse component of the electric field decreases, for the same given intensity, the longitudinal component of the electric field increases in strength thus the re-colliding electronic wavepackets gain higher kinetic energies before re-colliding with the ionic potential. Thus gaining higher kinetic energies up to $10U_P$. As the $S3$ is further reduced the

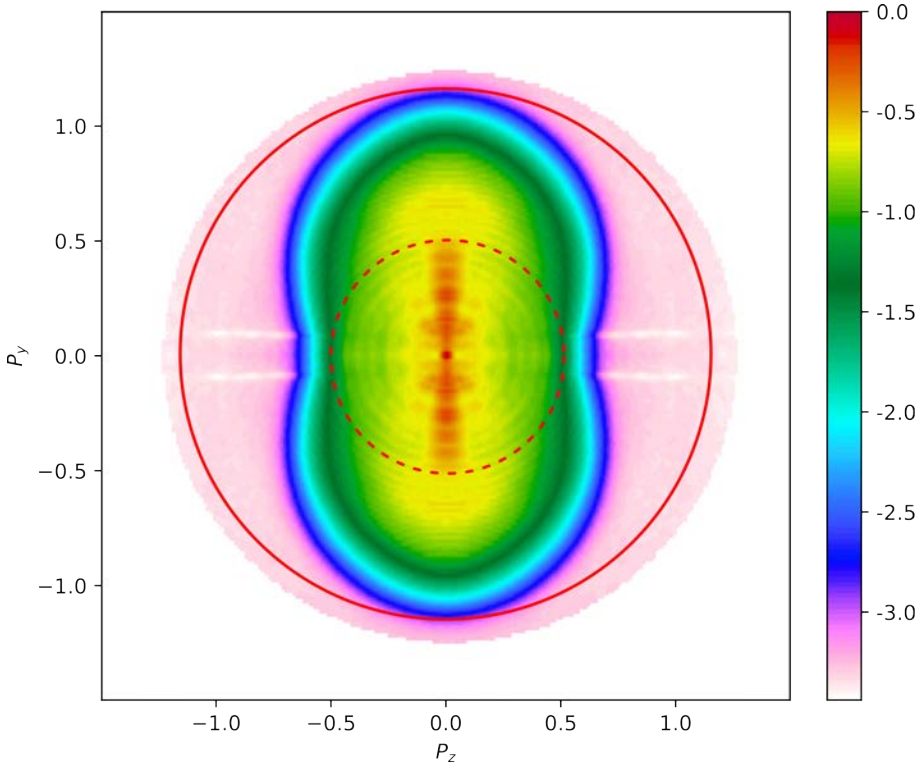

Figure 4.11 – *2-D projections of the 3-D photoelectron angular distribution acquired by the VMI, of Fenchone, in momentum co-ordinates, for linear polarization. The inner dashed red circle corresponds to $2U_p$ energy while the outer red circle corresponds to a photoelectron kinetic energy of $10U_p$. We can also the spider along with other interference structures appearing in the region below $2U_p$ due the interference of various electronic trajectories associated to strong-field ionization.*

direct and indirect electronic trajectories start interfering with each other more prominently as described in Section IV. 5. Thus producing strong holographic patterns, as already seen in (Fig. 4.11).

IV. 1 Rescattering PEELD Dependence with Ellipticity

The Fourier-reconstruction procedure is also used to extract the forward-backward asymmetry in the emission of electrons. This forward-backward asymmetry is normalized with respect to the PAD per pixel, as well as by the third Stokes parameter of the ionizing light S3. The pixel-by-pixel normalization by the PAD is done to extract a relative signal, and is necessary so as to account for the low signal in the rescattered compared to that of the direct electrons. The normalization by the S3 is done to take into account the percentage of circularly polarized light involved in the ionization process. The resultant asymmetry is the photoelectron elliptical dichroism (PEELD), introduced in the previous chapter.

As a sanity check of the measurement, we start by comparing the PEELDs obtained in opposite enantiomers (Fig. 4.13). A good mirroring is observed, validating the genuine enantiosensitive nature of the detected signal. We observe that slight differences still appear. They result from imperfections and artifacts in the electron imaging. A lot of work has been performed to optimize the VMI and reduce the contribution of these artifacts. To fully eliminate them,

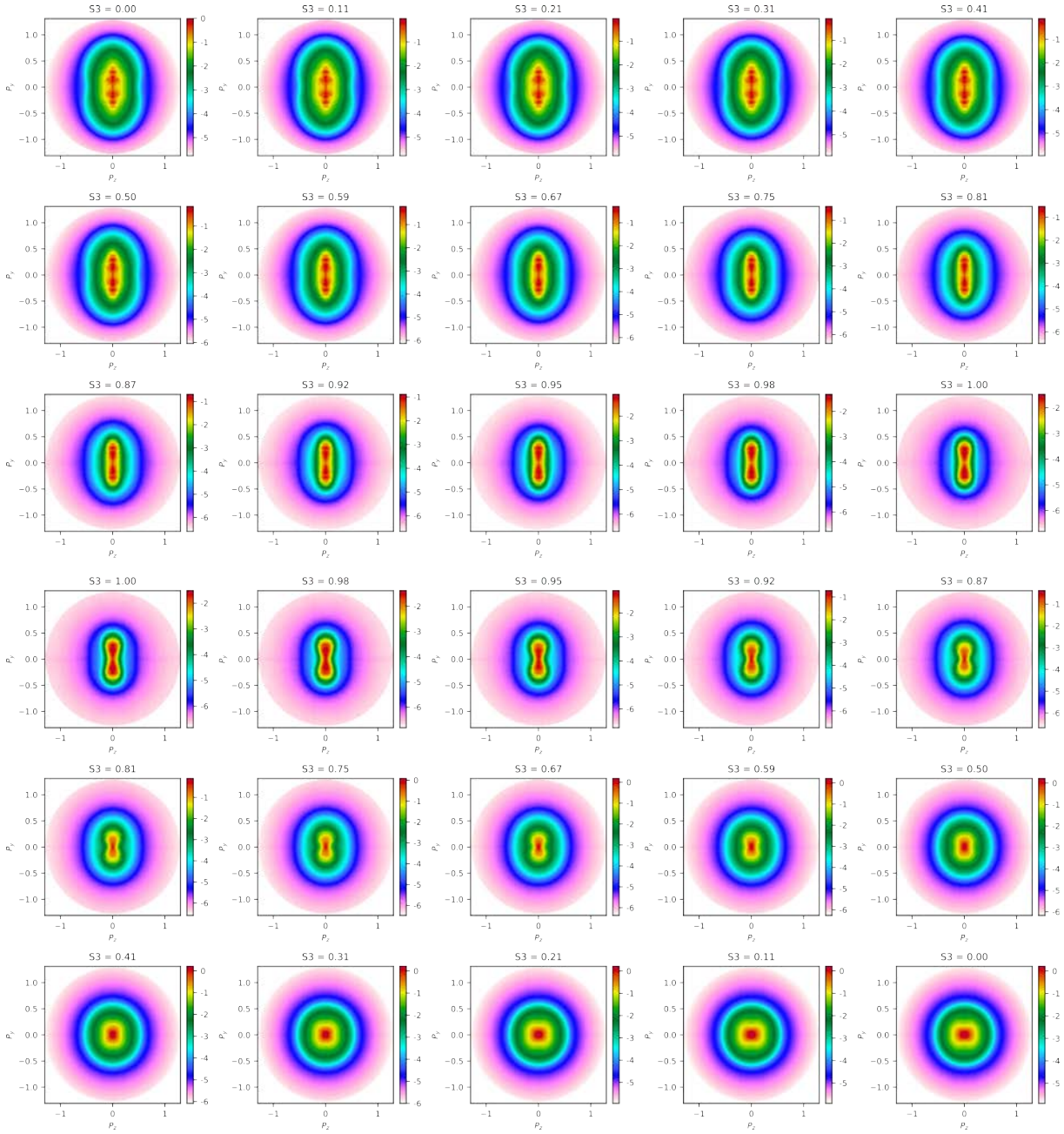

Figure 4.12 – *2-D projections of the 3-D photoelectron angular distribution acquired by the VMI, of Fenchone, in momentum co-ordinates for various ellipticities. Note that for a given orientation of the $\lambda/4$ waveplate a horizontal and vertical projection of the 3-D PAD is measured in the VMI.*

in the following we perform a differential measurement by subtracting the response of opposite enantiomers. The resulting PEELD are shown in Fig. 4.14.

PEELD is observed for all values of S3. An asymmetry of about 2% is observed for circularly polarized light. This asymmetry arises due to the scattering of the tunneled out electronic wavepacket in the continuum which is modified by the molecular chiral potential. Also there can be an influence of the chiral potential during the tunneling process [Bloch 21].

For S3$<$ 0.76 we see that the rescattered electrons, i.e. electron with kinetic energies higher than $2U_P$, show higher degree of asymmetry than direct electrons. As the S3 is reduced, the

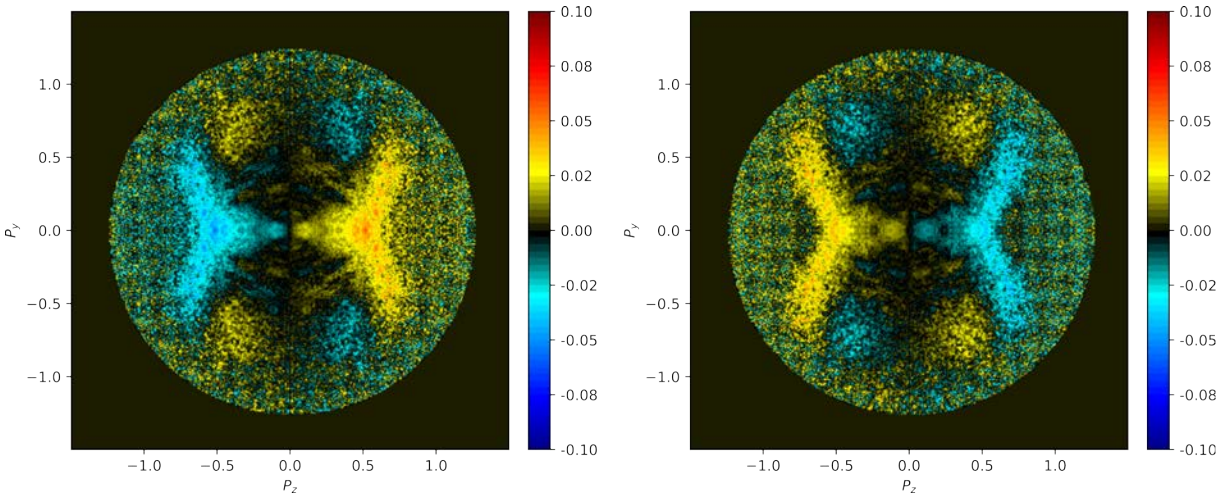

Figure 4.13 – *2-D projections of the PEELD for (+)α-Pinene (on left) and (-)α-Pinene (on right) are shown, in momentum co-ordinates for $S3 = 0.25$. We clearly see a good mirroring between the two enantiomers indicating that there are no artifacts in the measurements. We observe a* 10% *PEELD in both enantiomers.*

electronic wavepacket is driven back to ionic core, rescatters off the chiral potential and ends up asymmetric with respect to the laser propagation direction. On further reducing the S3 the rescattering electrons penetrate deeper inside the ionic core, showing a stronger forward-backward emission asymmetry. It is also to note that although the PEELD increases with a decrease in S3, its overall structure remains similar throughout.

Thus upon strong-field ionization of chiral molecules we observe a strong forward-backward asymmetry, upto 30%, in the emission of electrons. The 2-D PEELD spectra for strong-field ionization of α-Pinene, Fenchone, Camphor and Limonene for different ellipticities and at an intensity of 1.5×10^{13} W/cm^2, are shown in Fig. 4.15 *in energy coordinates*. Their respective molecular structure is shown in the inset. The 2-D PEELD shown is normalized with respect to the PES and S3. The outer red circle demarcates the maximum electron kinetic energy of $10U_P$ while the inner circle contains electrons with energies $< 2U_P$. We observe a forward-backward asymmetry in the emission of electrons for both direct and rescattered electrons. We observe a 4%, 4%, $<$ 0.5% and 0.6% asymmetry in the emission of electrons for α-Pinene, Fenchone, Camphor and Limonene respectively when strong field ionized by circularly polarized light.

An asymmetric emission of 6%, 8%, 1% and $\sim$ 0.7% is observed for α-Pinene, Fenchone, Camphor and Limonene respectively for an ellipticity of $S3 = 0.7$. When the laser ellipticity is further decreased to $S3 = 0.2$, an even higher asymmetric emission of 15%, 20%, 4% and $\sim$ 5% is observed for α-Pinene, Fenchone, Camphor and Limonene. Remarkably, the general structure of the 2-D distribution of asymmetric emission of the electrons does not vary much with ellipticity and is almost the same up to the ellipticities of $S3 = 0.7$. Most of the asymmetry is contributed by the rescattered electrons in the low ellipticity regime.

As we measure the 2-D asymmetric electron distribution for different molecules we not only see that the total strength of the asymmetry is different but also that the 2-D structure of the distribution varies for all the molecules. Even for isomers, Fenchone and camphor, the 2-D structure of the PEELD is significantly different in quantity and structure. Thus showing that

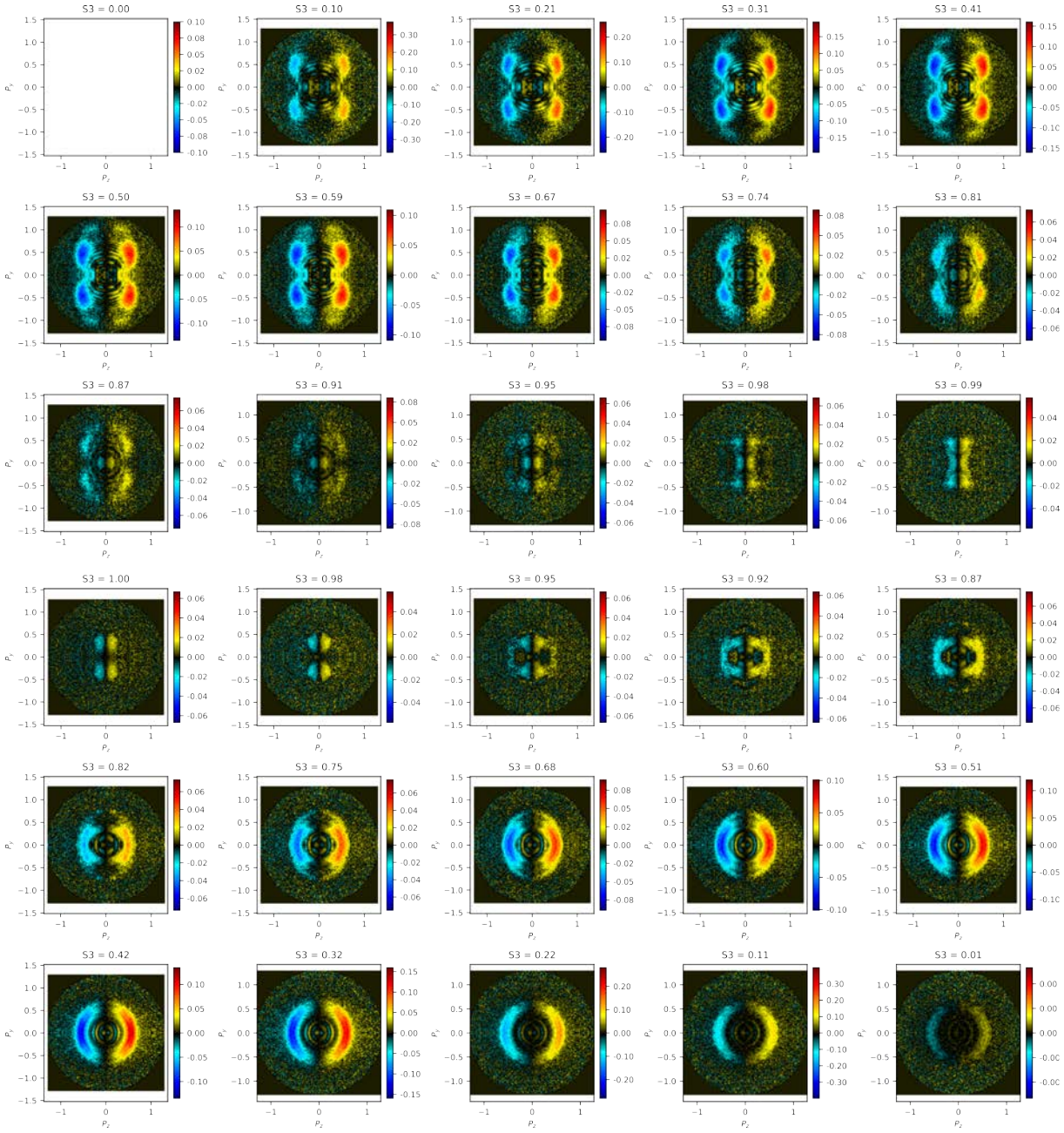

Figure 4.14 – *2-D projections of the 3-D photoelectron elliptical dichroism distribution acquired by the VMI, of Fenchone, in momentum co-ordinates for various ellipticities. Note that for a given orientation of the $\lambda/4$ waveplate a horizontal and vertical projection of the 3-D PEELD is measured in the VMI.*

the asymmetry in the rescattered electrons are extremely sensitive to the molecular structure or potential. This also provides a way to discriminate various chiral molecules from one another.

IV. 2 3D distributions

The acquisition procedure that we have used, where a rotating $\lambda/2$ waveplate is placed in front of a fixed $\lambda/4$ waveplate, enables recording two projections of the photoelectron angular distribution. Repeating the measurements for various orientations of the $\lambda/4$ waveplate provides

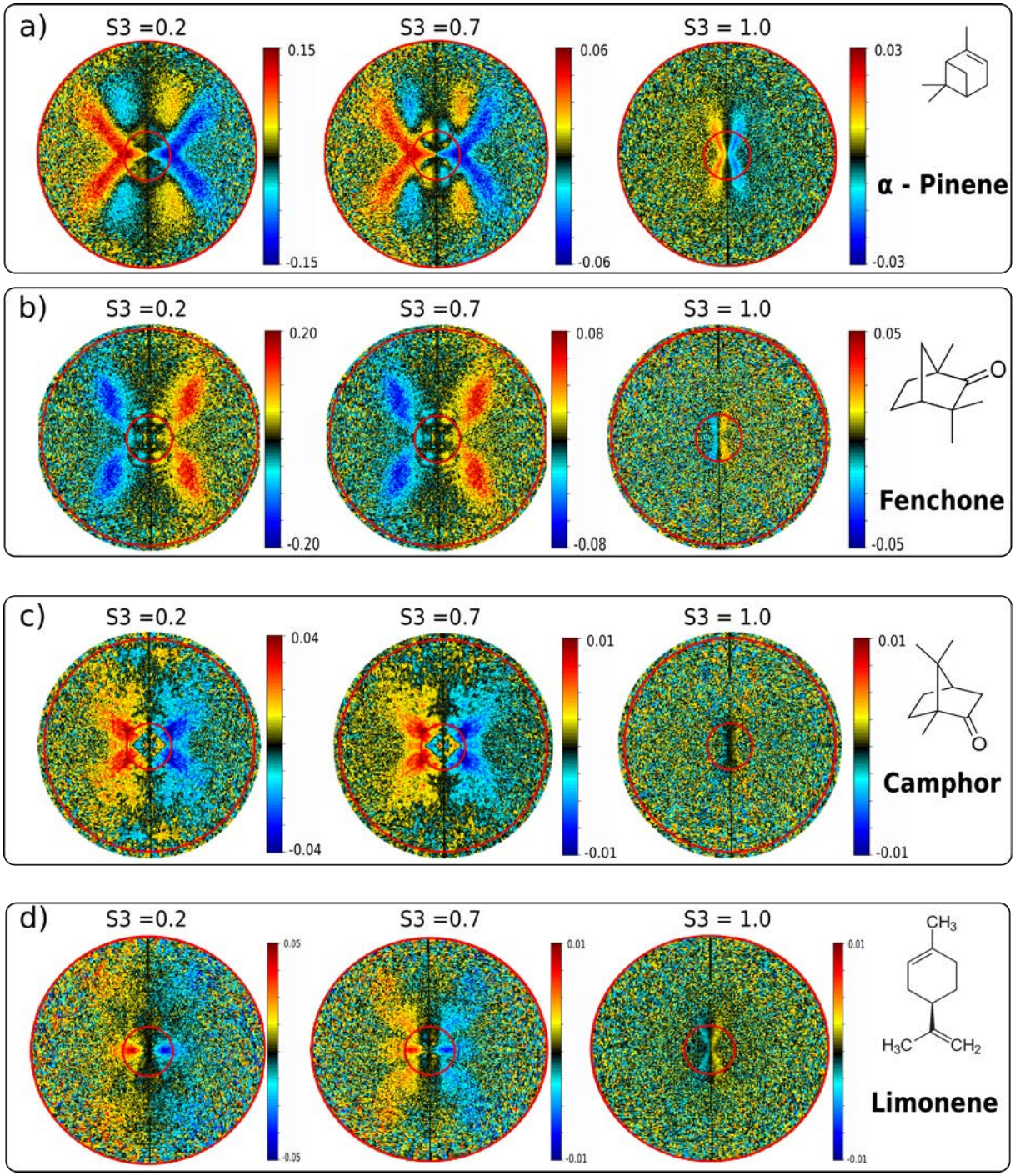

Figure 4.15 – *2-D PEELD distribution of α-Pinene, Fenchone, camphor and limonene (top-bottom) are shown in energy co-ordinates for various ellipticities. The molecular structure is shown in the inset for the respective molecules studied.*

multiple projections of the 3D distribution, which can be reconstructed tomographically. In the experiment we rotated the $\lambda/4$ waveplate by steps of 5 degrees and performed 72 measurements. Each measurement consisted in a 2000 images, acquired with 50 ms exposure time and in which the $\lambda/2$ waveplate was continuously rotated at 22.5°/s.

Figure 4.16 and 4.17 show the reconstructed 3D angular distributions obtained respectively

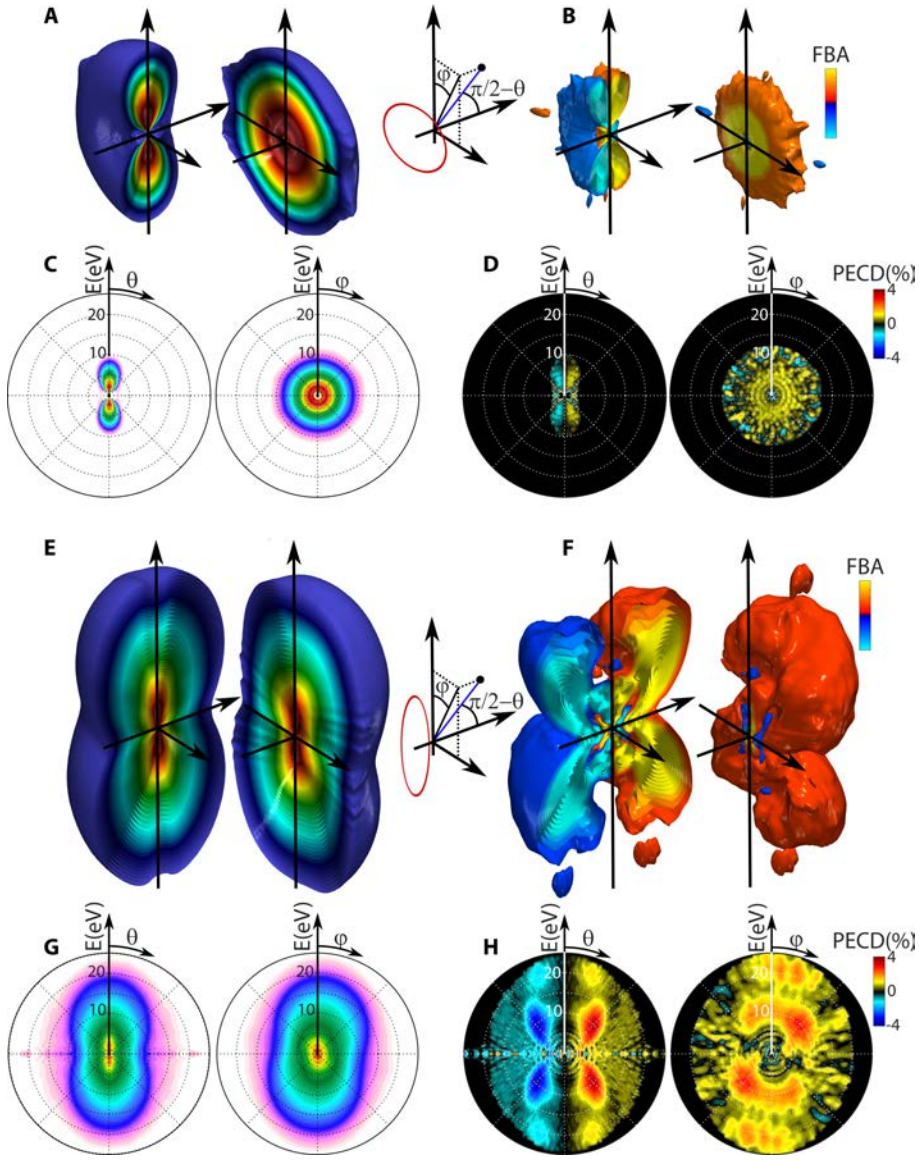

Figure 4.16 – *Strong-field photoelectron elliptical dichroism in Fenchone ionized by* 2.5×10^{13} $W.cm^{-2}$ *laser pulses at 1030 nm.* ***A*** *Energy-range 3D photoelectron angular distribution and* ***B*** *forward/backward asymmetric part of the angular distribution, in circularly polarized light.* ***C*** *Angular dependence of the photoelectron spectrum and* ***D*** *of the normalized PECD.****E*** *Energy-range 3D photoelectron angular distribution and* ***F*** *forward/backward asymmetric part of the angular distribution, in elliptically polarized light with* $\varepsilon = 0.3$. ***G*** *Angular dependence of the photoelectron spectrum and* ***H*** *of the normalized PEELD.*

in Fenchone and $\alpha-$Pinene, in energy range. The 3D distribution was tomographically reconstructed from the set of projections using inverse radon transform as described in Section II. 2. The 3-D PAD and the corresponding PEELD are shown for $\epsilon = 1\&0.3$ for both Fenchone and α-Pinene. We see a strong forward-backward asymmetry in the 3-D distributions of both the chiral molecule and both ellipticity. For the analysis we introduce spherical coordinates drawn in the inset of Fig. 4.16 & Fig. 4.17. Integrating the data over ϕ provides the photoelectron spectrum as a function of the electron ejection angle θ with respect to the polarization plane. For circular polarization we see that the electron spectrum extends to approximately 7 eV, which

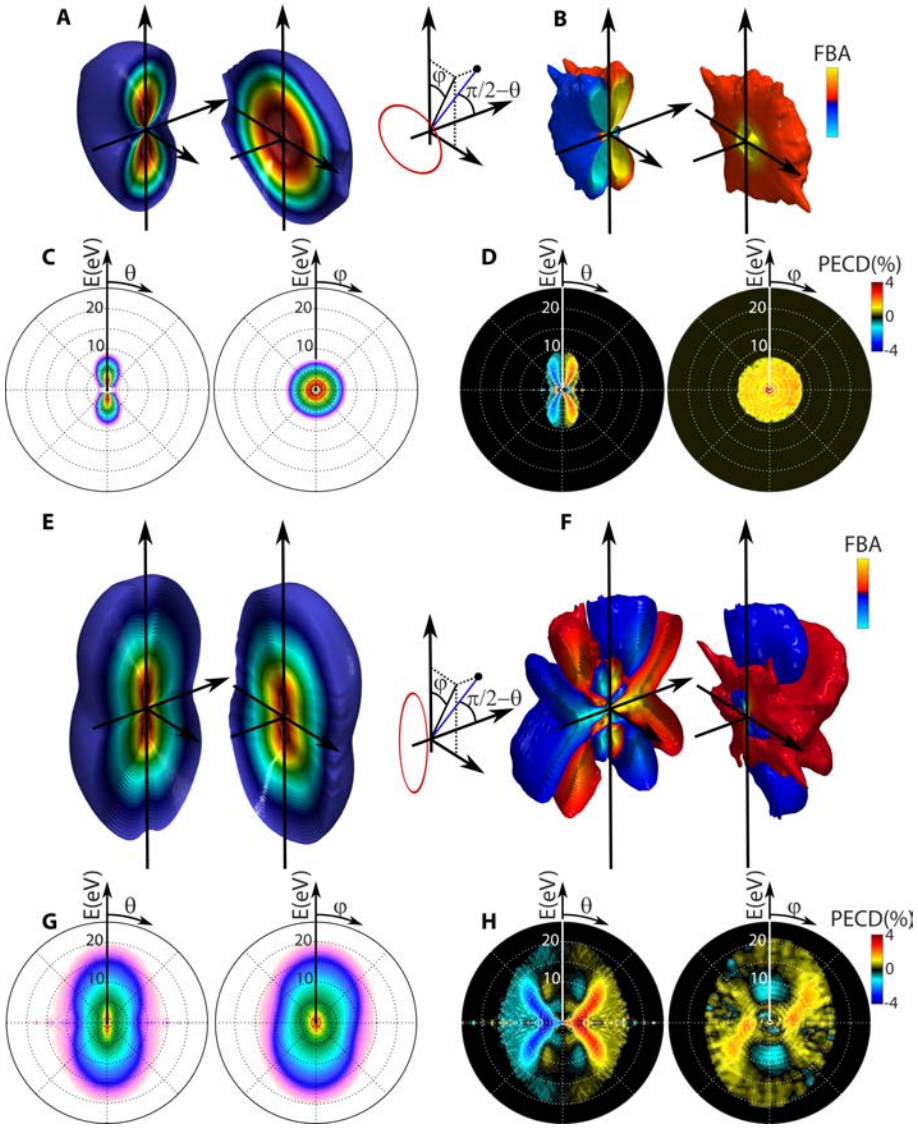

Figure 4.17 – *Strong-field photoelectron elliptical dichroism in α−-Pinene ionized by* 2.5×10^{13} $W.cm^{-2}$ *laser pulses at 1030 nm.* ***A*** *Energy-range 3D photoelectron angular distribution and* ***B*** *forward/backward asymmetric part of the angular distribution, in circularly polarized light.* ***C*** *Angular dependence of the photoelectron spectrum and* ***D*** *of the normalized PECD.****E*** *Energy-range 3D photoelectron angular distribution and* ***F*** *forward/backward asymmetric part of the angular distribution, in elliptically polarized light with* $\varepsilon = 0.3$. ***G*** *Angular dependence of the photoelectron spectrum and* ***H*** *of the normalized PEELD.*

corresponds to $2 - 3U_p$. This is due to the fact that the electrons driven by circularly polarized light do not recollide with their parent ion. Hence, the maximum kinetic energy they can gain from the field is $2U_p$, while the extra kinetic energy is gained by the photoelectron is due to the interaction of the escaping electron with the ionic potential. The PECD is rather low, in the $\sim 1\%$ range. This is typical of the strong field regime, where the influence of the chiral ionic potential on the departing electrons is weak [Beaulieu 16] [Bloch 21].

When the laser ellipticity is reduced to $\epsilon = 0.3$, we observe an important extension of the photoelectron spectrum towards high energies, with electrons emitted beyond 20 eV, in the $10U_p$

range. These high energies are reached by electrons that elastically collide with their parent ion, as in Fig. 4.16 & Fig. 4.17 D. The laser ellipticity clearly breaks the cylindrical symmetry of the electron distribution. The ϕ-resolved photoelectron spectrum shows that low energy components maximize toward negative ϕ angles, whereas high energy electrons maximize towards positive ϕ angles. These different angular streakings in the elliptical laser fields are characteristic of direct and rescattered electrons. The ϕ-integrated PEELD shows butterfly wings maximizing around $\theta = 45°$ at 10 eV electron energy. The PEELD reaches 4%, and is thus four times stronger than the PECD recorded with circularly polarized light. As the electron energy increases, the PEELD decreases but shows secondary maxima at high energy (> 20 eV) for small ejection angles θ.

In α-Pinene, the 3D photoelectron angular distributions and the FBA measured in circularly polarized light (Fig. 64.17 (A-D)) closely resemble the one measured in Fenchone. However the PEELD of is completely different. We observe a clear sign change in the PEELD from rescattering electrons. The electrons ejected at intermediate energies, close to the polarization plane, show an opposite PEELD compared to the electrons ejected at higher angles. We have seen that interference effects could play an important role in the shape of photoelectron angular distributions. The sign change we observe here is beyond the area in which direct electrons contribute. We can thus rule out the possibility that the sign change may be due to the interference between direct and indirect electrons. However we have seen earlier that several electron trajectories could lead to the same final energy after electron recollision. In the following we discuss the influence of these different trajectories and show how they can be identified.

IV. 3 Identification of Electron Trajectories

We have seen that from classical simulations, up to four electronic trajectories, first return short and long and second return short and long trajectories, can lead up to the same kinetic energies (Fig. 4.3). First return trajectories extend to 10Up, while second return trajectories extend to 7Up. Between 2Up and 7Up, four electronic trajectories can in principle coherently add up to form interference. It has been shown that the contribution of the short trajectories, in the photoelectron spectra, is relatively negligible because they are born late in the optical cycle where the tunneling probability decreases exponentially with the decrease in the field strength. Thus the electronic trajectories, beyond the cut-off energies of the second return electrons (7Up), are dominated by the long trajectories of the first return electrons. Below this energy, we can use the ellipticity dependence of the ionization signal to identify the trajectories at play.

It has been shown in the semi-classical picture of strong field ionization that the first and second return electrons behave differently with the ellipticity of the incident electromagnetic wave. Within the semi-classical description the electronic wavepacket exits the tunnel with no longitudinal velocity, but with a Gaussian transverse velocity distribution centered around zero [Dudovich 06]. The tunneled out electrons are then accelerated by the elliptical laser field and they re-collide back with the ionic core only if their initial transverse velocity exactly compensates for the lateral drift accumulated along the short axis of the polarization ellipse. It can be shown that the long trajectories of the first return electrons require a higher transverse velocity for them to return back to the ionic core compared to second return electrons. Consequently, the

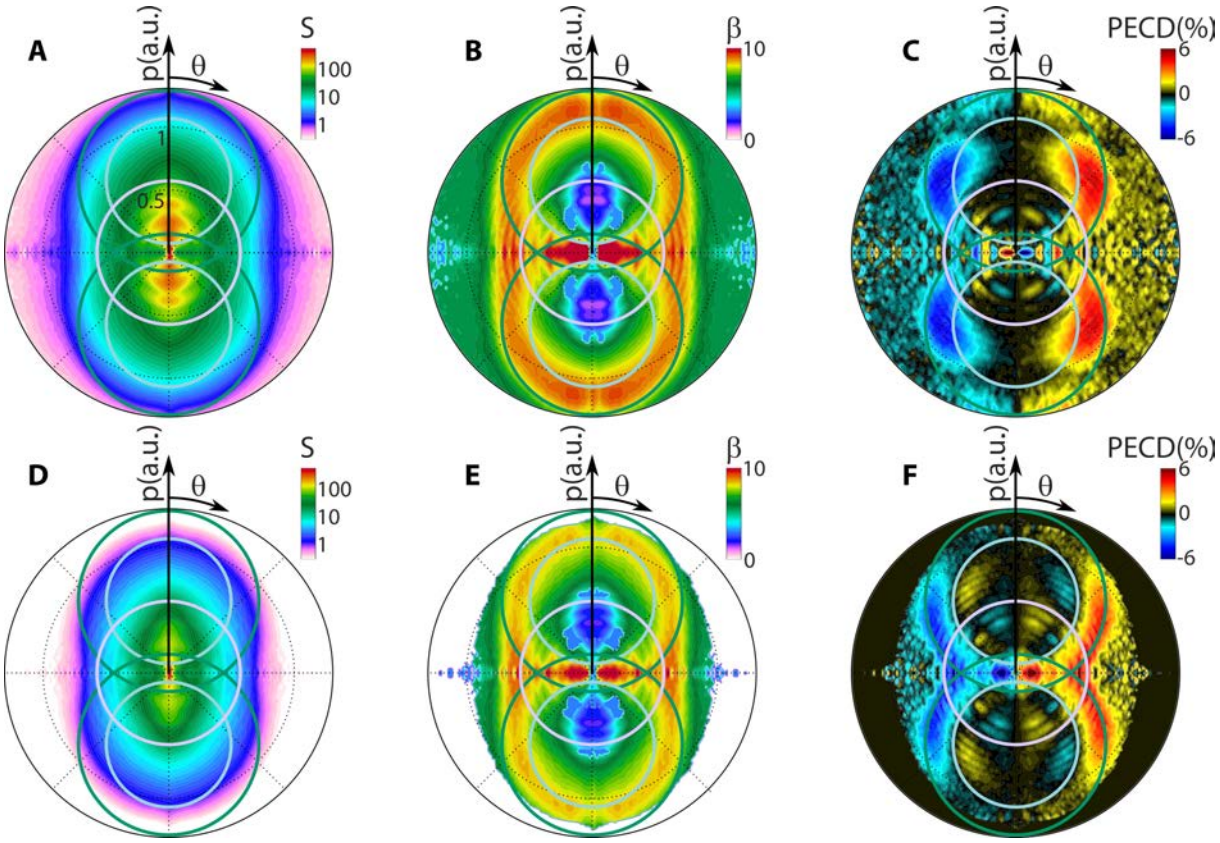

Figure 4.18 – *Trajectory identification by ellipticity dependence measurement. (a) Photoelectron momentum distribution produced in Fenchone by a 1030 nm laser pulse at 2.5×10^{13} W/cm^2 . The circles depict the maximum momentum expected from direct electrons (purple) and from first (green) and second (blue) recollisions. (b) Decay rate (β) of the photoelectron signal as a function of ellipticity. (c) Forward/backward asymmetry of the electron signal, at $\epsilon = 0.3$ laser ellipticity. (d)-(f) Shows the same measurements in α-Pinene.*

contribution of second return electrons was found to dominate in simulations as soon as the ellipticity is above 0.2 [Yu 15].

To identify the electron trajectories, each component of the 3-D photoelectron momentum distribution ($\mathcal{P}(\mathbf{p})$) is fitted to a Gaussian distribution as a function of ellipticity (ϵ) given as $\mathcal{P}(\mathbf{p}) \propto \exp(-\beta(\mathbf{p})\epsilon^2)$, where $\beta(\mathbf{p})$ is the decay rate of the photoelectron yield. The photoelectron distribution for $\epsilon = 0.3$ and the corresponding PEELD observed is shown Fig. 4.18 (A-C) and Fig. 4.18 (D-F) for Fenchone and α-Pinene respectively. Fig. 4.18 B and Fig. 4.18 E shows the 2-D decay rates of the photoelectron yield, for electrons ejected along the angle $\phi = 60° \pm 10°$, for Fenchone and α-Pinene respectively. The expected cutoffs of first and second return electrons, identified from the classical calculations shown in Fig. 4.3, are also depicted as circles on the figure.

The angle resolved decay rate maps clearly shows three distinct areas with similar structures for both Fenchone and α-Pinene. In the high energy part of the photoelectron momentum distribution, between the cut-off energy of the first and second return electronic trajectories, the photoelectron yield decays faster with an increase in the ellipticity of the electromagnetic radiation. The β value ranges between $10 - 8$. This can be explained from the discussion above

that the first return electrons generally have long trajectories and they require considerably high transverse tunnel exit velocities to compensate the lateral drift accumulated along the short axis of the polarization ellipse for their trajectories to be closed. Thus with a small increase in the ellipticity of the electromagnetic radiation these first return electron trajectories decay faster as their re-collision probability decreases.

Secondly, the decay rate sharply falls off at the cut-off energy of the second return electrons, with β values ranging between $7-5$. Thus indicating that the second return electronic trajectories are dominant in this regime due to the fact that the second return electrons require considerably lower transverse tunnel exit velocities to compensate the lateral drift accumulated along the short axis of the polarization ellipse for their trajectories to be closed. Thirdly, for electron energies below $(2U_P)$ show a very slow decay rate. This energy regime dominated by the direct electrons and is typical of them to have small decay rates as they are insensitive to re-collision.

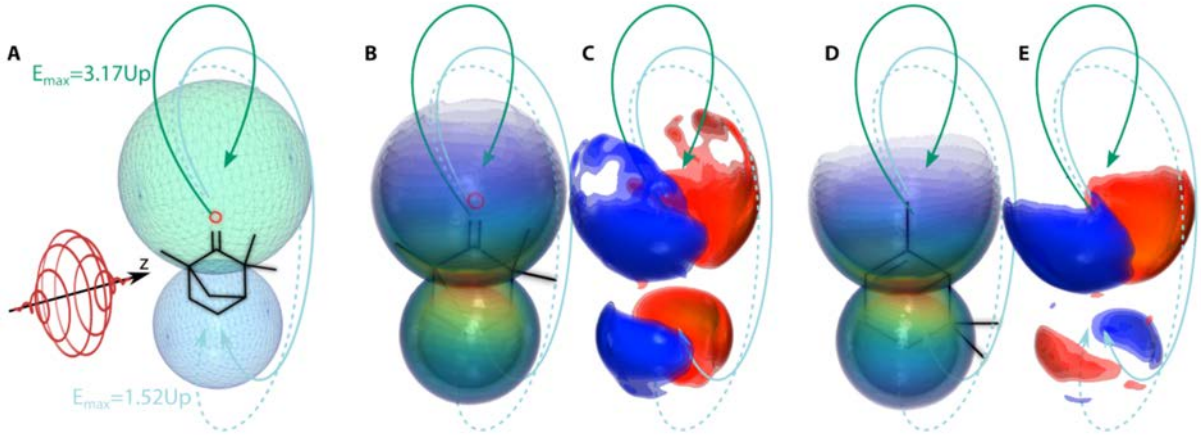

Figure 4.19 – *Chiral laser-induced electron diffraction. (a) Schematic representation of the 3-D momentum distribution upon recollision of first returns, short trajectories (green), and second return, short and long trajectories (blue). The orientation of the molecule is selected by tunnel ionization and the recollision angles are dictated by the laser field and ellipticity. (b) Shows the measured 3-D momentum distribution produced by recollision of first (top) and second (bottom) returns in Fenchone. (c) Forward/backward asymmetry of the momentum distribution, corresponding to the chiral laser induced electron diffraction pattern. (d)-(e) Shows the same measurements performed in α-Pinene, where the first and second return show opposite chiral responses.*

Looking at the PEELD maps and co-relating with the various regions of the β maps, we see that in Fenchone most of the asymmetric signal comes from the long trajectories of the first return electrons while there is hardly any signal from the second return electrons. On the other hand for α-Pinene the first and second return electrons show opposite asymmetric response, i.e. they show opposite sign of PEELD. The sign reversal of the PEELD is thus due to the sensitivity of this chiroptical signal to the orientation of the recolliding electron with respect to the molecule. The anisotropy of the tunnel ionization rate preferentially selects a subset of molecular orientations. The first and second return electrons re-collide from opposite sides of these oriented molecules. Figure 4.19 shows the angular distribution of first and second return rescattered electrons, obtained by cutting spheres throughout the measured 3-D electron

momentum distribution with radii of $3.17U_P$ (top) and $1.52U_P$ (bottom) and centered on the maxima of the vector potential, measured in Fenchone and α-Pinene. These spheres correspond to the maximum return kinetic energies of the first ($3.17U_P$) return and $1.52U_P$ for second return electrons. The evolution of the electron density over the sphere thus provides the 3D differential cross section (DCS) of the electron-ion scattering. Using this information we can try to perform trajectory resolved chiral laser induced electron diffraction (CHILIED).

IV. 4 CHIral Laser Induced Electron Diffraction (CHILIED)

For conventional LIED, molecules are ionized using linearly polarized laser, but no chirosensitivity is expected in this case. Thus we strong-field ionize the molecule with an electromagnetic wave with an elliptical polarization (S3 = 0.3). We have already seen that even for very small ellipticity, we observe a strong forward-backward elliptical dichroism. We have also observed that the PEELD contribution from direct electrons are an order of magnitude lower than that of the rescattered electrons for both Fenchone and α-Pinene.

A schematic view of the electronic trajectories involved in the laser induced electron diffraction process is depicted in Fig. 4.19. Due to the ellipticity and the chiral nature of the target, the DCS depends on the azimuthal (ϕ_{scat}) and the polar angle (θ_{scat}) of the rescattered photoelectron momentum distribution. To reduce the dimensionality of the problem at hand, the DCS is integrated over the azimuthal angle (θ_{scat}). We select the first return electrons with the highest return kinetic energies as they involve contribution from only one family of electron trajectories. We observe that for both Fenchone and α-Pinene the decay in the DCS is about one order of magnitude as the scattering angle increases from 40° to 120° , followed by a slight increase. The DCS of both the molecules have a minima at $\theta_{scat} = 126°$ and $\theta_{scat} = 132°$ for Fenchone and α-Pinene respectively (see Fig. 4.20 A).

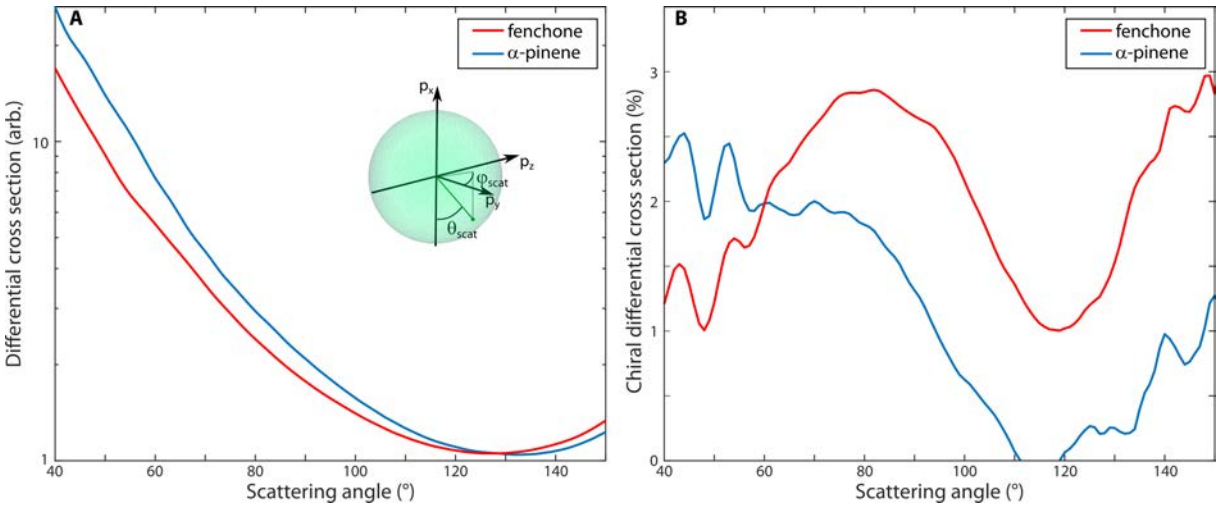

Figure 4.20 – *(a) Shows the DCS, red for Fenchone and blue for α-Pinene. They show a minima at $\theta_{scat} = 126°$ and 132° respectively but have the same overall structure. The coordinates are specified in the inset. (b) Shows the chiral DCS for the two molecules which show completely different structures for the two molecules.*

Although the minima of the two DCS are different they both look similar structure. This

is due to the fact that the de-Broglie wavelength of these electrons is not small enough to resolve the inter-nuclear distances between the atoms comprising the molecules – the de-Broglie wavelength of the electrons is about 4.5Å and the size of the molecules is 1.5Å. To extract the chiro-sensitivity of the laser induced electron diffraction process, we compare the DCS measured forward and backward and introduce the chiral DCS, defined as:

$$\mathrm{CDCS} = \frac{\int_{\pi/4}^{3\pi/4} \mathrm{DCS}(p, \theta_{scat}, \varphi_{scat}) d\varphi_{scat} - \int_{5\pi/4}^{7\pi/4} \mathrm{DCS}(p, \theta_{scat}, \varphi_{scat})}{\int_{\pi/4}^{3\pi/4} \mathrm{DCS}(p, \theta_{scat}, \varphi_{scat}) d\varphi_{scat} + \int_{5\pi/4}^{7\pi/4} \mathrm{DCS}(p, \theta_{scat}, \varphi_{scat})} \tag{4.6}$$

The measured CDCS for both Fenchone and α-Pinene is shown in Fig. 4.20 B. In Fenchone the CDCS maximizes at $\theta_{scat} = 80°$ and has a minima at $\theta_{scat} = 120°$ while having an asymmetry of higher than 1% for the $\theta_{scat} \in [40°, 160°]$. While in α-Pinene the CDCS lies higher than 2%. Then it drops down and has a minima at $\theta_{scat} = 110°$, where the CDCS drops to zero. Thus, even though the DCS is not so sensitive to the molecular structure for low energy electrons, the CDCS is sensitive to this structure.

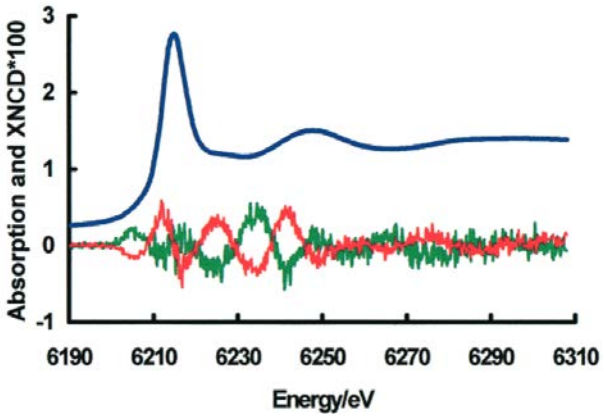

Figure 4.21 – *Axial absorption (blue) and XNCD spectra for single crystals of* Λ- *(red) and* Δ- *(green)* $Na_3[Nd(digly)_3]$fl2$NaBF_4$fl6H_2O. *Extracted from [Peacock 01]*

To understand the structural sensitivity of the CDCS at long de Broglie wavelengths we look into X-ray Absorption Near Edge Spectroscopy (XANES). Figure 4.21 shows the Nd L_3-edge absorption spectrum (in blue) of enantiomorphic single crystals of $Na_3[Nd(digly)_3]$,2$NaBF_4$,6H_2O [Peacock 01]. The spectrum shows slow oscillations, which are due to the scattering of the outgoing electrons onto the neighboring atoms. The green and red curves show the chirosensitive part of the XANES signal, measured using circularly polarized X rays, i.e. the X-ray Natural Circular Dichroism (XNCD). The XNCD spectra clearly shows faster modulations. The shorter energy spacing between the oscillations is characteristic of a longer distance between scatterers. This is due to the fact that CD is determined by chirality, which is a non-local property of matter. Thus, XNCD is sensitive to multiple scattering events, and "sees" bond lengths larger than the inter-nuclear distance between neighbors probed by XANES. An analogy between XANES-DCS and XNCD-CDCS can thus be made. The DCS is similar to XANES in the sense it is sensitive to the internuclear bond lengths, while the CDCS is similar to XNCD as it is sensitive to the overall shape of the chiral molecular potential, which extends over several Å, and can be revealed

using lower energy electrons with 4.5 Å de-Broglie wavelength.

IV. 5 Chiral Holography

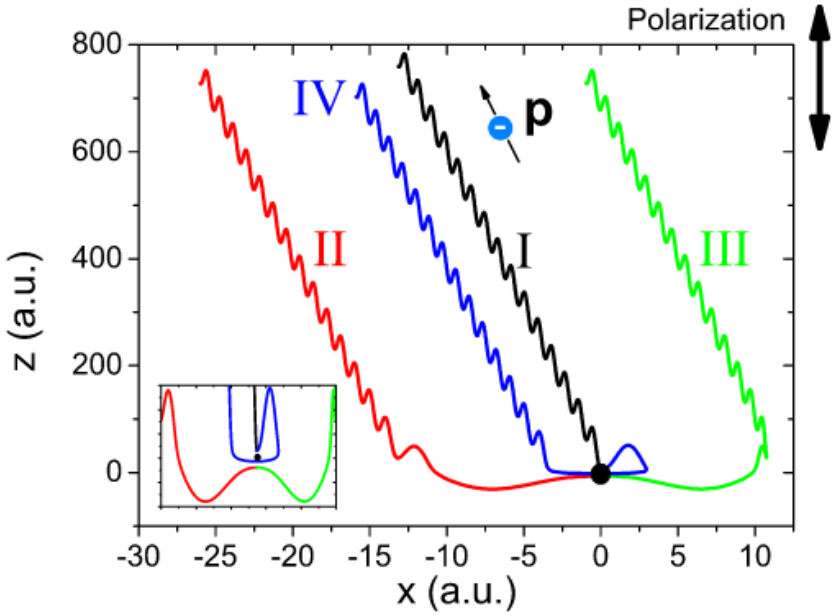

Figure 4.22 – *A schematic illustration of the four types of quantum orbits in the laser-polarization plane for electrons with fixed final momentum* **p**. *The type I, II, III and IV orbits are shown in black, red, cyan and blue respectively. The electronic orbits/trajectories are calculated for H atom at an intensity of* 2×10^{14} W/cm^2 *and* $\omega = 0.057$ *a.u. The black dot represents the position of the nucleus. The inset shows a zoomed in view of the electronic trajectories around the nucleus. Reproduced from [Figueira de Morisson Faria 20]*

We have seen that the high energy electrons are very sensitive to the chiral potential and can be used to perform chiral laser-induced electron diffraction. In the lower energy range, typically below $\sim 2 - 3U_P$, the superposition of several electron trajectories produces interference and can give rise to holographic patterns. The various interfering quantum orbits are depicted in Fig. 4.22. The direct electrons, which escape the molecule without revisiting the ionic core, reach a maximum energy of $2U_P$. Within the framework of the quantum-orbits analysis of photoionization, they are labelled "orbits 1" [Figueira de Morisson Faria 20]. The electrons that revisit the core and are forward deflected or scattered gain a small amount of kinetic energy through this interaction, reaching $\sim 3U_P$. Thus the PAD for energies below $2U_P$ can be written as a coherent sum of $\mid \psi_1 + \psi_2 + \psi_3 \mid^2$ while for energy range $2U_P < E < 3U_P$ the PAD can be written as a coherent sum of $\mid \psi_2 + \psi_3 \mid^2$, where ψ_i corresponds to the wave-function of type i electronic orbit.

Orbits 1 and 2 holographically interfere to produce a "fan"-like interference pattern. Orbits 2 and 3 holographically interfere to give rise to "spider leg"-like interference patterns which are observed in the 2-D PES for all the chiral molecules investigated here. This spider leg pattern appears as a hump in the iso-energy line-cut at $1.48eV$ (first row Fig. 4.23). Although it is much pronounced in α-Pinene than in Fenchone. It is interesting to note that the PEELD changes sign (for Fenchone) along this hump. Thus implying a phase change in the orbits along the angle

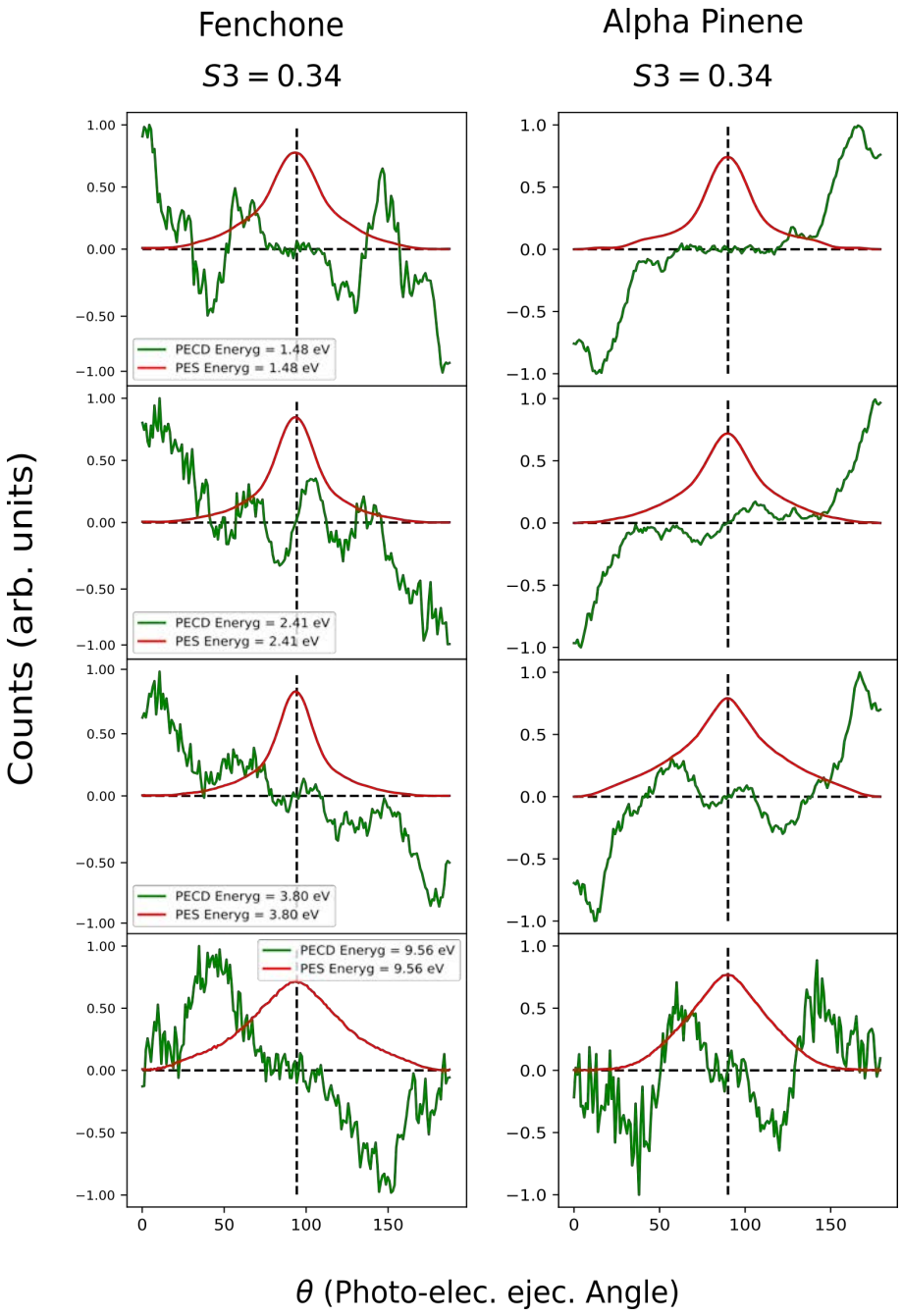

Figure 4.23 – *1-D iso-energy line cuts at* 1.48 2.41 3.8 *and* 9.56 *eV for Fenchone and α-Pinene at an intensity of* 2.5×10^{13} W/cm^2. *The PES is shown in red and the correspond PEELD at the given energy is shown in green. A bump in the PES is observed around which the PEELD changes sign in Fenchone indicating a phase change along the angle of emission of the electronic wavepacket for the electronic orbits interfering.*

of emission of the electronic wave-packet.

IV. 6 Rescattering PEELD Dependence with Intensity

The electron trajectories are mostly governed by the laser electric field in the strong field ionization process. Hence, a change in the field strength induces a variation in the electronic

wavepacket trajectories.

G-Function

To reduce the dimensionality of the problem, an asymmetry parameter $\mathcal{G}$ is defined as the angle- and energy-integrated PEELD, reflecting the overall forward/backward asymmetry of the signal. For each laser intensity, this parameter is normalized to its maximum value as a function of $S3$. It is observed (Figure4.24) that for given compound this asymmetry parameter $\mathcal{G}$ varies non-linearly and non-monotonically with ellipticity of the incident electromagnetic wave. The origin of the non-linearity of $\mathcal{G}$ with $S3$ can qualitatively understood as follows. For circular polarization we do not observe any electron rescattering as there are no closed electronic trajectories to facilitate the propagation of the tunnel ionized electronic wave-packet back to the molecule. Hence, the whole dichroic response obtained is due to the scattering of the electronic wave-packet in molecular potential after tunnel ionization. This leads to asymmetries of up to 2%. As the ellipticity is reduced , for $S3 =\mid 0.64 \mid$, the rescattering probability of the electronic wave-packet starts to increase and hence the electronic wave-packets rescatters from the molecular potential leading to a higher asymmetries of about 8%.

In the intermediate regime of ellipticity, $S3 =\mid 0.26 \mid$, the rescattering probability of the electronic wave-packet increases and they penetrate deeper into the ionic core, and hence we observe higher asymmetries of about 20%. On further reducing the ellipticity to quasi-linear, $S3 =\mid 0.02 \mid$, the rescattering electron wave-packet penetrates deeper into the core but due to the reduction of circularity of the probe, the amount of dichroic signal decreases, hence leading to a decrease in the total asymmetry. This results in the asymmetry parameter $\mathcal{G}$ maximizing for a given ellipticity.

The maxima of the asymmetry parameter $\mathcal{G}$ varies with intensity of the incident electromagnetic wave. It is observed that the maxima shifts towards lower ellipticity with an increase in intensity. This phenomena can be understood by resolving the incident elliptical electromagnetic wave into two perpendicular components E_x and E_y. As we increase the intensity for a given ellipticity both E_x and E_y components increases. While an increase in E_x results in a higher return kinetic energy of the re-colliding electronic wave-packet but a higher E_y results in the suppression of re-collision probability of the electrons as the electronic wave-packet gains a tangential momentum p_y and is thus driven further away from the ionic core.

To further understand the variation of forward-backward asymmetry, we normalize the asymmetry parameter $\mathcal{G}$ by the third Stokes parameter to define $\mathcal{G}_{\mathrm{S3}}$. We observe that $\mathcal{G}_{\mathrm{S3}}$ decreases monotonically with $S3$ for Fenchone in the range $S3 <\mid 0.8 \mid$. This can be understood by the sole reason that the electron rescattering probability increases with a decrease in the ellipticity and hence the indirect electrons which contributes mostly to the PEELD starts to decrease.

It is important to note that for linear polarization, by construction, the asymmetry parameter $\mathcal{G}_{\mathrm{S3}}$ is undefined. This does not in anyway imply that there is no dichroic response for linear polarization. In our case, while reconstruction of the 2-D PEELD spectra, we assume that the dichroic response is strictly an odd function. This assumption leads to the fact that there is no dichroic response at linear polarization and hence $\mathcal{G}_{\mathrm{S3}}$ is undefined. This singularity can be removed by replacing the asymmetry at $S3 = 0$ by the dichroic response due to electric

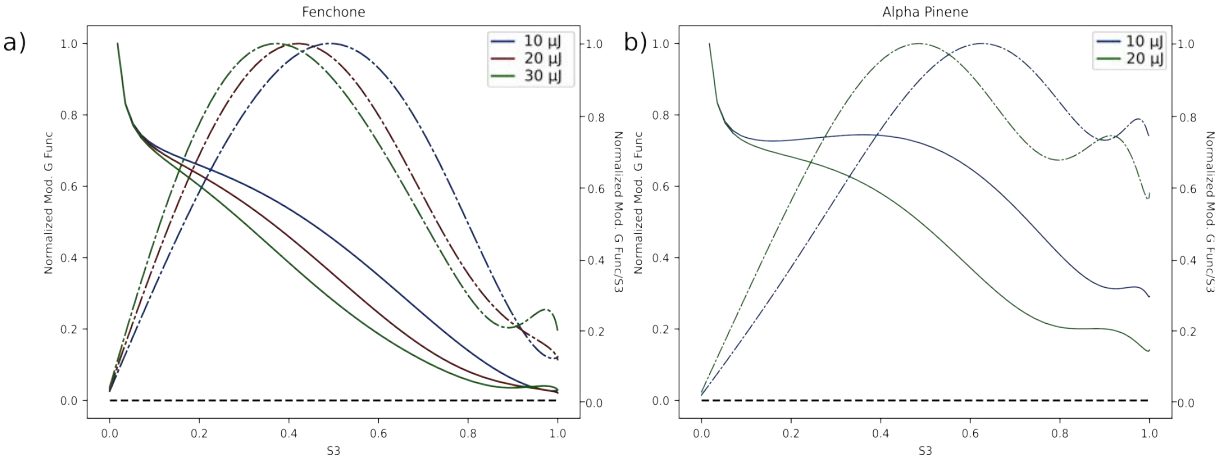

Figure 4.24 – *$\mathcal{G}$ in dotted lines and $\mathcal{G}_{S3}$ in bold lines $Y = 0$ given in black dashed line.* ***a)*** *Fenchone ($\mathcal{G}$ defined on the forward hemisphere)* ***b)*** *Alpha Pinene ($\mathcal{G}$ defined on the backward hemisphere) for different intensities.*

quadrupole, magnetic dipole and higher order expansion of the electric and magnetic dipole terms.

V Photoelectron Angular Rotation Linear Dichroism

Since chiral molecules respond asymmetrically to a chiral object we do not expect to see any photoelectron dichroism upon strong field ionization of chiral molecules with linearly polarized light. But it was observed by Arago [Arago 11] that the orientation of linearly polarized light gets rotated while passing through a quartz crystal. Similar rotations in the orientation of a linearly polarized light was reported in liquids by Biot [Biot 15] [Biot 19]. The schematics of the experimental setup to measure optical rotation is shown in Fig. 4.25.

This optical rotation of linearly polarized light can be addressed at a fundamental level as a result of circular birefringence. In the common linear birefringence in a crystal, the phase velocity of the light polarized along different directions is slightly different. In circular birefringence, there is slight difference in the velocities of the left and right handed circularly polarized light, which means a difference in the index of refraction for left and right circularly polarized light:

$$\Delta n = n_{RCP} - n_{LCP} \tag{4.7}$$

To understand optical rotation we can represent linearly polarized light as a superposition of two counter rotating circular electromagnetic waves. The phase difference ($2\phi_0$) between the two waves determines the orientation ϕ_0 of the linearly polarized light. Thus one can write an initial linearly polarized wave ($\mathbf{E}_{\phi_0}$) propagating along the $+\hat{z}$ direction, before entering a chiral medium, as:

$$\mathbf{E}_{\phi_0} = \frac{1}{\sqrt{2}}\left(e^{-i\phi_0}\mathbf{E}_{RCP} + e^{i\phi_0}\mathbf{E}_{LCP}\right) \tag{4.8}$$

where $\mathbf{E}_{RCP}$ and $\mathbf{E}_{LCP}$ are the two circularly polarized basis functions. Where $\mathbf{E}_{RCP}$ and $\mathbf{E}_{LCP}$

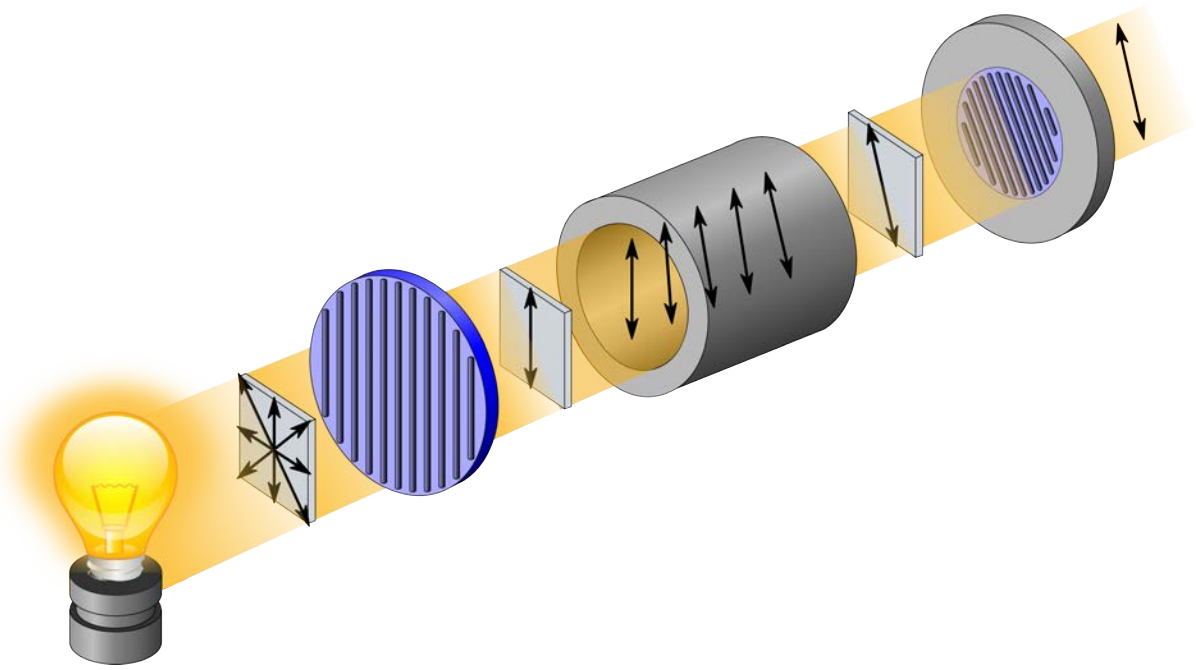

Figure 4.25 – *Principle of operation of a polarimeter to measure optical rotation. Extracted from [Kaidor]*

can be written in $\hat{x}$ and $\hat{y}$ coordinates as:

$$\mathbf{E}_{RCP} = \frac{1}{\sqrt{2}}\Big(\hat{x} + i\hat{y}\Big) \tag{4.9}$$

$$\mathbf{E}_{LCP} = \frac{1}{\sqrt{2}}\Big(\hat{x} - i\hat{y}\Big) \tag{4.10}$$

where i is the imaginary unit representing a 90° phase shift between the x and y components. When the lineraly polarized light, oriented at an angle ϕ_0, passes through an optically active medium due to circular birefringence an additional phase difference is introduced between the LCP and RCP waves. A phase difference of $-\Delta\phi$ is added to the RCP and $\Delta\phi$ is added to the LCP. Thus the outgoing linearly polarized wave can be expressed as:

$$\mathbf{E}_{out} = \frac{1}{\sqrt{2}}\left(e^{-i\Delta\phi}e^{-i\phi_0}\mathbf{E}_{RCP} + e^{i\Delta\phi}e^{i\phi_0}\mathbf{E}_{LCP}\right) \tag{4.11}$$

or substituting Eqn. 4.9 in the above equation we have:

$$\mathbf{E}_{out} = \cos(\phi_0 + \Delta\phi)\hat{x} + \sin(\phi_0 + \Delta\phi)\hat{y} \tag{4.12}$$

Thus describing a linearly polarized wave rotated by an angle $\Delta\phi$ from its initial orientation of ϕ_0. This physical phenomena is called optical rotation. This rotation of the orientation of the linearly polarized light is opposite for the left and right handed chiral molecules. The difference in the refractive indices of the RCP and LCP arises from magnetic dipole response of the atoms.

At first sight it may appear surprising that molecular chirality can be resolved using linearly polarized light, which is not a chiral object. Taking a closer look at Fig. 4.25 shows that chirality

is actually introduced in the measurement through the orientated rotation of the analyzer: light does not need to be chiral if we have a chiral observer [Ayuso 22].

The measurements of 3D photoelectron angular distributions by tomographic reconstruction in the VMI constitute a chiral observer: they are able to resolve electrons ejected at different angles from a linear laser polarization. The question thus arises of a possible rotation of the photoelectron angular distribution around the light propagation axis, oppositely for a left and right handed chiral molecule. The chiroptical asymmetries we have detected up to now were based on the electric dipole approximation: only the electric transition dipole moment of the molecule was assumed to interact with the incident electromagnetic field and the effects of higher order dipole moments are neglected. This is a reasonable assumption as the molecule (with a size of a few Å) is orders of magnitude smaller compared to the wavelength of the light (1030 nm), and as the effect of the laser magnetic field is generally much weaker than that of the electric field. Nevertheless, the high signal-to-noise ratio of our experiment, provided by the combined high repetition rate of the laser source and the Fourier-type lock-in detection, led us to investigate the possibility to observe a chirosensitivity in the photoelectron angular distribution upon strong field ionization of chiral molecules with linearly polarized light.

V. 1 Experimental Setup

To observe a rotation of the photoelectron angular distribution, analogous to optical rotation, we perform strong field ionization of Fenchone. Schematics of the experimental setup is shown in Fig. 4.26. The 2^{nd} arm (TG2) of the Blast Beat fiber laser system is used for the experiment, described in Section I. The incident laser has an average power of 35W, at the input of VMI, with a pulse width of 130 fs, wavelength centered at 1030 nm and working at repetition rate of 1 MHz. Two thin film polarizers are used to clean the laser polarization from any polarization artifacts. This is done as amplified spontaneous emission from the laser or improper reflections from mirrors can introduce a small orthogonal component in the laser electric field and thus making the incident electromagnetic wave elliptically polarized. The linearly polarized light is then incident onto a B. Halle $\lambda/2$ waveplate, mounted on a continuously rotating Newport mount, as in previous experiments. The beam is then expanded using a $\times 4$ telescope ($-75/+300$ mm) before being focused into the VMI using a +200 mm focusing lens. The focal spot-size is measured using a CCD camera with a FWHM of 17.94 μm. The polarization state of the laser beam at the exit of the VMI window is measured using a continuously rotating quarter-wave polarimeter (see Fig. 2.6 (c)).

The 2-D projections of the photoelectron angular distribution is recorded using a VMI for different orientations of the linearly polarized light in a lock-in detection mechanism, similar to the method used for measuring rescattering PEELD. The chiroptical signal can only be detected by comparing the photoelectron distributions from opposite enantiomers. This means that the stability of the setup is crucial, to avoid any drift during acquisition, and that multiple consecutive sets of measurements are necessary to ensure that the results are not due to random fluctuations. The laser is allowed to run through the whole experimental setup for 3 hours to reach thermal stability and avoid any drifts. Furthermore, to minimize the impact of drifts

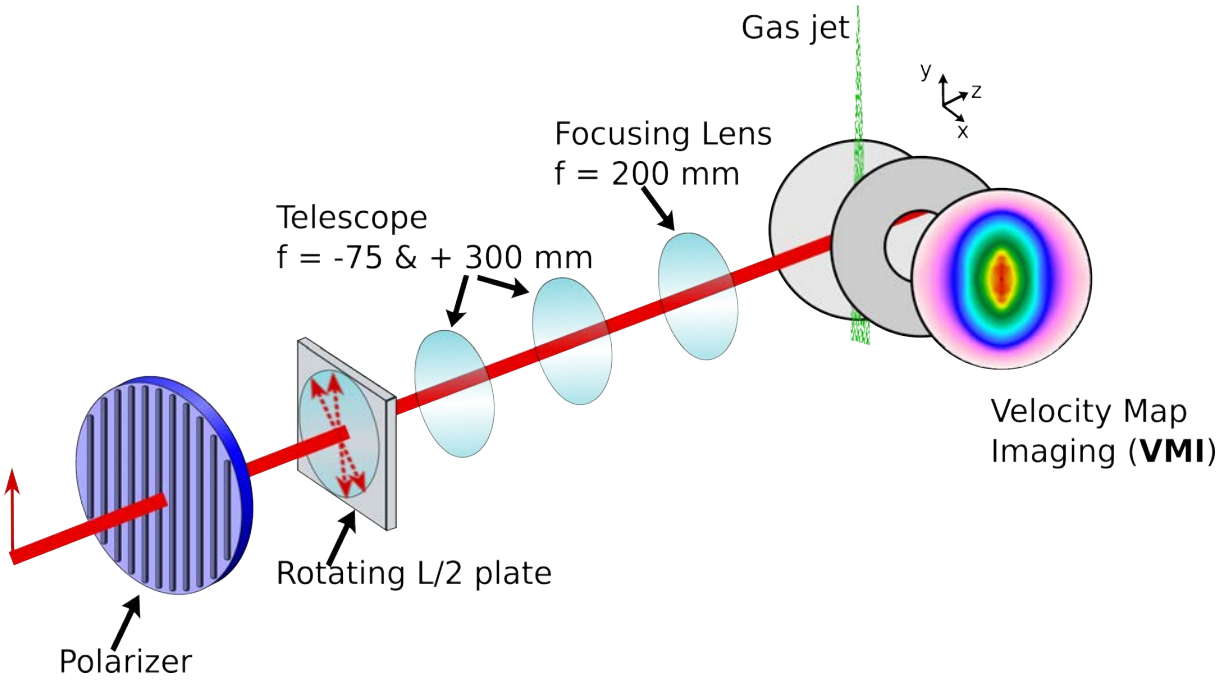

Figure 4.26 – *Schematics of the experimental setup for measuring photoelectron rotation linear dichroism. The* 1030 *nm wavelength laser is incident on a thin film polarizer of high contrast to get rid of any polarization artifacts. The laser is then incident on a continuously rotating* $\lambda/2$ *waveplate. The laser beam is then expanded using a times 4 telescope and focused into the VMI using a* $f = +200$ *mm lens. @-D projections of the 3-D photoelectron angular distributions are recorded in the VMI in a lock-in measurement scheme.*

in the differential measurements, we implemented an active stabilization of the beam pointing using a motorized mirror and a position sensitive detector in the far field. Measurements are conducted by switching 20 times between opposite enantiomers, and recording a movie of the 2D projection of the PAD as a function of the waveplate orientation for each case.

V. 2 Lock-in detection

The $\lambda/2$ waveplate continuously rotates at 22.5°/sec. Thus the orientation of the linearly polarized light in the lab frame rotates at 45°/sec, going from s-polarized to p-polarized in every 2 seconds (see Fig. 4.27 (a) (b) (c)). The photoelectron distribution is recorded every 50ms with the Hammatsu ORCA camera for 300 seconds, with no deadtime. The change in the orientation of the incident linearly polarized light results in a sinusoidal oscillation of the total photoelectron signal recorded. This is due to saturation of the MCPs at the center when the laser polarization is along the axis of the VMI (see Fig. 4.27 (a)). The images obtained on the camera of the VMI are 2-D projections of the 3-D photoelectron angular distribution given as $\mathcal{P}(p_y, p_z, \phi) = \int P(p_x, p_y, p_z, \phi) dp_x$, where ϕ is the orientation of the linearly polarized light in the lab frame. A Fourier transform is done along the ϕ axis per pixel for the length of the images acquired. A schematics of the Fourier transform of the total photoelectron yield is shown in Fig. 4.27 (d). The total photoelectron signal oscillates at $n\Omega_0$ where $n \in \mathbb{W}$. The 2-D photoelectron angular distribution can be reconstructed using inverse discrete Fourier transform, with frequencies $n\Omega_0$. Higher frequencies, $n > 7$ are neglected during the inverse transform as

the FFT amplitude of the photoelectron yield is in the noise. Thus the PAD can be extracted using a lock-in detection mechanism and this allows us to record a noise free 2-D projections of the 3-D photoelectron momentum distribution.

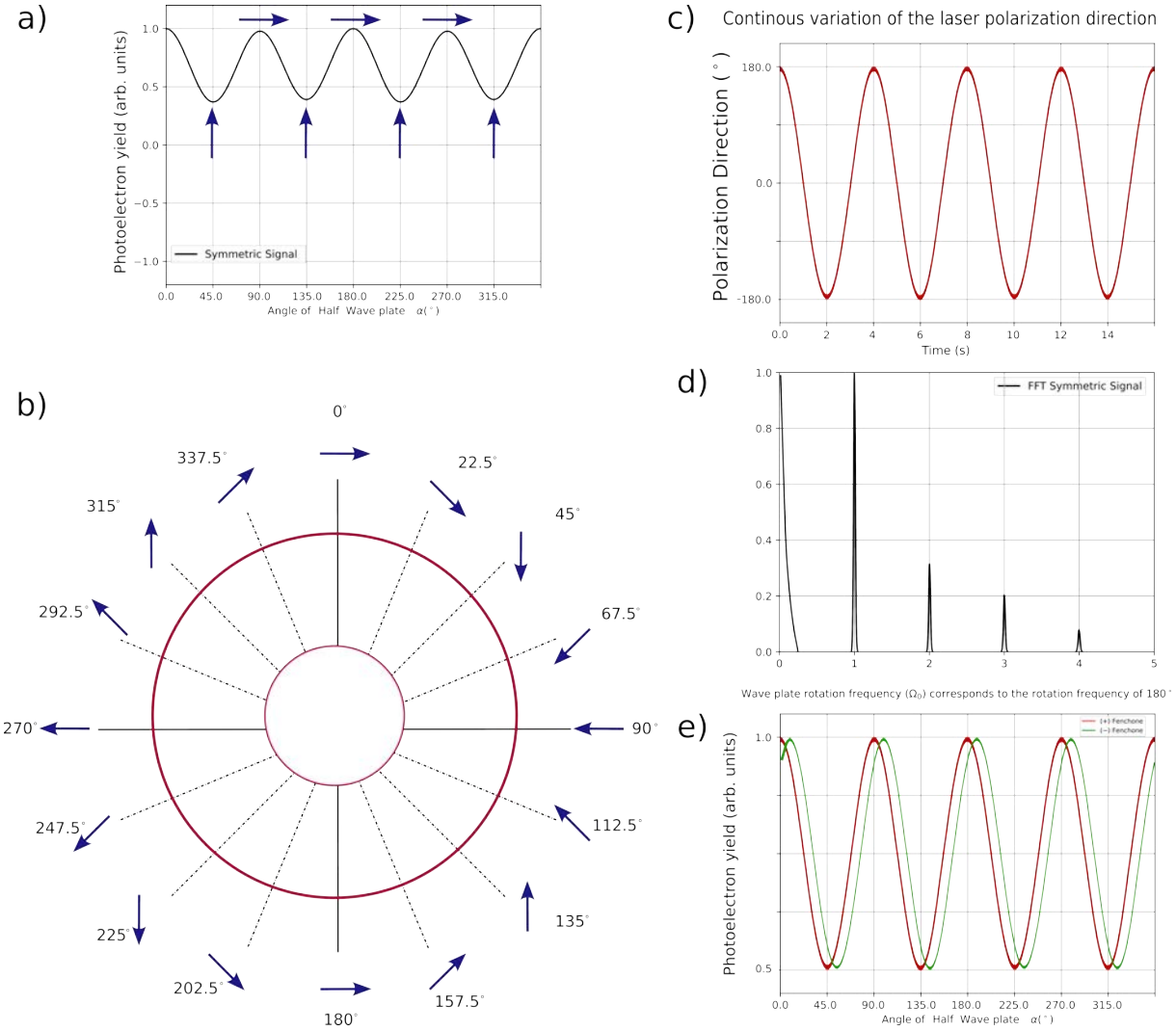

Figure 4.27 – *The schematic of the working principle of lock-in detection measurement of photoelectron rotation linear dichroism is shown in the figure. (a) Shows the evolution of the photoelectron signal measured in the VMI. (b) Shows the evolution of the orientation of the linearly polarized light as a function of the half waveplate angle. (c) Shows the evolution of the total photoelectron signal in time for various orientation of the linearly polarized light. (d) Shows the corresponding Fourier transform of the photoelectron signal. (e) Shows an exaggerated view, per pixel, if the photoelectron signal rotates oppositely for two different enantiomers of Fenchone.*

If the photoelectron angular distribution rotates by $\Delta\phi$ for the right handed enantiomer then it should rotate by $-\Delta\phi$ for the left handed enantiomer. Thus resulting in a phase difference of $2\Delta\phi$ between the two enantiomers. This would result in a phase shift, per pixel, in the total photoelectron yield signal between the two enantiomers, as shown in an exaggerated form in Fig. 4.27 where (+) Fenchone is shown in red and (-) Fenchone in green. As this rotation can happen due to magnetic dipole or electric quadrupole interactions, this effect should be $\sim 10^2 - 10^3$ times weaker in strength compared to the electric dipole effects or PEELD. This

makes lock-in measurements absolutely necessary to observe it. Directly comparing the 3D-PADs of opposite enantiomers is not the best way to track a possible enantiosensitive rotation of the angular distributions. Our measurement intrinsically directly resolves the orientation of this PAD through the phases of the Fourier components. We thus rely on this phase detection, because phase measurements are less sensitive to imperfections of the detector than amplitude measurements.

V. 3 Results & Discussions

To observe the rotation in the PAD a fast Fourier transform is performed along the axis of orientation of the linearly polarized light (ϕ) per pixel and the 2-D FFT amplitude is obtained for each of the components oscillating at $n\Omega_0$, where $n \in \mathbb{W}$. The 2-D FFT amplitudes are shown in Fig. 4.28 (a), oscillating components only up to $3\Omega_0$ are shown here. The 2-D $0\Omega_0$ component of the oscillation corresponds to the continuous signal. While the 2-D FFT amplitudes, oscillating at $1\Omega_0$, $2\Omega_0$ and $3\Omega_0$, corresponds to structures in the photoelectron angular distribution oscillating at the respective frequencies with the change in the orientation of the linearly polarized light (ϕ) per pixel. With an increase in the oscillating frequency, up to $7\Omega_0$, sharper structures starts to appear in the 2-D FFT amplitude map. On further increasing the oscillating frequency the 2-D FFT amplitudes becomes more noisy and without any discernible structures. Thus frequencies higher than $7\Omega_0$ are neglected here. Note that there is a direct relationship between the different components of the Fourier decomposition and the decomposition of the PAD in Legendre polynomials, and that it was recently shown that these Fourier coefficients could directly provide the tomographic reconstruction of the 3D data, without relying on inverse Radon transform [Sparling 22].

The Fourier analysis not only provides the amplitude of each component, but also its phase. The phases are shown in Fig. 4.28 (c). We restrict the plot to areas where the signal to noise ratio is sufficiently high. We see a $\pi/2$ phase jump in the phase map corresponding to the $1\Omega_0$ frequency. This phase jump is due to the fact that the signal oscillates from linear horizontal polarization, for which the PAD is more centered, to linear vertical where the PAD is more spread out over the detector. Similar phase jumps are observed for the higher frequencies where the number of phase jump is increases with the increase in the frequency component.

The 2-D phase distribution is acquired for 40 individual measurements and the phase of the left enantiomer is subtracted from the right enantiomer and is averaged over all the 20 sets. The difference in the phase recorded is shown in Fig. 4.29, for the frequency components oscillating at $1\Omega_0$, $2\Omega_0$ and $3\Omega_0$. A 100 mdeg shift in the 2-D phase distribution is observed between the two enantiomers for the frequency component oscillating at Ω_0. A phase shift in the opposite direction is observed in the center, in the area in which the signal maximizes around linear horizontal polarization. A phase difference of about $200 - 300$ mdeg and as high as 500 mdeg is obtained for the $2\Omega_0$ and $3\Omega_0$ frequency components.

The small values of the measured phase shifts raises the question of error bars in the measurements. We can calculate these error bars using the standard deviation σ of the 20 individual measurements, and calculating the 70% confidence interval as $\pm 1.064\sigma/\sqrt{20}$, where

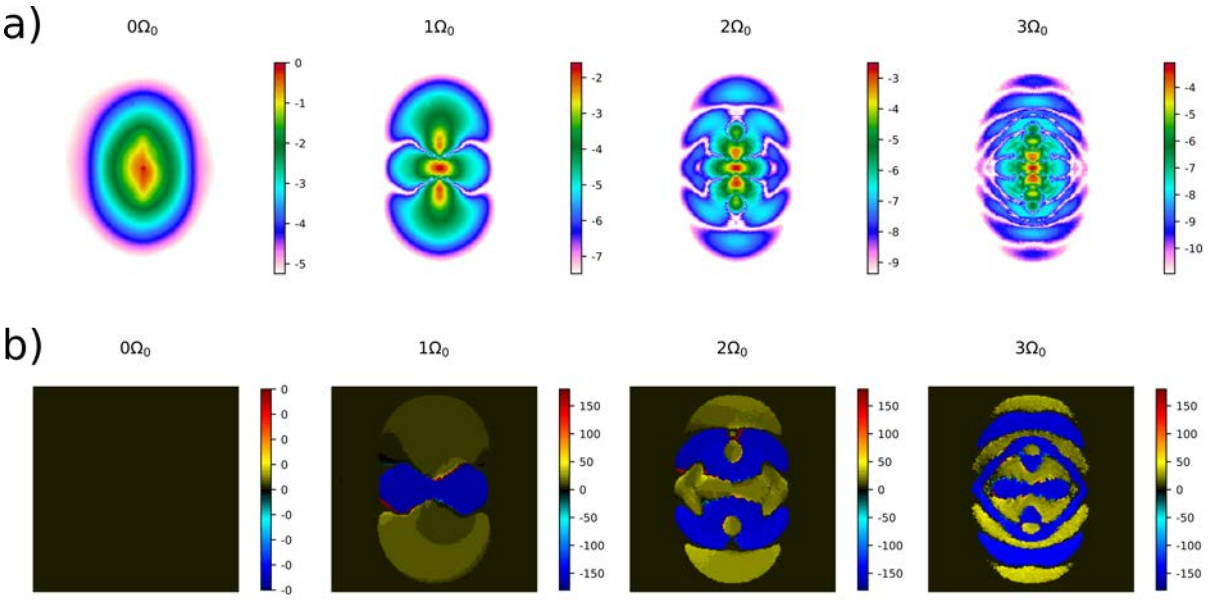

Figure 4.28 – *(a) Show the Fourier amplitude per pixel. (b) Shows the phase of the different Fourier frequency components.*

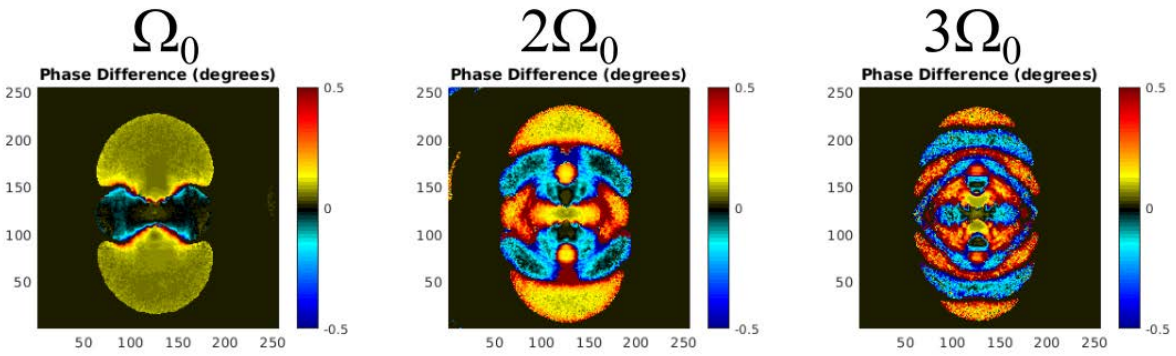

Figure 4.29 – *Enantiomeric phase difference measured in Fenchone, for the first three frequency components excluding the continuous components. A phase difference corresponding a few 100 mdeg is observed.*

1.064 is the Student coefficient associated with the number of measurements. The upper and lower bounds of this confidence interval are shown in Fig. 4.30, confirming the existence of a well defined and robust enantiomeric phase difference.

This difference in the phase maps between the two enantiomers implies a rotation of the photoelectron angular distribution in opposite directions by opposite enantiomers in the plane of polarization. This rotation of the photoelectron angular distribution leads to a photoelectron dichroism in the polarization plane. This effect can be quantified by reconstructing the 3D photoelectron angular distributions using inverse Radon transform, and subtracting the 3D PADs of the two enantiomers. Cuts of the reconstructed distributions, in the laser polarization plane, are shown in Fig 4.31. The left panel shows that the PAD narrowly peaks around the vertical laser polarization. The signal is mostly confined to the central circle, which depicts the $2U_P$ cutoff of direct electrons. The outer circles depict the expected cutoffs of the first

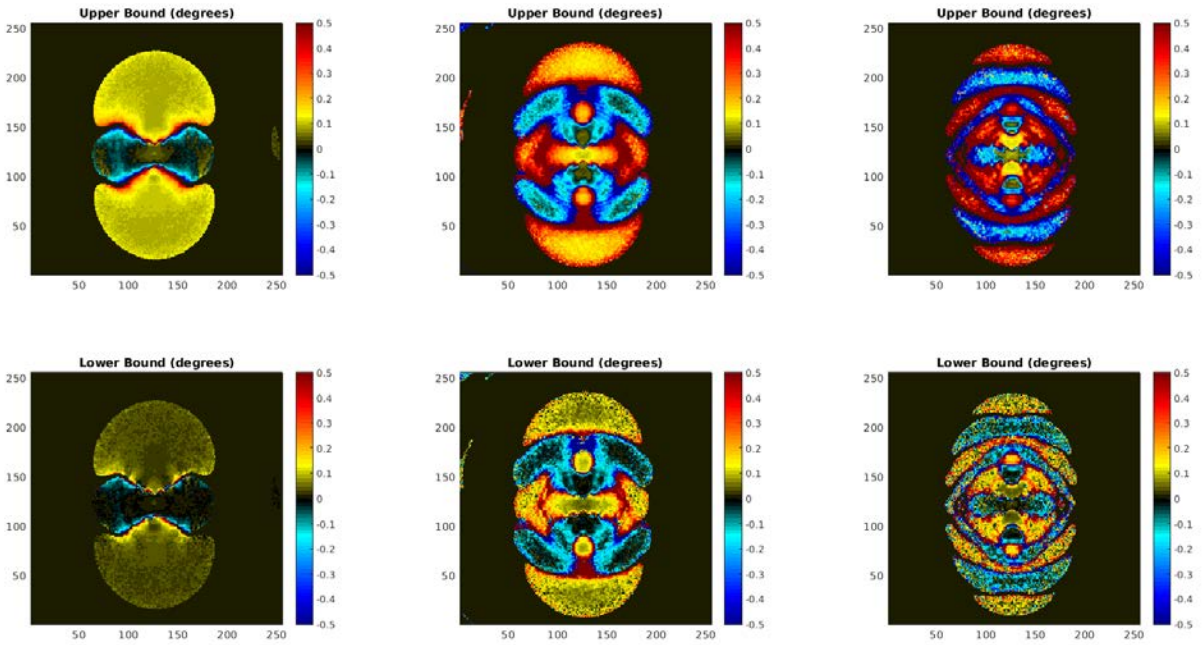

Figure 4.30 – *Upper and lower bound of the 70% confidence interval of the enantiomeric phase difference measured in Fenchone, for the first three frequency components excluding the continuous components.*

return backscattered electrons. Subtracting the PADs obtained in (+) and (-) Fenchone reveals the enantiosensitive differential signal resulting from the rotation of the PADs. Normalizing this signal pixel by pixel enables evaluating the magnitude of the dichroism effect, which is surprisingly large, reaching the 1% range.

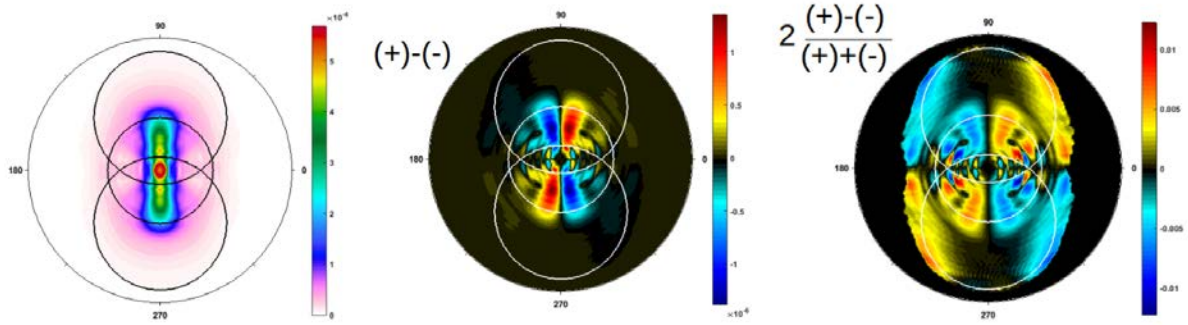

Figure 4.31 – *(Left) The photoelectron angular distributions of (+) Fenchone is shown along with the $2U_p$ ans $10U_p$ energy circles. (Center) The enantiomeric difference is shown. (Left) We see that the normalized linear dichroism of $\sim 1\%$ is observed.*

An analogy can be formed with photoelectron circular dichroism to understand the origin of photoelectron angular rotation linear dichroism. In PECD, when a circularly polarized light is incident on chiral molecules, the electrons rotate in the polarization plane $(\hat{x}, \hat{y})$. The chirality of the molecular potential converts this rotation into translation along the orthogonal direction $\hat{z}$, which is the light propagation axis. The direction of the translation is determined by the handedness of the molecule and the rotation direction, i.e. the helicity of the light. What

happens if the light is linearly polarized along $\mathbf{E_x}$, but we take into account its magnetic field $\mathbf{B_y}$? This magnetic field exerts a Lorentz force on the emitted electrons, inducing their rotation in the $(\hat{x}, \hat{z})$ plane. The chirality of the molecular potential will convert this rotation into translation along the orthogonal direction, i.e. $\hat{y}$. The electrons ejected up and down the polarization axis $\hat{x}$ rotate in opposite directions, and thus experience opposite chirosensitive translations. This explains why electrons are pushed towards positive $\hat{y}$ in the upper hemisphere and towards negative $\hat{y}$ in the lower hemisphere, inducing a rotation of the distribution around the propagation direction. The large magnitude of this effect is probably due to an enhancement by the molecular orientation selectivity during tunnel ionization.

VI Conclusion & Perspectives

In this chapter we have shown that strong field ionization is an excellent probe for molecular chirality. The rescattered electrons act as an extremely sensitive probe of the chiral molecular potential and show a stronger forward-backward asymmetric emission compared to conventional dichroism process, as they scatters from deep inside the molecular potential. Using chiral laser induced electron diffraction one can also probe the chiral molecular structure with Angstrom resolutions. Future experiments could involve using stronger electromagnetic fields to ionize chiral molecules such that the potential barrier is sufficiently lowered to allow multiple electronic orbitals to participate in the ionization process. This will provide a way to probe the underlying attosecond multi-electron dynamics, including the dynamics of electron rearrangement upon ionization. Increasing the field wavelength would also be very beneficial, allowing higher return kinetic energies of the electrons such that their de-Broglie wavelength are comparable to the size of the inter-nuclear distances and thus providing a tool to probing the chiral molecular structure in greater details. In addition one could also use a weak second harmonic of the fundamental strong laser field to dynamically change the electron dynamics and perform time-dependent laser induced electron diffraction. One could also use such synthetically polarized light fields to reveal the sub-optical nature of the chiral light-chiral matter interaction [Bloch 21] and manipulate electronic trajectories involved in the rescattering process [Porat 18].

In addition to this, photoelectron rotation linear dichroism pushes the interactions beyond the dipole interaction limit and provides us with an excellent sensitive tool to reveals non-dipole strong field light-matter processes. One may also use chiral molecules to generate optical Schrödinger cat states using intense laser–matter interactions [Lewenstein 21].

Chapter 5

General Conclusion and Perspectives

Throughout the manuscript we have generated and used a broad range of ultrashort pulses, from the near infrared to the XUV, with the goal to probe chiral light-matter interactions at ultrashort timescales. In this chapter we will briefly summarize our results and discuss some ongoing projects along with the short and long term perspectives they have opened.

I High Power High Repetition-rate Beamlines

The use of high power and high repetition rate Yb:Fiber lasers has multiple benefits. The high repetition rate of the laser source coupled with the lock-in detection enables us to measure photoelectron distribution with a high signal-to-noise ratio. We have also seen that this can be used to easily increase the dimensionality of the experiment as it takes significantly less time to perform measurements. This is very important as PECD and PEELD are signals that are typically in the few % range. The high repetition rate of the laser also helps in performing coincidence measurements with high statistics in a significant less time, for example it would take 700 times more time to acquire data using a conventional 1 kHz Ti:sa laser compared to the data that we have produced in the manuscript. Finally, the high power and high repetition rate of the laser also helps in the production of high flux XUV sources, reaching a flux of $\sim 5.7 \times 10^{12}$ photons sec^{-1} at 21.6 eV (up to 4×10^{11} photons sec^{-1} on target) with ellipticities as high as 90%. This high flux XUV source coupled with the ability to produce quasi circularly polarized XUV photons, with an ellipticity as high as 90%, using the XUV quarter wave-plate enables us to perform table-top PECD measurements in the single photoionization regime and with coincidence electron ion detection, which had up to now only been performed using synchrotron radiation.

II Single & Multiphoton chiral light-matter interaction

Throughout Chapter 3, we have seen that using elliptically polarized light rather than circularly polarized light could be extremely beneficial to probe chiral molecules in the multiphoton ionization regime. The PEELD provides a wealth of information with a higher sensitivity than PECD, revealing states which did not participate in PECD. The use of a lock-in ellipticity modulation

scheme provides an enrichment of the dichroic response of chiral molecules, and has been implemented for continuous isomeric and enantiomeric content monitoring. We have also seen that the coefficient (b_3) of the Legendre Polynomial, used to describe the PAD, is associated to the selectivity in the molecular orientation induced by resonances. Thus, the continuous variation of $|S3|$ combined with Fourier filtering could be used as an additional dimensionality in time-resolved photoelectron imaging. Furthermore, variation with S3 and the wavelength provides a multi-dimensional approach to decouple the bound-bound and bound-continuum transitions. However a leftover question of fundamental interest is how is the PECD affected by continuum-continuum transitions? Answering this question requires ionizing the chiral molecules with XUV light, to directly access the continuum, and then making a continuum-continuum transition with a synchronized laser pulse.

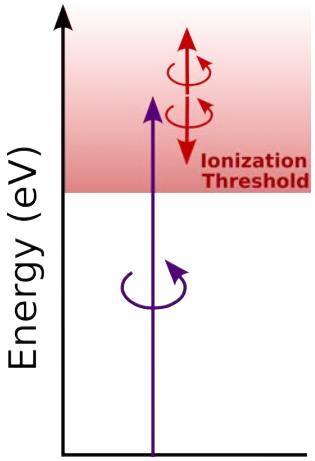

Figure 5.1 – *A Schematic representation of side-band formation. Where the photoelectron is produced by absorption of a single XUV photon (in purple) and reaches the continuum. Consequently the photoelectron can absorb an additional visible (515 nm) photon or emit the same while in the continuum.*

The schematics of the two-color chiral photoionization experiment is depicted in Fig. 5.1. A linearly or circularly polarized XUV pulse is used to ionize a chiral molecule and then additional circularly 515 nm pulse, either linear, co-rotating or counter-rotating with respect to the XUV, is used to generate side-bands by [1+1] or [1-1] photon process. By playing with the polarization steps of the two beams, it will be possible to disentangle the contribution of bound-continuum and continuum transitions, in a similar manner as done in [Beaulieu 18] where bound-bound and bound-continuum transitions were disentangled. This experiment is highly challenging because XUV photoionization produces broad photoelectron spectra, containing contributions from multiple molecular orbitals. Isolating the presence of side-bands is thus not easy. This is where coincidence electron ion detection becomes crucial. Figure 5.2 shows the fragment-resolved photoelectron angular distributions (top halves) and PECDs (bottom halves) measured by photoionizing $\alpha-$Pinene molecules. The measurements were performed by running the HHG source 24/24 for several days and recording a total of 9.4×10^7 counts in coincidence. The COLTRIMS measures the 3D electron distribution, but to improve signal to noise ratios we reconstructed this distribution from its 2D projection using pBasex inversion. We see that α-Pinene, which

has a mass of 136 amu. and ionization potential of 8.07 eV, when ionized with XUV photons with $\sim 80\%$ ellipticity shows a significant PECD of $\sim 6\%$. The three rings in the photoelectron angular distribution measured in coincidence with the parent ion originate from the three harmonics (H5,7,9 of the 515 nm laser) lying above the ionization threshold of the target. The XUV ionization produces a strong fragmentation of the molecule, producing masses of 121, 105, 93, 75, 67, 55, 41 amu. We see that the lighter fragments show less energetic electrons, which probably indicates that they are produced by ionizing deeper molecular orbitals. A significant PECD of is also observed for all fragments, and can be of opposite sign with respect to that of the parent ion. The measurments of multiphoton ionization of methyl-lactate in chapter 3 were not revealing a strong interest of using coincidence imaging. It seemed like all the signal was originating from one main fragment, and that VMI and COLTRIMS were thus providing the same information, the former being much faster. Here, there is no doubt that COLTRIMS is crucial, as a VMI would detect a sum of the different contributions depicted in Fig. 5.2, making spectroscopic assignments impossible.

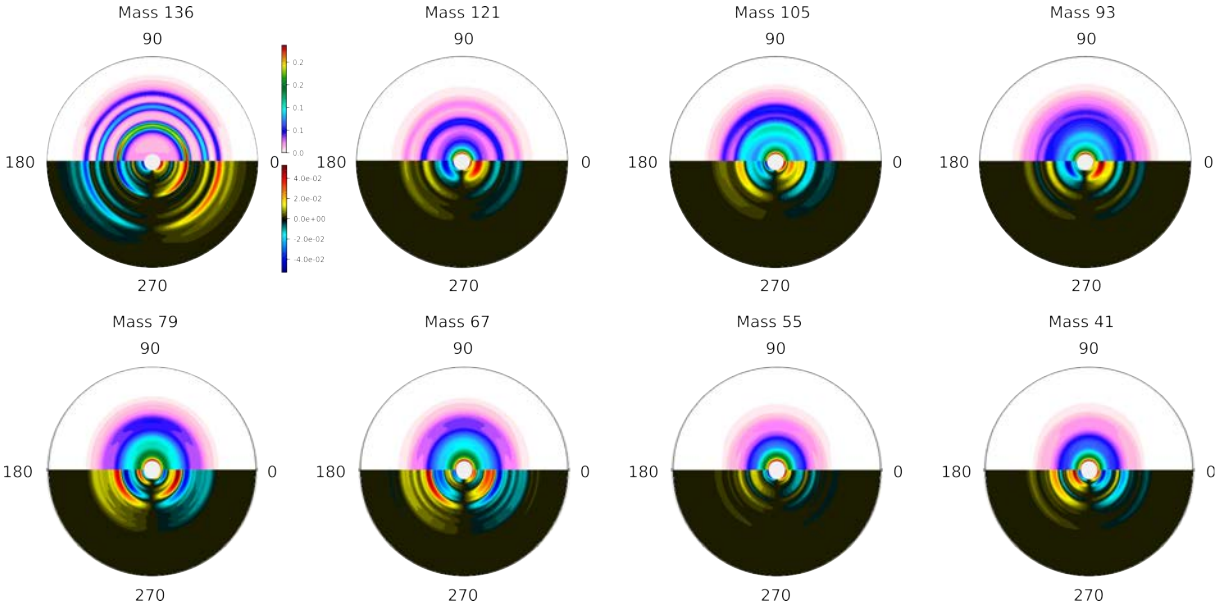

Figure 5.2 – *Single photoionization of α-Pinene. Elliptically polarized XUV ($\epsilon = 0.8$) was used to perform single photoionization of α-Pinene. The photoelectron angular (shown on the top half) was measured in coincidence with the photo-fragments generated. We see that the molecule fragments into multiple ionic fragments with masses of 136 (parent), 121, 105, 93, 75, 67, 55, 41 amu. We observe a significant PECD of $\sim 6\%$ from the parent ion, and all fragments show significant PECD.*

The data reported in Fig. 5.2 only represents the first step of the two-color chiral photoionization experiment. Since then, the temporal and spatial overlap of the XUV and 515 nm beams has been found, and two-color acquisition is ongoing.

III Strong Field Ionization

The experiments we have conducted with intense laser pulses have proved that strong field ionization is an excellent probe for molecular chirality. The rescattered electrons act as an

extremely sensitive probe of the chiral molecular potential and show a stronger forward-backward asymmetric emission compared to conventional dichroism process, as they scatters from deep inside the molecular potential. Using chiral laser induced electron diffraction one can probe the chiral molecular structure with angstrom resolutions. Extending these measurements to longer laser wavelengths will enable decreasing the de-Broglie wavelength of the electrons, providing the perfect tool to probe ultrafast chirality. This can be done by adding an optical parametric amplifier at the output of the laser, as we have done to obtain tunability in the visible range in chapter 4, and performing difference-frequency generation. We have observed signatures of holographic patterns in the chiral signals, and there is definitely room for more investigations of these patterns. Both techniques – CHILIED and holography – will benefit from using a two-color scheme, with a weak second harmonic of the fundamental strong laser field. This will help to decouple and dynamically change the relative phase of the direct and indirect electrons, involved in the strong field interaction by changing the relative phase of the fundamental and SH field. This will help us to infer the separate roles of the ionization time and the continuum electron dynamics [Porat 18]. Two color fields can also be used to manipulate the instantaneous chirality of light [Rozen 19], as well as the recollision angle of the electrons.

The discovery of the chirosensitivity of strong-field ionization by linearly polarized fields constitutes an unexpected result. The large magnitude of the observed effect, which leads to relative asymmetries in the % range, is probably due to the orientation sensitivity of tunneling, further confirming the unique spectroscopic interest of the strong-field regime.

IV General perspectives

On the longer term, there are two main directions which could lead to new fundamental insights into the chiral light-matter interaction.

Spin-resolved photoionization: The first direction would consist in resolving the spin of the electrons. The collision of spin-polarized electrons with chiral molecules have been studied theoretically and experimentally. In our measurements we have demonstrated the possibility to observe chirosensitive effects in electron-ion collisions without relying on spin polarization, which constitutes an important fundamental step – the electrons do not need to be spin-polarized to give rise to chiral laser-induced electron diffraction. This does not mean that spin cannot induce additional effects in the process. Strong field ionization naturally produces spin-polarized electrons [Barth 13, Hartung 16]. Resolving the spin of the diffracted electrons could provide important insights onto the mechanism of chiral-induced spin selectivity [Ray 99], which is at the heart of many applications, from chemistry to spintronics [Kulkarni 20], but whose fundamental origin remains debated.

Using orbital angular momentum: So far we have studied the effect of interactions of the spin angular momentum of photons, which manifest as polarization of the electromagnetic wave, with chiral matter. But photons can also carry unbounded orbital angular momentum (OAM) [Allen 92], which manifests as the spatial phase distribution of the wave front. It was previously believed that imprinting the influence of OAM on a matter wave, specifically on a propagating electron, was very challenging and virtually undetectable [Kaneyasu 17] [Sen 22].

But it has been recently experimentally observed that OAM in fact does influence propagating electron and that the phase information survives ensemble averaging out to macroscopic distances, where the electron is detected [De Ninno 20]. In addition, electronic transitions are conventionally forbidden by selection rules can become accessible in the presence of OAM, and could influence PECD. Furthermore, OAM has been used to study magnetic helicoidal dichroism [Fanciulli 22] and can be used to perform time-resolved non-linear chiral measurements [Rouxel 22]. With these results in mind, measuring the influence of OAM in the various photoionization regimes we have investigated throughout this thesis appears very appealing. The high sensitivity of the methods we have implemented will enable detecting what could be very weak effects with high confidence and discover new physical processes mixing light polarization, OAM, and molecular chirality.

Appendices

I Atomic Units

Atomic units or Hatree units are a system of natural units of measurement used in atomic physics for convenience. It can be viewed as unit in the world of an electron. By definition, in atomic units the four fundamental constants: reduced Planck constant ($\hbar$), elementary charge (e), Bhor radius (a_0) and mass of electron m_e are set to a numerical value of 1. Atomic units are abbreviated as 'a.u.' or 'au'.

Name	Symbol/Definition	Value in atomic units
Reduced Planck Constant	$\hbar = 1.054571817 \times 10^{-34} J \cdot s$	1
Elementary charge	$\mathrm{e} = 1.602176634 \times 10^{-19} C$	1
Electorn mass	$m_\mathrm{e} = 9.1093837015(28) \times 10^{-31} Kg$	1
Bohr radius	$a_0 = \frac{4\pi\epsilon_0\hbar^2}{m_\mathrm{e}e^2}$	1
Speed of light	c	$(1/\alpha)a_0E_\mathrm{h}/\hbar \approx 137a_0E_\mathrm{h}/\hbar$
Proton mass	m_p	$\approx 1836\, m_\mathrm{e}$
Classical electron radius	$r_\mathrm{e} = \frac{1}{4\pi\epsilon_0}\frac{e^2}{m_\mathrm{e}c^2}$	$\alpha^2 a_0 \approx 0.0000532\, a_0$

Table 1 – *Some physical constants expressed in atomic units.*

II Gaussian Beam Characteristics

In optics a Gaussian beam is a beam of monochromatic electromagnetic radiation whose amplitude envelope in the transverse plane is a Gaussian. It is a transverse electromagnetic mode (TEM_{00}) and is the solution to the Helmholtz equation under paraxial approximation [Siegman 86]. For a Gaussian beam propagating in the $(+z)$ direction with polarization along the $(+x)$ direction is given as:

$$E(r,z) = E_0 \exp\left(\frac{-r^2}{w(z)^2}\right)\frac{w_0}{w(z)}\exp\left(-i\Big(kz + \frac{kr^2}{2R(z)} - \phi(z)\Big)\right)\hat{x} \tag{1}$$

where r is the radial distance from the center of the beam, z is the axial distance from the focus, k is the wavenumber, E_0 is the peak amplitude, w is the beam waist radius, $R(z)$ is the radius of curvature of the beam wavefront at z and $\phi(z)$ is the Gouy phase.

The evolution of a Gaussian beam along the propagation direction, z, is given by:

$$w(z) = w_0\sqrt{1 + \left(\frac{z\lambda}{\pi w_0^2}\right)^2} \tag{2}$$

One of the beam parameter used to describe the geometrical profile of the beam is Rayleigh Range z_R. The Rayleigh range is defined as the distance from the waist where the width (w) of the beam reaches $\sqrt{2}$ times larger than at the focus and is given as:

$$z_R = \frac{\pi w_0^2}{\lambda} \tag{3}$$

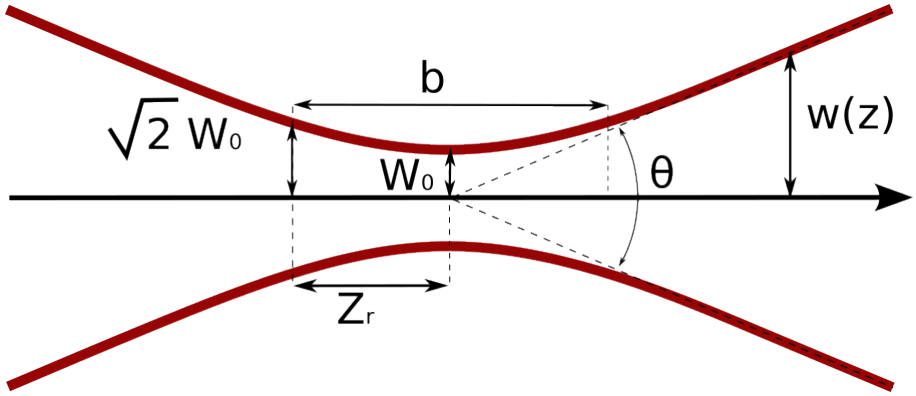

Figure 3 – *Longitudinal profile of a focusing Gaussian beam.*

The distance between the two points $z = \pm z_R$ is called the confocal parameter or depth of focus of the beam.

As the Gaussian beam propagates along z it acquires a phase shift compared to a plane and this is called the Guoy Phase and expressed as:

$$\phi(z) = \arctan\left(\frac{z}{z_R}\right) \tag{4}$$

While the radius of curvature $R(z)$ is given as:

$$R(z) = z\left[1 + \left(\frac{z_R}{z}\right)^2\right] \tag{5}$$

III Effective Ionization Length in Multiphoton Ionization

Lets assume we have a Gaussian beam propagating in the z direction. Then the beam can be described by the equation

$$F(x, z) = A \exp\Big(-\frac{-x^2}{w(z)}\Big) \tag{6}$$

The transition rate in multiphoton ionization follows the power law given as $\mathbb{P}_{a\to b} \propto I^N$, where N is the number of photon absorbed for ionization and $\mathbb{P}_{a\to b}$ is the probability of transition from a bound state a to the final state b, described by the wavefuction ψ_a abd ψ_b respectively. The same power law also holds true for bound to continuum transition: ionization. Hence the evolution of the effective length of multiphoton ionization along the propagation direction of the Gaussian beam can be given as:

$$F(x,z) = A\exp\Big(-\frac{x^2}{w(z)}\Big) \tag{7}$$

$$F(x,z)^N = \left[A\exp\Big(-\frac{x^2}{w(z)}\Big)\right]^N \tag{8}$$

$$\implies w(z) = w_0\sqrt{1+\left(\frac{z\lambda}{\pi w_0^2}\right)^2}\sqrt{\frac{1}{N}} \tag{9}$$

Hence an effective ionization length, z_{eff}, given as:

$$z_{eff} = \frac{\pi w_0^2}{\lambda}\sqrt{\frac{1}{N}}. \tag{10}$$

IV Convolution of two Gaussian

Given that the two Gaussian PDFs are given by

$$F(x) = \frac{1}{\sqrt{2\pi}\sigma_f}\exp\Big(-\frac{(x-\mu_f)^2}{2\sigma_f^2}\Big) \tag{11}$$

$$G(x) = \frac{1}{\sqrt{2\pi}\sigma_g}\exp\Big(-\frac{(x-\mu_g)^2}{2\sigma_g^2}\Big) \tag{12}$$

Thus the resultant convolution of the two Gaussian functions $F(x)$ and $G(x)$ is given as

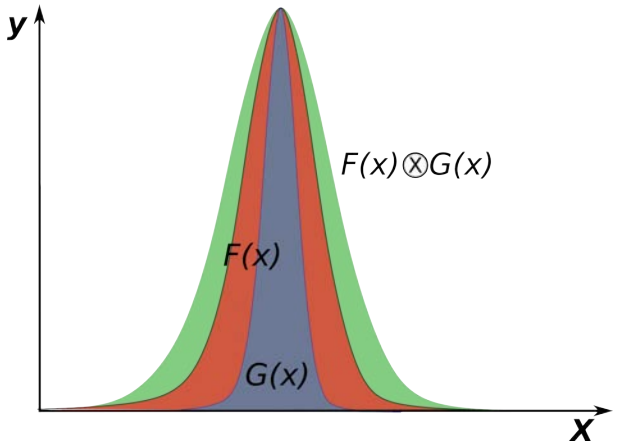

Figure 4 – *Schematic representation of convolution of two Gaussian distributions $F(x)$ (shown in red) and $G(x)$ (shown in blue) is $F \circledast G$ (shown in green).*

$$F \circledast G = \frac{1}{\sqrt{2\pi(\sigma_f^2+\sigma_g^2)}}\exp\Big(-\frac{(x-(\mu_f+\mu_g))^2}{2(\sigma_f^2+\sigma_g^2)}\Big) \tag{13}$$

Thus the result of the convolution of two Gaussian PDFs is a Gaussian function with the mean given as

$$\mu_{f \circledast g} = \mu_f + \mu_g \tag{14}$$

and the standard deviation is given as

$$\sigma_{f \circledast g} = \sqrt{\sigma_f^2 + \sigma_g^2} \tag{15}$$

Full width of half maximum is defined for a Gaussian function as:

$$FWHM = 2\sqrt{2\ln 2}\sigma \approx 2.35\sigma \tag{16}$$

V Retardation of Quarter-Waveplate

The principle of the method to extract the retardation of a waveplate can be understood by Mueller calculations. The Mueller matrix for any wave plate rotated through an angle θ is given by

$$M(\phi,\theta) = \begin{pmatrix} 1 & 0 & 0 & 0 \\ 0 & cos^2 2\theta + cos\phi sin^2 2\theta & (1-cos\phi)sin2\theta cos2\theta & -sin\phi sin2\theta \\ 0 & (1-cos\phi)sin2\theta cos2\theta & sin^2 2\theta + cos\phi cos^2 2\theta & sin\phi cos2\theta \\ 0 & sin\phi sin2\theta & -sin\phi cos2\theta & cos\phi \end{pmatrix} \tag{17}$$

with ϕ its phase shift. Taking an incident LHP beam $S_{\mathrm{LHP}} = I_0 \begin{bmatrix} 1 & 1 & 0 & 0 \end{bmatrix}^T$ passing through the wave plate leads to the modified Stokes vector S'

$$S' = I_0 \begin{pmatrix} 1 \\ cos^2 2\theta + cos\phi sin^2 2\theta \\ (1-cos\phi)sin2\theta cos2\theta \\ sin\phi sin2\theta \end{pmatrix} \tag{18}$$

Tuning the orientation of the WP enables reaching a zero intensity on the detector, when the fast axis of the WP is aligned with the incident polarisation at $\theta = 0°$. In that case Eq. 18 reduces to

$$S' = I_0 \begin{bmatrix} 1 & 1 & 0 & 0 \end{bmatrix}^T \tag{19}$$

The WP is then rotated by $\theta = 45°$ leading for Eq. 18

$$S' = I_0 \begin{bmatrix} 1 & cos\phi & 0 & sin\phi \end{bmatrix}^T \tag{20}$$

Upon tilting the analyzing polarizer by angle an α. Its Mueller matrix is

$$M(\phi) = \frac{1}{2}\begin{pmatrix} 1 & cos2\alpha & sin2\alpha & 0 \\ cos2\alpha & cos^2 2\alpha & sin2\alpha cos2\alpha & 0 \\ sin2\alpha & sin2\alpha cos2\alpha & sin^2 2\alpha & 0 \\ 0 & 0 & 0 & 0 \end{pmatrix} \tag{21}$$

and consequently the Stokes vector after the analyser (using Eq. 20 and 21)

$$S = \frac{I_0}{2}(1 + cos\phi cos2\alpha)\begin{bmatrix} 1 & cos2\alpha & sin2\alpha & 0 \end{bmatrix}^T \tag{22}$$

As a result, the intensity on the detector is given by

$$I(\alpha, \phi) = \frac{I_0}{2}(1 + \cos\phi \cos 2\alpha) \tag{23}$$

The phase shift ϕ, as shown in Eq. 23, is evaluated from an analyser at $\alpha = 0°$ and $\alpha = 90°$ leading to the measurements $I(0°, \phi) = \frac{I_0}{2}(1 + \cos\phi)$ and $I(90°, \phi) = \frac{I_0}{2}(1 - \cos\phi)$ from which we obtain:

$$\phi = cos^{-1}\Big(\frac{I(0°, \phi) - I(90°, \phi)}{I(0°, \phi) + I(90°, \phi)}\Big) \tag{24}$$

Bibliography

[Agostini 79] P. Agostini, F. Fabre, G. Mainfray, G. Petite & N. K. Rahman. *Free-free transitions following six-photon ionization of xenon atoms.* Physical Review Letters, **42**, 17, page 1127, (1979). [Cited on page 122.]

[Allen 92] L. Allen, M. W. Beijersbergen, R. Spreeuw & J. Woerdman. *Orbital angular momentum of light and the transformation of Laguerre-Gaussian laser modes.* Physical review A, **45**, 11, page 8185, (1992). [Cited on page 162.]

[Amini 20] K. Amini & J. Biegert. *Chapter Three - Ultrafast Electron Diffraction Imaging of Gas-Phase Molecules.* In L. F. Dimauro, H. Perrin & S. F. Yelin, editeurs, Advances In Atomic, Molecular, and Optical Physics, volume 69, pages 163–231. Academic Press, (2020). [Cited on pages 120, 123, and 126.]

[Antoine 97] P. Antoine, B. Carré, A. L'Huillier & M. Lewenstein. *Polarization of high-order harmonics.* Physical Review A, **55**, 2, page 1314, (1997). [Cited on page 35.]

[Arago 11] Arago. *Mémoire sur une modification remarquable qu'éprouvent les rayons lumineux dans leur passage à travers certains corps diaphanes et sur quelques autres nouveaux phénomènes d'optique.* Mémoires de la classe des sciences mathématiques et physiques de l'Institut Impérial de France, **1st part**, page 93–134, (1811). [Cited on pages 16 and 149.]

[Arnoldt 11] S. Arnoldt. *Rotating quarter-wave plate Stokes polarimeter.* PhD thesis, B. Sc. thesis, Universität Bonn, (2011). [Cited on pages 30 and 31.]

[Awasthi 08] M. Awasthi, Y. V. Vanne, A. Saenz, A. Castro & P. Decleva. *Single-active-electron approximation for describing molecules in ultrashort laser pulses and its application to molecular hydrogen.* Physical Review A, **77**, 6, page 063403, (2008). [Cited on page 121.]

[Ayuso 22] D. Ayuso, A. F. Ordonez & O. Smirnova. *Ultrafast chirality: the road to efficient chiral measurements.* arXiv preprint arXiv:2203.00580, (2022). [Cited on page 151.]

[Azoury 19] D. Azoury, O. Kneller, M. Krüger, B. D. Bruner, O. Cohen, Y. Mairesse & N. Dudovich. *Interferometric attosecond lock-in measurement of extreme-ultraviolet circular dichroism.* Nature Photonics, **13**, 3, pages 198–204, (2019). [Cited on page 34.]

[Barreau 18] L. Barreau, K. Veyrinas, V. Gruson, S. J. Weber, T. Auguste, J.-F. Hergott, F. Lepetit, B. Carré, J.-C. Houver, D. Dowek*et al. Evidence of depolarization and ellipticity of high harmonics driven by ultrashort bichromatic circularly polarized fields.* Nature communications, **9**, 1, pages 1–10, (2018). [Cited on page 36.]

[Barreau 20] L. Barreau, A. D. Ross, S. Garg, P. M. Kraus, D. M. Neumark & S. R. Leone. *Efficient table-top dual-wavelength beamline for ultrafast transient absorption spectroscopy in the soft X-ray region.* Scientific Reports, **10**, 1, page 5773, (2020). [Cited on page 34.]

[Barth 13] I. Barth & O. Smirnova. *Spin-polarized electrons produced by strong-field ionization.* Physical Review A, **88**, 1, page 013401, (2013). [Cited on page 162.]

[Beaulieu 16] S. Beaulieu, A. Ferré, R. Géneaux, R. Canonge, D. Descamps, B. Fabre, N. Fedorov, F. Légaré, S. Petit, T. Ruchon, V. Blanchet, Y. Mairesse & B. Pons. *Universality of photoelectron circular dichroism in the photoionization of chiral molecules.* New Journal of Physics, **18**, 10, page 102002, (2016). [Cited on pages 18, 81, 82, 127, 128, and 140.]

[Beaulieu 18] S. Beaulieu, A. Comby, D. Descamps, S. Petit, F. Légaré, B. Fabre, V. Blanchet & Y. Mairesse. *Multiphoton photoelectron circular dichroism of limonene with independent polarization state control of the bound-bound and bound-continuum transitions.* The Journal of Chemical Physics, **149**, 13, page 134301, (2018). [Cited on pages 82 and 160.]

[Beauvarlet 22] S. Beauvarlet, E. Bloch, D. Rajak, D. Descamps, B. Fabre, S. Petit, B. Pons, Y. Mairesse & V. Blanchet. *Photoelectron elliptical dichroism spectroscopy of resonance-enhanced multiphoton ionization via the 3s, 3p and 3d Rydberg series in fenchone.* Physical Chemistry Chemical Physics, **24**, 11, pages 6415–6427, (2022). [Cited on pages 18, 86, and 100.]

[Belsa 21] B. Belsa, K. Amini, X. Liu, A. Sanchez, T. Steinle, J. Steinmetzer, A. T. Le, R. Moshammer, T. Pfeifer, J. Ullrich, R. Moszynski, C. D. Lin, S. Gräfe & J. Biegert. *Laser-induced electron diffraction of the ultrafast umbrella motion in ammonia.* Structural Dynamics, **8**, 1, page 014301, (2021). [Cited on page 127.]

[Biot 15] J. B. Biot. *Phenomene de polarisation successive, observés dans des fluides homogenes.* Bulletin des Sciences, par la Société Philomatique de Paris, **1**, page 190–192, (1815). [Cited on pages 16 and 149.]

[Biot 19] J. B. Biot. *Extrait d'un mémoire sur les rotations que certaines substances impriment aux axes de polarisation des rayons lumineux.* Annales de Chimie et de Physique, **2**, pages 372–389, (1819). [Cited on pages 16 and 149.]

[Blaga 12] C. I. Blaga, J. Xu, A. D. DiChiara, E. Sistrunk, K. Zhang, P. Agostini, T. A. Miller, L. F. DiMauro & C. D. Lin. *Imaging Ultrafast Molecular Dynamics with Laser-Induced Electron Diffraction.* Nature, **483**, 7388, pages 194–197, (2012). [Cited on pages 120, 126, and 127.]

[Bloch 20] E. Bloch. *Femtosecond and attosecond chiral dynamics investigated by velocity map imaging and photoelectron photoion coincidence spectroscopy.* These de doctorat, Bordeaux, (2020). [Cited on pages 25, 47, 50, 83, 113, and 124.]

[Bloch 21] E. Bloch, S. Larroque, S. Rozen, S. Beaulieu, A. Comby, S. Beauvarlet, D. Descamps, B. Fabre, S. Petit, R. Taïeb*et al.* *Revealing the Influence of Molecular Chirality on Tunnel-Ionization Dynamics.* Physical Review X, **11**, 4, page 041056, (2021). [Cited on pages 126, 128, 135, 140, and 157.]

[Boesl 13] U. Boesl, A. Bornschlegl, C. Logé & K. Titze. *Resonance-enhanced multiphoton ionization with circularly polarized light: chiral carbonyls.* Analytical and Bioanalytical Chemistry, **405**, pages 6913–6924, (2013). [Cited on page 106.]

[Born 27] R. Born M. ; Oppenheimer. *Zur Quantentheorie der Molekeln.* Annalen der Physik , Issue , pp.457-484, **389**, 20, pages 457–484, (1927). [Cited on page 78.]

[Böwering 01] N. Böwering, T. Lischke, B. Schmidtke, N. Müller, T. Khalil & U. Heinzmann. *Asymmetry in Photoelectron Emission from Chiral Molecules Induced by Circularly Polarized Light.* Physical

Review Letters, **86**, 7, pages 1187–1190, (2001). [Cited on pages 16, 18, 76, and 121.]

[Brown 56] K. Brown & G. Tautfest. *Faraday-cup monitors for high-energy electron beams.* Review of Scientific Instruments, **27**, 9, pages 696–702, (1956). [Cited on page 44.]

[Budil 93] K. Budil, P. Salières, A. L'Huillier, T. Ditmire & M. Perry. *Influence of ellipticity on harmonic generation.* Physical Review A, **48**, 5, page R3437, (1993). [Cited on pages 34, 35, and 128.]

[Calegari 16] F. Calegari, A. Trabattoni, A. Palacios, D. Ayuso, M. C. Castrovilli, J. B. Greenwood, P. Decleva, F. Martín & M. Nisoli. *Charge migration induced by attosecond pulses in bio-relevant molecules.* Journal of Physics B: Atomic, Molecular and Optical Physics, **49**, 142001, (2016). [Cited on page 34.]

[Chen 10] M.-C. Chen, P. Arpin, T. Popmintchev, M. Gerrity, B. Zhang, M. Seaberg, D. Popmintchev, M. M. Murnane & H. C. Kapteyn. *Bright, Coherent, Ultrafast Soft X-Ray Harmonics Spanning the Water Window from a Tabletop Light Source.* Physical Review Letters, **105**, 17, page 173901, (2010). [Cited on page 34.]

[Comby 16] A. Comby, S. Beaulieu, M. Boggio-Pasqua, D. Descamps, F. Légaré, L. Nahon, S. Petit, B. Pons, B. Fabre, Y. Mairesse & V. Blanchet. *Relaxation Dynamics in Photoexcited Chiral Molecules Studied by Time-Resolved Photoelectron Circular Dichroism: Toward Chiral Femtochemistry.* The Journal of Physical Chemistry Letters, **7**, 22, pages 4514–4519, (2016). [Cited on pages 82 and 114.]

[Comby 18] A. Comby, E. Bloch, C. M. M. Bond, D. Descamps, J. Miles, S. Petit, S. Rozen, J. B. Greenwood, V. Blanchet & Y. Mairesse. *Real-time determination of enantiomeric and isomeric content using photoelectron elliptical dichroism.* Nature Communications, **9**, 1, (2018). [Cited on pages 82, 84, 85, 100, 104, and 106.]

[Comby 20a] A. Comby, S. Beaulieu, E. Constant, D. Descamps, S. Petit & Y. Mairesse. *Absolute gas density profiling in high-order harmonic generation: erratum.* Optics Express, **28**, 21, pages 32105–32105, (2020). [Cited on page 38.]

[Comby 20b] A. Comby, E. Bloch, S. Beauvarlet, D. Rajak, S. Beaulieu, D. Descamps, A. Gonzalez, F. Guichard, S. Petit, Y. Zaouter*et al. Bright, polarization-tunable high repetition rate extreme ultraviolet beamline for coincidence electron–ion imaging.*

Journal of Physics B: Atomic, Molecular and Optical Physics, **53**, 23, page 234003, (2020). [Cited on pages 34, 35, and 44.]

[Comby 22] A. Comby, D. Rajak, D. Descamps, S. Petit, V. Blanchet, Y. Mairesse, J. Gaudin & S. Beaulieu. *Ultrafast polarization-tunable monochromatic extreme ultraviolet source at high-repetition-rate*. Journal of Optics, **24**, 8, page 084003, (2022). [Cited on pages 41, 42, 43, and 44.]

[Condon 26] E. Condon. *A theory of intensity distribution in band systems*. Physical Review, **28**, 6, page 1182, (1926). [Cited on page 78.]

[Dasch 92] C. J. Dasch. *One-dimensional tomography: a comparison of Abel, onion-peeling, and filtered backprojection methods*. Applied optics, **31**, 8, pages 1146–1152, (1992). [Cited on page 46.]

[De Ninno 20] G. De Ninno, J. Wätzel, P. R. Ribič, E. Allaria, M. Coreno, M. B. Danailov, C. David, A. Demidovich, M. Di Fraia, L. Giannessi*et al. Photoelectric effect with a twist*. Nature Photonics, **14**, 9, pages 554–558, (2020). [Cited on page 163.]

[De Oliveira 11] N. De Oliveira, M. Roudjane, D. Joyeux, D. Phalippou, J.-C. Rodier & L. Nahon. *High-resolution broad-bandwidth Fourier-transform absorption spectroscopy in the VUV range down to 40 nm*. Nature Photonics, **5**, 3, pages 149–153, (2011). [Cited on page 100.]

[Descamps 21] D. Descamps, F. Guichard, S. Petit, S. Beauvarlet, A. Comby, L. Lavenu & Y. Zaouter. *High-power sub-15 fs nonlinear pulse compression at 515 nm of an ultrafast Yb-doped fiber amplifier*. Optics letters, **46**, 8, pages 1804–1807, (2021). [Cited on page 36.]

[Dinu 02] L. Dinu, A. Eppink, F. Rosca-Pruna, H. Offerhaus, W. Van der Zande & M. Vrakking. *Application of a time-resolved event counting technique in velocity map imaging*. Review of Scientific Instruments, **73**, 12, pages 4206–4213, (2002). [Cited on page 44.]

[Dowek 07] D. Dowek, M. Lebech, J. Houver & R. Lucchese. *Circular dichroism in molecular frame photoemission*. Molecular Physics, **105**, 11-12, pages 1757–1768, (2007). [Cited on page 79.]

[Dreissigacker 14] I. Dreissigacker & M. Lein. *Photoelectron circular dichroism of chiral molecules studied with a continuum-state-corrected strong-field approximation*. Physical Review A, **89**, 053406, (2014). [Cited on pages 127 and 128.]

[Dribinski 02] V. Dribinski, A. Ossadtchi, V. A. Mandelshtam & H. Reisler. *Reconstruction of Abel-transformable images: The Gaussian basis-set expansion Abel transform method.* Review of Scientific Instruments, **73**, 7, pages 2634–2642, (2002). [Cited on page 46.]

[Dudovich 06] N. Dudovich, J. Levesque, O. Smirnova, D. Zeidler, D. Comtois, M. Y. Ivanov, D. Villeneuve & P. Corkum. *Attosecond temporal gating with elliptically polarized light.* Physical review letters, **97**, 25, page 253903, (2006). [Cited on page 141.]

[Eppink 97] A. T. J. B. Eppink & D. H. Parker. *Velocity map imaging of ions and electrons using electrostatic lenses: Application in photoelectron and photofragment ion imaging of molecular oxygen.* Review of Scientific Instruments, **68**, 9, pages 3477–3484, (1997). [Cited on pages 44 and 45.]

[Fanciulli 22] M. Fanciulli, M. Pancaldi, E. Pedersoli, M. Vimal, D. Bresteau, M. Luttmann, D. De Angelis, P. R. Ribič, B. Rösner, C. David*et al.* *Observation of magnetic helicoidal dichroism with extreme ultraviolet light vortices.* Physical Review Letters, **128**, 7, page 077401, (2022). [Cited on page 163.]

[Fehre 19] K. Fehre, S. Eckart, M. Kunitski, C. Janke, D. Trabert, J. Rist, M. Weller, A. Hartung, L. P. H. Schmidt, T. Jahnke, R. Dörner & M. Schöffler. *Link between Photoelectron Circular Dichroism and Fragmentation Channel in Strong Field Ionization.* The Journal of Physical Chemistry A, **123**, 30, pages 6491–6495, (2019). [Cited on page 111.]

[Ferray 88] M. Ferray, A. L'Huillier, X. F. Li, L. A. Lompre, G. Mainfray & C. Manus. *Multiple-harmonic conversion of 1064 nm radiation in rare gases.* Journal of Physics B: Atomic, Molecular and Optical Physics, **21**, 3, pages L31–L35, (1988). [Cited on pages 33 and 122.]

[Ferré 15a] A. Ferré, A. E. Boguslavskiy, M. Dagan, V. Blanchet, B. D. Bruner, F. Burgy, A. Camper, D. Descamps, B. Fabre, N. Fedorov, J. Gaudin, G. Geoffroy, J. Mikosch, S. Patchkovskii, S. Petit, T. Ruchon, H. Soifer, D. Staedter, I. Wilkinson, A. Stolow, N. Dudovich & Y. Mairesse. *Multi-channel electronic and vibrational dynamics in polyatomic resonant high-order harmonic generation.* Nature Communications, **6**, 5952, (2015). [Cited on pages 34 and 44.]

[Ferré 15b] A. Ferré, C. Handschin, M. Dumergue, F. Burgy, A. Comby, D. Descamps, B. Fabre, G. A. Garcia, R. Géneaux, L. Merceron, E. Mével, L. Nahon, S. Petit, B. Pons, D. Staedter, S. Weber, T. Ruchon, V. Blanchet & Y. Mairesse. *A table-top ultrashort light source in the extreme ultraviolet for circular dichroism experiments.* Nature Photonics, **9**, pages 93–98, (2015). [Cited on page 79.]

[Figueira de Morisson Faria 20] C. Figueira de Morisson Faria & A. S. Maxwell. *It is all about phases: ultrafast holographic photoelectron imaging.* Reports on Progress in Physics, **83**, 3, page 034401, (2020). [Cited on pages 125 and 146.]

[Fleischer 14] A. Fleischer, O. Kfir, T. Diskin, P. Sidorenko & O. Cohen. *Spin angular momentum and tunable polarization in high-harmonic generation.* Nature Photonics, **8**, 7, pages 543–549, (2014). [Cited on pages 36, 37, and 128.]

[Fomichev 02] S. Fomichev, P. Breger, B. Carre, P. Agostini & D. Zaretsky. *Non-collinear high-harmonic generation.* Laser physics, **12**, 2, pages 383–388, (2002). [Cited on pages 39 and 40.]

[Franck 26] J. Franck & E. Dymond. *Elementary processes of photochemical reactions.* Transactions of the Faraday Society, **21**, February, pages 536–542, (1926). [Cited on page 78.]

[Frassetto 11] F. Frassetto, C. Cacho, C. A. Froud, I. E. Turcu, P. Villoresi, W. A. Bryan, E. Springate & L. Poletto. *Single-grating monochromator for extreme-ultraviolet ultrashort pulses.* Optics Express, **19**, 20, page 19169, (2011). [Cited on page 40.]

[Gademann 09] G. Gademann, Y. Huismans, A. Gijsbertsen, J. Jungmann, J. Visschers & M. J. Vrakking. *Velocity map imaging using an in-vacuum pixel detector.* Review of Scientific Instruments, **80**, 10, page 103105, (2009). [Cited on page 44.]

[Ganjitabar 18a] H. Ganjitabar, R. Hadidi, G. A. Garcia, L. Nahon & I. Powis. *Vibrationally-resolved photoelectron spectroscopy and photoelectron circular dichroism of bicyclic monoterpene enantiomers.* Journal of Molecular Spectroscopy, **353**, pages 11–19, (2018). [Cited on page 79.]

[Ganjitabar 18b] H. Ganjitabar, R. Hadidi, G. A. Garcia, L. Nahon & I. Powis. *Vibrationally-resolved photoelectron spectroscopy and photoelectron circular dichroism of bicyclic monoterpene enantiomers.*

Journal of Molecular Spectroscopy, **353**, pages 11–19, (2018). [Cited on page 100.]

[Ganjitabar 20] H. Ganjitabar, G. A. Garcia, L. Nahon & I. Powis. *Decoupling vibration and electron energy dependencies in the photoelectron circular dichroism of a terpene, 3-carene.* The Journal of Chemical Physics, **153**, 3, page 034302, (2020). [Cited on pages 78 and 79.]

[Ganjitabar 21] H. Ganjitabar, D. P. Singh, R. Chapman, A. Gardner, R. S. Minns, I. Powis, K. L. Reid & A. Vredenborg. *The role of the intermediate state in angle-resolved photoelectron studies using (2+ 1) resonance-enhanced multiphoton ionization of the chiral terpenes, α-pinene and 3-carene.* Molecular Physics, **119**, 1-2, page e1808907, (2021). [Cited on page 100.]

[Garcia 03] G. A. Garcia, L. Nahon, M. Lebech, J.-C. Houver, D. Dowek & I. Powis. *Circular Dichroism in the Photoelectron Angular Distribution from Randomly Oriented Enantiomers of Camphor.* The Journal of Chemical Physics, **119**, 17, pages 8781–8784, (2003). [Cited on page 121.]

[Garcia 04] G. A. Garcia, L. Nahon & I. Powis. *Two-dimensional charged particle image inversion using a polar basis function expansion.* Review of Scientific Instruments, **75**, 11, pages 4989–4996, (2004). [Cited on page 46.]

[Garcia 05] G. A. Garcia, L. Nahon, C. J. Harding, E. A. Mikajlo & I. Powis. *A refocusing modified velocity map imaging electron/ion spectrometer adapted to synchrotron radiation studies.* Review of Scientific Instruments, **76**, 5, page 053302, (2005). [Cited on page 52.]

[Garcia 13] G. A. Garcia, L. Nahon, S. Daly & I. Powis. *Vibrationally induced inversion of photoelectron forward-backward asymmetry in chiral molecule photoionization by circularly polarized light.* Nature Communications, **4**, 2132, (2013). [Cited on page 79.]

[Garcia 14] G. A. Garcia, H. Dossmann, L. Nahon, S. Daly & I. Powis. *Photoelectron circular dichroism and spectroscopy of trifluoromethyl- and methyl-oxirane: a comparative study.* Physical Chemistry Chemical Physics, **16**, page 16214, (2014). [Cited on pages 77 and 111.]

[Gaumnitz 17] T. Gaumnitz, A. Jain, Y. Pertot, M. Huppert, I. Jordan, F. Ardana-Lamas & H. J. Wörner. *Streaking of 43-attosecond*

soft-X-ray pulses generated by a passively CEP-stable mid-infrared driver. Optics Express, **25**, 22, page 27506, (2017). [Cited on page 34.]

[Goldstein 03] D. Goldstein. *Polarized light Marcel Dekker Inc.* New York, pages 126–128, (2003). [Cited on page 30.]

[Goulielmakis 10] E. Goulielmakis, Z.-H. Loh, A. Wirth, R. Santra, N. Rohringer, V. S. Yakovlev, S. Zherebtsov, T. Pfeifer, A. M. Azzeer, M. F. Kling, S. R. Leone & F. Krausz. *Real-time observation of valence electron motion.* Nature, **466**, pages 739–743, (2010). [Cited on page 34.]

[Haessler 11] S. Haessler, J. Caillat & P. Salières. *Self-probing of molecules with high harmonic generation.* Journal of Physics B: Atomic, Molecular and Optical Physics, **44**, 20, page 203001, (2011). [Cited on page 120.]

[Handschin 13] C. Handschin. *Spectroscopie EUV résolue temporellement à l'échelle femtoseconde par imagerie de vecteur vitesse et génération d'harmoniques d'ordres élevés.* These de doctorat, Bordeaux 1, (2013). [Cited on pages 50 and 51.]

[Hartmann 19] G. Hartmann, M. Ilchen, P. Schmidt, C. Küstner-Wetekam, C. Ozga, F. Scholz, J. Buck, F. Trinter, J. Viefhaus, A. Ehresmann, M. Schöffler, A. Knie & P. Demekhin. *Recovery of High-Energy Photoelectron Circular Dichroism through Fano Interference.* Physical Review Letters, **123**, 043202, (2019). [Cited on page 78.]

[Hartung 16] A. Hartung, F. Morales, M. Kunitski, K. Henrichs, A. Laucke, M. Richter, T. Jahnke, A. Kalinin, M. Schöffler, L. P. H. Schmidt, M. Ivanov, O. Smirnova & R. Dörner. *Electron spin polarization in strong-field ionization of xenon atoms.* Nature Photonics, **10**, 8, pages 526–528, (2016). [Cited on page 162.]

[Heck 95] A. J. Heck & D. W. Chandler. *Imaging techniques for the study of chemical reaction dynamics.* Annual Review of Physical Chemistry, **46**, 1, pages 335–372, (1995). [Cited on page 46.]

[Hergenhahn 04] U. Hergenhahn, E. E. Rennie, O. Kugeler, S. Marburger, T. Lischke, I. Powis & G. Garcia. *Photoelectron circular dichroism in core level ionization of randomly oriented pure enantiomers of the chiral molecule camphor.* The Journal of Chemical Physics, **120**, 10, pages 4553–4556, (2004). [Cited on page 76.]

[Hertel 08] I. V. Hertel & C.-P. Schulz. Atome, moleküle und optische physik 1, volume 1. Springer, (2008). [Cited on page 121.]

[Hickstein 12] D. D. Hickstein, P. Ranitovic, S. Witte, X.-M. Tong, Y. Huismans, P. Arpin, X. Zhou, K. E. Keister, C. W. Hogle, B. Zhang, C. Ding, P. Johnsson, N. Toshima, M. J. J. Vrakking, M. M. Murnane & H. C. Kapteyn. *Direct Visualization of Laser-Driven Electron Multiple Scattering and Tunneling Distance in Strong-Field Ionization.* Physical Review Letters, **109**, 073004, (2012). [Cited on page 125.]

[Hickstein 15] D. D. Hickstein, F. J. Dollar, P. Grychtol, J. L. Ellis, R. Knut, C. Hernández-García, D. Zusin, C. Gentry, J. M. Shaw, T. Fan*et al. Non-collinear generation of angularly isolated circularly polarized high harmonics.* Nature Photonics, **9**, 11, pages 743–750, (2015). [Cited on page 44.]

[Hong 18] A. Hong, C. J. Moon, H. Jang, A. Min, M. Y. Choi, J. Heo & N. J. Kim. *Isomer-Specific Induced Circular Dichroism Spectroscopy of Jet-Cooled Phenol Complexes with (-)-Methyl l-Lactate.* The journal of physical chemistry letters, **9**, 3, pages 476–480, (2018). [Cited on page 100.]

[Huang 18] P.-C. Huang, C. Hernández-García, J.-T. Huang, P.-Y. Huang, C.-H. Lu, L. Rego, D. D. Hickstein, J. L. Ellis, A. Jaron-Becker, A. Becker*et al. Polarization control of isolated high-harmonic pulses.* Nature Photonics, **12**, 6, pages 349–354, (2018). [Cited on page 44.]

[Huismans 11] Y. Huismans, A. Rouzee, A. Gijsbertsen, J. H. Jungmann, A. S. Smolkowska, P. S. W. M. Logman, F. Lepine, C. Cauchy, S. Zamith, T. Marchenko, J. M. Bakker, G. Berden, B. Redlich, A. F. G. van der Meer, H. G. Muller, W. Vermin, K. J. Schafer, M. Spanner, M. Y. Ivanov, O. Smirnova, D. Bauer, S. V. Popruzhenko & M. J. J. Vrakking. *Time-Resolved Holography with Photoelectrons.* Science, **331**, 6013, pages 61–64, (2011). [Cited on page 125.]

[Itatani 04] J. Itatani, J. Levesque, D. Zeidler, H. Niikura, H. Pépin, J. C. Kieffer, P. B. Corkum & D. M. Villeneuve. *Tomographic imaging of molecular orbitals.* Nature, **432**, 7019, pages 867–871, (2004). [Cited on page 120.]

[Jungmann 10] J. Jungmann, A. Gijsbertsen, J. Visser, J. Visschers, R. Heeren & M. Vrakking. *A new imaging method for understanding chemical dynamics: Efficient slice imaging using an in-vacuum pixel*

detector. Review of Scientific Instruments, **81**, 10, page 103112, (2010). [Cited on page 44.]

[Kaidor] Kaidor. *Schematic of a polarimeter showing the principles behind its operation. Unpolarised light is passed through a polarising filter before travelling through a sample. The degree of rotation of polarisation is determined by a second, rotatable filter.* `https://en.wikipedia.org/wiki/Optical_rotation#/media/File:Polarimeter_(Optical_rotation).svg`. [Online; accessed 19-July-2022]. [Cited on pages 17 and 150.]

[Kaneyasu 17] T. Kaneyasu, Y. Hikosaka, M. Fujimoto, T. Konomi, M. Katoh, H. Iwayama & E. Shigemasa. *Limitations in photoionization of helium by an extreme ultraviolet optical vortex*. Physical Review A, **95**, 2, page 023413, (2017). [Cited on page 162.]

[Karamatskos 19] E. T. Karamatskos, G. Goldsztejn, S. Raabe, P. Stammer, T. Mullins, A. Trabattoni, R. R. Johansen, H. Stapelfeldt, S. Trippel, M. J. J. Vrakking, J. Küpper & A. Rouzée. *Atomic-resolution imaging of carbonyl sulfide by laser-induced electron diffraction*. The Journal of Chemical Physics, **150**, 24, page 244301, (2019). [Cited on page 127.]

[Kastner 16] A. Kastner, C. Lux, T. Ring, S. Züllighoven, C. Sarpe, A. Senftleben & T. Baumert. *Enantiomeric Excess Sensitivity to Below One Percent by Using Femtosecond Photoelectron Circular Dichroism*. ChemPhysChem, **17**, 8, pages 1119–1122, (2016). [Cited on page 82.]

[Kastner 17] A. Kastner, T. Ring, B. C. Krüger, G. B. Park, T. Schäfer, A. Senftleben & T. Baumert. *Intermediate state dependence of the photoelectron circular dichroism of fenchone observed via femtosecond resonance-enhanced multi-photon ionization*. The Journal of Chemical Physics, **147**, 1, page 013926, (2017). [Cited on pages 82 and 86.]

[Kfir 15] O. Kfir, P. Grychtol, E. Turgut, R. Knut, D. Zusin, D. Popmintchev, T. Popmintchev, H. Nembach, J. M. Shaw, A. Fleischer, H. Kapteyn, M. Murnane & O. Cohen. *Generation of bright phase-matched circularly-polarized extreme ultraviolet high harmonics*. Nature Photonics, **9**, 2, pages 99–105, (2015). [Cited on pages 36 and 44.]

[Kfir 16] O. Kfir, E. Bordo, G. Ilan Haham, O. Lahav, A. Fleischer & O. Cohen. *In-line production of a bi-circular field for generation*

of helically polarized high-order harmonics. Applied Physics Letters, **108**, 21, page 211106, (2016). [Cited on pages 36 and 128.]

[Kling 14] N. G. Kling, D. Paul, A. Gura, G. Laurent, S. De, H. Li, Z. Wang, B. Ahn, C. H. Kim, T. K. Kim, I. V. Litvinyuk, C. L. Cocke, I. Ben-Itzhak, D. Kim & M. F. Kling. *Thick-lens velocity-map imaging spectrometer with high resolution for high-energy charged particles.* Journal of Instrumentation, **9**, 05, pages P05005–P05005, (2014). [Cited on page 52.]

[Kothe 13] A. Kothe, J. Metje, M. Wilke, A. Moguilevski, N. Engel, R. Al-Obaidi, C. Richter, R. Golnak, I. Y. Kiyan & E. F. Aziz. *Time-of-flight electron spectrometer for a broad range of kinetic energies.* Review of Scientific Instruments, **84**, 2, page 023106, (2013). [Cited on page 44.]

[Krausz 09] F. Krausz & M. Ivanov. *Attosecond physics.* Reviews of Modern Physics, **81**, 1, pages 163–234, (2009). [Cited on page 34.]

[Kulkarni 20] C. Kulkarni, A. K. Mondal, T. K. Das, G. Grinbom, F. Tassinari, M. F. Mabesoone, E. Meijer & R. Naaman. *Highly Efficient and Tunable Filtering of Electrons' Spin by Supramolecular Chirality of Nanofiber-Based Materials.* Advanced Materials, **32**, 7, page 1904965, (2020). [Cited on page 162.]

[Kunitski 19] M. Kunitski, N. Eicke, P. Huber, J. Köhler, S. Zeller, J. Voigtsberger, N. Schlott, K. Henrichs, H. Sann, F. Trinter, L. P. H. Schmidt, A. Kalinin, M. S. Schöffler, T. Jahnke, M. Lein & R. Dörner. *Double-slit photoelectron interference in strong-field ionization of the neon dimer.* Nature Communications, **10**, 1, page 1, (2019). [Cited on page 126.]

[Lee 12] E. A. Lee & D. G. Messerschmitt. Digital communication. Springer Science & Business Media, (2012). [Cited on page 32.]

[Lee 20] C. Lee, T. Rohwer, E. J. Sie, A. Zong, E. Baldini, J. Straquadine, P. Walmsley, D. Gardner, Y. S. Lee, I. R. Fisher*et al. High resolution time-and angle-resolved photoemission spectroscopy with 11 eV laser pulses.* Review of Scientific Instruments, **91**, 4, page 043102, (2020). [Cited on pages 39 and 40.]

[Lehmann 13] C. S. Lehmann, N. B. Ram, I. Powis & M. H. M. Janssen. *Imaging photoelectron circular dichroism of chiral molecules by femtosecond multiphoton coincidence detection.* The Journal

of Chemical Physics, **139**, 23, page 234307, (2013). [Cited on pages 79, 82, and 111.]

[Lewenstein 94] M. Lewenstein, P. Balcou, M. Y. Ivanov, A. L'huillier & P. B. Corkum. *Theory of high-harmonic generation by low-frequency laser fields.* Physical Review A, **49**, 3, page 2117, (1994). [Cited on page 121.]

[Lewenstein 21] M. Lewenstein, M. Ciappina, E. Pisanty, J. Rivera-Dean, P. Stammer, T. Lamprou & P. Tzallas. *Generation of optical Schrödinger cat states in intense laser–matter interactions.* Nature Physics, **17**, 10, pages 1104–1108, (2021). [Cited on page 157.]

[Lin 10] C. Lin, A.-T. Le, Z. Chen, T. Morishita & R. Lucchese. *Strong-field rescattering physics—self-imaging of a molecule by its own electrons.* Journal of Physics B: Atomic, Molecular and Optical Physics, **43**, 12, page 122001, (2010). [Cited on page 120.]

[Lin 12] C. D. Lin & J. Xu. *Imaging ultrafast dynamics of molecules with laser-induced electron diffraction.* Physical Chemistry Chemical Physics, **14**, 38, page 13133, (2012). [Cited on page 121.]

[Liu 21] X. Liu, K. Amini, A. Sanchez, B. Belsa, T. Steinle & J. Biegert. *Machine learning for laser-induced electron diffraction imaging of molecular structures.* Communications Chemistry, **4**, 1, page 154, (2021). [Cited on pages 121 and 127.]

[Lux 12] C. Lux, M. Wollenhaupt, T. Bolze, Q. Liang, J. Köhler, C. Sarpe & T. Baumert. *Circular Dichroism in the Photoelectron Angular Distributions of Camphor and Fenchone from Multiphoton Ionization with Femtosecond Laser Pulses.* Angewandte Chemie International Edition, **51**, 20, pages 5001–5005, (2012). [Cited on pages 18, 79, and 82.]

[Lux 15] C. Lux, M. Wollenhaupt, C. Sarpe & T. Baumert. *Photoelectron Circular Dichroism of Bicyclic Ketones from Multiphoton Ionization with Femtosecond Laser Pulses.* ChemPhysChem, **16**, 1, pages 115–137, (2015). [Cited on pages 82 and 84.]

[Mancuso 16] C. A. Mancuso, D. D. Hickstein, K. M. Dorney, J. L. Ellis, E. Hasović, R. Knut, P. Grychtol, C. Gentry, M. Gopalakrishnan, D. Zusin, F. J. Dollar, X.-M. Tong, D. B. Milošević, W. Becker, H. C. Kapteyn & M. M. Murnane. *Controlling*

electron-ion rescattering in two-color circularly polarized femtosecond laser fields. Physical Review A, **93**, 053406, (2016). [Cited on pages 126 and 128.]

[Manzhos 03] S. Manzhos & H.-P. Loock. *Photofragment image analysis using the Onion-Peeling Algorithm.* Computer physics communications, **154**, 1, pages 76–87, (2003). [Cited on page 46.]

[Marangos 16] J. P. Marangos. *Development of high harmonic generation spectroscopy of organic molecules and biomolecules.* Journal of Physics B: Atomic, Molecular and Optical Physics, **49**, 13, page 132001, (2016). [Cited on page 34.]

[Maxwell 17] A. Maxwell, A. Al-Jawahiry, T. Das & C. F. de Morisson Faria. *Coulomb-corrected quantum interference in above-threshold ionization: Working towards multitrajectory electron holography.* Physical Review A, **96**, 2, page 023420, (2017). [Cited on page 124.]

[McPherson 87] A. McPherson, G. Gibson, H. Jara, U. Johann, T. S. Luk, I. A. McIntyre, K. Boyer & C. K. Rhodes. *Studies of multiphoton production of vacuum-ultraviolet radiation in the rare gases.* Journal of the Optical Society of America B, **4**, 2, pages 595–601, (1987). [Cited on pages 120 and 122.]

[Meckel 08a] M. Meckel, D. Comtois, D. Zeidler, A. Staudte, D. Pavičić, H. C. Bandulet, H. Pépin, J. C. Kieffer, R. Dörner, D. M. Villeneuve & P. B. Corkum. *Laser-Induced Electron Tunneling and Diffraction.* Science, **320**, 5882, pages 1478–1482, (2008). [Cited on page 120.]

[Meckel 08b] M. Meckel, D. Comtois, D. Zeidler, A. Staudte, D. Pavicic, H. C. Bandulet, H. Pepin, J. C. Kieffer, R. Dorner, D. M. Villeneuve & P. B. Corkum. *Laser-Induced Electron Tunneling and Diffraction.* Science, **320**, 5882, pages 1478–1482, (2008). [Cited on page 126.]

[Miles 17] J. Miles, D. Fernandes, A. Young, C. Bond, S. Crane, O. Ghafur, D. Townsend, J. Sá & J. Greenwood. *A new technique for probing chirality via photoelectron circular dichroism.* Analytica Chimica Acta, **984**, pages 134–139, (2017). [Cited on pages 82 and 84.]

[Mills 12] A. K. Mills, T. J. Hammond, M. H. C. Lam & D. J. Jones. *XUV frequency combs via femtosecond enhancement cavities.* Journal

of Physics B: Atomic, Molecular and Optical Physics, **45**, 14, page 142001, (2012). [Cited on page 40.]

[Moulton 86] P. F. Moulton. *Spectroscopic and laser characteristics of Ti: Al 2 O 3.* JOSA B, **3**, 1, pages 125–133, (1986). [Cited on page 23.]

[Nahon 04] L. Nahon & C. Alcaraz. *SU5: a calibrated variable-polarization synchrotron radiation beam line in the vacuum-ultraviolet range.* Applied optics, **43**, 5, pages 1024–1037, (2004). [Cited on pages 18 and 36.]

[Nahon 06] L. Nahon, G. A. Garcia, C. J. Harding, E. Mikajlo & I. Powis. *Determination of chiral asymmetries in the valence photoionization of camphor enantiomers by photoelectron imaging using tunable circularly polarized light.* The Journal of Chemical Physics, **125**, 11, page 114309, (2006). [Cited on pages 76, 77, and 83.]

[Nahon 15] L. Nahon, G. A. Garcia & I. Powis. *Valence shell one-photon photoelectron circular dichroism in chiral systems.* Journal of Electron Spectroscopy and Related Phenomena, **204**, pages 322–334, (2015). [Cited on page 34.]

[Nahon 16] L. Nahon, L. Nag, G. A. Garcia, I. Myrgorodska, U. Meierhenrich, S. Beaulieu, V. Wanie, V. Blanchet, R. Géneaux & I. Powis. *Determination of accurate electron chiral asymmetries in fenchone and camphor in the VUV range: sensitivity to isomerism and enantiomeric purity.* Physical Chemistry Chemical Physics, **18**, 18, pages 12696–12706, (2016). [Cited on pages 43, 76, and 78.]

[Neufeld 18] O. Neufeld & O. Cohen. *Optical Chirality in Nonlinear Optics: Application to High Harmonic Generation.* Physical Review Letters, **120**, 133206, (2018). [Cited on page 128.]

[Nisoli 96] M. Nisoli, S. De Silvestri & O. Svelto. *Generation of high energy 10 fs pulses by a new pulse compression technique.* Applied Physics Letters, **68**, 20, pages 2793–2795, (1996). [Cited on page 23.]

[Nisoli 17] M. Nisoli, P. Decleva, F. Calegari, A. Palacios & F. Martín. *Attosecond Electron Dynamics in Molecules.* Chemical Reviews, **117**, 16, pages 10760–10825, (2017). [Cited on page 34.]

[Paulus 94] G. G. Paulus, W. Nicklich, H. Xu, P. Lambropoulos & H. Walther. *Plateau in above Threshold Ionization Spectra.*

Physical Review Letters, **72**, 18, pages 2851–2854, (1994). [Cited on pages 120 and 122.]

[Paulus 98] G. G. Paulus, F. Zacher, H. Walther, A. Lohr, W. Becker & M. Kleber. *Above-Threshold Ionization by an Elliptically Polarized Field: Quantum Tunneling Interferences and Classical Dodging.* Physical Review Letters, **80**, 3, pages 484–487, (1998). [Cited on page 120.]

[Paulus 00] G. Paulus, F. Grasbon, A. Dreischuh, H. Walther, R. Kopold & W. Becker. *Above-threshold ionization by an elliptically polarized field: interplay between electronic quantum trajectories.* Physical Review Letters, **84**, 17, page 3791, (2000). [Cited on page 55.]

[PD-USGov-NASA] W. PD-USGov-NASA. *A "chiral" molecule is one that is not superimposable with its mirror image. Like left and right hands that have a thumb.* `https://commons.wikimedia.org/wiki/File:Chirality_with_hands.svg`. [Online; accessed 19-July-2022]. [Cited on page 16.]

[Peacock 01] R. D. Peacock & B. Stewart. *Natural Circular Dichroism in X-ray Spectroscopy.* The Journal of Physical Chemistry B, **105**, 2, pages 351–360, (2001). [Cited on page 145.]

[Peatross 94] J. Peatross, J. Chaloupka & D. Meyerhofer. *High-order harmonic generation with an annular laser beam.* Optics letters, **19**, 13, pages 942–944, (1994). [Cited on page 40.]

[Poletto 07] L. Poletto, P. Villoresi, E. Benedetti, F. Ferrari, S. Stagira, G. Sansone & M. Nisoli. *Intense femtosecond extreme ultraviolet pulses by using a time-delay-compensated monochromator.* Optics Letters, **32**, 19, page 2897, (2007). [Cited on page 40.]

[Porat 18] G. Porat, G. Alon, S. Rozen, O. Pedatzur, M. Krüger, D. Azoury, A. Natan, G. Orenstein, B. D. Bruner, M. J. J. Vrakking & N. Dudovich. *Attosecond time-resolved photoelectron holography.* Nature Communications, **9**, 2805, (2018). [Cited on pages 125, 157, and 162.]

[Powis 00] I. Powis. *Photoelectron Circular Dichroism of the Randomly Oriented Chiral Molecules Glyceraldehyde and Lactic Acid.* The Journal of Chemical Physics, **112**, 1, pages 301–310, (2000). [Cited on pages 16, 18, 76, and 121.]

[Powis 08] I. Powis, C. J. Harding, G. A. Garcia & L. Nahon. *A Valence Photoelectron Imaging Investigation of Chiral Asymmetry in the Photoionization of Fenchone and Camphor*. ChemPhysChem, **9**, 3, pages 475–483, (2008). [Cited on page 77.]

[Powis 14] I. Powis. *Communication: The influence of vibrational parity in chiral photoionization dynamics*. The Journal of Chemical Physics, **140**, 11, page 111103, (2014). [Cited on page 79.]

[Pronin 11] O. Pronin, V. Pervak, E. Fill, J. Rauschenberger, F. Krausz & A. Apolonski. *Ultrabroadband efficient intracavity XUV output coupler*. Optics Express, **19**, 11, page 10232, (2011). [Cited on page 40.]

[Pullen 15] M. G. Pullen, B. Wolter, A.-T. Le, M. Baudisch, M. Hemmer, A. Senftleben, C. D. Schröter, J. Ullrich, R. Moshammer, C. D. Lin & J. Biegert. *Imaging an aligned polyatomic molecule with laser-induced electron diffraction*. Nature Communications, **6**, 1, page 7262, (2015). [Cited on page 127.]

[Rabinovitch 65] K. Rabinovitch, L. Canfield & R. Madden. *A method for measuring polarization in the vacuum ultraviolet*. Applied Optics, **4**, 8, pages 1005–1010, (1965). [Cited on page 35.]

[Rafiee Fanood 14] M. M. Rafiee Fanood, I. Powis & M. H. M. Janssen. *Chiral Asymmetry in the Multiphoton Ionization of Methyloxirane Using Femtosecond Electron–Ion Coincidence Imaging*. The Journal of Physical Chemistry A, **118**, 49, pages 11541–11546, (2014). [Cited on page 82.]

[Rafiee Fanood 15] M. M. Rafiee Fanood, N. B. Ram, C. S. Lehmann, I. Powis & M. H. M. Janssen. *Enantiomer-specific analysis of multicomponent mixtures by correlated electron imaging–ion mass spectrometry*. Nature Communications, **6**, 7511, (2015). [Cited on page 82.]

[Rafiee Fanood 16] M. M. Rafiee Fanood, M. H. M. Janssen & I. Powis. *Wavelength dependent photoelectron circular dichroism of limonene studied by femtosecond multiphoton laser ionization and electron-ion coincidence imaging*. The Journal of Chemical Physics, **145**, 12, page 124320, (2016). [Cited on page 111.]

[Rafiee Fanood 18] M. M. Rafiee Fanood, H. Ganjitabar, G. A. Garcia, L. Nahon, S. Turchini & I. Powis. *Intense Vibronic Modulation of the*

Chiral Photoelectron Angular Distribution Generated by Photoionization of Limonene Enantiomers with Circularly Polarized Synchrotron Radiation. ChemPhysChem, **19**, 8, pages 921–933, (2018). [Cited on page 111.]

[Ray 99] K. Ray, S. Ananthavel, D. Waldeck & R. Naaman. *Asymmetric scattering of polarized electrons by organized organic films of chiral molecules*. Science, **283**, 5403, pages 814–816, (1999). [Cited on page 162.]

[Reid 12] K. L. Reid. *Photoelectron angular distributions: developments in applications to isolated molecular systems*. Molecular Physics, **110**, 3, pages 131–147, (2012). [Cited on page 82.]

[Ritchie 76] B. Ritchie. *Theory of the angular distribution of photoelectrons ejected from optically active molecules and molecular negative ions*. Physical Review A, **13**, 4, pages 1411–1415, (1976). [Cited on pages 16, 18, and 76.]

[Rouxel 22] J. R. Rouxel & S. Mukamel. *Molecular chirality and its monitoring by ultrafast X-ray pulses*. Chemical Reviews, (2022). [Cited on page 163.]

[Rozen 19] S. Rozen, A. Comby, E. Bloch, S. Beauvarlet, D. Descamps, B. Fabre, S. Petit, V. Blanchet, B. Pons, N. Dudovich*et al.* *Controlling subcycle optical chirality in the photoionization of chiral molecules*. Physical Review X, **9**, 3, page 031004, (2019). [Cited on page 162.]

[Salières 01] P. Salières, B. Carré, L. Le Déroff, F. Grasbon, G. Paulus, H. Walther, R. Kopold, W. Becker, D. Milosevic, A. Sanpera*et al.* *Feynman's path-integral approach for intense-laser-atom interactions*. Science, **292**, 5518, pages 902–905, (2001). [Cited on pages 121 and 122.]

[Sansone 10] G. Sansone, F. Kelkensberg, J. Pérez-Torres, F. Morales, M. F. Kling, W. Siu, O. Ghafur, P. Johnsson, M. Swoboda, E. Benedetti*et al.* *Electron localization following attosecond molecular photoionization*. Nature, **465**, 7299, pages 763–766, (2010). [Cited on page 120.]

[Schaefer 07] B. Schaefer, E. Collett, R. Smyth, D. Barrett & B. Fraher. *Measuring the Stokes polarization parameters*. American Journal of Physics, **75**, 2, pages 163–168, (2007). [Cited on pages 30 and 31.]

[Schmidt 17] B. E. Schmidt, A. Hage, T. Mans, F. Légaré & H. J. Wörner. *Highly stable, 54mJ Yb-InnoSlab laser platform at 0.5 kW average power.* Optics express, **25**, 15, pages 17549–17555, (2017). [Cited on page 23.]

[Schrøder 15] S. D. Schrøder, J. H. Wallberg, J. A. Kroll, Z. Maroun, V. Vaida & H. G. Kjaergaard. *Intramolecular hydrogen bonding in methyl lactate.* The Journal of Physical Chemistry A, **119**, 37, pages 9692–9702, (2015). [Cited on page 100.]

[Sen 22] A. Sen, A. Sinha, S. Sen & R. Gopal. *Above-threshold ionization of argon with ultrashort orbital-angular-momentum beams.* Physical Review A, **106**, 2, page 023103, (2022). [Cited on page 162.]

[Shafir 12] D. Shafir, H. Soifer, B. D. Bruner, M. Dagan, Y. Mairesse, S. Patchkovskii, M. Y. Ivanov, O. Smirnova & N. Dudovich. *Resolving the time when an electron exits a tunnelling barrier.* Nature, **485**, 7398, pages 343–346, (2012). [Cited on page 125.]

[Siegman 86] A. E. Siegman. Lasers. University science books, (1986). [Cited on page 167.]

[Singh] D. Singh & R. Minns. *Ultrafast Multiphoton Photoelectron Circular Dichroism in α-Pinene.* [Cited on page 100.]

[Skruszewicz 14] S. Skruszewicz, J. Passig, A. Przystawik, N. X. Truong, M. Köther, J. Tiggesbäumker & K.-H. Meiwes-Broer. *A new design for imaging of fast energetic electrons.* International Journal of Mass Spectrometry, **365-366**, pages 338–342, (2014). [Cited on page 52.]

[Smirnova 09] O. Smirnova, Y. Mairesse, S. Patchkovskii, N. Dudovich, D. Villeneuve, P. Corkum & M. Y. Ivanov. *High harmonic interferometry of multi-electron dynamics in molecules.* Nature, **460**, 7258, pages 972–977, (2009). [Cited on page 120.]

[Sparling 22] C. Sparling & D. Townsend. *Tomographic reconstruction techniques optimized for velocity-map imaging applications.* The Journal of Chemical Physics, **157**, 11, page 114201, (2022). [Cited on pages 47 and 154.]

[Stark 21] H. Stark, J. Buldt, M. Müller, A. Klenke & J. Limpert. *1 kW, 10 mJ, 120 fs coherently combined fiber CPA laser system.* Optics Letters, **46**, 5, pages 969–972, (2021). [Cited on page 23.]

[Stener 04] M. Stener, G. Fronzoni, D. Di Tommaso & P. Decleva. *Density functional study on the circular dichroism of photoelectron angular distribution from chiral derivatives of oxirane.* Journal of Chemical Physics, **120**, 7, pages 3284–3296, (2004). [Cited on page 77.]

[Strasser 00] D. Strasser, X. Urbain, H. Pedersen, N. Altstein, O. Heber, R. Wester, K. Bhushan & D. Zajfman. *An innovative approach to multiparticle three-dimensional imaging.* Review of Scientific Instruments, **71**, 8, pages 3092–3098, (2000). [Cited on page 44.]

[Strickland 85] D. Strickland & G. Mourou. *Compression of amplified chirped optical pulses.* Optics communications, **55**, 6, pages 447–449, (1985). [Cited on page 23.]

[Szipöcs 94] R. Szipöcs, K. Ferencz, C. Spielmann & F. Krausz. *Chirped multilayer coatings for broadband dispersion control in femtosecond lasers.* Optics letters, **19**, 3, pages 201–203, (1994). [Cited on page 23.]

[Tajima 95] S. Tajima, Y. Nagai, O. Sekiguchi, M. Fujishige & N. Uchida. *Fragmentation of the metastable molecular ion of methyl lactate: The formation of oxygen-protonated methanol [CH3OH2]+ involving double hydrogen atom transfers.* Journal of the American Society for Mass Spectrometry, **6**, 3, pages 202–206, (1995). [Cited on pages 112 and 115.]

[Takahashi 04] E. J. Takahashi, H. Hasegawa, Y. Nabekawa & K. Midorikawa. *High-throughput, high-damage-threshold broadband beam splitter for high-order harmonics in the extreme-ultraviolet region.* Optics letters, **29**, 5, pages 507–509, (2004). [Cited on pages 39 and 40.]

[Tao 16] Z. Tao, C. Chen, T. Szilvási, M. Keller, M. Mavrikakis, H. Kapteyn & M. Murnane. *Direct time-domain observation of attosecond final-state lifetimes in photoemission from solids.* Science, **353**, 6294, pages 62–67, (2016). [Cited on page 34.]

[Tia 17] M. Tia, M. Pitzer, G. Kastirke, J. Gatzke, H.-K. Kim, F. Trinter, J. Rist, A. Hartung, D. Trabert, J. Siebert, K. Henrichs, J. Becht, S. Zeller, H. Gassert, F. Wiegandt, R. Wallauer, A. Kuhlins, C. Schober, T. Bauer, N. Wechselberger, P. Burzynski, J. Neff, M. Weller, D. Metz, M. Kircher, M. Waitz, J. B. Williams, L. P. H. Schmidt, A. D. Müller, A. Knie, A. Hans, L. Ben Ltaief, A. Ehresmann, R. Berger, H. Fukuzawa, K. Ueda,

H. Schmidt-Böcking, R. Dörner, T. Jahnke, P. V. Demekhin & M. Schöffler. *Observation of Enhanced Chiral Asymmetries in the Inner-Shell Photoionization of Uniaxially Oriented Methyloxirane Enantiomers.* The Journal of Physical Chemistry Letters, **8**, 13, pages 2780–2786, (2017). [Cited on pages 79 and 111.]

[Turchini 09] S. Turchini, D. Catone, G. Contini, N. Zema, S. Irrera, M. Stener, D. Di Tommaso, P. Decleva & T. Prosperi. *Conformational Effects in Photoelectron Circular Dichroism of Alaninol.* ChemPhysChem, **10**, 11, pages 1839–1846, (2009). [Cited on page 77.]

[Turchini 13] S. Turchini, D. Catone, N. Zema, G. Contini, T. Prosperi, P. Decleva, M. Stener, F. Rondino, S. Piccirillo, K. C. Prince & M. Speranza. *Conformational Sensitivity in Photoelectron Circular Dichroism of 3-Methylcyclopentanone.* ChemPhysChem, **14**, 8, pages 1723–1732, (2013). [Cited on pages 76, 77, and 78.]

[Uiberacker 07] M. Uiberacker, T. Uphues, M. Schultze, A. J. Verhoef, V. Yakovlev, M. F. Kling, J. Rauschenberger, N. M. Kabachnik, H. Schröder, M. Lezius*et al. Attosecond real-time observation of electron tunnelling in atoms.* Nature, **446**, 7136, pages 627–632, (2007). [Cited on page 120.]

[Ullrich 03] J. Ullrich, R. Moshammer, A. Dorn, R. Dörner, L. P. H. Schmidt & H. Schmidt-Böcking. *Recoil-ion and electron momentum spectroscopy: reaction-microscopes.* Reports on Progress in Physics, **66**, 9, page 1463, (2003). [Cited on pages 44 and 57.]

[Vallance 14] C. Vallance, M. Brouard, A. Lauer, C. S. Slater, E. Halford, B. Winter, S. J. King, J. W. Lee, D. E. Pooley, I. Sedgwick*et al. Fast sensors for time-of-flight imaging applications.* Physical Chemistry Chemical Physics, **16**, 2, pages 383–395, (2014). [Cited on page 44.]

[van der Laan 14] G. van der Laan & A. I. Figueroa. *X-ray magnetic circular dichroism—A versatile tool to study magnetism.* Coordination Chemistry Reviews, **277**, pages 95–129, (2014). [Cited on page 34.]

[Veyrinas 16] K. Veyrinas, V. Gruson, S. J. Weber, L. Barreau, T. Ruchon, J.-F. Hergott, J.-C. Houver, R. Lucchese, P. Salières & D. Dowek. *Molecular frame photoemission by a comb of elliptical high-order*

harmonics: a sensitive probe of both photodynamics and harmonic complete polarization state. Faraday discussions, **194**, pages 161–183, (2016). [Cited on page 36.]

[Wiley 55] W. Wiley & I. H. McLaren. *Time-of-flight mass spectrometer with improved resolution.* Review of scientific instruments, **26**, 12, pages 1150–1157, (1955). [Cited on page 44.]

[Wollenhaupt 13] M. Wollenhaupt, C. Lux, M. Krug & T. Baumert. *Tomographic Reconstruction of Designer Free-Electron Wave Packets.* ChemPhysChem, **14**, 7, pages 1341–1349, (2013). [Cited on page 47.]

[Würzler 18] D. Würzler, N. Eicke, M. Möller, D. Seipt, A. M. Sayler, S. Fritzsche, M. Lein & G. G. Paulus. *Velocity map imaging of scattering dynamics in orthogonal two-color fields.* Journal of Physics B: Atomic, Molecular and Optical Physics, **51**, 1, page 015001, (2018). [Cited on page 52.]

[Würzler 19] D. Würzler. *Untersuchung und Simulation der Ionisations- und Streudynamik von Photoelektronen mithilfe von Zwei-Farben-Feldern.* PhD thesis, Friedrich-Schiller-Universität Jena, (2019). [Cited on page 52.]

[Yao 20] K. Yao, F. Willems, C. von Korff Schmising, C. Strüber, P. Hessing, B. Pfau, D. Schick, D. Engel, K. Gerlinger, M. Schneider*et al. A tabletop setup for ultrafast helicity-dependent and element-specific absorption spectroscopy and scattering in the extreme ultraviolet spectral range.* Review of Scientific Instruments, **91**, 9, page 093001, (2020). [Cited on pages 41 and 44.]

[Yu 15] J. Yu, X. Sun, Y. Shao, M. Li, Q. Gong & Y. Liu. *Retrieving the ionization dynamics of high-energy photoelectrons in elliptically polarized laser fields.* Physical Review A, **92**, 4, page 043411, (2015). [Cited on page 142.]

[Zhang 14] X. Zhang, Q. Liu, J.-W. Luo, A. J. Freeman & A. Zunger. *Hidden spin polarization in inversion-symmetric bulk crystals.* Nature Physics, **10**, 5, pages 387–393, (2014). Number: 5 Publisher: Nature Publishing Group. [Cited on page 40.]

[Zhao 20] X. Zhao, S.-J. Wang, W.-W. Yu, H. Wei, C. Wei, B. Wang, J. Chen & C. D. Lin. *Metrology of Time-Domain Soft X-Ray Attosecond Pulses and Reevaluation of Pulse Durations of Three Recent Experiments.* Physical Review Applied, **13**, 3, page 034043, (2020). [Cited on page 34.]

Mesure et contrôle de l'interaction lumière-matière chirale à l'échelle attoseconde

Résumé : Les molécules chirales existent sous deux formes images mirroir, appelées énantiomères, qui ont les mêmes propriétés physiques et chimiques et ne peuvent être distinguées que via leur interaction avec un autre système chirale, comme de la lumière polarisée circulairement. De nombreux processus biologiques sont chiro-sensibles, et élucider les aspects dynamiques de la chiralité est d'importance primordiale pour la chimie, la biologie et la pharmacologie. L'étude des processus chiraux ultrarapides nécessite de nouvelles techniques expérimentales à l'échelle attoseconde. L'objectif de cette thèse sera de développer de nouvelles approches pour mesurer et contrôler l'interaction lumière-matière chirale en utilisant les trois pilliers de la science attoseconde: la génération d'harmoniques d'ordre élevé, la photoionisation, et l'absorption transitoire.

Mots-clés : Chiralité - Laser à haute cadence - Spectroscopie de coïncidence - Dichroisme circulaire de photoelectrons - Dynamiques Femtoseconde et Attoseconde

Measuring and manipulating chiral light-matter interaction on the attosecond timescale

Abstract : Chiral molecules exist as two mirror forms, so-called enantiomers, which have essentially the same physical and chemical properties and can only be distinguished via their interaction with a chiral system, such as circularly polarized light. Many biological processes are chiral-sensitive and unraveling the dynamical aspects of chirality is of prime importance for chemistry, biology and pharmacology. Studying the ultrafast electron dynamics of chiral processes requires characterization techniques at the attosecond timescale. The thesis aims at developing new approaches to measure and manipulate chiral lightmatter interaction using the three pillars of attosecond science: high-order harmonic generation, photoionization, and transient absorption.

Key-words : Chirality - High repetition rate laser - Coincidence spectroscopy - Photoelectron circular dichroism - Femtosecond and Attosecond Dyncamics